APPLICATION OF FINITE ELASTIC THEORY TO THE BEHAVIOR OF RUBBER-LIKE MATERIALS

Thesis by

William L. Ko

In Partial Fulfillment of the Requirements
For the Degree of
Doctor of Philosophy

California Institute of Technology
Pasadena, California
1963

ACKNOWLEDGMENT

The author, William L. Ko, expresses his deep appreciation to Professor M. L. Williams, and especially to Dr. P. J. Blatz, for their valuable advice, many ideas, sound constructive criticisms, and above all, their personal interest, friendly attitude, continuous encouragement which made this investigation most stimulating and enjoyable.

He also wishes to express his sincere thanks to Mr. F. Salcedo, Aerojet General Corporation, and to Dr. R. F. Landel and Mr. R. E. Neal of the Jet Propulsion Laboratory, for their technical cooperation during the course of the experimental phases of this work and to Mrs. Eileen E. Walsh for help in preparing the manuscript.

Finally it is a pleasure to acknowledge the important financial assistance of the Aerojet General Corporation, during the past three years, as well as the National Aeronautics and Space Administration Fellowship for the 1962-1963 school year.

ABSTRACT

In Part I, methods for determining the strain energy function and the associated constitutive stress-deformation law for rubber-like materials is undertaken and the mechanics of data reduction needed to determine some parameters of the theory are displayed. Experiments were performed in four different stress fields on a foamed polyurethane rubber (dilatable rubber) and on several kinds of continuum rubbers. A new strain energy function and the associated stress-deformation law for a foamed rubber are generated which correlate most of the data to a high degree of accuracy. A parameter appearing in the functional expression for a foam rubber has the same significance as Poisson's ratio in infinitesimal elastic theory. For continuum rubbers, the isotropic Neo-Hookean representations of quasi-static behavior is found to be sufficient over most of the whole range of extension.

In Part II, geometrical representations of an isotropic failure surface based on various criteria are depicted both in principal stress and principal stretch spaces for elastic materials. The experimental data are compared with all criteria and the results are discussed.

In Part III, finite elastic theory is used to determine the stress and deformation fields around the base of a radial crack in an infinitely long rubber log opened by a facially bonded rigid wedge-shaped bellow.

In the last Part, the topology of interstices idealized as closest packed spherical holes (idealized foam structure) is investigated. Equivalent elastic constants are calculated for rubbery interstices of both hexagonal and face-centered cubic closest packings under small displacement.

TABLE OF CONTENTS

PART I

DETERMINATION OF STRAIN ENERGY FUNCTION AND THE ASSOCIATED CONSTITUTIVE STRESS-DEFORMATION LAW FOR LARGE DEFORMATIONS

I.1. INTRODUCTION

In classical infinitesimal elastic theory the Hookean strain and rotation are so small that the product of Hookean strains, or the product of Hookean strain and rotation, or the product of rotations are disregarded. However, this is not legitimate for deformations in which the above products may be many times greater than the Hookean strain itself. A hyper-elastic (or rubbery) material is a good example of a material which can evince such deformation, and whose typical features are high extensibility under relatively small applied load (uniaxial ultimate extension may go up to 1000 per cent), high recoverability without noticeable hysteresis, and no yielding.

Since Hooke, a number of theoreticians have attempted to extend the classical infinitesimal elastic theory to formulate more general constitutive stress-deformation law to account for large deformations. As a result of the formalism of continuum elasticity enunciated by Rivlin (17), Reiner (18), and Truesdell (19) etc., there has developed a rational foundation for the analytical representation of the elastic deformation of continuous media under the assumption that the elastic material is (i) a homogeneous continuum, ii) isotropic both in its natural and its deformed state, and iii) quasi-static (infinitely slow motion) during a deformation process. Inherent in these representations is the notion of a strain energy function, W, which, for a homogeneous, isotropic, isothermal elastomeric continuum, is an explicit function of certain invariants, which in turn are functions only of the proper values of the deformation tensor. Assuming the smoothness of W on these invariants, it can be expanded in triply-infinite series in these invariants and the leading terms can be identified by comparison with infinitesimal Hooke-Cauchy theory, however, the determination of the coefficients of higher order terms depends entirely on experiments. The importance of finding the explicit form of W lies in the fact that the method of solution in large deformation theory is usually inverse to that of linear theory, i.e. a class of deformations is first assumed and reduced, then the stresses necessary to produce such deformations are calculated provided the strain energy function, W, is known.

In this part we proceed to show how the nature of the strain energy function can be deduced from experiments on rubbery materials with the aid of a new parameter ν which in the limit has the same significance as Poisson's ratio in infinitesimal elastic theory. A great deal of work (17) has been carried out along this line. Most of it has been limited to nearly incompressible materials, and in the course of data reduction, incompressibility was assumed since most rubber ($\nu = 0.49997$) is practically incompressible. In order to investigate the dilatational effect, a highly dilatable elastic material (foamed rubber) is used, and data are obtained in uniaxial, strip-biaxial, homogeneous-biaxial, and triaxial tensile tests. Several kinds of continuum rubbers are also tested in the same stress fields in order to determine the nature of the gradients of W with respect to its invariants which appear in the stress-deformation law.

I. 2 THE CONSTITUTIVE STRESS-DEFORMATION LAW IN FINITE ELASTIC THEORY

A. General Stress Field

Let an isotropic continous elastic body be referred to a rectangular Cartesian system. Initially at time, t=0, a typical point in the undeformed body having coordinates $p_o(x^i)$ is displaced continuously to a new position $P(X^i)$ at t=t. The Cauchy-Green's deformation tensor which characterizes this mapping is denoted by:

$$C_{ik} = \frac{\partial X^i}{\partial x^m}\frac{\partial X^k}{\partial x^m} \qquad (I.1)$$

Under isothermal deformation the strain energy function, W, measured per unit volume of the undeformed homogeneous isotropic continuous body in three dimensional space, is a function only of the three invariants* of the deformation tensor C_{ik}. Hence, from the principle of virtual work the physical stresses resulting in the deformed body are given by (see Appendix and (19))

$$\bar{\sigma}_{ik} = \frac{2}{\sqrt{I_3}}\left[\frac{\partial W}{\partial I_1}C_{ik} - I_3\frac{\partial W}{\partial I_2}(C^{-1})_{ik} + \left(I_2\frac{\partial W}{\partial I_2} + I_3\frac{\partial W}{\partial I_3}\right)\delta_{ik}\right] \qquad (I.2)$$

where $\bar{\sigma}_{ik}$ are the true stresses referred to the deformed body, and I_1, I_2, I_3 are invariants of the deformation tensor C_{ik} given by:

$$I_1 = \mathrm{Tr}\, C_{ik} = C_{ii} \qquad (I.3)$$

$$I_2 = \sum_{i \neq k} C_{ii}C_{kk} = \frac{1}{2}\left[I_1^2 - C_{ik}C_{ki}\right] \qquad (I.4)$$

---

*These invariants are defined by equations I. 3, I. 4, I. 5.

$$I_3 = \text{Det}\, C_{ik} \tag{I.5}$$

It is our purpose to evaluate the gradients of W with respect to these invariants which appear in the constitutive law. I.2. To do so it is convenient to introduce a new set of invariants defined by:

$$J_1 = I_1 = C_{ii} \tag{I.6}$$

$$J_2 = \frac{I_2}{I_3} = (C^{-1})_{ii} \tag{I.7}$$

$$J_3 = \sqrt{I_3} = \frac{V}{V_0} = \sqrt{\text{Det}\, C_{ik}} \tag{I.8.}$$

It may be noted in passing that the invariant J_3 is the ratio of the volume of an element of the deformed body, V, to that of the undeformed body, V_0. After substitution, equation I.2 becomes;

$$\sigma_{ik} = \frac{2}{J_3}\left[W_1 C_{ik} - W_2 (C^{-1})_{ik}\right] + W_3 \delta_{ik} \tag{I.9}$$

where

$$W_k \equiv \frac{\partial W}{\partial J_k} \tag{I.10}$$

Consider now a special case of a uniform orthogonal deformation field, i.e. the deformation tensor has only the diagonal components, λ_1^2, λ_2^2, λ_3^2, where

$$\lambda_i = \frac{\partial X^i}{\partial x^i} = \text{stretch ratio} \qquad (I.11)$$

(i not summed)

In this case, equations I.6, I.7 and I.8 become:

$$J_1 = \sum_i \lambda_i^2 \qquad (I.12)$$

$$J_2 = \sum_i \frac{1}{\lambda_i^2} \qquad (I.13)$$

$$J_3 = \prod \lambda_i \qquad (I.14)$$

And the constitutive law I.2 is reduced to:

$$\tilde{\sigma}_i J_3 = \sigma_i \lambda_i = 2\left[W_1 \lambda_i^2 - \frac{W_2}{\lambda_i^2}\right] + J_3 W_3 \qquad (I.15)$$

(i not summed)

where $\tilde{\sigma}_i$ is the true stress referred to the deformed cross-section, and σ_i is the so-called engineering stress referred to the undeformed cross-section.

Before using equation I.15 in connection with experimental data to determine W-gradients, the character of the leading terms of W-gradients under small strain will firstly be established from linear theory. If W is a smooth function of the deformation invariants, it can be expanded in a triply-infinite series in its scalar invariants:

$$W = \sum_{\substack{\ell, m, n \\ =0}}^{\infty} C_{\ell m n} (J_1 - 3)^{\ell} (J_2 - 3)^{m} (J_3 - 1)^{n} \tag{I.16}$$

in which $C_{ooo}=0$, since the reference state is undeformed. The deformation invariants can be expressed in terms of the small strain invariants in the following way:

$$\lambda_i = 1 + e_i \tag{I.17}$$

where

$$e_i = \frac{\partial u_i}{\partial x_i} = \text{Hookean strain}$$

$$J_1 = 3 + 2\vartheta + \vartheta^2 - 2\vartheta_2 \approx 3 + 2\vartheta \tag{I.18}$$

$$J_2 = 3 - 2\vartheta + 3\vartheta^2 - 6\vartheta_2 \approx 3 - 2\vartheta \tag{I.19}$$

$$J_3 = 1 + \vartheta + \vartheta_2 + \vartheta_3 \approx 1 + \vartheta \tag{I. 20}$$

where

$$\vartheta = \sum_i e_i \tag{I. 21}$$

$$\vartheta_2 = \sum_{i \neq k} e_i e_k \tag{I. 22}$$

$$\vartheta_3 = \prod e_i \qquad \text{(I. 23)}$$

After differentiating equation I. 16 with respect to J-invariants, substituting the ϑ-invariants, and grouping terms, the W-gradients are given by:

$$W_1 = A + B\vartheta + \cdots \qquad \text{(I. 24)}$$

$$W_2 = C + D\vartheta + \cdots \qquad \text{(I. 25)}$$

$$W_3 = E + F\vartheta + \cdots \qquad \text{(I. 26)}$$

Equation I. 15 can now be written up to linear terms as following:

$$\sigma_i \approx (1-e_i)\left[2(1+2e_i)(A+B\vartheta) - 2(1-2e_i)(C+D\vartheta) + (1+\vartheta)(E+F\vartheta)\right] \qquad \text{(I. 27)}$$

which is to be compared with the more conventional form of Hooke's law,

$$\sigma_i = (K - \tfrac{2}{3}\mu)\vartheta + 2\mu e_i \qquad \text{(I. 28)}$$

After comparing the corresponding coefficients, there results three equations for six parameters:

$$2A - 2C + E = 0 \qquad \text{(I. 29)}$$

$$2A + 6C - E = 2\mu \qquad \text{(I. 30)}$$

$$2B + 2D + E + F = K - \frac{2}{3}\mu \text{ , from which results} \qquad \text{(I. 31)}$$

$$A + C = \frac{\mu}{2} \qquad \text{I. 32)}$$

It is observed that the parameters A and C are related to the Mooney-Rivlin parameters C_1 and C_2* in such a way that $C_1 = A$, $C_2 = \frac{C}{J_3}2$, so that the constancy of C does not necessarily imply the constancy of C_2, and vice versa due to the factor $J_3{}^2$.

After introducing the notation:

$$A = \frac{\mu}{2}f \qquad \text{(I. 33)}$$

$$C = \frac{\mu}{2}(1-f) \quad \text{there results} \qquad \text{(I. 34)}$$

$$E = \mu(1-2f) \qquad \text{(I. 35)}$$

$$2B - 2D + F = K - \mu\left(\frac{5}{3} - 2f\right) \qquad \text{(I. 36)}$$

where f is a material parameter such that $o \leqslant f \leqslant 1$.

---

*Mooney-Rivlin Strain Energy Function:
$W = C_1(I_1 - 3) + C_2(I_2 - 3)$, $C_1 = \frac{\partial W}{\partial I_1} = \frac{\partial W}{\partial J_1} = A$, $C_2 = \frac{\partial W}{\partial I_2} = \frac{1}{J_3^2}\frac{\partial W}{\partial J_2} = \frac{C}{J_3^2}$

We shall now consider materials which evince a behavior such that W_1 and W_2 are constants, i.e. - B, D and the coefficients of higher order terms in equations I. 24, I. 25 vanish. This is a good postulation which agreesvery well with the data of dilatable rubber as will be seen later. For those materials equation I. 36 becomes:

$$F = K - \mu\left(\frac{5}{3} - 2f\right) \tag{I. 37}$$

In addition, since W_1 and W_2 are constants, $W_{13} = W_{23} = 0$; and therefore W_3 is independent of J_1 and J_2. In view of equations I. 26, I. 35, I. 37, W_3 becomes:

$$W_3 = \mu(1-2f) + \left[K - \mu\left(\frac{5}{3} - 2f\right)\right](J_3 - 1) + O\left[(J_3-1)^2\right] + \cdots \tag{I. 38}$$

and from equation I.15 the constitutive stress-deformation law becomes:

$$\bar{\sigma}_i J_3 = \sigma_i \lambda_i = \mu\left[f\lambda_i^2 - \frac{1-f}{\lambda_i^2}\right] + J_3 W_3 \,(J_3 \text{ only}) \tag{I. 39}$$

(i not summed)

Since the principal stress difference is independent of W_3, the use of it permits one to determine $\{\mu, f\}$ directly by plotting:

$$\frac{\sigma_i\lambda_i - \sigma_j\lambda_j}{\lambda_i^2 - \lambda_j^2} = \mu\left[f + \frac{1-f}{\lambda_i^2\lambda_j^2}\right] \qquad \text{vs.} \qquad \frac{1}{\lambda_i^2\,\lambda_j^2} \tag{I. 40}$$

(i, j not summed)

in which $\mu f\ [= 2W_1]$ is the intercept and $\mu\,(1-f)\ [= 2W_2]$ is the slope if the plot is linear which turned out to be so in our experiments.

B. Special Stress Fields

In order to determine W_3, it is necessary to express λ_i as functions of J_3 and evaluate W_3 from equation I. 39 in one direction of i, j, k for which stress is to be presumed zero. This is done in the following way.

1. Uniaxial Tension

For this case:

$$\lambda_1 = \lambda, \quad \lambda_2 = \lambda_3 = \lambda_{lat} \; ; \quad \sigma_1 = \sigma_{uni} \; , \quad \sigma_2 = \sigma_3 = 0 \qquad \text{(I. 41)}$$

$$J_3 = \lambda \lambda_{lat}^2 \qquad \text{(I. 42)}$$

And by setting i = 1, j = 2 or 3, equation I. 40 becomes:

$$\frac{\sigma_{uni}\lambda}{\lambda^2 - \lambda_{lat}^2} = \mu\left[f + \frac{1-f}{\lambda^2\lambda_{lat}^2}\right] \qquad \text{(I. 43)}$$

Equation I. 39 for the lateral directions (set i = 2 or 3) becomes:

$$0 = \mu\left[f\lambda_{lat}^2 - \frac{1-f}{\lambda_{lat}^2}\right] + J_3 W_3 \qquad \text{(I. 44)}$$

Substitution of equation I. 42 into equation I. 44 yields :

$$W_3 = -\mu\left[\frac{f}{\lambda} - \frac{(1-f)\lambda}{J_3^2}\right] \qquad \text{(I. 45)}$$

It remains now to relate J_3 and λ. We define a new parameter ν for large deformation as follows:

$$\nu = -\frac{\ln \lambda_{lat}}{\ln \lambda} \qquad \text{(I. 46)}$$

or
$$\lambda^{\nu}\lambda_{lat} = 1 \qquad (I.47)$$

which turned out to correlate the data very nicely. For small strains equation I. 46 may be linearized to a familiar form:

$$\nu = -\frac{\epsilon_{lat}}{\epsilon} \qquad (I.48)$$

where
$$\epsilon = \lambda - 1 , \qquad \epsilon_{lat} = \lambda_{lat} - 1 \qquad (I.49)$$

Thus ν has the significance of Poisson's ratio under small deformations. Under the above definition equation I. 42 becomes:

$$J_3 = \lambda^{1-2\nu} \qquad (I.50)$$

The relation I. 46 is not unique in large deformation theory, since there are many ways of defining ν which could be reduced to the form I. 48 of linear theory (e. g. $\lambda^2_{lat} = \frac{1}{1+2\nu(\lambda-1)}$ etc.); which of these functions is useful can only be decided by experimental evidence. Of these functions the definition I. 46 was found to fit the data best.

Now using equation I. 50, equation I. 45 becomes:

$$J_3 W_3 = -\mu\left[f\, J_3^{-\frac{2\nu}{1-2\nu}} - (1-f)\, J_3^{\frac{2\nu}{1-2\nu}} \right] \qquad (I.51)$$

which, after integration and use of equations I. 24, I. 25, in which B and D are set to zero according to the postulation, leads to :

$$W(J_1, J_2, J_3) = \frac{\mu}{2} f\left[(J_1 - 3) + \frac{1-2\nu}{\nu}\left(J_3^{-\frac{2\nu}{1-2\nu}} - 1\right)\right] + \frac{\mu}{2}(1-f)\left[(J_2 - 3) + \frac{1-2\nu}{\nu}\left(J_3^{\frac{2\nu}{1-2\nu}} - 1\right)\right] \qquad (I.52)$$

where

$$J_1 = I_1 = C_{ii} \tag{I.12}$$

$$J_2 = \frac{I_2}{I_3} = (C^{-1})_{ii} \tag{I.13}$$

$$J_3 = \sqrt{I_3} = \sqrt{\operatorname{Det} C_{ik}} = \frac{V}{V_o} \tag{I.14}$$

We thus have an isothermal elastic equation of state for large deformations, from which one can predict the stress-deformation behavior in any stress or displacement fields by using (I. 15). For small strain equation I. 52 reduces to the usual Hookean strain energy function. As we shall see, the prediction of equation I. 52 agrees with most of the data very nicely for a foamed rubber. In order to apply it to continuum rubbers however, very accurate large deformation data in certain stress fields, especially those close to hydrostatic ones, are needed to evaluate the dilatational term $J_3^{\pm \frac{2\nu}{1-2\nu}}$. (Since the linear value of ν is 0.49997, therefore the exponent is of the order of 3×10^4.)

The constitutive stress-deformation law associated with (I. 52) becomes:

$$\bar{\sigma}_i J_3 = \sigma_i \lambda_i = \mu f\left[\lambda_i^2 - J_3^{-\frac{2\nu}{1-2\nu}}\right] - \mu(1-f)\left[\frac{1}{\lambda_i^2} - J_3^{\frac{2\nu}{1-2\nu}}\right] \tag{I.53}$$

(i not summed)

which also reduces to the ordinary Hooke-Cauchy law for small strains.

2. Strip-Biaxial Tension* (Plane-Strain)

For this case:

$$\lambda_1 = \lambda, \quad \lambda_2 = 1, \quad \lambda_3 = \lambda_{th}; \quad \sigma_1 = \sigma_{s-bi}, \quad \sigma_2 = \sigma_{lat}, \quad \sigma_3 = 0 \tag{I.54}$$

---

* If the Poisson's ratio is 1/2, this stress field becomes pure shear for small deformations.

And the dilatation-stretch relation becomes:

$$J_3 = \lambda \lambda_{th} \tag{I.55}$$

Setting i = 1, j = 3, equation I.40 becomes:

$$\frac{\sigma_{s\text{-}bi}\, \lambda}{\lambda^2 - \lambda^2_{th}} = \mu \left[f + \frac{1-f}{\lambda^2 \lambda^2_{th}} \right] \tag{I.56}$$

and by setting i= 3 equation I.53 is reduced to:

$$f \left[\lambda^2_{th} - J_3^{-\frac{2\nu}{1-2\nu}} \right] = (1-f) \left[\frac{1}{\lambda^2_{th}} - J_3^{\frac{2\nu}{1-2\nu}} \right] \tag{I.57}$$

An additional check on the theory would be using the equation corresponding to i = 2, however, since the measurement of σ_{lat} is not easy, it is not used.

Solution of equation I.57 leads to

$$\lambda_{th} = J_3^{-\frac{\nu}{1-2\nu}} \tag{I.58}$$

and by using equation I.55 it follows that:

$$\lambda^{\frac{\nu}{1-\nu}} \lambda_{th} = 1 , \qquad \text{or} \qquad J_3 = \lambda^{\frac{1-2\nu}{1-\nu}} \tag{I.59}$$

These expressions may be linearized to the result that is given by the plane-strain case in linear theory, thus reinforcing the interpretation of the parameter ν as a large deformation Poisson's ratio. Namely, expressions I.59 can be obtained by replacing ν by $\frac{\nu}{1-\nu}$ in the uniaxial expression I.50.

3. Homogeneous-Biaxial Tension

For this case:

$$\lambda_1 = \lambda_2 = \lambda\,, \quad \lambda_3 = \lambda_{th}\,; \quad \sigma_1 = \sigma_2 = \sigma_{h\text{-}bi}\,, \quad \sigma_3 = 0 \qquad (I.60)$$

The dilatation-stretch relation becomes:

$$J_3 = \lambda^2 \lambda_{th} \qquad (I.61)$$

The constitutive relations are identical with equations I.56 and I.57. Solution of equation I.57 for this case also leads to the form I.58, but after combining with equation I.61, it leads to :

$$\lambda^{\frac{2\nu}{1-\nu}} \lambda_{th} = 1\,, \qquad \text{or} \qquad J_3 = \lambda^{\frac{2(1-2\nu)}{1-\nu}} \qquad (I.62)$$

Equation I.62 differs from equation I.59 only by the presence of factor 2 in the numerator of the exponent which arises from the equal deformations imposed on two coordinates.

4. Triaxial Tension

This stress field will provide information about the nature of W_3, which can not be obtained from uniaxial and biaxial fields because of the low stresses involved and the high value of the exponent $\frac{1}{1-2\nu}$. For this case:

$$\lambda_1 = \lambda\,, \quad \lambda_2 = \lambda_3 = 1\,; \quad \sigma_1 = \sigma_{tri}\,, \quad \sigma_2 = \sigma_3 = \sigma_{lat} \qquad (I.63)$$

The dilatation-stretch relation becomes:

$$J_3 = \lambda \qquad (I.64)$$

And the constitutive law is reduced to the form:

$$\frac{\sigma_{tri}}{\mu} = \left[J_3^{\frac{2(1-\nu)}{1-2\nu}} - 1 \right]\left[f J_3^{-\frac{1}{1-2\nu}} + \frac{(1-f)}{J_3^3} \right] \tag{I. 65}$$

Since in this equation there are three unknown parameters, μ, ν, f to be determined, one must know any two of them in order to determine the third one. Therefore it is necessary to use the data obtained in the previous three different stress fields. Thus equation I. 65 can only be used for double check of the accuracy of the theory. Hence, the averaged shear modulus, μ , is to be used, and f (shear modulus fractional factor) is determined by taking the value ν the same as that of the other three stress fields, or alternatively determine ν by using the value of f based on the previous three stress fields. Under such viewpoint one can make two kinds of plots from equation I. 65, namely: i) If ν is known equation I.65 yields:

$$\frac{\sigma_{tri}}{\mu\left[J_3 - J_3^{-\frac{1}{1-2\nu}}\right]} = f + (1-f)\, J_3^{-\frac{2(1-3\nu)}{1-2\nu}} \tag{I. 66}$$

and f is determined by the plot of $\dfrac{\sigma_{tri}}{\mu\left[J_3 - J_3^{-\frac{1}{1-2\nu}}\right]}$ vs. $J_3^{-\frac{2(1-3\nu)}{1-2\nu}}$

ii) If f is known equation I. 65 could be written in the form:

$$\left[\frac{\sigma_{tri}}{\mu} J_3^3 - f J_3^4 - (1-f) \right] = -f J_3^{\frac{2(1-3\nu)}{1-2\nu}} + (1-f) J_3^{\frac{2(1-\nu)}{1-2\nu}} \tag{I. 67}$$

which is hardly plotted except for special cases for which $f = 0$ or $f = 1$. As we shall see later the value f for the foam rubber is $f = 0$, and $f = 1$ for certain continuum rubbers tested. Hence, for $f = 0$ equation I. 67 is reduced to the form:

$$\left[\frac{\sigma_{tri}}{\mu} J_3^3 + 1\right] = J_3^{\frac{2(1-\nu)}{1-2\nu}} , \qquad f = 0 \tag{I. 68}$$

which permits one to determine ν from log $\left[\frac{\sigma_{tri}}{\mu} J_3^3 + 1\right]$ vs. a log J_3 plot.

Taking $f = 1$ equation I. 67 can be written as:

$$\left[\frac{\sigma_{tri}}{\mu J_3} - 1\right] = - J_3^{-\frac{2(1-\nu)}{1-2\nu}} , \qquad f = 1 \tag{I. 69}$$

Again ν is determined from the plot of log $\left[\frac{\sigma_{tri}}{\mu J_3} - 1\right]$ vs. log J_3

5. Hydrostatic Compression

Like triaxial tension, this stress field also serves the purpose of finding the nature of W_3.

For this case:

$$\lambda_1 = \lambda_2 = \lambda_3 = J_3^{\frac{1}{3}} , \qquad \sigma_1 = \sigma_2 = \sigma_3 = -p \tag{I. 70}$$

The constitutive law is reduced to the form:

$$-\frac{p}{\mu} = \left[J_3^{\frac{2(1+\nu)}{3(1-2\nu)}} - 1\right]\left[f\, J_3^{-\frac{1}{1-2\nu}} + (1-f)\, J_3^{-\frac{5}{3}}\right] \tag{I. 71}$$

Again there are three unknown parameters μ, ν, f to be determined, and the method of determining them is the same as triaxial tension.

Namely:

i) If ν is given equation I. 71 is reduced to:

$$\frac{p J_3^{\frac{1}{3}}}{\mu\left[J_3^{-\frac{2(1+\nu)}{1-2\nu}} - 1\right]} = f + (1-f)\, J_3^{-\frac{2(1-5\nu)}{3(1-2\nu)}} \tag{I. 72}$$

and the plot of $pJ_3^{\frac{1}{3}}/\mu\left[J_3^{\frac{-2(1+\nu)}{1-2\nu}} - 1\right]$ vs. $J_3^{-\frac{2(1-5\nu)}{3(1-2\nu)}}$ will determine f .

ii) If f is given equation I. 71 can be written in the form:

$$\left[\frac{p}{\mu}+\frac{f}{J_3^{1/3}}-\frac{(1-f)}{J_3^{5/3}}\right]=f\,J_3^{\frac{-1}{1-2\nu}}-(1-f)\,J_3^{\frac{-1+4\nu}{1-2\nu}} \tag{I. 73}$$

Again we will consider special cases for which f = 0 and f = 1.

For f = 0:

$$\frac{p}{\mu}-\frac{1}{J_3^{5/3}}=-J_3^{-\frac{1+4\nu}{1-2\nu}} \tag{I. 74}$$

For f = 1:

$$\frac{pJ_3^{1/3}}{\mu}+1=J_3^{-\frac{2(1+\nu)}{3(1-2\nu)}} \tag{I. 75}$$

Equations I. 74, I. 75 allow one to determine ν from the plots $\log\left[\frac{p}{\mu}-\frac{1}{J_3^{5/3}}\right]$ vs. $\log J_3$, and $\log\left[\frac{pJ_3^{1/3}}{\mu}+1\right]$ vs. $\log J_3$ respectively for f = 0 and f = 1.

I. 3 EXPERIMENTAL ADDUCTIONS

A. Description of the Experiments

In order to test the hypothesis i) that W_1 and W_2 or $\{\mu, f\}$ are constant for certain rubbers, and ii) that dilatation may be expressed by equation I. 51 with ν a constant parameter, tests were run on polyurethane foamed rubber and several kinds of continuum rubbers listed below.

1. Materials

(i) Foamed Rubber[*]

A castable polyurethane elastomer was first mixed with sodium-chloride powder, about 40μ in diameter. After curing, the foam was obtained by leaching out salt from a filled composite in hot water. The resultant foam has approximately forty seven volume per cent of voids. It is highly dilatable, and is mechanically ideal since no hysteresis is observed.

ii) Continuum Rubbers

These were prepared by curing gum stocks at 307° F or 180° F in a hot-press mold for the prescribed cure-time listed below, and then cooling the mold containing the specimen in an ambient atmosphere.

TYPE OF RUBBERS[*]	Cured at 307° F for indicated number of minutes
i) SBR-1500 (1.75 per cent Sulfur)	45
ii) SBR-1500 (3 per cent Sulfur)	45
iii) Natural Rubber (2 per cent Sulfur)	20
iv) Natural Rubber (4 per cent Sulfur)	20
v) CIS-4 Rubber	20
vi) Paracril-B Rubber	45
vii) Neoprene-GNA Rubber	20
viii) Butyl-217 Rubber	45
ix) Polyurethane Rubber	Cured at 180° F for 4 hours

---

[*] This test material was prepared by the Aerojet-General Corporation, courtesy of Mr. F. Salcedo.

[**] The materials i)~viii) were prepared by Phillip's Petroleum Corporation and cured at the Jet Propulsion Laboratory, courtesy of Dr. R. F. Landel and Mr. R. E. Neal.

2. Test Setups

All the tests were performed in an INSTRON testing machine, and all the specimens were prestressed isothermally up to 40 percent ~ 50 percent extension to eliminate hysteresis which was observed to be nearly zero. In all tests only isothermal equilibrium values were measured up to 10^{-4} inches accuracy, so that the application of the load was continuously interrupted until all friction effects were adjusted and relaxation had died out.

Figures I.1, I.2 show the technique used to evaluate uniaxial tension. A specimen is JANAF type (50, p.92) and a grid of circles was inked on the gage section. The longitudinal and lateral deformations were read under an optical comparator. Figure I.3 shows the other type of technique mainly used for the thin continuum rubbers. The ends of a specimen were glued around circular bolts by Eastman 910 adhesive, and by making use of friction between the unglued portion of specimen and the bolt surfaces, the end effect was successfully minimized, causing the rupture to take place at the middle region of the specimen. The method of measuring the deformations remains the same.

The strip-biaxial tension was produced in wide rectangular sheets (7" x 1" x 3/16" for foamed rubber, 12" x 1/2" or 1" x 0.08" for continuum rubbers) by gluing two pairs of rigid metal plates to both of the long edges (see the left and the middle pictures of figures I.6, I.7) or by gripping the long edges of specimen which has a dog bone (JANAF) cross-section (see the right hand side pictures of figures I.6, I.7). The corners of the bonding metal plates of the second type and of the grips of the third type were rounded so that the stretch ratios at the edges of a specimen was made lower than that in the center section, thus reducing the corner stress concentration. The rounded corners of the grip of the third type also served as stops against lateral contraction of a specimen after stretching. The pictures at the left hand side of figures I. 6, I. 7 show how edge contraction was prevented by gluing to the two edges retractors which were bent over rollers mounted on the rails. Load was applied normal to the long edges. Longitudinal deformation was measured by an optical comparator as in the previous case, but the thickness change was measured by twin micrometers from each side of the specimen up to 10^{-4} inches accuracy (see figure I. 4). A conducting liquid film was painted on the surface of the specimen in order to connect an electric circuit when the end points of the micro-meters come into contact with the soft rubber surface. Thus preventing the specimen from being squeezed by the micrometers. However, due to poor conductivity of the film at large strain and due to the additional thickness of the film, this method was used only for a few tests.

The homogeneous-biaxial stress field was produced in square thin sheets (3" x 3" x 3/16" for foam, 3" x 3" x 0.08" for continuum rubbers) to which were glued retractors which in turn were bent over rollers mounted on the four outer edges of two boomerang rods. The measurement of deformations was similar to that in strip-biaxial field (see figures I. 5, I. 8, I. 9).

The triaxial stress field was produced by using a thin circular disk (diameter x thickness = 2-1/2" or 3" x 1/4") whose both disk faces were bonded on plexiglass or metal flanges. The specimen was pulled in a direction normal to the disk surface (see figure I.10). The displacements for the foam material were read from the INSTRON dial gage, while the displacements of continuum rubber were measured by standard Baldwin microformers (linear differential transformers) whose signal was fed into the INSTRON X-Y plotter.

B. Data Reduction

1. Foamed Rubber

Figure I.11 shows the uniaxial stress-deformation plots, and figure I.12 shows the dimensional changes associated with the uniaxial tensile test. The plots in figure I.13 are rectified in a manner suggested by equation I.43. The straightness of the rectified curve indicates that the dependency of W_1, W_2 to the invariants is negligible and that the hypothesis of constancy of W_1 and W_2 is reasonable for the foamed rubber. It is observed that, for this foam rubber, W_1 is very small, whereas W_2 is large and positive, so that, figuratively speaking, most of the shear behavior arises from the second Mooney-Rivlin type constant. When the data of figure I.12 are plotted in the form suggested by the definition I.50, namely log J_3 against log λ as shown in figure I.14, there results a straight line with slope 1/2, giving Poisson's ratio a value 1/4. This value is used to predict theoretical slopes for the data obtained in the other stress fields. Based on this value, the theoretical uniaxial stress-deformation curve calculated from equation I.53 is plotted in figure I.11. It is seen to fit the experimental points very nicely.

Figures I.15, I.19 show the stress-deformation plots in strip-biaxial and homogeneous-biaxial tensile tests respectively. The plots based on equation I.56 also yield straight lines giving $W_1 \approx 0$ for both biaxial fields, as shown in figures I.17, I.21. Figures I.18, I.22 show the excellent agreement evinced between the log-log dilatation data and the theoretical line based on $\nu = 1/4$ in the both biaxial fields. Again we notice that the theoretical stress-deformation curves computed from equation I.53 for both biaxial stress fields agree with the experimental data very well. The results of the above three tests are summarized in table I.1.

TABLE I.1

Type of Test	Shear Modulus, (psi)	Shear Modulus Fractional Factor, f	Poisson's Ratio
Uniaxial Tension	38	0.13	1/4
Strip-Biaxial Tension	30	0.07	1/4
Homogeneous-Biaxial Tension	27	- 0.19	1/4
Average	32	0	1/4

It follows that the general stress deformation behavior of a forty seven volume per cent foamed polyurethane rubber is completely contained within the strain energy function I.52, with the experimentally determined values $\{ f = 0, \ \nu = 1/4 \}$, for which

$$W = \frac{\mu}{2}(J_2 + 2J_3 - 5) \qquad \text{(I. 76)}$$

and the constitutive law becomes:

$$\bar{\sigma}_i J_3 = \sigma_i \lambda_i = \mu \left(J_3 - \frac{1}{\lambda_i^2}\right) \qquad \text{(I. 77)}$$

(i not summed)

The averaged values in table I.1 are now to be used in plotting the triaxial data to check the validity of the theory for internal consistency. Figure I. 23 shows the triaxial stress-deformation plots based on experiment, and the theoretical curve calculated from equation I. 53 for $f = 0$, $\nu = 1/4$. Due to the premature pulling away of the specimen from the flanges, the experimental points are more or less scattered; however, the theoretical curve falls within the middle region of this scattering band thus indicating that the theory correlates well with at least the mean values of the experimental points. Figure I. 24 shows that the theoretical curve suggested by equation I. 68, for which $f = 0$, $\nu = 1/4$, falls in the middle region of the band of scattering of the experimental points. The other theoretical curve based on equation I. 66 for which $f = 0$, $\nu = 1/4$ as shown in figure I. 25 also lies on the averaged region of the scattered experimental points. Indeed, if one used a better bonded specimen containing less imperfections, one would expect the experimental points to fall even closer to the vicinity of the theoretical curve.

The experimental evidence therefore strongly suggests the conclusion: the strain energy function I. 52 and its associated constitutive stress-deformation law I. 53, incorporating the effect of volume change and the proposed definition of a large deformation Poisson's ratio, is universal in any kind of stress or deformation fields in a foamed rubber. Furthermore the same conclusion should also be expected for continuum rubbers.

2. Continuum Rubbers

a. Uniaxial, Strip-Biaxial, Homogeneous-Biaxial Tensions

All the rubbers tested show similar behavior in biaxial stress fields, however, the uniaxial behavior can be classified into three categories: i) Neo-Hookean behavior (evinced by polyurethane and butyl rubbers), ii) Mooney-Rivlin type behavior (SBR, CIS-4, paracril-B rubbers), and iii) Non-Neo-Hookean, non-Mooney-Rivlin type (natural and neoprene-GNA rubbers). Thus, we shall only use the data of polyurethane, SBR and natural rubbers to represent the 1st, 2nd and 3rd type of behaviors respectively. The data for the rest of rubbers appear in (9). Figures I.26 ~ I.45 show; the isothermal equilibrium stress-deformation plots, reduced stress-deformation plots for evaluating $W_1 (= \frac{\mu}{2} f)$ and W_2 $(= \frac{\mu}{2} (1-f))$suggested by equations I.43, I.56; in uniaxial, strip-biaxial, homogeneous-biaxial and triaxial tensions (polyurethane rubber only). Note that the way of plotting reduced strip-biaxial data for evaluation of f is different from those in uniaxial and homogeneous-biaxial stress fields. Since deviation of J_3 from unity in the first three types of stress fields is undetectable within the measurement accuracy, the incompressibility condition is used for the reduced strip-biaxial plot in which W_1 and W_2 cannot be determined separately but only their sum, $W_1 + W_2$. It is noted that the excellent straight line with zero slope in reduced stress-deformation plots in the homogeneous-biaxial stress field for all the rubbers* tested,

---

* Data for polyurethane rubber are not as good for the homogeneous-biaxial stress field.

indicates that $W_2 = 0$, $f = 1$; the intercept of this line determines the shear modulus $\mu = 2W_1$ (see the representative figures I. 31, I. 39, I. 45). So, all the rubbers tested behave excellently in a Neo-Hookean way up to rupture in the homogeneous-biaxial field.

In the strip-biaxial field, there is no difference between the behaviors in extension and retraction cycles as shown in figure I. 42. The reduced stress-deformation plot also gives a nice straight line for all the rubbers tested, and the slope gives the shear modulus, $\mu = 2(W_1+W_2)$. This constancy of the sum of W_1 and W_2 does not necessarily imply the individual constancy of W_1 and W_2, however, as will be seen later W_2 is actually zero, indicating all the rubbers tested are also Neo-Hookean type in this stress field (see figures I. 29, I. 37, I. 43). The relatively high value of shear modulus in the homogeneous-biaxial stress field is due to the unavoidable grip-effect which tends to give a higher stress level than the ideal one under the same extensions.

Figures I. 27, I. 35, I. 41 show the uniaxial reduced stress-deformation plots represented by the three types of rubbers. Figure I. 27 shows the plot is almost linear for polyurethane rubber with $W_2 = 0$, indicating the material has Neo-Hookean character (type 1 rubbers). Figure I. 37 shows the plot is also linear for SBR, but with a positive slope, $W_2 > 0$; the intercept of this line determines W_1, and the sum, $2(W_1+W_2)$ gives the shear modulus. Thus, such materials have Mooney-Rivlin type character (type 2 rubbers) in this stress field. Figure I. 41 shows that the plots for both extension and retraction cycles for natural rubber have upturns near high extensions but with $(W_2)_{\lambda=1} > 0$ and $(W_2)_{\lambda=1} \approx 0$ for the two cycles respectively. Any rubber which evinces a remarkable upward curvature during high extensions in its stress-deformation curve will give such a reduced plot (see figure I. 40 for an example). It is noted that the retractional stress is far below than that of extensional one at the same extension. This remarkable hysteresis loop is possibly caused by the result of crystallization which diminishes at high temperature (24, pp. 213-214). This inconsistancy of W_1 and W_2 in uniaxial and in biaxial stress fields makes one suspect that W_1 and W_2 may not be constants although the experimental data indicate them to be so in biaxial stress fields. Hence, for better representation of the materials, non-linear terms of the series expansion of an isotropic strain energy function about its scalar invariants, must be included. We therefore choose the following strain energy function (modified Signorini function) with some coefficients already compared with linear theory:

$$W = \frac{\mu}{2} f (J_1 - 3) + \frac{\mu}{2}(1-f)(J_2 - 3) + B(J_1-3)^2 + D(J_2-3)^2 + F(J_1-3)(J_2-3)$$
$$+ \mu(1-2f)(J_3-1) + \left[\frac{K}{2} + \mu\left(f - \frac{5}{6}\right) - 4(B+D+F)\right](J_3-1)^2 \tag{I. 78*}$$

where B, D, F are not the same as B, D, F as in equations I. 24, I. 25, I. 26.

The constitutive law I. 15 now takes the form (allowing compressibility)

---

* The third, the fourth, and the fifth terms are the same order of magnitude in small strain invariants, however, the Signorini function includes only the third term.

$$\bar{\sigma}_i J_3 = \sigma_i \lambda_i = \lambda_i^2\left[\mu f + 4B(J_1-3) + 2F(J_2-3)\right] - \frac{1}{\lambda_i^2}\left[(1-f)\mu + 4D(J_2-3) + F(J_1-3)\right]$$

$$+ J_3\left[\mu(1-2f) + \{K + 2\mu(f-\tfrac{5}{6}) - 8(B+D+F)(J_3-1)\right] \qquad (I.\,79)$$

And, for any stress field with zero stress at least in one coordinate, the principal stress difference takes the form:

$$\frac{\sigma\lambda}{\lambda^2-\lambda^2_{\substack{lat,\\ th}}} = \mu f + 4B(J_1-3) + 2F(J_2-3) + \frac{(1-f)\mu + 4D(J_2-3) + 2F(J_1-3)}{\lambda^2\lambda^2_{\substack{lat,\\ th}}} \qquad (I.\,80)$$

where the stress in lateral or thickness direction is zero. For uniaxial tension the constitutive law I. 80 becomes:

$$\frac{\sigma_{uni}}{\lambda - J_3/\lambda^2} = \mu f + 4B(J_1-3) + 2F(J_2-3) + \frac{(1-f)\mu + 4D(J_2-3) + 2F(J_1-3)}{J_3\lambda} \qquad (I.\,81)$$

or for the incompressible case, we have:

$$\frac{\sigma_{uni}}{\lambda - 1/\lambda^2} = \mu f + 4B(J_1-3) + 2F(J_2-3) + \frac{(1-f)\mu + 4D(J_2-3) + 2F(J_1-3)}{\lambda} \qquad (I.\,82)$$

where

$$J_1 = \lambda^2 + \frac{2}{\lambda} \quad , \qquad J_2 = \frac{1}{\lambda^2} + 2\lambda \qquad (I.\,83)$$

For strip-biaxial tension equation I. 80 takes the form:

$$\frac{\sigma_{s\text{-}bi}}{\lambda - J_3^2/\lambda^3} = \mu f + 4B(J_1-3) + 2F(J_2-3) + \frac{(1-f)\mu + 4D(J_2-3) + 2F(J_1-3)}{J_3^2} \qquad (I.\,84)$$

or for the incompressible case, we have:

$$\frac{\sigma_{s\text{-}bi}}{\lambda - 1/\lambda^3} = \mu + 4\,(B+D+F)(J_1-3) \qquad (I.\,85)$$

where

$$J_1 = J_2 = \lambda^2 + \frac{1}{\lambda^2} + 1 \qquad (I.\,86)$$

And for homogeneous-biaxial tension equation I. 80 becomes:

$$\frac{\sigma_{h\text{-}bi}}{\lambda - J_3^2/\lambda^5} = \mu f + 4B(J_1-3) + 2F(J_2-3) + \frac{\left[(1-f)\mu + 4D(J_2-3) + 2F(J_1-3)\right]\lambda^2}{J_3^2} \qquad (I.\,87)$$

or under the incompressibility condition; we have:

$$\frac{\sigma_{h-bi}}{\lambda - 1/\lambda^5} = \mu f + 4B(J_1-3) + 2F(J_2-3) + \left[(1-f)\mu + 4D(J_2-3) + 2F(J_1-3)\right]\lambda^2 \quad (I.88)$$

where

$$J_1 = 2\lambda^2 + \frac{1}{\lambda^4} \quad , \quad J_2 = \frac{2}{\lambda^2} + \lambda^4 \quad (I.89)$$

Since the data show $J_3 \approx 1$, we will assume incompressibility here and use equations I.82, I.85, I.88 for an investigation. By fitting these equations to the corresponding data of natural rubber, it develops that

$$f = 1, \; B = D = F = 0 \quad (I.90)$$

for a homogeneous-biaxial stress field, and,

$$B + D + F = 0 \quad (I.91)$$

for strip-biaxial stress field. In order to be consistent, equation I.90 must also be applicable to I.91. Thus, the material really behaves in Neo-Hookean way in biaxial stress fields.

The uniaxial data fitting was performed in such a way that the values of f and μ were firstly obtained from the intercept and slope at $\lambda = 1$ of the reduced stress-deformation plot (see figure I.41). Next, the remaining three parameters, B. D. F, were found by collocation of the data at three points giving

$$\mu = 72 \text{ psi}$$

$$f = 0.417$$

$$B/\mu = 0.003$$

$$D/\mu = -0.009$$

$$F/\mu = +0.001$$

It is seen that B, D and F are very small numbers. The theoretical curve based on these parameters gives excellent agreement with the uniaxial data (see figure I.40, I.41). In figure I.41 we note that the uniaxial shear modulus for extensional and retracatioal cycles are remarkably different; the retractional shear modulus is comparable with that of biaxial fields, while that for an extensional cycle is comparatively larger. This may be attributed to non-affine deformation of molecular network of the rubber resulting from the slip of interlooping points of the network. Thus the configurations of the network at the beginning of the extensional cycle where the extensional shear modulus is evaluated, and at the end of retractional cycle where the retractional shear modulus is evaluated, are considered to be quite different (20). However, this phenomenon does not arise in biaxial stress fields as is shown by the strip-biaxial data (see figure I.42) in which both the extensional and retractional data are in good agreement. Since in biaxial stress fields the interlooping points may act like molecular junction points (or cross-linkage points), so that there is almost no relative slip between the molecular chains at these points, the deformation in biaxial stress fields is affine type.

The modified Signorini function I.78, when applied to uniaxial and two biaxial stress fields, gives very poor fit to the data. On the other hand, the Neo-Hookean function when applied to uniaxial and to two biaxial stress fields gives a better overall fit to the data, except for a slight deviation in uniaxial data (see figure I.40). It is seen that this deviation is only 10 % at $\lambda = 3.5$ and becomes larger at the non-Gaussian region. Thus the rubber tested is Neo-Hookean in character rather than modified-Signorini in character.

The small amount of deviation of uniaxial extensional data from the Neo-Hookean curve, we believe, must be attributed mainly to anisotropic behavior and, for better representation of such materials, the use of a transversely isotropic strain energy function is suggested, i.e.,

$$W = W(J_1, J_2, J_3, K_1, K_2)$$

where $K_1 = e_{33}$

$$K_2 = e_{3\alpha} e_{3\alpha} \qquad (\alpha = 1, 2)$$

$$e_{ik} = \frac{1}{2}\left(\frac{\partial X^m}{\partial x^i}\frac{\partial X^m}{\partial x^k} - \delta_{ik}\right) \qquad (i=3\text{: axis of anisotropy})$$

Since, i) the anisotropy may arise from anisotropic orientation of molecular chains when stretched, and ii) examination of anisotropic stress-deformation law derived from $W(J_1, J_2, J_3, K_1, K_2)$ indicates that a better overall fit might be obtained, the above strain energy function is recommended. However, this has not been done until additional data are procured, because, as indicated above, the need for anisotropic analysis is not important over most of the range of extension. However, in problems in which it is desired to analyze either; failure behavior, or stress singularities, then anisotropy must be accounted for.

But, in theoretical stress analysis where mathematical simplicity is important, and where other than a pure uniaxial stress field is involved, the isotropic Neo-Hookean or Mooney-Rivlin (which becomes Neo-Hookean in plane strain case) representations of quasi-static behavior of incompressible rubbers will suffice over most of the whole range of extension.

In general, for compressible rubbers, the strain energy function I. 52 and its associated constitutive law I. 53, will give an excellent representation in any kind of multiaxial stress or deformation fields.

b. Hydrostatic Compression

Next, we will apply our constitutive law, I. 53 under hydrostatic compression conditions in a continuum rubber and examine the resulting correlation with existing data. For the Neo-Hookean solid (f = 1) in this stress field, equation I. 75 can be rewritten in the form:

$$p = \frac{\mu}{J_3^{1/3}}\left[J_3^{-\frac{2(1+\nu)}{3(1-2\nu)}} - 1\right] = \mu\left[J_3^{-\frac{1}{1-2\nu}} - J_3^{-\frac{1}{3}}\right], \quad f = 1 \qquad \text{(I. 92)}$$

where the first and second terms on the right hand side are similar to the repulsive and the attractive terms respectively in an interatomic potential function. Murnaghan (25) also developed the following equation for hydrostatic stress field:

$$p = \frac{K}{k}\left(J_3^{-k} - 1\right) \qquad \text{(I. 93)}$$

and fitted the data for the atomic alkali metals. He found the parameter k to be of the order of 4. Since J_3 is a measure of the cube of change in interatomic distance, Murnaghan's observation suggests an inverse twelfth power dependence of interatomic forces. When the equivalent terms in equation I. 92, I. 93 are compared, it follows that:

$$\frac{K}{k} \sim \frac{\mu}{J_3^{1/3}} \qquad (I.94)$$

$$k \sim \frac{2(1+\nu)}{3(1-2\nu)} \qquad (I.95)$$

and in view of these relations, if $J_3^{1/3} \rightarrow 1$, K will obey the linear definition of bulk modulus.

Now the functional behavior of equation I.92 for butyl tread rubber is shown in figure I.46 where Bridgman's data up to 350,000 psi (10) are plotted. The rectified straight line is characterized by the finite strain value of Poisson's ratio, $\nu = 0.463$ which gives a linear bulk modulus of K = 475,000 psi. This value compares fairly well with data (49) on polyisobutylene, and the value $\nu = 0.463$ indicates that an actual rubber is not as incompressible as the linear theory would indicate. The value $\nu = 0.463$ corresponds to k = 13.3 in Murnaghan's equation I.93, and the reason why the value of k = 13.3 is larger than that Murnaghan found for monatomic molecules may be inferred from the fact that the small monomeric units are tied together in long polymer chains.

c. Triaxial Tension

Finally, the constitutive law I.53 will be applied to a triaxial tensile stress field in continuum rubber. Figure I.32 shows a triaxial stress-deformation curve of polyurethane rubber for which f=1, and figure I.33 shows the plot based on equation I.69. The rectified straight line is characterized by the finite strain value of Poisson's ratio, $\nu = 0.473$, indicating this rubber is partially compressible.

PART II

TOPOLOGY OF FAILURE SURFACES

II. 1 INTRODUCTION

Following the determination of an adequate strain energy function and the associated constitutive law, we will proceed to focus attention upon the rupture behavior of the previous materials in different stress fields, i.e., the geometrical surfaces generated by the failure points in different principal stress or deformation space.

Various hypotheses have been suggested as to the condition under which an isotropic material fails; however, in relating stress and strain, a linear constitutive law was generally used. Thus the surfaces generated in this way are not applicable in large deformations.

The geometry of failure surfaces based on stress criteria depicted in stress space or the failure surfaces based on stretch criteria depicted in stretch space where no constitutive law is used, remains the same both in linear and large deformation theories.

In the linear theory the shape of failure surfaces based on a stress criterion remains unchanged (but not geometrically similar) either plotted in principal stress or principal stretch space except for a change in values of the parameters. Similarly, a geometry based on a strain criterion has the same shape (not geometrically similar) depicted in either principal stress or principal stretch space. In large deformation representation the situation is different. Since the constitutive law is non-linear and multivalued, a given surface in principal stress space may be associated with a plurality of surfaces in principal stretch space. Likewise, to a given surface in principal stretch space can be associated with a plurality of surfaces in principal stress space.

The purpose of the discussion in this part is to furnish a geometrical representation of failure surfaces based on all possible different criteria depicted in principal stress, principal stretch and invariant spaces for elastic materials, and to compare these surfaces with the data obtained in uniaxial, strip-biaxial, homogeneous-biaxial, and triaxial stress fields for foamed and continuum rubbers. It is desired, therefore, to reach a tentative conclusion, based on the up to date data, as to the shape of these surfaces.

II. 2 FAILURE CRITERIA AND THE CORRESPONDING GEOMETRIES

Since in large deformations the stretch ratio can not be expressed explicitly in terms of stresses, it is not easy to postulate failure surfaces based on a stretch criterion and plotted in stress space, or based on a stress criterion and plotted in stretch space: however, some special cases do occur depending on the value of f and ν in the constitutive law.

We will consider a special material for which $f = 0$, $\nu = 1/4$ and simplify the constitutive law I. 53 in the following form:

$$\overline{\sigma}_i = \mu \left[1 - \frac{1}{\lambda_i^2 J_3} \right] \qquad \text{(II. 1)}$$

which shows that the maximum achievable value of true stress in an infinitely extensible material ($f = 0$, $\nu = 1/4$) under any arbitrary tensile stress field is its shear modulus. Equation II. 1 immediately sets an upper bound to the stresses expected in a deformed foam rubber. This equation is nonlinear and multivalued in the displacements, so that to a given surface in principal stress space is associated a plurality of surfaces in principal stretch space. Likewise to a given surface in stretch space there is associated a plurality of surfaces in principal stress space. This non-uniqueness is highlighted as follows:

Inverting equation II. 1:

$$\lambda_i^2 = \frac{1}{J_3}\left[\frac{1}{1-\frac{\bar{\sigma}_i}{\mu}}\right] \qquad \text{(II. 2)}$$

and multiplying λ_i^2 by λ_j^2, λ_k^2, J_3 can be expressed in terms of stresses:

$$J_3 = \left[\left(1-\frac{\bar{\sigma}_i}{\mu}\right)\left(1-\frac{\bar{\sigma}_j}{\mu}\right)\left(1-\frac{\bar{\sigma}_k}{\mu}\right)\right]^{-\frac{1}{5}} \qquad \text{(II. 3)}$$

Substitution of equation II. 3 into equation II. 2 yields:

$$\lambda_i^2 = \left(1-\frac{\bar{\sigma}_i}{\mu}\right)^{-\frac{4}{5}}\left(1-\frac{\bar{\sigma}_j}{\mu}\right)^{\frac{1}{5}}\left(1-\frac{\bar{\sigma}_k}{\mu}\right)^{\frac{1}{5}} \qquad \text{(II. 4)}$$

Thus the stretch, now expressed explicitly in terms of stresses, can be used in plotting a stretch criterion in principal stress space. We shall discuss several geometries of the failure surface in the following.

A. Stress Criteria

1. Maximum Principal Stress Criterion (Rankine's Theory) (28)

This criterion states that the failure is measured by the greatest principal stress. The geometry based on this criterion is given by:

$$\bar{\sigma}_c \leq \bar{\sigma}_i \leq \bar{\sigma}_T \qquad (i = 1, 2, 3) \tag{II. 5}$$

where $\bar{\sigma}_T$ is the ultimate uniaxial tensile true stress, and $\bar{\sigma}_C$ is the unspecified ultimate uniaxial compressive stress. Equation II. 5 gives a cube in principal stress space, three faces of which intersect the positive $\{i, j, k\}$ axes at each of three points at a distance $\bar{\sigma}_T$ from the coordinate origin, and which intersect mutually at an apex which lies on the positive ray of the hydrostatic vec tor at a distance $\sqrt{3}\,\bar{\sigma}_T$ from the coordinate origin. The other three faces of this cube will intersect the negative $\{i, j, k\}$ axes at each of three points $\bar{\sigma}_C$ whose position is unspecified (see figure II. 1). Based on this criterion any combined stress field which falls inside this surface is considered to be safe. Since the compression failure point is unspecified and may theoretically approach infinity, in the following discussion the geometry in the negative $\{i, j, k\}$ octant is disregarded.

In order to plot equation II. 5 in principal stretch space we use relation II. 1 and express formula II. 5 in term of stretches. Thus:

$$\lambda^2 \leq \lambda_T^2 \qquad (i = 1, 2, 3) \tag{II. 6}$$

where λ_T is ultimate uniaxial stretch ratio. Equation II. 6 represents a maximum stretch criterion and depicts a cube in λ^2-space whose three faces intersect positive $\{i, j, k\}$ at λ_T^2 from the coordinate origin (see figure II. 2).

2. Maximum Shear Criterion (Guest's Theory) (28)

Under this hypothesis the failure is measured by the greatest principal stress difference (or Tresca condition)(29), and the geometry is represented by:

$$\bar{\sigma}_i - \bar{\sigma}_j \leq \bar{\sigma}_T \qquad \text{(II. 7)}$$

which defines six planes in $\bar{\sigma}$-space, each of which makes a 45° angle with two of the coordinate axes and mutually intersect to form a regular hexagonal prism whose axis is coaxial with the hydrostatic vector. This prism is infinitely long since the shear remains small as long as the three principal stresses are nearly equal. Thus, this criterion permits unlimited nearly equal principal stresses which contradicts with reality. The six edges of the prism pass through the six vertices of the cube defined by equation II. 5, and the six sides of which pass through the six edges of the same cube (see figure II. 1).

3. Maximum First Stress Invariant Criterion

Based on this criterion, failure should occur when the mean principal tensile stress (or hydrostatic tension) reaches the extreme value. The geometry for this criterion is defined by:

$$\sum_i \bar{\sigma}_i \leq \bar{\sigma}_T \qquad \text{(II. 8)}$$

which gives a plane normal to the hydrostatic vector in $\bar{\sigma}$-space and located at a distance $\sqrt{3} \times$ (Maximum hydrostatic tension) $= \bar{\sigma}_T / \sqrt{3}$ from the coordinate origin, passing through the positive

$\{i, j, k\}$ axes at $\overline{\sigma}_T$ (see figure II. 1). Equation II. 8 can be plotted in stretch space by the use of equation II. 1 to express stress in terms of stretches:

$$\sum_i \left(1 - \frac{1}{\lambda_i^3 \lambda_j \lambda_k}\right) \leq \frac{\overline{\sigma}_T}{\mu} \qquad \text{(II. 9)}$$

(i, j, k permute cyclically)

which depict a dish shaped hyperboloid in λ^2-space and allowing unlimited uniaxial and biaxial deformations (see figure II. 3).

4. <u>Maximum Second Stress Invariant Criterion</u>

The failure is to be measured by the extreme value of the second stress invariant. The geometry based on this criterion is represented by:

$$\sum_{i \neq j} \overline{\sigma}_i \overline{\sigma}_j \leq 3\overline{\sigma}_H^2 \qquad \text{(II. 10)}$$

where $\overline{\sigma}_H$ is the maximum attainable hydrostatic tensile stress (= $\overline{\sigma}_T/3$) . This geometry depicts a dish-shaped triangular hyperboloid in $\overline{\sigma}$-space allowing unlimited deformation near the uniaxial stress field (see figure II. 4). Expressing equation II. 10 in terms of stretches by using equation II. 1 it follows that:

$$\sum_i \left(1 - \frac{1}{\lambda_i^3 \lambda_j \lambda_k}\right)\left(1 - \frac{1}{\lambda_i \lambda_j^3 \lambda_k}\right) \leq \frac{3\overline{\sigma}_H^2}{\mu^2} \qquad \text{(II. 11)}$$

(i, j, k permute cyclically)

which also depicts a dish shaped surface in the positive $\{i, j, k\}$ octant of stretch space, and allows infinite uniaxial and biaxial extensions (see figure II. 5). The position of the dilatational failure point on this surface is also indicated.

5. Maximum Third Stress Invariant Criterion

Based on this criterion, failure is to be predicted when the third stress invariant reaches the extreme value. The geometry is defined by:

$$\prod \overline{\sigma}_i \leq \overline{\sigma}_H^3 \tag{II. 12}$$

which depicts a concave dish-shaped surface in the positive $\{i, j, k\}$ octant of stress space. This surface also allows unlimited stretches in one or two coordinates (see figure II. 6).

6. Maximum Octahedral Shear Stress Criterion

This corresponds to a maximum distortional strain energy criterion (Von Mises-Hencky Theory (26)) in linear theory. The geometry associated with this criterion is represented by:

$$\sum_{i \neq j} (\overline{\sigma}_i - \overline{\sigma}_j)^2 \leq 2\overline{\sigma}_T^2 \tag{II. 13}$$

which depicts an infinitely long circular cylinder in $\overline{\sigma}$-space and coaxial with the hydrostatic vector, circumscribing the hexagonal prism defined by the maximum shear criterion (see figure II. 1). This criterion also allows unlimited deformations near hydrostatic tension and compression.

By using relation II. 1 equation II. 13 can be written in terms of stretch ratios:

$$\sum_{i} \left(\frac{\lambda_i^2 - \lambda_j^2}{\lambda_i^3 \lambda_j^3 \lambda_k} \right)^2 \leqslant 2\,\bar{\sigma}_T^2 \qquad \text{(II. 14)}$$

(i, j, k permute cyclically)

which depicts a wavy dish-shaped surface in the positive $\{i, j, k\}$ octant in λ^2-space allowing unlimited uniaxial and biaxial extensions. This criterion predicts dilatational failure to occur at natural state ($\lambda_i = 1$) which is not real (see figure II. 7).

7. Maximum stress Resultant Criterion

Based on this criterion the rupture is to be anticipated when the resultant stress reaches its ultimate value. The geometry is defined by:

$$\sum_{i} \bar{\sigma}_i^2 \leqslant \bar{\sigma}_T^2 \qquad \text{(II. 15)}$$

which depicts a sphere with radius $\bar{\sigma}_T$ in principal stress space. This theory also predicts failure (negative $\{i, j, k\}$ octant) which is not observed in reality (see figure II. 8).

Using relation II. 1, formula II. 15 can be written in terms of stretch ratios:

$$\sum_{i} \left(1 - \frac{1}{\lambda_i^3 \lambda_j \lambda_k} \right)^2 \leqslant \bar{\sigma}_T^2 \qquad \text{(II. 16)}$$

(i, j, k permute cyclically)

which depicts a surface with two dish-shaped hyperboloid-like surfaces joined and extends to positive infinite in $\{i, j, k\}$direction, thus allowing unlimited extension for a near uniaxial stress field (see figure II. 9).

8. Maximum Mean Deviatoric Stress Criterion

This theory is to predict failure by the extreme value of the mean deviatoric stress. The corresponding geometry is defined by:

$$\sum_i \overline{\sigma}_i - 3\overline{\sigma}_k \leq \overline{\sigma}_T , \qquad \overline{\sigma}_k \leq 0 \tag{II. 17}$$

which depicts three planes in $\overline{\sigma}$-space, each of which is parallel to the hydrostatic vector and intersect mutually to form an infinitely long regular triangular prism inscribing the circular cylinder defined by the maximum octahedral shear stress criterion (see figure II. 1).

B. Stretch Criteria

1. Maximum Principal Stretch Criterion

This theory predicts failure to occur at the maximum principal stretch. The corresponding geometry is defined by:

$$\lambda_i^2 \leq \lambda_T^2 \tag{II. 18}$$

where λ_T is uniaxial ultimate stretch ratio. Equation II. 18 represents three faces of a cube cutting positive $\{i, j, k\}$ at λ_T^2 in λ^2-space (see figure II. 2).

By the use of relation II. 4, equation II. 18 can be expressed in terms of stresses:

$$\lambda_T^{10}\left(1-\frac{\overline{\sigma}_i}{\mu}\right)^4 \geq \left(1-\frac{\overline{\sigma}_j}{\mu}\right)\left(1-\frac{\overline{\sigma}_k}{\mu}\right) \tag{II. 19}$$

Taking $\lambda_T = 2.4$, based on the experimental data for foamed polyurethane rubber, the geometry of equation II. 19 consists of three concave surfaces in principal stress space, each of which intersects the three negative coordinate axes at $1-\lambda_T^{-2.5}$ and forming a concave trigonal pyramid with convex edges and concave faces which extend to negative infinity. The vertex lies on the hydrostatic vector at a position $(1-\lambda_T^{-5},\ 1-\lambda_T^{-5},\ 1-\lambda_T^{-5})$. We notice that the maximum uniaxial failure point falls within this surface (see figure II. 10).

2. Maximum Principal Strain Criterion (Saint Venant's Theory)(28)

This criterion predicts fracture when the extreme value of the principal strain is reached. Since the linear stress-strain law is used to depict the criterion in stress space the theory is valid only for small deformations. The geometry is obtained from the equation:

$$\sigma_i - \nu(\sigma_j + \sigma_k) \leq E\epsilon_T = \sigma_T \qquad \text{(II. 20)}$$

where σ_T, ϵ_T are uniaxial yield stress and strain respectively. Equation II. 20 gives three planes in σ-space each of which intersects the coordinate axes at $\{\sigma_i/\sigma_T, \sigma_j/\sigma_T, \sigma_k/\sigma_T\} = \{1, -1/\nu, -1/\nu\}$, and form a trigonal pyramid whose faces extend out to negative infinity. The vertex of the pyramid lies on the hydrostatic vector at a position $\left\{\frac{1}{1-2\nu}, \frac{1}{1-2\nu}, \frac{1}{1-2\nu}\right\}$ (see figure II. 11). The slope and intercepts of these faces change with the value ν. When the material is incompressible ($\nu = 1/2$) it becomes an infinitely long trigonal prism circumscribing the circular cylinder defined by the maximum octahedral shear stress criterion. When $\nu = 0$, the three surfaces will coincide with that of the cube defined by maximum principal stress criterion.

3. Maximum Principal Stretch Difference Criterion

This theory predicts failure to start under the maximum value of stretch difference, whose geometry is defined by:

$$\lambda_i^2 - \lambda_j^2 \leq K \tag{II. 21}$$

where $K = \lambda_T^2 - \lambda_L^2$, and λ_L is the uniaxial ultimate contraction ratio. Equation II. 21 represents a regular hexagonal prism in λ^2-spare whose axis is perpendicular to the octahedral plane and three edges of which intersect the positive $\{i, j, k\}$ axes at a position $(\lambda_T^2 - \lambda_L^2)$ (see figure II. 12).

When stretches are expressed in terms of stresses by the use of relation II. 4, equation II. 21 takes the form:

$$\left(\frac{\bar{\sigma}_i}{\mu} - \frac{\bar{\sigma}_j}{\mu}\right)\left(1 - \frac{\bar{\sigma}_k}{\mu}\right) \leq K^5\left[\left(1-\frac{\bar{\sigma}_i}{\mu}\right)\left(1-\frac{\bar{\sigma}_j}{\mu}\right)\right]^4 \tag{II. 22}$$

which gives six slightly concave surfaces in $\bar{\sigma}$-space, mutually intersected at $\left\{\frac{\bar{\sigma}_i}{\mu}, \frac{\bar{\sigma}_j}{\mu}, \frac{\bar{\sigma}_k}{\mu}\right\} = \{1. 1. 1\}$ on the hydrostatic vector forming a concave hexagonal pyramid whose faces extend out to negative infinity (see figure II. 13).

4. Maximum First Stretch Invariant Criterion

Initiation of failure is to be predicted by the extreme value of the first stretch invariant. The corresponding geometry is defined by:

$$I_1 = \sum_i \lambda_i^2 \leq K \tag{II. 23}$$

where $K = \lambda_T^2 + 2\lambda_L^2$. This equation gives a plane in λ^2-space which intersects the three positive $\{i, j, k\}$ axes at a distance $(\lambda_T^2 + 2\lambda_L^2)/\sqrt{3}$ from the coordinate origin (see figure II. 2).

When equation II. 23 is expressed in terms of stresses, it takes the form:

$$\left[\sum_{j\neq k}\left(1-\frac{\bar{\sigma}_j}{\mu}\right)\left(1-\frac{\bar{\sigma}_k}{\mu}\right)\right]^5 \leq K^5\left[\prod\left(1-\frac{\bar{\sigma}_i}{\mu}\right)\right]^4 \qquad \text{(II. 24)}$$

which gives a waving surface in $\bar{\sigma}$-space, intersecting the hydrostatic vector at $\{1-(3/K)^{5/2}, 1-(3/K)^{5/2}, 1-(3/K)^{5/2}\}$ enclosing the uniaxial failure point within it and extending out to negative infinity (see figure II. 14).

5. Maximum Second Stretch Invariant Criterion (I_2).

This theory predicts fracture to be started at the maximum second stretch invariant. The geometry based on it is defined by:

$$I_2 = \sum_{i\neq j}\lambda_i^2\lambda_j^2 \leq K \qquad \text{(II. 25)}$$

where $K = 2\lambda_T^2\lambda_L^2 + \lambda_L^4$, giving a dish shaped triangular hyperboloid. This criterion allows unlimited stretch in the vicinity of a uniaxial stress field (see figure II. 15).

Rewrite equation II. 25 in terms of stresses by using relation II. 4 in the form:

$$\left[\sum_{i}\left(1-\frac{\bar{\sigma}_i}{\mu}\right)\right]^5 \leq K^5\left[\prod\left(1-\frac{\bar{\sigma}_j}{\mu}\right)\right]^3 \qquad \text{(II. 26)}$$

which depicts a convex surface in $\bar{\sigma}$-space extending out to negative infinity, and intersecting the hydrostatic vector at a position

$\left\{\frac{\bar{\sigma}_i}{\mu}, \frac{\bar{\sigma}_j}{\mu}, \frac{\bar{\sigma}_k}{\mu}\right\} = \left\{1-\left(\frac{3}{K}\right)^{\frac{5}{4}}, 1-\left(\frac{3}{K}\right)^{\frac{5}{4}}, 1-\left(\frac{3}{K}\right)^{\frac{5}{4}}\right\}$. The uniaxial failure point falls within this surface (see figure II. 16).

6. Maximum Second Stretch Invariant Criterion (J_2)

The equation of this criterion is given by:

$$J_2 = \sum_i \frac{1}{\lambda_i^2} \leq K \tag{II. 27}$$

where $K = 1/\lambda_T^2 + 2/\lambda_L^2$. The corresponding geometry depicts a concave dish shaped surface in λ^2-space (see figure II. 17). This criterion allows unlimited uniaxial and biaxial stretches. Rewrite equation II. 27 in terms of stresses by the aid of relation II. 4:

$$\left[\sum_i \left(1-\frac{\bar{\sigma}_i}{\mu}\right)\right]^5 \leq K^5 \prod \left(1-\frac{\bar{\sigma}_i}{\mu}\right) \tag{II. 28}$$

and plotting this in $\bar{\sigma}$-space we have a convex surface intersecting the hydrostatic vector at the position $\left(\frac{\bar{\sigma}_i}{\mu}, \frac{\bar{\sigma}_j}{\mu}, \frac{\bar{\sigma}_k}{\mu} = 1, 1, 1\right)$ where the surface forms a rectangular corner (see figure II. 18).

7. Maximum Third Stretch Invariant Criterion (I_3)

Failure is measured when the third stretch invariant reaches its extreme value. The corresponding geometry is given by:

$$I_3 = \prod \lambda_i^2 \leq K \tag{II. 29}$$

where $K = \lambda_T^2 \lambda_L^4$, which depicts a concave dish-shaped surface extending out to positive infinity in λ^2-space (see figure II. 19). Thus, the theory permits unrealistic unlimited uniaxial and biaxial stretches. Applying the relation II. 4 to equation II. 29 there results:

$$K^5\left[\prod\left(1-\frac{\overline{\sigma}_i}{\mu}\right)\right]^2 \geq 1 \tag{II. 30}$$

which depicts an almost spherical convex surface in the first octant of $\overline{\sigma}$-space intersecting the hydrostatic vector at a position, $\left\{\frac{\overline{\sigma}_i}{\mu}, \frac{\overline{\sigma}_j}{\mu}, \frac{\overline{\sigma}_k}{\mu}\right\} = \left\{1-K^{-\frac{5}{6}}, 1-K^{-\frac{5}{6}}, 1-K^{-\frac{5}{6}}\right\}$, and extending out to negative infinity. The round edges will become sharper as the negative infinity is approached (see figure II. 20).

8. Maximum Mean Deviatoric Stretch Criterion

Maximum mean deviatoric stretch criterion assumes failure to take place at its extreme value according to the formula:

$$\sum_i \lambda_i^2 - 3\lambda_k^2 \leq K \tag{II. 31}$$

where $K = \lambda_T^2 - \lambda_L^2$. The geometry of this formula consists of three planes in λ^2-space, which mutually intersect to form an infinitely long triangular prism whose axis is perpendicular to the octahedral plane and inscribe the hexagonal prism defined by the maximum stretch difference criterion (see figure II. 12).

Substitution of relation II. 4 into formula II. 31 yields:

$$\left[\sum_{j\neq k}\left(1-\frac{\overline{\sigma}_j}{\mu}\right)\left(1-\frac{\overline{\sigma}_k}{\mu}\right) - 3\left(1-\frac{\overline{\sigma}_r}{\mu}\right)\left(1-\frac{\overline{\sigma}_s}{\mu}\right)\right]^5 \leq K^5\left[\prod\left(1-\frac{\overline{\sigma}_i}{\mu}\right)\right]^4 \tag{II. 32}$$

$$(r \neq s)$$

which depicts in $\overline{\sigma}$-space three convex surfaces which intersect mutually on the hydrostatic vector at a position, $\left\{\frac{\overline{\sigma}_i}{\mu}, \frac{\overline{\sigma}_j}{\mu}, \frac{\overline{\sigma}_k}{\mu}\right\} = \{1. 1. 1\}$ where the surface forms a sharp corner, and extending out to negative infinity. The uniaxial failure point falls almost on this surface (see figure II. 21).

C. Maximum Strain Energy Criterion

The failure surface based on this criterion in large deformation theory will be entirely different from that based on linear theory. And in large deformation the geometry will vary as the values of ν and f.

i) For large deformation, there will be multiple surfaces based on the different values of f and ν. Here we will consider the representative materials for which $\nu = 1/4$, $f = 0$; and $\nu = 1/2$, $f = 1$.

For $\nu = 1/4$, $f = 0$, the strain energy function I. 76 can be rewritten in the form:

$$\sum_i \frac{1}{\lambda_i^2} + 2\prod \lambda_j \leq \frac{2W}{\mu} + 5 \qquad \text{(II. 33)}$$

which depicts surfaces in λ^2-space and λ-space and which look like figures II. 22 and II. 23 respectively. These two surfaces are not closed and thus allow unlimited stretch near the uniaxial stress field.

Using the constitutive law II. 4, equation II. 33 can be written in the form:

$$\left[\sum_i \left(1-\frac{\bar{\sigma}_i}{\mu}\right)+2\right]^5 \leq K^5 \prod \left(1-\frac{\bar{\sigma}_j}{\mu}\right) \qquad \text{(II. 34)}$$

where $K = \frac{2W}{\mu} + 5$

Equation II. 34 depicts a convex surface in the first octant of $\bar{\sigma}$-space which extends out to negative infinity. (See figure II. 24). Moreover, equation I. 76 will depict a plane in the invariant space as shown in figure II. 25.

For $\nu = 1/2$, $f = 1$, the strain energy function is reduced to the form:

$$W = \frac{\mu}{2}(J_1 - 3) \qquad \text{(Neo-Hookean solid)} \qquad \text{(II. 35)}$$

or

$$\sum_i \lambda_i^2 \leqslant \frac{2W}{\mu} + 3 \qquad \text{(II. 36)}$$

which is a plane in λ^2-space, passing positive $\{i, j, k\}$ axes at the position, $\frac{2W}{\mu} + 3$ (see figure II. 26).

ii) For infinitesimal deformations the geometry in the stress space is based on:

$$2EW \geqslant \sum_i \sigma_i^2 - 2\nu \sum_{j \neq k} \sigma_j \sigma_k \qquad \text{(II. 37)}$$

which depicts a symmetrical ellipsoid, passing the coordinate axes at $\pm\ \sigma_T$, and whose major axis coincides with the hydrostatic vector (27) (see figure II. 27). The shape of this surface varies with different values of Poisson's ratio. For example, when $\nu = 1/2$ (incompressible case) the ellipsoid becomes an infinitely long circular cylinder coaxial to the hydrostatic vector and, when $\nu = 0$

it becomes a sphere. This criterion predicts fracture under hydrostatic compression which is not observed in reality.

D. Failure Surfaces Based on Experimental Data

In order to reduce sample to sample variation of material properties, all the specimens used for different stress fields were cut out from one piece of material. Failures in the two types of uniaxial specimens, the third type of strip-biaxial specimen (see right pictures of figure I. 6, I. 7), and the triaxial specimen were successfully caused to start at the middle region of the specimens, thus giving good rupture data in each of the above stress fields. But in the homogeneous-biaxial field, due to the gripping effect, failure usually starts at the vicinity of the grips. Thus the failure data are considered to be far below the ideal homogeneous-biaxial failure values and such points were used just for reference.

We believe that the variation in the failure data is due to sample to sample variation which depends on the presence of local defects in the sample rather than solely the size effect (see figures I. 26, I. 28, and I. 30 for polyurethane rubber which is used for failure surface study). The lower rupture data were not used in plotting the failure surface but only the averaged ultimate values of those falling within a narrow region. Note that the variation of the failure values in stress-wise is less than that in stretch-wise.

The so-called isotropic failure criterion can only be obtained when the standard deviation of the measured ultimate values becomes independent of sample dimensions (this we observed in our data) in the limit of large dimensions in which local defects are randomly distributed and are averaged out in testing a large number of samples. However, this criterion does not give a true picture of fracture initiation. In order to obtain a true one, defect free samples must be prepared, and presumably one has to work in the region of relatively small dimensions. This is extremely difficult to perform, as evidenced by the analogy with studies on single crystals in metals. An alternative method is to introduce a well defined crack or notch and study the growth of this effect. Nevertheless, failure data obtained from medium sized samples as in our tests should be able to give a fairly good initial representation of the failure surfaces.

In plotting the data, ultimate lateral stresses in strip-biaxial and triaxial fields were calculated from equation I. 53, f being taken to be zero or unity respectively for a foam and a continuum rubber. Figures II. 28 and II. 30 show the plot of ultimate values, in normal stress space, of 47% voided polyurethane foam rubber and polyurethane continuum rubber obtained from different stress fields.

The (+++) data of the foam rubber seems to depict a plane in normal stress space (see figure II. 28), dish-shaped trigonal hyperboloid in λ^2-space (see figure II. 15), and almost a plane in λ-space (see figure II. 29). Based on all the present available data and considering all the failure surfaces investigated, the failure surface in normal stress space for a foam rubber looks like a frustum of a prism i) whose distortional carpet cannot exceed that of a circular cylinder defined by maximum octahedral shear stress criterion and can not fall within a triangular prism defined by mean deviatoric stress criterion; ii) whose frustrated facet in the (+++) octant is a carpet of the dilatational plane. Thus the foamed material fails in a dilatational mode in the first octant of stress space.

While the (+++) data of the continuum rubber (polyurethane) seems to depict a triangular pyramid in normal stress space, which obeys the equation

$$\overline{\sigma}_i + \overline{\sigma}_j - \alpha \overline{\sigma}_k \leq \overline{\sigma}_T \qquad \text{(II. 38)}$$

where $- \leq \alpha \leq 1$

with its vertex lying between the hydrostatic plane for which $\alpha = -1$, and the vertex of a cube for which $\alpha = 1$ (see figure II. 30). Thus the continuum rubber fails in a distortional mode in the first octant of stress space. Moreover, the same (+++) data depicts a plane in normal stretch space obeying

$$\sum_i \lambda_i \leq \text{Const.} \qquad \text{(II. 39)}$$

For determining more precisely the location of the distortional sides of the failure surfaces, it is recommended that additional stress fields should be investigated; in particular one should investigate i) uniaxial tension under hydrostatic compression, and ii) biaxial tension combined with hydrostatic compression. These additional tests, however, have not been presented in this discussion.

PART III

FINITE PLANE STRAIN TANGENTIAL SPREADING OF A RADIALLY CRACKED INFINITELY LONG INCOMPRESSIBLE RUBBER LOG BY A RADIALLY RIGID BONDED WEDGE-SHAPED BELLOWS

III. 1. Introduction

In Part I we have presented experimental evidence that a Neo-Hookean representation of the behaviors of elastomers under quasi-static deformation provides a good representation of material behavior even up to rupture, except in a pure uniaxial stress field. In the subsequent analysis of this part, we shall therefore assume that the elastomer will be a Neo-Hookean solid. Also, we mentioned in Part II that an alternate method of studying failure is to introduce a well defined crack or notch and study its growth. This situation arouses our interest in studying stress-deformation fields near the point of a stationary crack under large deformations. Based on linear theory many investigations have been conducted on the elastic stress-strain behavior around the crack tip and the similar situation of sharp corners (35, 36, 37, 38). It is generally noticed that there exists some sort of stress or strain singularities at the base of crack or in the neighborhood of any geometrical discontinuities. Occasionally inconsistencies (or paradoxes) (38) arise. For a large deformation analysis of a particular crack problem, Blatz (2) considered the plane strain problem of an infinitely long radially cracked rubber log tangentially spread by a frictionless rigid wedge. It turned out that the non-linear displacements were non-singular as compared to the linear displacements which were singular. In this problem, it has been noticed that in order to eliminate shear stress, the base of a crack must be allowed to deform into a "keyhole" shape; furthermore, a radial compression stress must be applied at the boundary so that equilibrium is maintained. Due to this "keyhole" effect, i.e., - the undeformed point (crack base) is deformed into a sector of a circle, the tangential stress at the crack base becomes infinite, while the radial stress remains non-singular.

In order to eliminate the keyhole effect (or to take into account the shear component) the above problem is modified, in the present discussion, such that the faces of the wedge are bonded to the crack, and for simplicity in analysis a special displacement field is assumed. At present this approach is the conventional method for facile application of finite elastic theory. It resulted that a particular surface traction is needed to maintain equilibrium. It is desired to compare this surface traction with the two-dimensional hydrostatic stress needed in the previously described problem. In such non-linear solution with non-hydrostatic surface traction it is required to modify the deformation field by Adkin's perturbation technique (23) so that the surface traction is reduced to a pure two-dimensional hydrostatic traction, however, in this discussion we consider only the solution for a particular displacement field and the associated stress deformation fields near the crack tip.

III. 2. Geometry of the Problem

A schematic diagram of the problem under consideration is shown in figure III. 1. An infinitely long rubber log of radius a is split lengthwise by a radial crack of depth a. Into this crack an infinitely long wedge of flank angle 2ϕ is inserted and bonded to the rubber in such a way that the tip of the wedge comes to meet the base of the crack and the radius of the rubber on the bonded plane still remains a.

Let an arbitrary point p_o of the undeformed body with cylindrical polar coordinates (r, θ, z) be displaced to a new position P (see figure III. 1) with deformed coordinates $(\bar{r}, \bar{\theta}, \bar{z})$ under the displacement field:

$$\bar{r} = r\lambda(\theta) \tag{III. 1}$$

$$\bar{\theta} = K(\theta) \tag{III. 2}$$

$$\bar{z} = z \tag{III. 3}$$

where $\lambda(\theta)$ and $K(\theta)$ are functions only of undeformed coordinate, θ, and could be determined by the aid of equations of equilibrium.

III. 3. Finite Elastic Solution

Since in large deformations one is interested in true stresses, let the deformed coordinates be chosen to be orthogonal (in this fashion mutually orthogonal planes in the deformed body will in general be non-orthogonal in the undeformed state), then the metric tensors, g_{ij}, of the undeformed body, and G_{ij}, of the deformed body, are respectively given by:

$$g_{ij} = \begin{pmatrix} \frac{1}{\lambda^2} & \frac{-\bar{r}\lambda'}{\lambda^3 K'} & 0 \\ \frac{-\bar{r}\lambda'}{\lambda^3 K'} & \frac{\bar{r}^2}{\lambda^2 K'^2}\left[\left(\frac{\lambda'}{\lambda}\right)^2+1\right] & 0 \\ 0 & 0 & 1 \end{pmatrix} \qquad \text{(III. 4)}$$

where $\lambda' = \frac{d\lambda}{d\theta}$ $\qquad K' = \frac{dK}{d\theta}$

$$G_{ij} = \begin{pmatrix} 1 & 0 & 0 \\ 0 & \bar{r}^2 & 0 \\ 0 & 0 & 1 \end{pmatrix} \qquad \text{(III. 5)}$$

The determinant of these two matrixes are respectively given by:

$$g = \text{Det}\, g_{ij} = \frac{\bar{r}^2}{\lambda^4 K'^2} \qquad \text{(III. 6)}$$

$$G = \text{Det}\, G_{ij} = \bar{r}^2 \qquad \text{(III. 7)}$$

Assuming the material is incompressible, one can set the above two determinants equal. It follows that:

$$K'(\theta) = \frac{d\bar{\theta}}{d\theta} = \frac{1}{\lambda^2(\theta)} \qquad \text{(III. 8)}$$

which relates the two undetermined functions K and λ . Relation III. 8 leads to expressing the two associated contravariant tensors for each configuration in the form:

$$g^{ij} = \begin{pmatrix} \lambda + \lambda'^2 & \frac{\lambda'}{\bar{r}\lambda} & 0 \\ \frac{\lambda'}{\bar{r}\lambda} & \frac{1}{\lambda^2 \bar{r}^2} & 0 \\ 0 & 0 & 1 \end{pmatrix} \qquad \text{(III. 9)}$$

$$G^{ij} = \begin{pmatrix} 1 & 0 & 0 \\ 0 & \frac{1}{\bar{r}^2} & 0 \\ 0 & 0 & 1 \end{pmatrix} \qquad \text{(III. 10)}$$

Now assume the material behaves in a Neo-Hookean or Mooney-Rivlin way (in plane strain there is no difference between the above two types of behavior), the constitutive stress-deformation law takes the form (22):

$$\frac{\tau^{ij}}{\mu} = g^{ij} + \bar{k}\, G^{ij} \qquad \text{(III. 11)}$$

where τ^{ij} are true stresses referred to the deformed body, and $\bar{k}$ is an unknown invariant function of coordinates, representing homogeneous stress fields, and could be determined from the equations of equilibrium and boundary conditions.

Substitution of formulas III. 9, and III. 10 into the constitutive law III. 11, yields the tensorial true stress components:

$$\frac{1}{\mu}\begin{pmatrix} \tau^{rr} & \tau^{r\theta} & \tau^{rz} \\ \tau^{\theta r} & \tau^{\theta\theta} & \tau^{\theta z} \\ \tau^{zr} & \tau^{z\theta} & \tau^{zz} \end{pmatrix} = \begin{pmatrix} \lambda^2 + \lambda'^2 + \bar{k} & \frac{\lambda'}{\bar{r}\lambda} & 0 \\ \frac{\lambda'}{\bar{r}\lambda} & \frac{1}{\bar{r}^2}\left(\frac{1}{\lambda^2} + \bar{k}\right) & 0 \\ 0 & 0 & 1 + \bar{k} \end{pmatrix} \qquad \text{(III. 12)}$$

and the physical stress components become:

$$\frac{\bar{\sigma}_{rr}}{\mu} = \lambda^2 + \lambda'^2 + \bar{k} \tag{III. 13}$$

$$\frac{\bar{\sigma}_{\theta\theta}}{\mu} = \frac{1}{\lambda^2} + \bar{k} \tag{III. 14}$$

$$\frac{\bar{\sigma}_{zz}}{\mu} = 1 + \bar{k} \tag{III. 15}$$

$$\frac{\bar{\tau}_{r\theta}}{\mu} = \frac{\bar{\tau}_{\theta r}}{\mu} = \frac{\lambda'}{\lambda} \tag{III. 16}$$

$$\bar{\tau}_{rz} = \bar{\tau}_{zr} = \bar{\tau}_{\theta z} = \bar{\tau}_{z\theta} = 0 \tag{III. 17}$$

The equations of equilibrium referred to the deformed coordinates are the familiar form:

$$\frac{\partial \bar{\sigma}_{rr}}{\partial \bar{r}} + \frac{1}{\bar{r}} \frac{\partial \bar{\tau}_{r\theta}}{\partial \bar{\theta}} + \frac{\bar{\sigma}_{rr} - \bar{\sigma}_{\theta\theta}}{\bar{r}} = 0 \tag{III. 18}$$

$$\frac{\partial \bar{\tau}_{\theta r}}{\partial \bar{r}} + \frac{1}{\bar{r}} \frac{\partial \bar{\sigma}_{\theta\theta}}{\partial \bar{\theta}} + \frac{2\,\bar{\tau}_{r\theta}}{\bar{r}} = 0 \tag{III. 19}$$

$$\frac{\partial \bar{\sigma}_{zz}}{\partial \bar{z}} = 0 \tag{III. 20}$$

It is noticed that λ appears in the stress formulas III. 13, III. 14, III. 16 is a function of θ . Hence before substitution of stress expressions into the equilibrium equations, the equilibrium equations are firstly transformed to the undeformed coordinates, giving the forms:

$$\frac{\partial \bar{\sigma}_{rr}}{\partial \ln r} + \lambda^2 \frac{\partial \bar{\tau}_{r\theta}}{\partial \theta} - \lambda \lambda' \frac{\partial \bar{\tau}_{r\theta}}{\partial \ln r} + \bar{\sigma}_{rr} - \bar{\sigma}_{\theta\theta} = 0 \qquad \text{(III. 21)}$$

$$\frac{\partial \bar{\tau}_{r\theta}}{\partial \ln r} + \lambda^2 \frac{\partial \bar{\sigma}_{\theta\theta}}{\partial \theta} - \lambda \lambda' \frac{\partial \bar{\sigma}_{\theta\theta}}{\partial \ln r} + 2 \bar{\tau}_{r\theta} = 0 \qquad \text{(III. 22)}$$

$$\frac{\partial \bar{\sigma}_{zz}}{\partial z} = 0 \qquad \text{(III. 23)}$$

Now, substitution of formulas III. 13 ~ III. 16 into equilibrium equations III. 21, III. 22, III. 23 yields:

$$\frac{\partial \bar{k}}{\partial \ln r} + \lambda \lambda'' + \lambda^2 - \frac{1}{\lambda^2} = 0 \qquad \text{(III. 24)}$$

$$\frac{\partial \bar{k}}{\partial \ln r} = \frac{\partial \bar{k}}{\partial \ln \lambda} \qquad \text{(III. 25)}$$

$$\frac{\partial \bar{k}}{\partial z} = 0 \qquad \text{(III. 26)}$$

Equation III. 26 shows that $\bar{k}$ is a function of r and θ only, hence equation III. 25 immediately yields a solution:

$$\bar{k} = \bar{k}(\ln r\lambda) \qquad \text{(III. 27)}$$

Putting equation III. 25 into equation III. 24 and integrating with respect to θ, we have:

$$\bar{k} + \frac{\lambda'^2}{2} + \frac{\lambda^2}{2} + \frac{1}{2\lambda^2} = f(\ln r) \qquad \text{(III. 28)}$$

where f is a function of $\ln r$ only. Now differentiating equation III. 28 with respect to $\ln r$ and using equation III. 24, we have:

$$\frac{df}{d\ln r} = -\lambda\lambda'' - \lambda^2 + \frac{1}{\lambda^2} = -m \qquad \text{(III. 29)}$$

where m is a separation constant to be determined from boundary conditions.

After integrating the two differential equations generated from equation III. 29 with respect to the corresponding variables, one obtains:

$$f = -m\ln r + c \qquad \text{(III. 30)}$$

$$\lambda' = \frac{d\lambda}{d\theta} = \pm\sqrt{m\ln\lambda^2 + B - \lambda^2 - \frac{1}{\lambda^2}} \qquad \text{(III. 31)}$$

where B and C are integration constants and are also to be determined from boundary conditions.

Upon combining equations III. 28, and III. 30, $\bar{k}$ is given in the form:

$$\bar{k}(r,\theta) = C - m\ln r - \frac{\lambda'^2}{2} - \frac{\lambda^2}{2} + \frac{1}{2\lambda^2} \qquad \text{(III. 32)}$$

And, integrating equation III. 31, θ and λ are related as:

$$\theta = \int_1^{\lambda} \frac{d\tilde{\lambda}}{\sqrt{m\ln\tilde{\lambda}^2 + B - \tilde{\lambda}^2 - \frac{1}{\tilde{\lambda}^2}}} \qquad \text{(III. 33)}$$

with the boundary conditions:

$$\bar{\theta} = \phi \;, \quad \bar{r} = r \;, \quad \lambda_0 = 1 \quad \text{at} \quad \theta = 0 \tag{III. 34}$$

$$\bar{\theta} = 2\pi - \phi \;, \quad \bar{r} = r \;, \quad \lambda_{2\pi} = 1 \quad \text{at} \quad \theta = 2\pi \tag{III. 35}$$

$$\bar{\theta} = \alpha, \pi \;, \quad \frac{\partial \bar{r}}{\partial \theta} = 0 \;, \quad \lambda'_{\alpha,\pi} = 0 \quad \text{at} \quad \theta = \alpha, \pi \tag{III. 36}$$

where α is an angle other than π where λ also becomes extreme. This is known in the following way:

From relation III. 31 the extreme condition is given by:

$$m \ln \lambda^2_{\alpha,\pi} + B - \lambda^2_{\alpha,\pi} - \frac{1}{\lambda^2_{\alpha,\pi}} = 0 \tag{III. 37}$$

where $\lambda_{\alpha, \pi}$ are to represent the two extreme values of λ at $\theta = \alpha$ and $\theta = \pi$ respectively. The existence of these two extreme values can be more easily visualized by the aid of following transformation:

$$X = \ln \lambda^2 \tag{III. 38}$$

then, condition III. 37 takes the form:

$$m X_{\alpha,\pi} + B - 2 \cosh X_{\alpha,\pi} = 0 \tag{III. 39}$$

where $X_{\alpha, \pi}$ are the two extreme values of X corresponding to λ_α, λ_π respectively. In view of formula III. 31, the quantity under the square root must be positive, so after using the transformation III. 38 it is easy to see that B $\geqslant$ 2. And since m $>$ 0 (this will be shown later) the straight line mX + B will intersect the cosh X curve at two points $X_{min} < 0$, $X_{max} > 0$ in a fashion as shown in figure III. 2 giving two extreme values of $\lambda_{min} < 1$, $\lambda_{max} > 1$. As will be seen later, λ_{min}, λmax are identified to be $\lambda_\pi = \lambda_{min}$, $\lambda_\alpha = \lambda_{max}$.

Integrating equation III. 8 with respect to θ, and making use of relation III. 31 and the boundary condition at $\theta = 0$, we have:

$$\bar{\theta} = \phi + \int_1^\lambda \frac{d\tilde{\lambda}}{\tilde{\lambda}^2\sqrt{m\ln\tilde{\lambda}^2 + B - \tilde{\lambda}^2 - \frac{1}{\tilde{\lambda}^2}}} \tag{III. 40}$$

where m, B are related from the extreme condition III. 37.

The non-zero stress components, after using relations III. 31, and III. 32, and assuming $\bar{\sigma}_{rr} = 0$* at r=a, $\theta = \alpha$ become:

$$\frac{\bar{\sigma}_{rr}}{\mu} = m\ln\frac{a}{r}\frac{\lambda}{\lambda_\alpha} + \frac{1}{\lambda_\alpha^2} - \frac{1}{\lambda^2} \xrightarrow[r\to 0]{} m\ln\frac{a}{r} \tag{III. 41}$$

$$\frac{\bar{\sigma}_{\theta\theta}}{\mu} = m\ln\frac{a}{r}\frac{\lambda_\alpha}{\lambda} + \lambda_\alpha^2 + \frac{1}{\lambda^2} \xrightarrow[r\to 0]{} m\ln\frac{a}{r} \tag{III. 42}$$

$$\frac{\bar{\sigma}_{zz}}{\mu} = m\ln\frac{a}{r}\frac{\lambda_\alpha}{\lambda} - \lambda^2 + 1 \xrightarrow[r\to 0]{} m\ln\frac{a}{r} \tag{III. 43}$$

$$\frac{\bar{\tau}_{r\theta}}{\mu} = \frac{1}{\lambda}\sqrt{m\ln\lambda^2 + B - \lambda^2 - \frac{1}{\lambda^2}} \tag{III. 44}$$

Eliminating B by using the extreme condition III. 37 and using the

---

* This is just one of the ways to determine constant C.

boundary condition III. 36 for $\theta = \pi$, the two formulas III. 33, III. 40 become:

$$\pi = \int_{1}^{\lambda_{\alpha-}} \frac{\lambda d\lambda}{\sqrt{(\lambda^2_{\alpha,\pi}-\lambda^2)(\lambda^2-\frac{1}{\lambda^2_{\alpha,\pi}})-\lambda^2 m \ln\frac{\lambda^2_{\alpha,\pi}}{\lambda^2}}} + \int_{\lambda_{\alpha+}}^{\lambda_{\pi-}} \frac{\lambda d\lambda}{\sqrt{(\lambda^2_{\alpha,\pi}-\lambda^2)(\lambda^2-\frac{1}{\lambda^2_{\alpha,\pi}})-\lambda^2 m \ln\frac{\lambda^2_{\alpha,\pi}}{\lambda^2}}} \qquad \text{(III. 45)}$$

$$\pi-\phi = \int_{1}^{\lambda_{\alpha-}} \frac{d\lambda}{\lambda\sqrt{(\lambda^2_{\alpha,\pi}-\lambda^2)(\lambda^2-\frac{1}{\lambda^2_{\alpha,\pi}})-\lambda^2 m \ln\frac{\lambda^2_{\alpha,\pi}}{\lambda^2}}} + \int_{\lambda_{\alpha+}}^{\lambda_{\pi-}} \frac{d\lambda}{\lambda\sqrt{(\lambda^2_{\alpha,\pi}-\lambda^2)(\lambda^2-\frac{1}{\lambda^2_{\alpha,\pi}})-\lambda^2 m \ln\frac{\lambda^2_{\alpha,\pi}}{\lambda^2}}} \qquad \text{(III. 46)}$$

It is noted that in the above integrals, singularities arise, at $\theta = \alpha$ and $\theta = \pi$ due to the extreme condition III. 37. The relations III. 45, III. 46, III. 37 (which is double valued) determine the four parameters, B, m, λ_α and λ_π. Since these integrals do not yield elementary forms, a graphical method will be used for special flank angles.

Before doing this however, we will first consider the case of a small flank angle for which parameters m and λ_{max} can be related to ϕ in a simple form in the following way.
For $\phi \ll 1$, assume $\lambda_\alpha = \lambda_{max}$ and write:

$$\lambda^2 = \lambda^2_\alpha(1-\epsilon), \qquad \epsilon \ll 1 \qquad \text{(III. 47)}$$

The integrands of formula III. 45 can be expanded and integrated out to give the following relation for m and λ_α :

$$\pi \approx \frac{2\sqrt{\lambda^2_\alpha - 1}}{\sqrt{\lambda^2_\alpha - \frac{1}{\lambda^2_\alpha} - m}} \qquad \text{(III. 48)}$$

It must be noted that the expansion of the integrands must be based on λ_{max} otherwise the result will include an imaginary term. In case $\lambda_\pi = \lambda_{max}$ we also obtain the same form III.48 only with λ_α replaced by λ_π.

Similarly, writing (let $\lambda_\alpha = \lambda_{max}$)

$$\lambda^2 = \frac{\lambda_\alpha^2}{1+\epsilon} \quad , \qquad \epsilon \ll 1 \tag{III.49}$$

then the formula III.46 can be integrated to give:

$$\lambda_\alpha(\pi-\phi) \approx \frac{2\sqrt{\lambda_\alpha^2-1}}{\sqrt{\lambda_\alpha^2-\frac{1}{\lambda_\alpha^2}-m}} \tag{III.50}$$

From relations III.48, III.50 one obtains:

$$\lambda_\alpha \approx \frac{1}{1-\frac{\phi}{\pi}} \tag{III.51}$$

Combine relations III.48, III.51 it follows that:

$$m \approx 4\left(1-\frac{2}{\pi^2}\right)\frac{\phi}{\pi} + O\left(\frac{\phi}{\pi}\right)^2 + \cdots \tag{III.52}$$

from which we know that m can never be negative. B is obtained from relations III.37, III.51, III.52 to be:

$$B \approx 2 + O\left(\frac{\phi}{\pi}\right)^2 + \cdots \tag{III.53}$$

The above three relations III.51, III.52, III.53 can be used to estimate the starting trial values of λ_α, m, B in the graphical evaluation of integrals III.45, III.46 for the case of large ϕ.

Now we will integrate equations III.45 and III.46 graphically for the case of large flank angle $2\phi = 90^{\circ}$ and of small angle $2\phi = 9^{\circ}$. λ_{max} is firstly determined from formula III.51 and m is estimated from formula III.52. Tentatively fix the point X_{max} (see figure III.2) and vary the slope m and obtain the best values m, B, λ_{min} such that the equalities of equations III.45 and III.46 hold. We note that there are two types of order of integration, i.e.:

i) From $\lambda = 1 \longrightarrow \lambda_{max} \longrightarrow \lambda_{min}$ (III.54)

ii) From $\lambda = 1 \longrightarrow \lambda_{min} \longrightarrow \lambda_{max}$ (III.55)

The second type never makes the equal signs of equations III.45 and III.46 hold, but the first type does. Therefore, it is identified that:

$$\lambda_{\alpha} = \lambda_{max} \tag{III.56}$$

$$\lambda_{\pi} = \lambda_{min} \tag{III.57}$$

In this graphical evaluation the regions near infinity were cut off and the total error was kept far less than 1 percent of the total value, and the best values of parameters are found to be:

For $2\phi = 90^{\circ}$:

$$\begin{aligned} \lambda_{\alpha} &= 1.330 \\ \lambda_{\pi} &= 0.965 \\ m &= 0.514 \\ B &= 2.041 \\ \alpha &= 83^{\circ} \\ (\bar{\theta}-\phi)_{\alpha} &= 61^{\circ} \end{aligned} \tag{III.58}$$

For $2\phi = 9^\circ$:

$$\begin{aligned}
\lambda_\alpha &= 1.025\\
\lambda_\pi &= 0.999\\
m &= 0.470\\
B &= 2.00003\\
\alpha &= 88^\circ\\
(\bar{\theta}-\phi)_\alpha &= 85^\circ
\end{aligned} \tag{III.59}$$

Thus the periphery of the rubber log is deformed in such a way that at $\theta = \alpha$ the material is squeezed out and at $\theta = \pi$ it is moved in as shown in figures III.3, and III.6 respectively for large and small flank angles. For large flank angle $2\phi = 90^\circ$, $\lambda_\alpha = \lambda_{max}$ occurs at $\bar{\theta} - \phi = 61^\circ$ which corresponds to $\theta = \alpha = 83^\circ$, and $\lambda = 1$ also occurs at $\bar{\theta} - \phi = 120^\circ$ (or $\theta = 166^\circ$) . For small flank angle $2\phi = 9^\circ$, $\lambda_\alpha = \lambda_{max}$ occurs at $\bar{\theta} - \phi = 85^\circ$ (or $\theta = \alpha = 88^\circ$) and $\lambda = 1$ occurs at $\bar{\theta} - \phi = 170^\circ$ (or $\theta = 174^\circ$), and for very small flank angle, $\phi \ll 1$, the position of λ_α will approach $(\pi-\phi)/2$. Figure III.5 shows the relation of θ and $\bar{\theta}$ for the two flank angles. For very small strain θ and $\bar{\theta}$ are nearly linearly related. Figrue III.4, and III.7 show the boundary stresses which must be applied in order that the deformation field III.1, III.2, and III.3 is maintained for the two cases of different flank angles. It is seen from the stress formulas III.41 $\sim$ III.44 that shear stress is independent of the radial coordinate, while the three normal stresses behave as $\ln(a/r)$ as the crack base is approached. Thus the crack base is subjected to infinite hydrostatic tensions.

Also we notice that the surface tractions are somewhat different from the two-dimensional hydrostatic traction. Hence the stress field must be modified so that the surface tractions are reduced to the two-dimensional hydrostatic traction, which however is not our interest at present.

PART IV

DEFORMATIONS OF FOAMED ELASTOMERS

IV. 1. Introduction

Beside the widespread practical use, a foamed material (a metal foam is also included, which may be used as an impact energy absorber) can be used, as in Part I, to investigate the dilatational effect of continuum rubbers; it can also be used for studying the behavior of unfilled composite propellants. The thermodynamic properties of composites generally depend on the weight percent of filler material, and conversely the mechanical properties of foam depend largely on volume percent of the binder (≡ foam structure).

Furthermore, the structure of continuum rubbers in the region of non-Gaussian extension, i.e., - the finite length of the chains of the network become distributed in a non-Gaussian fashion at large extensions, may be represented by that of a highly voided foam. Since such foam consists of a number of thin threads joined at their ends to form a three dimensional network, these threads and joints may be considered as equivalent molecular chains and junction points of a rubber network. The foam rubber also serves for a phenomenological study of crack growth in rubbers since the intrinsic nature of tearing in rubbers is nothing but continuous breakage of molecular chains which can be visualized as tearing of the foam threads.

In this discussion a theoretical treatment of an idealized open cell model for a foam structure is presented. For this we first investigate the geometry of interstices of idealized packings of uniform spherical voids and, by using three dimensional beam analysis, equivalent elastic constants of the system are calculated and compared with the experimental data.

IV. 2. Packing of Spheres

Spheres of identical size can be piled and packed together in fourteen different ways (46). Of these only typical closest packings will be considered.

For closest packing in a flat plane, each circle contacts six surrounding circles, and the packing density (area of circles in unit area/unit area) or the void content (when one considers circles as void and the interstices material) is 0.907.

In an ordinary space there are two ways for closest packing of uniform spheres, i.e., - hexagonal and face-centered cubic packings. Suppose the first layer is the plane closest packing, the second layer is formed by placing spheres in alternate hollows of the first layer. In making the third layer there are two different ways: i) Place each sphere on a hollow that is directly above a sphere in the first layer, which structure leads to a hexagonal-closest packing as shown in figure IV. 1. ii) Place each sphere in a hollow directly above a hollow in the first layer, which piling is obtained by rotating the third layer of the hexagonal packing by 60°. The structure becomes a face-centered cubic closest packing as shown in figure IV. 3. In both types of packing each sphere makes contact with twelve other surrounding ones, in these cases the packing density (or void content) is 0. 74 for both. This is the hitherto known maximum density of packing uniform spheres, however densities higher than this could be obtained if the spheres are not uniform in sizes, since smaller spheres will fill the interstices of the big ones. The closest packing of spheres has also been studies in four and five dimensional spaces, however, the packing density is always lower than that in ordinary space. The following table shows the packing densities of some typical ways of packing uniform spheres:

Ways of Packing	Packing Density
Plane Closest Packing	0.907
Hexagonal Closest Packing	0.740
Face Centered Cubic Closest Packing	0.740
Body Centered Cubic Closest Packing	0.681
Cubic Packing	0.524
Four-Dimensional Packing	0.617
Five-Dimensional Packing	0.465
Tetrahedral Packing	0.340
Random Packing (41)	0.59 ~ 0.63

IV. 3. Geometry of Interstices

In order that the interstices can be easily visualized, let each sphere expand uniformly, so that a contacting surface becomes flat and tangent to a contact point. Thus, each sphere becomes a polyhedron. The hexagonal-closest packing will turn each sphere into a trapezo-rhombic dodecahedron (we will call this unit cell) with six equilateral trapezoids and six congruent rhombics. Most of the interstices are then squeezed to form 24 edges of this dodecahedron as shown in figure IV. 2. If the whole system of the interstices is oriented in the way shown in this figure, each unit cell will involve three members vertically connected with that of neighboring cells, forming straight-through members of the whole system, and three vertical members connected to that of the neighboring cell by means of inclined members, forming non-straight through members of the entire system.

The face centered cubic packing will transform each sphere into rhombic-dodecahedron, the twelve faces of which are congruent rhombics. The interstices now form the 24 edges of this dodecahedron as shown in figure IV. 4. If the system is oriented in the way shown in this figure, all the vertical members will be connected by means of the inclined members and form non straight - through members of the entire system. Clearly if a trapezo-rhombic dodecahedron is sliced in half by a horizontal plane and one half of it is rotated by 60°, it will become a rhombic dodecahedron.

In an actual highly voided foam structure, most of the cells are observed to be pentagonal dodecahedrons, as shown in figure IV.7, which are formed by packing five spheres around the hollow of two adjacent spheres as shown in figure IV.5 and then the spheres are allowed to expand uniformly (see figure IV.6). In this packing the spheres do not contact each other before expansion.

The obtuse angle in either trapezoid or rhombic is $109^{\circ}28'$ which is the angle made by any two of the four members extended radially from the same point and equally spanned in a space (tetrahedral angle).

In the two dimensional case, if the circles are allowed to expand uniformly, a contacting point of two circles will become a line, thus each circle will be transformed into a regular hexagon.

IV.4. Deformation of Interstices

A. Hexagonal Closest Packing

For simplicity let all the members of the interstices have a uniform equilateral triangular cross section (this is very representative for a highly voided foam structure). Let the system be oriented in such a way that the straight through members lie in the z-direction (see figure IV.2 and figure IV.8.a) and subjected to a small uniaxial deformation. Since the unit structure cut out by a hexagonal cylinder shown in figure IV.8.a is repeated in the whole system, the deformation of the whole system can be represented by this unit structure. It consists of one straight through member connected to six non-straight through members by means of three inclined members joined at one point. Figure IV.8.b shows a top view of the whole structure divided by the unit structures.

Let the stress σ_z be transformed into axial forces P and P' acting on the straight-through and non-straight-through members respectively. Since only a one third part of a non-straight-through member is within the unit hexagonal cylinder, the axial force P' is divided into three parts so that the axial force acting on this one third part is P'/3. The stress σ_z could relate to the forces P and P' in the following fashion:

$$P + P' = \frac{3\sqrt{3}}{2} \ell^2 \sin^2\theta \ \sigma_z \qquad \text{(IV.1)}$$

where P and P' can be related in such a way that after deformation points A and C still lie on the same plane perpendicular to the z-axis, and $\pi - \theta = 109^\circ 28'$ or $\cos\theta = 1/3$, and ℓ is the length of the member.

1. Deformation of System AOBC

The deformation of the unit hexagonal cylinder under the present orientation can be represented by that of the system AOBC, since it is repeated in the unit structure.

i) Member OA

At point O, four members OA, OB', OI', OJ' are equally spanned in the space from a point O, - similarly for the rest of the four members OA', OB, OI, OJ. Thus, the six moments at O are mutually balanced out, causing null net bending at O of member OA (see figure IV.10.a). The only contribution to the deformation of OA is an axial force P. Hence, the displacement of A in the z-direction with respect to O is given by:

$$\delta_{A_z} = \frac{P\ell}{2AE}(1+\cos\theta) \tag{IV.2}$$

where A is the cross sectional area of any member, and E its elastic modulus.

ii) <u>Member BC</u>

From point B, there are four members extending out and equally spanned in the space. The three moments at this point are mutually balanced, so that there is no net bending on member BC (see figure IV.10.b). Hence, the deformation of BC is due to the simple tensile force P' only, and the axial displacement of C with respect to B is given by:

$$\delta_{C_z} = \frac{P'\ell}{2AE}(1-\cos\theta) \tag{IV.3}$$

iii) <u>Member OB</u>

This member is subjected to tension, shear and bending as shown in diagrams a, b, c of figure IV.9 . Figure IV.10.c shows the free body diagram of OB. The displacement of B with respect to O in OB direction due to the tensile force $\frac{P'}{3}\cos\theta$ is:

$$\delta_B = \frac{P'\ell}{3AE}\cos\theta \tag{IV.4}$$

And the shear displacement of B due to shearing force $\frac{P'}{3}\sin\theta$ is:

$$\delta'_B = \frac{2P'\ell(1+\nu)}{3AE}\sin\theta \tag{IV.5}$$

where ν is the Poisson's ratio of any member. Finally the moment displacement of B with respect to O due to moments M is:

$$\delta''_B = \frac{M\ell^2}{6EI} = \frac{\sqrt{3}\,M\ell^2}{EA^2} \tag{IV.6}$$

where $I = \frac{\sqrt{3}}{18} A^2$ is the moment of inertia taken about the principal axis of the cross section. Since the moment M at both ends of OB is balanced by the shear force, $\frac{P'}{3}\cos\theta$, we have:

$$M = \frac{P'\ell}{6}\sin\theta \tag{IV.7}$$

Now the total displacement of C with respect to O in z, r directions, D_{cz}, D_{cr} become:

$$\begin{aligned} D_{cz} &= \delta_{cz} + \delta_{Bz} + \delta'_{Bz} + \delta''_{Bz} \\ &= \frac{P'\ell}{6AE}\left[5 - 3\cos\theta + \left\{2(1+2\nu) + \sqrt{3}\frac{\ell^2}{A}\right\}\sin^2\theta\right] \end{aligned} \tag{IV.8}$$

$$\begin{aligned} D_{cr} &= \delta_{Br} + \delta'_{Br} + \delta''_{Br} \\ &= -\frac{P'\ell}{6AE}\left[2(1+2\nu) + \sqrt{3}\frac{\ell^2}{A}\right]\sin\theta\cos\theta \end{aligned} \tag{IV.9}$$

The strains in z, r directions are respectively given by:

$$\epsilon_z = \frac{2\,\delta_{Az}}{\ell\,(1+\cos\theta)} = \frac{P}{AE} \qquad \text{(IV. 10)}$$

$$\epsilon_r = \frac{D_{cr}}{\ell\sin\theta} = -\frac{P'}{6AE}\left[2(1+2\nu)+\sqrt{3}\,\frac{\ell^2}{A}\right]\cos\theta \qquad \text{(IV. 11)}$$

And the equivalent Poisson's ratio of the unit structure is given by:

$$\nu^* = -\frac{\epsilon_r}{\epsilon_z} = \frac{P'}{6P}\left[2(1+2\nu)+\sqrt{3}\,\frac{\ell^2}{A}\right]\cos\theta \qquad \text{(IV. 12)}$$

As mentioned before, we will relate P and P' such that after deformation points A and C are still coplaner. Hence by equating equation IV. 2 and IV. 8, it follows that:

$$\frac{P}{P'} = \frac{5-3\cos\theta+\left\{2(1+2\nu)+\sqrt{3}\,\frac{\ell^2}{A}\right\}\sin^2\theta}{3\,(1+\cos\theta)} \qquad \text{(IV. 13)}$$

which after combining with equation IV. 1 yields:

$$P = \frac{3\sqrt{3}\,\ell^2\,\sigma_z\sin^2\theta}{2\left[1+\frac{3\,(1+\cos\theta)}{Q}\right]} \qquad \text{(IV. 14)}$$

$$P' = \frac{3\sqrt{3}\,\ell^2\,\sigma_z\sin^2\theta}{2\left[1+\frac{Q}{3(1+\cos\theta)}\right]} \qquad \text{(IV. 15)}$$

where $$Q = 5 - 3\cos\theta + \left\{2(1+2\nu) + \sqrt{3}\,\frac{\ell^2}{A}\right\}\sin^2\theta$$

Substitution of relation IV.13 into equation IV.12 yields:

$$\nu^* = \frac{\left[2(1+2\nu) + \sqrt{3}\,\frac{\ell^2}{A}\right]\left[1+\cos\theta\right]\cos\theta}{2\left[5 - 3\cos\theta + \left\{2(1+2\nu) + \sqrt{3}\,\frac{\ell^2}{A}\right\}\sin^2\theta\right]} \tag{IV.16}$$

Since $\pi - \theta = 109^\circ 28'$ or $\cos\theta = 1/3$, $\sin\theta = \frac{2\sqrt{2}}{3}$, this formula becomes:

$$\nu^* = \frac{1}{4}\,\frac{2(1+2\nu) + \sqrt{3}\,\frac{\ell^2}{A}}{\frac{13}{2} + 4\nu + \sqrt{3}\,\frac{\ell^2}{A}} \tag{IV.17}$$

Thus the equivalent Poisson's ratio of the entire system depends on i) Poisson's ratio of the interstices, and ii) the slenderness of each member $\frac{\ell^2}{A}$, which is related to the density of packing, and independent of the cell size. For incompressible interstices, $\nu = 1/2$, it follows that:

$$\nu^* = \frac{1}{4}\left[1 - \frac{9}{17 + 2\sqrt{3}\,\frac{\ell^2}{A}}\right] \xrightarrow[\frac{\ell^2}{A}\to\infty]{} \frac{1}{4} \tag{IV.18}$$

which is always less that 1/4.

The equivalent elastic modulus of the system is given by:

$$\frac{E^*}{E} = \frac{\sigma_z}{\epsilon_z E} = \frac{\sqrt{3}}{4}\left[1 + \frac{9}{4\left\{13 + 8\nu + 2\sqrt{3}\,\frac{\ell^2}{A}\right\}}\right]\left[\frac{A}{\ell^2}\right] \tag{IV.19}$$

which also depends on Poisson's ratio and slenderness of the members of interstices, and for incompressible interstices this formula becomes:

$$\frac{E^*}{E} = \frac{\sqrt{3}}{4}\left[1 + \frac{9}{4\left[17 + 2\sqrt{3}\frac{\ell^2}{A}\right]}\right]\left[\frac{A}{\ell^2}\right] \xrightarrow[\frac{\ell^2}{A}\to\infty]{} 0 \tag{IV.20}$$

By the aid of figure IV.8.a , the slenderness, $\frac{\ell^2}{A}$ can be related to the density of voids, d:

$$\frac{A}{\ell^2} = \frac{2\sqrt{3}}{9}(1-d) \tag{IV.21}$$

Thus for a given void content the elastic constants E* , ν * can be calculated in terms of those of elastomeric binders.

B. Face-Centered Cubic Closest Packing

The unit structure for this case is shown in figure IV.11.a, which consists of one vertical member and twelve inclined members. In this case, there is no straight through member in the entire system. The deformation of this unit structure is represented by that of sub-system AOBC which in turn is governed by the deformation of the rhombic AOB'C' . All the vertical members in the entire structure are subjected to the same tensile load P.

1. Deformation of System AOBC

i) Member OA

Like the previous case, the end moments at A and O cause null net bending moment (see figure IV.11.c), thus the deformation of OA is only caused by the uniaxial tensile load P. Hence, the displacement A with respect to O is:

$$\delta_{Az} = \frac{P\ell}{AE} \tag{IV.22}$$

ii) Member OB (or AC)

As in the previous case, this member is subjected to tension, shear and bending. Figure IV.11.b shows its free body diagram. The displacement at B is one half that at B' which can immediately be obtained by replacing P' for the previous case by P. Hence, the z, r displacements at B become:

$$\delta_{Bz} = \frac{P\ell}{12AE}\left[2 + \left\{2(1+2\nu) + \sqrt{3}\frac{\ell^2}{A}\right\}\sin^2\theta\right] \qquad \text{(IV.23)}$$

$$\delta_{Br} = \frac{-P\ell}{12AE}\left[2(1+2\nu) + \sqrt{3}\frac{\ell^2}{A}\right]\sin\theta\cos\theta \qquad \text{(IV.24)}$$

The total displacement at B in the z-direction with respect to O takes the form:

$$D_{Bz} = \delta_{Az} + \delta_{Bz} = \frac{P\ell}{AE}\left[1 + \frac{1}{12}\left\{2 + \left\{2(1+2\nu) + \sqrt{3}\frac{\ell^2}{A}\right\}\sin^2\theta\right\}\right] \qquad \text{(IV.25)}$$

The strains in z, r directions become:

$$\epsilon_z = \frac{D_{Bz}}{\ell(1+\frac{\cos\theta}{2})} = \frac{2P}{AE(2+\cos\theta)}\left[1 + \frac{1}{12}\left\{2 + \left\{2(1+2\nu) + \sqrt{3}\frac{\ell^2}{A}\right\}\sin^2\theta\right\}\right] \qquad \text{(IV.26)}$$

$$\epsilon_r = \frac{2\,\delta_{Br}}{\ell\sin\theta} = -\frac{P}{6AE}\left[2(1+2\nu) + \sqrt{3}\frac{\ell^2}{A}\right]\cos\theta \qquad \text{(IV.27)}$$

After substituting the known values, the equivalent Poisson's ratio takes the form:

$$\nu^* = -\frac{\epsilon_r}{\epsilon_z} = \frac{7}{8}\,\frac{\left[2 + 4\nu + \sqrt{3}\,\frac{l^2}{A}\right]}{\left[\frac{71}{4} + 4\nu + \sqrt{3}\,\frac{l^2}{A}\right]} \tag{IV.28}$$

And for incompressible interstices ($\nu = 1/2$) this becomes:

$$\nu^* = \frac{7}{8}\,\frac{4 + \sqrt{3}\,\frac{l^2}{A}}{\frac{79}{4} + \sqrt{3}\,\frac{l^2}{A}} \xrightarrow[\frac{l}{A}\to\infty]{} \frac{7}{8} \tag{IV.29}$$

This value of ν^* is nothing unusual, because the structure of the interstices is non-isotropic and the value of ν^* will vary with the axis of orientation. For example if a square frame is pulled uniaxially in the direction perpendicular to its faces the value of ν^* is zero. On the other hand if it is pulled in the diagonal direction the value ν^* becomes ≈ 1. The equivalent elastic modulus for this case becomes:

$$\frac{E^*}{E} = \frac{63\sqrt{3}}{71 + 16\nu + \sqrt{3}\,\frac{l^2}{A}}\,\frac{A}{l^2} \tag{IV.30}$$

or for incompressible interstices:

$$\frac{E^*}{E} = \frac{63\sqrt{3}}{79 + 4\sqrt{3}\,\frac{l^2}{A}}\,\frac{A}{l^2} \xrightarrow[\frac{l}{A}\to\infty]{} 0 \tag{IV.31}$$

C. Combined Structure

Now, in order to represent the actual foamed structure by combining the above two types of structure, we adjust the amount of content of each type of structure in the combined structure such that the over-all value of ν^* is equal to the experimental value for certain typical voids content (we use 47% voids). For such a void content, the hexagonal-closest packing gives the equivalent Poisson's ratio as:

$$\nu^* = 0.184$$

while the face-centered-cubic-closest packing gives a value of:

$$\nu^* = 0.386$$

If the combined foam structure consists of 67.4% hexagonal packing and 32.6% face-centered-cubic packing then the equivalent Poisson's ratio of such structure will give the value exactly the same as the previously measured value,

$$\nu^* = 0.25$$

Now we use this combined structure containing the two types of structure in the above ratio and calculate the value ν^* for 87% voided foam structure for an example, we obtain

$$\nu^* = 0.35$$

which compares favorably with Gent and Thomas' (44) observed value $\nu^* = 0.33$ for the similar void content. In actual foam it is observed that there is no systematic trend of dependence of Poisson's ratio on void contents and the Poisson's ratios of natural rubber for a wide range of void contents fall in the vicinity of 0.33 (44). This maybe ascribed not only to the errors involved in measuring small dimensional changes but also to the buckling of threads at the extensions for which measurement is possible. Thus the calculated values of ν^* based on the above combined structure should be reasonable predictions for whole range of void contents of an actual foam rubber, and thus the idealized model is reasonably good.

APPENDIX

DERIVATION OF CONSTITUTIVE STRESS-DEFORMATION LAW FOR A HOMOGENEOUS, CONTINUOUS, ISOTROPIC MATERIALS (22)

Let

$$g_{ik} = \frac{\partial x^m}{\partial \theta^i} \frac{\partial x^m}{\partial \theta^k} \qquad G_{ik} = \frac{\partial X^m}{\partial \theta^i} \frac{\partial X^m}{\partial \theta^k} \tag{A. 1}$$

be the metric tensors respectively for the undeformed and deformed bodies, where

x^i : undeformed rectangular cartesian coordinates

X^i : deformed rectangular cartesian coordinates

θ^i : general curvilinear coordinates.

Define a deformation tensor, $M^i_{\cdot k}$ as:

$$M^i_{\cdot k} = g^{im} G_{mk} \tag{A. 2}$$

(not necessarily symmetric)

The strain energy per unit undeformed volume for the above material is a function only of the three invariants of the deformation tensor, $M^i_{\cdot k}$, i.e.,

$$W = W(I_M, II_M, III_M) \tag{A. 3}$$

where

$$I_M = \frac{1}{1!} \delta^i_j M^j_{\cdot i} = \mathrm{Tr}\, M^i_{\cdot k} \tag{A. 4}$$

$$\mathrm{II}_M = \frac{1}{2!}\delta^{ik}_{jl} M^{l}_{\cdot k} M^{j}_{\cdot i} = \frac{1}{2}\left(\mathrm{I}^2_M - M^{i}_{\cdot k} M^{k}_{\cdot i} \right) \tag{A.5}$$

$$\mathrm{III}_M = \frac{1}{3!}\delta^{ikm}_{jln} M^{n}_{\cdot m} M^{l}_{\cdot k} M^{j}_{\cdot i} = \mathrm{Det}\, M^{i}_{\cdot k} \tag{A.6}$$

From the principle of virtual work we obtain:

$$\delta W = \sqrt{\mathrm{III}_M}\, \tau^{ik} \delta \gamma_{ik} = \sqrt{\mathrm{III}_M}\, \frac{\tau^{ik}\delta G_{ik}}{2} \tag{A.7}$$

where

$$\gamma_{ik} = \frac{1}{2}\left(G_{ik} - g_{ik} \right) \tag{A.8}$$

Then the tensorial stresses at a point in the deformed body, referred to curvilinear coordinates θ^i, become:

$$\tau^{ik} = \frac{2}{\sqrt{\mathrm{III}_M}} \frac{\partial W}{\partial G_{ik}} = \frac{2}{\sqrt{\mathrm{III}_M}} \frac{\partial W}{\partial M^{m}_{\cdot k}} \frac{\partial M^{m}_{\cdot k}}{\partial G_{ik}} = \frac{2}{\sqrt{\mathrm{III}_M}} g^{mi} \frac{\partial W}{\partial M^{m}_{\cdot k}} \tag{A.9}$$

or

$$\tau^{ik} = \frac{2}{\sqrt{\mathrm{III}_M}} g^{mi} \left[\frac{\partial W}{\partial \mathrm{I}_M} \frac{\partial \mathrm{I}_M}{\partial M^{m}_{\cdot k}} + \frac{\partial W}{\partial \mathrm{II}_M} \frac{\partial \mathrm{II}_M}{\partial M^{m}_{\cdot k}} + \frac{\partial W}{\partial \mathrm{III}_M} \frac{\partial \mathrm{III}_M}{\partial M^{m}_{\cdot k}} \right] \tag{A.10}$$

Now, differentiating equations A.4, A.5, and A.6 with respect to the deformation tensor M, we have:

$$\frac{\partial \mathrm{I}_M}{\partial M^{m}_{\cdot k}} = \delta^{k}_{m} \tag{A.11}$$

$$\frac{\partial \mathrm{II}_M}{\partial M^{m}_{\cdot k}} = \mathrm{I}_M \delta^{k}_{m} - M^{k}_{\cdot m} = \mathrm{II}_M (M^{-1})^{k}_{\cdot m} - \mathrm{III}_M (M^{-1})^{k}_{\cdot n} (M^{-1})^{n}_{\cdot m} \tag{A.12}$$

$$\frac{\partial \mathrm{III}_M}{\partial M^{m}_{\cdot k}} = \mathrm{II}_M \delta^{k}_{m} - \mathrm{I}_M M^{k}_{\cdot m} + M^{k}_{\cdot n} M^{n}_{\cdot m} = \mathrm{III}_M (M^{-1})^{k}_{\cdot m} \tag{A.13}$$

where $(M^{-1})^{k}_{\cdot m}$ is the inverse of $M^{k}_{\cdot m}$, and the second halves of relations A. 12 and A. 13 are obtained by using Cayley-Hamilton's Theorem.

Substitution of relations A. 11, A. 12, and A. 13 into A. 10 yields a general form of constitutive stress-deformation law:

$$\tau^{ik} = \frac{2}{\sqrt{\mathrm{III}_M}} \left[\frac{\partial W}{\partial \mathrm{I}_M} g^{ki} - \mathrm{III}_M \frac{\partial W}{\partial \mathrm{II}_M} G^{k\ell} g_{\ell n} G^{ni} + \left(\mathrm{II}_M \frac{\partial W}{\partial \mathrm{II}_M} + \mathrm{III}_M \frac{\partial W}{\partial \mathrm{III}_M} \right) G^{ki} \right] \quad \text{(A. 14)}$$

Now the physical stresses $\bar{\sigma}^{ik}$ at a point X^i in the deformed body, referred to the rectangular cartesian coordinates X^i are obtained by setting $\theta^i = X^i$. By so doing, the relations A. 4, A. 5 and A. 6 are reduced to

$$\mathrm{I}_M = \mathrm{I}_1 \ , \quad \mathrm{II}_M = \mathrm{I}_2 \ , \quad \mathrm{III}_M = \mathrm{I}_3 \qquad \text{(A. 15)}$$

and equation A. 14 is reduced to the form:

$$\bar{\sigma}_{ik} = \bar{\sigma}^{ik} = \frac{2}{\sqrt{\mathrm{I}_3}} \left[\frac{\partial W}{\partial \mathrm{I}_1} C_{ik} - \mathrm{I}_3 \frac{\partial W}{\partial \mathrm{I}_2} (C^{-1})_{ik} + \left(\mathrm{I}_2 \frac{\partial W}{\partial \mathrm{I}_2} + \mathrm{I}_3 \frac{\partial W}{\partial \mathrm{I}_3} \right) \delta_{ik} \right] \qquad \text{(A. 16)}$$

which is equation I. 2.

REFERENCES

1. Blatz, P. J.; Ko, W. L.: Application of Finite Elastic Theory to the Deformation of Rubbery Materials. Trans. Soc. Rheo. Vol. 6, pp. 223-251 (1962).

2. Blatz, P. J.: Finite Elastic Deformation of a Plane Strain Wedge-Shaped Radial Crack in a Compressible Cylinder. GALCIT SM 61-8, California Institute of Technology (1961).

3. Blatz, P. J.: The Yield Surface in Normal Stress or Normal Strain Space. (GALCIT SM 60-14, California Institute of Technology (1960).) 19th Meeting Bulletin of JANAF Physical Properties Panel, p. 165, September, (1960).

4. Blatz, P. J.: Application of Finite Elastic Theory to the Deformation of Rubbery Materials. GALCIT SM 61-7, California Institute of Technology (1961).

5. Blatz, P. J.: Application of the Strain Energy Criterion to the Fracture of Rubbery Materials. GALCIT SM 60-22, California Institute of Technology (1960).

6. Blatz, P. J.: The Equation of State of Polymeric Materials. GALCIT SM 61-26, California Institute of Technology, (1961).

7. Blatz, P. J.: Application of Finite Elastic Theory in Predicting the Performance of Solid Propellant Rocket Motors. GALCIT SM 60-25, California Institute of Technology, (1960).

8. Blatz, P. J.: Thermomechanical Behavior of the Ideal Elastomer, GALCIT SM 62-44, California Institute of Technology, (1962).

9. Blatz, P. J.; Ko, W. L.; Zak, A. R.: Fundamental Studies Relating to the Mechanical Behavior of Solid Propellants, Rocket Grains and Rocket Motors.

   GALCIT SM 61-15, California Institute of Technology (1961)
   GALCIT SM 61-19, California Institute of Technology (1961)
   GALCIT SM 62-14, California Institute of Technology (1962)
   GALCIT SM 62-23, California Institute of Technology (1962)
   GALCIT SM 62-27, California Institute of Technology (1962)
   GALCIT SM 63- 5, California Institute of Technology (1963)

10. Bridgman, P.: Compression of 61 Organic Substances. Proc. of American Acad. of Sci., p. 9, Vol. 76, No. 1, February (1945).

11. Coleman, B. D.; Noll, W.: On the Thermostatics of Continuous Media. Arch. Rational Mech. Anal. Vol. 4, pp. 97 - 128 (1959).

12. Coleman, B. D.: Mechanical and Thermodynamical Admissibility of Stress-Strain Function. Arch Rational Mech. Anal. Vol. 9, pp. 172-186 (1962).

13. Spencer, J. M.: On Finite Elastic Deformations with a Perturbed Strain-Energy Function. Quat. J. Mech. and App. Math., Vol. 12, pp. 129-145 (1959).

14. Gent, A. N.; Lindley, P. B.: Internal Rupture of Bonded Rubber Cylinders in Tension. Proc. Roy. Soc., A, Vol. 249, pp. 195-205 (1959).

15. Mooney, M.: Theory of Large Elastic Deformation. J. App. Phys. Vol. 11, No. 9, pp. 582 - 592, September (1940).

16. Carmichael, A. J.; Holdaway, H. W.: Phenomenological Elastomechanical Behavior of Rubber over Wide Ranges of Strain. J. App. Phys., Vol. 32, No. 2, February (1961).

17. Rivlin, R. A.: Large Elastic Deformations of Isotropic Materials.

I,	Fundamental Concepts,	Phil. Trans. Roy. Soc. (A) Vol. 240, pp. 459-490, (1948).
II,	Some Uniqueness Theorem for Pure Homogeneous Deformation	Phil. Trans. Roy. Soc. (A) Vol. 240, pp. 491-508 (1948).
III,	Some Simple Problems in Cylindrical Polar Coordinates	Phil. Trans. Roy. Soc. (A) Vol. 240, pp. 509-525, (1948).
IV,	Further Developments of the General Theory	Phil. Trans. Roy. Soc. (A) Vol. 241, pp. 379-397, (1949).
V,	The Problem of Flexure	Proc. Roy. Soc. London (A), Vol. 195, pp. 463-475, (1949).
VI,	Further Results on the Theory of Torsion, Shear and Flexure	Phil. Trans. Roy. Soc. (A) Vol. 242, pp. 173-195, (1950).
VII,	Experiments on Deformation of Rubber	Phil. Trans. Roy. Soc. (A) Vol. 243, pp. 251-288, (1951).

18. Reiner, M.: Elasticity Beyond the Elastic Limit. Am. J. Math., Vol. 70, pp. 433-446 (1948).

19. Truesdell, C.: Mechanical Foundation of Elasticity and Fluid Dynamics. J. Ratl. Mech. and Anal., Vol. 1, pp. 125-300 (1952).

20. Cifferri, A.; Flory, P. J.: Stress-Strain Isotherm for Polymer Networks. J. App. Phys., Vol. 30, No. 10, pp. 1498-1507, October (1959).

21. Murnaghan, F.: Finite Deformations of an Elastic Solid, Am. J. Math., Vol. 59, pp. 235-260, (1937).

22. Green, A. E.; Zerna, W.: Theoretical Elasticity. Oxford Univ. Press (1960).

23. Green, A. E.; Adkins, J. E.: Large Elastic Deformations. Oxford Univ. Press (1960).

24. Treloar, L. R. G.: The Physics of Rubber Elasticity. Second Edition, Oxford University Press (1958).

25. Murnaghan, F. D.: Finite Deformations of an Elastic Solid. John Wiley and Sons, Inc., New York (1951).

26. Nadai, A.: Theory of Strength. J. App. Mech., Vol. 1, pp. 111-129 (1933).

27. Haigh, B. P.: The Strain-Energy Function and the Elastic Limit. Engineering, Vol. 190, pp. 158-160 (1920).

28. Westergaard, H. M.: On the Resistance of Ductile Materials to Combined Stresses in Two or Three Directions Perpendicular to One Another. Jl. Franklin Inst., pp. 627-640 (1920).

29. Jaeger, J. C.: Elasticity, Fracture and Flow. John Wiley and Sons, Inc., New York (1956).

30. Westergaard, H. M.: Theory of Elasticity and Plasticity. John Wiley and Sons, Inc., New York (1952).

31. Gent, A. N.; Thomas, A. G.: Failure of Foamed Elastic Materials. J. App. Polymer Sci., Vol. II, pp. 354-357 (1959).

32. Rivlin, R. S.; Thomas, A. G.: Rupture of Rubber. I. Characteristic Energy for Tearing. J. Polym. Sci., Vol. 10, pp. 291-318 (1952).

33. Thomas, A. G.: Rupture of Rubber. II. The Strain Concentration at an Incision. J. Polym. Sci., Vol. 18, pp. 177-188 (1955).

34. Greensmith, H. W.; Thomas, A. G.: Rupture of Rubber. III. Determination of Tear Properties, J. Polym. Sci., Vol. 18, pp. 189-200 (1955).

35. Williams, M. L.: Stress Singularities Resulting from Various Boundary Conditions in Angular Corners of Plates in Extension. J. App. Mech., Vol. 19, pp. 526-528 (1952).

36. Sneddon, I. N.: The Distribution of Stress in the Neighbourhood of a Crack in an Elastic Solid. Proc. Roy. Soc. A., Vol. 187, pp. 229 - 260. (1946).

37. Murch, S. A.; Nagdhi, P. M.: On Infinite Elastic Perfectly Plastic Wedge. Proc. Third U. S. Nat. Cong. App. Mech., pp. 611-624, June (1958).

38. Stenberg, E.; Loiter, W. T.: The Wedge Under a Concentrated Couple. J. App. Mech., Vol. 25, pp. 575-581, (1958).

39. Smith, T. L.: Elastomeric-Binder and Mechanical Property Requirements for Solid Propellants. Memo. No. 20-178, Jet Propulsion Laboratory, January (1959).

40. Smith, T. L.: Volume Changes and Dewetting in Glass Bead-Polyvinyl Chloride Elastomeric Composites Under Large Deformations. Trans. Soc. Rheo., Vol. 3, pp. 113-136 (1959).

41. Gardner, M.: Mathematical Games (Reflections on the Packing of Spheres). Scientific American, Vol. 202, pp. 174-180, May (1960).

42. Horvay, G.: The Plane-Stress Problem of Perforated Plates. J. App. Mech., Vol. 19, pp. 355-360 (1952).

43. Horvay, G.: Thermal Stresses in Perforated Plates. Proc. 1st. U. S. Natl. Cong. App. Mech., pp. 247-257, June (1951).

44. Gent, A. N.; Thomas, A. G.: The Deformation of Foamed Elastic Materials. J. App. Poly. Sci., Vol. 1, pp. 107-113 (1959).

45. Talalay, J. A.: Load Carrying Capacity of Latex Foam Rubber, Indus. and Eng. Chem., Vol. 46, No. 7, pp. 1530-1538, July (1954).

46. Hilbert, D.; Cohn-Vossen, S.: Geometry and the Imagination. Chelsea Pub. Co., New York (1952).

47. Van Vlack; Lawrence, H.: Elements of Materials Science, Addison-Wesley Pub. Co. Reading, Mass. (1959).

48. Hashin (Haifa), Z.: The Moduli of an Elastic Solid Containing Spherical Particles of Another Elastic Material. Non-Homogeneity in Elasticity and Plasticity (International Union of Theoretical and Applied Mechanics). pp. 463-478, W. Olszak, Pergamon Press, New York (1958).

49. Marvin, R. S.; Aldrichi, R.: J. App. Phys., Vol. 25, pp. 1213-1218 (1954).

50. Williams, M. L.; Blatz, P. J.; Schapery, R. A.: Fundamental Studies Relating to Systems Analysis of Solid Propellants, GALCIT SM 61-5, California Institute of Technology (1961).

51. Noll, W.: A Mathematical Theory of the Mechanical Behavior of Continuous Media. Arch. Rat. Mech. Anal., Vol. 2 pp. 197-226 (1958).

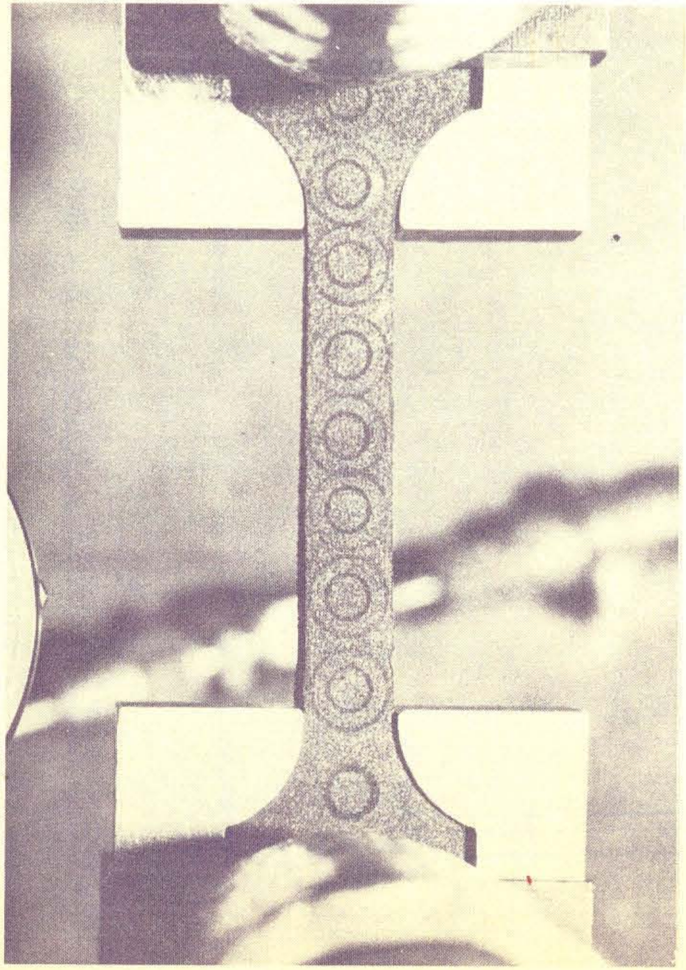

FIG. I. 1. Uniaxial Tension at $\lambda = 1$

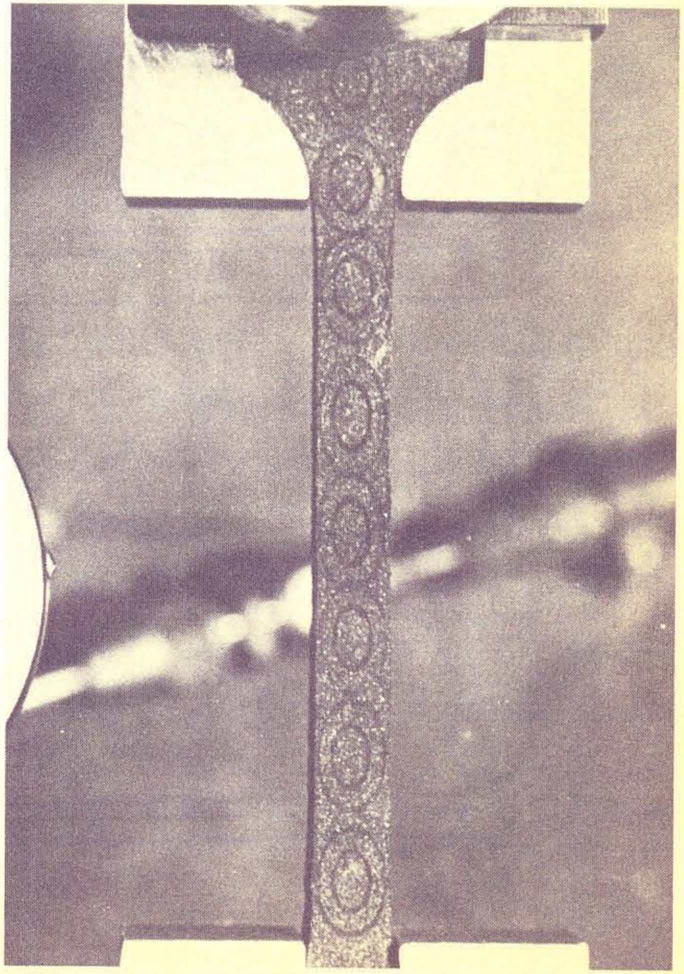

FIG. I. 2. Uniaxial Tension at $\lambda = 1.57$

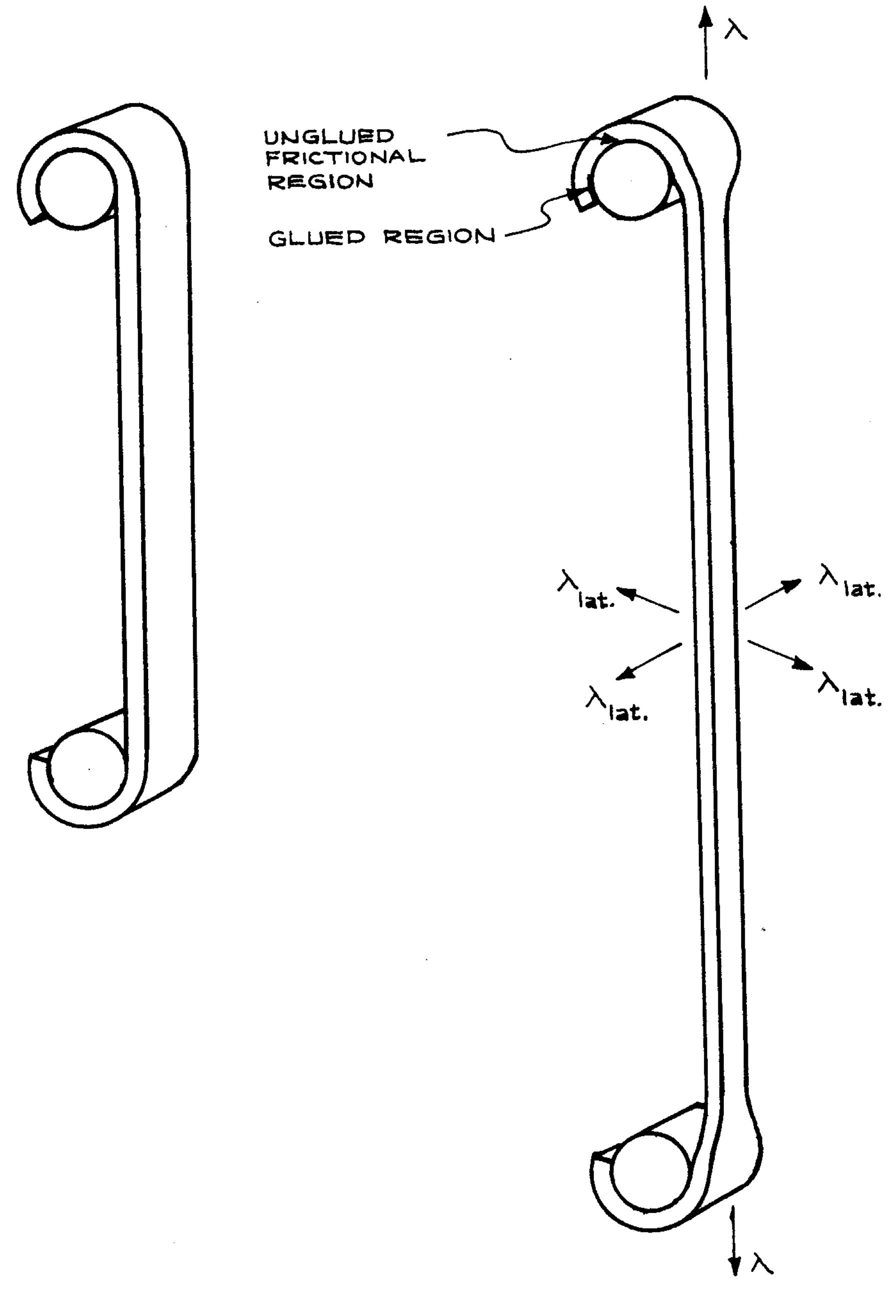

UNDEFORMED DEFORMED

FIG. I.3 UNIAXIAL TENSILE TEST SPECIMENS

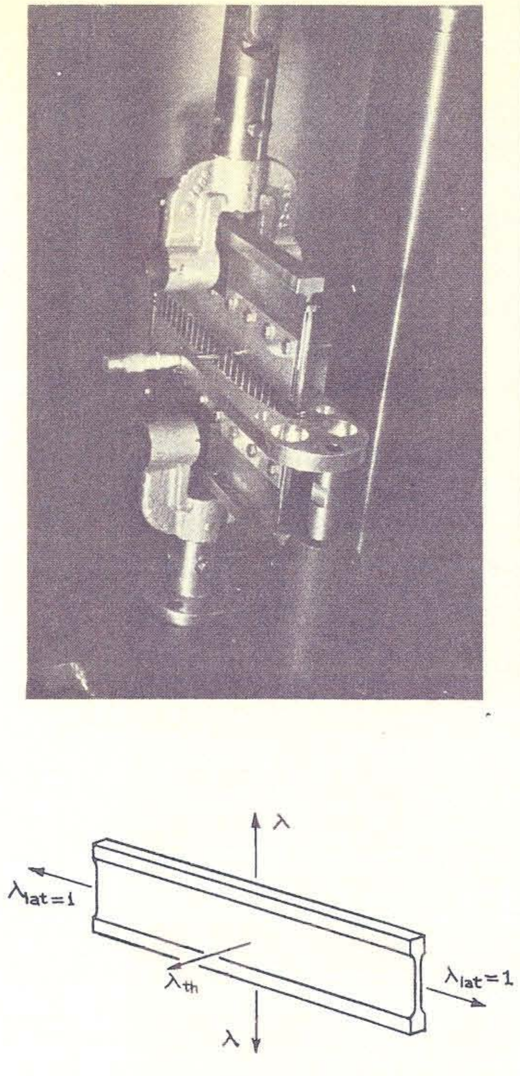

FIG. I. 4. Strip-Biaxial Tension

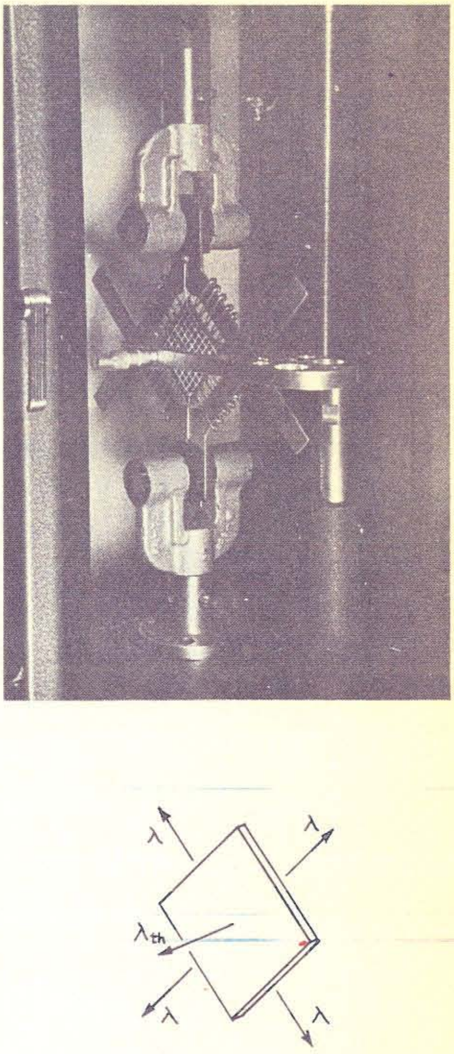

FIG. I. 5. Homogeneous-Biaxial Tension

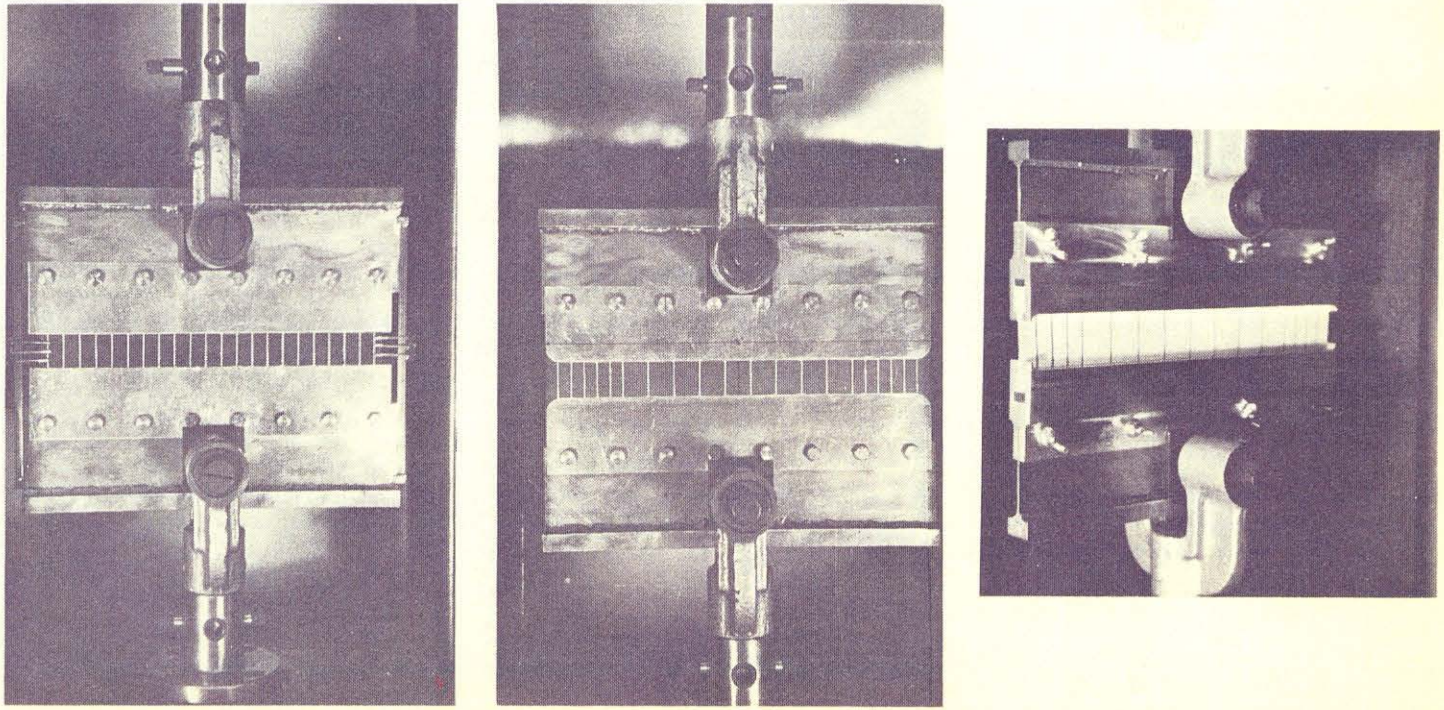

FIG. I.6. Three Types of Strip-Biaxial Tensions at $\lambda = 1$

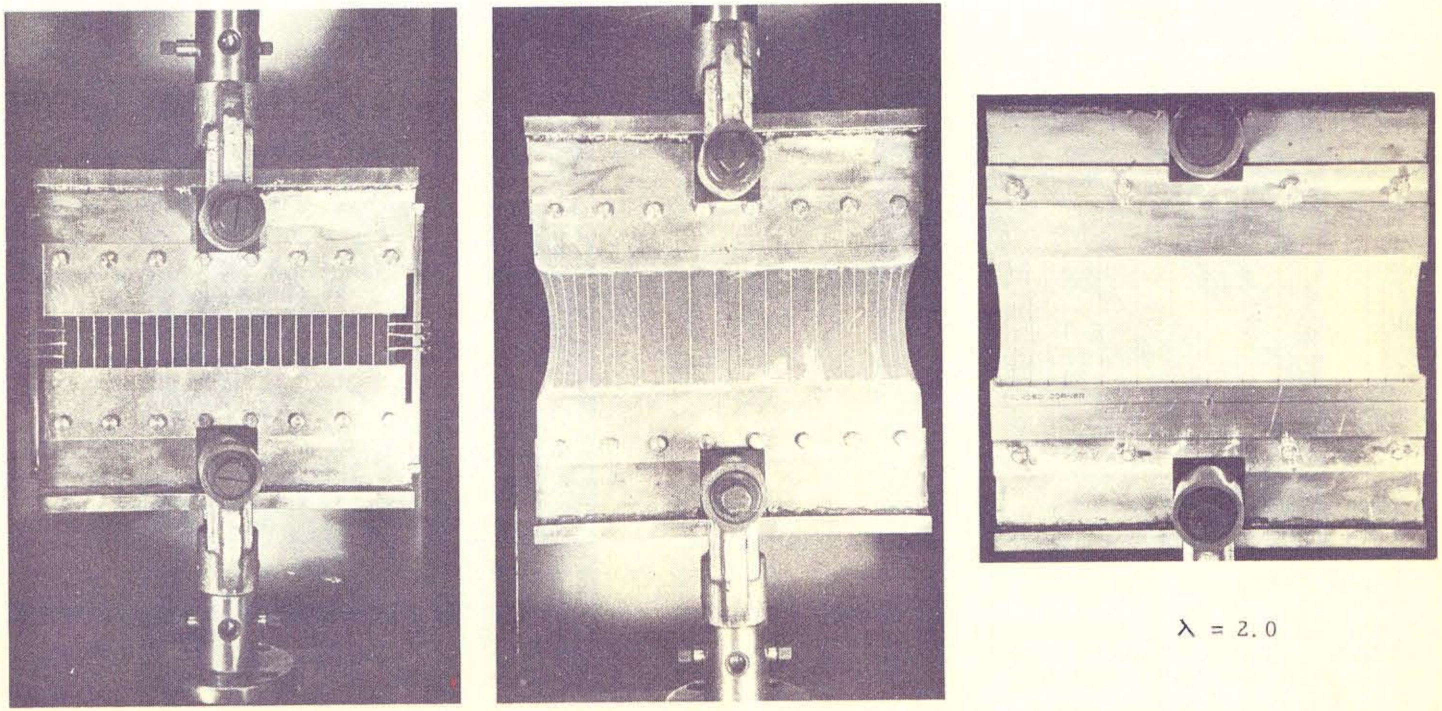

$\lambda = 1.6$

$\lambda = 3.5$

$\lambda = 2.0$

FIG. I.7. Three Types of Strip-Biaxial Tensions after Deformation.

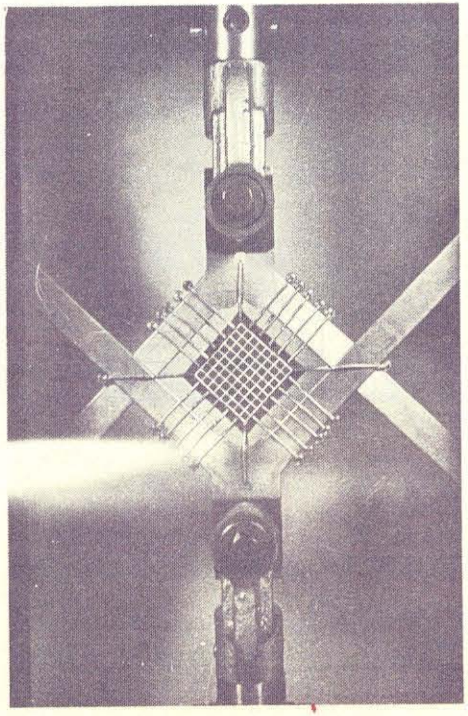

FIG. I.8. Homogeneous-Biaxial Tension at $\lambda = 1$

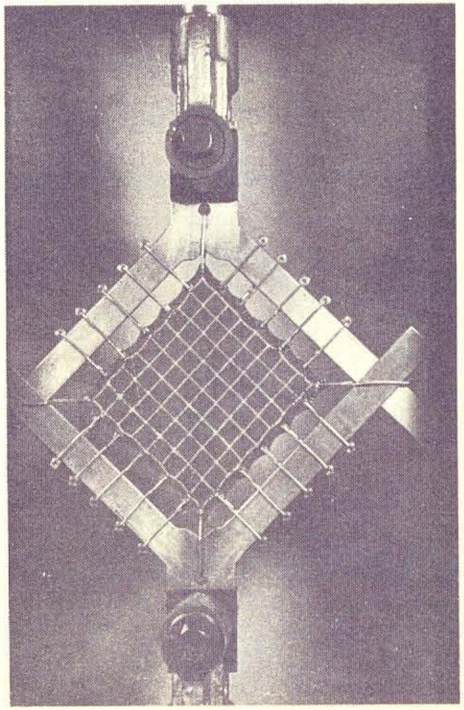

FIG. I.9. Homogeneous-Biaxial Tension at $\lambda = 2.3$

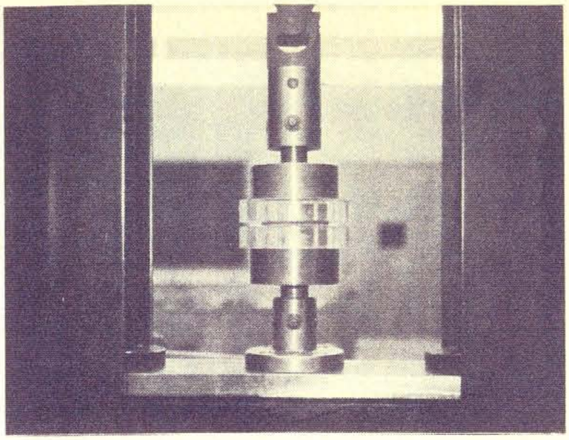

$\lambda = 1$

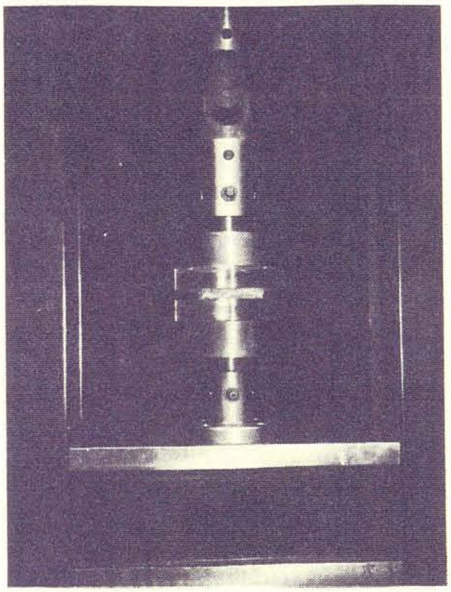

$\lambda = 2.0$

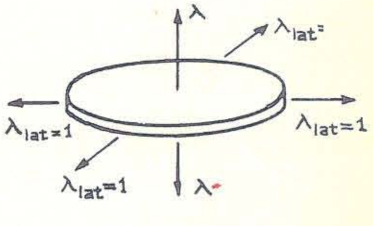

FIG. I. 10. Triaxial Tension

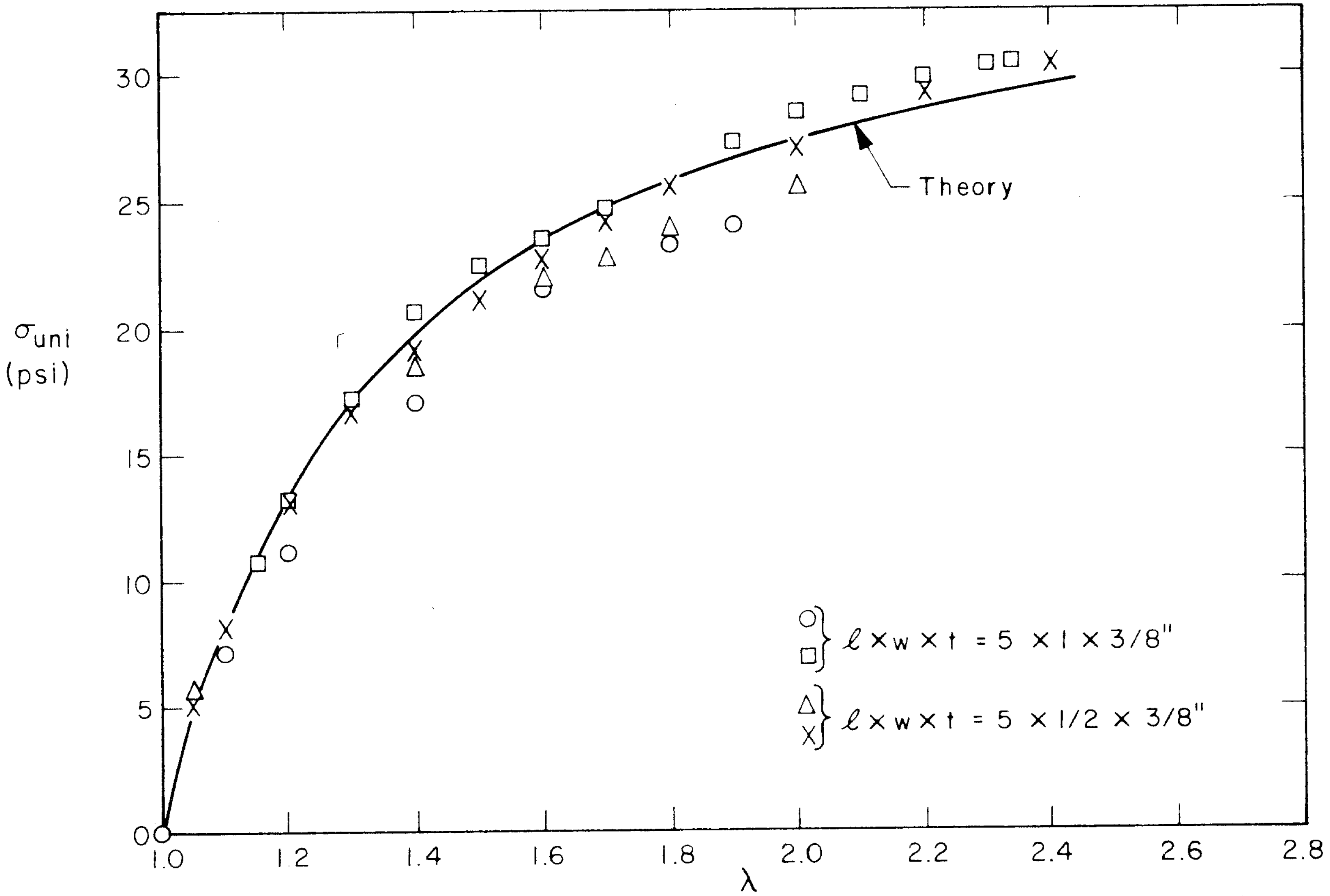

FIG. I. 11. Uniaxial Stress vs. Longitudinal Extension Ratio (Polyurethane Foam, 47 °/o Voids).

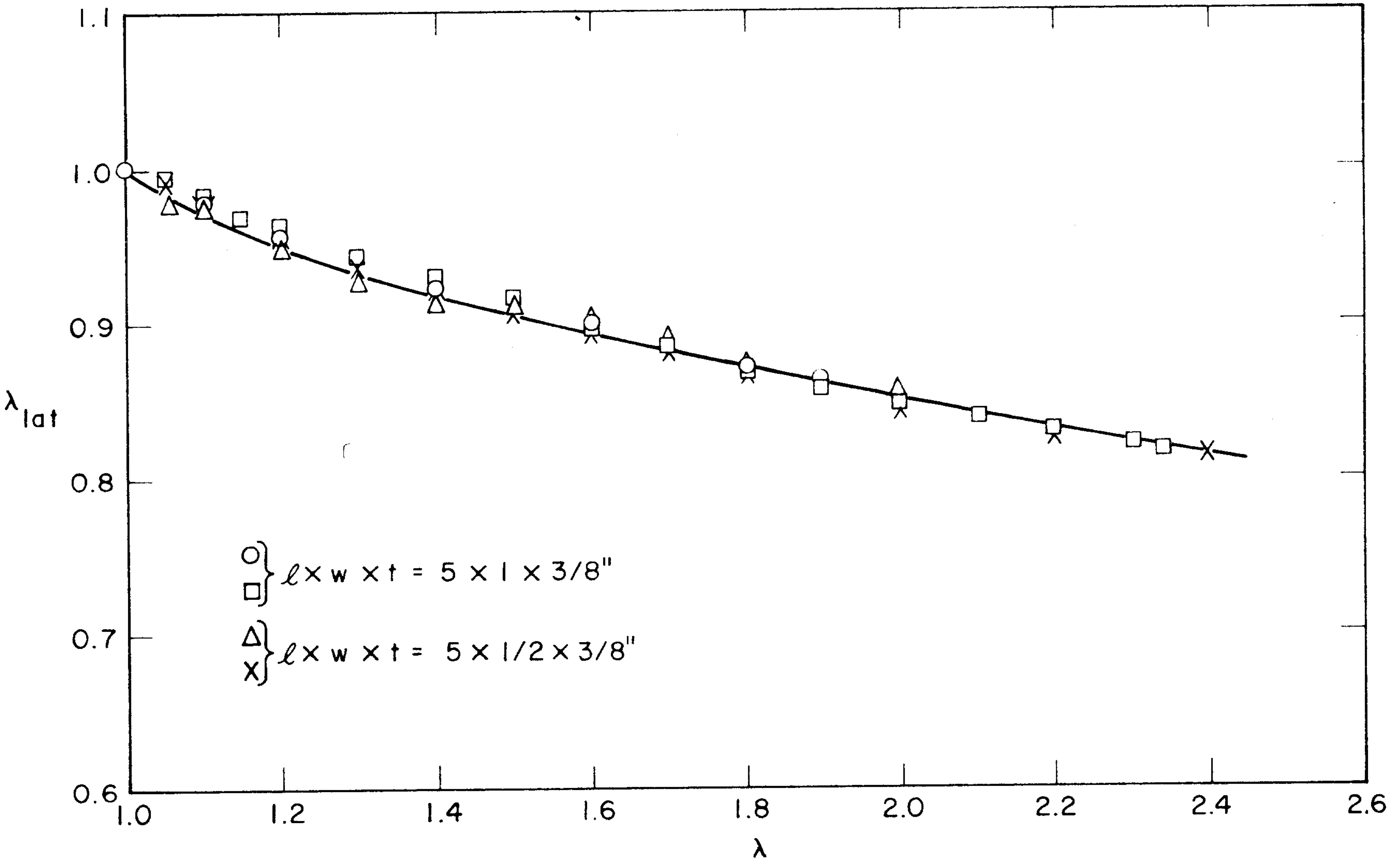

FIG. I. 12. Uniaxial Lateral Contraction Ratio vs. Longitudinal Extension Ratio (Polyurethane Foam, 47 °/o Voids).

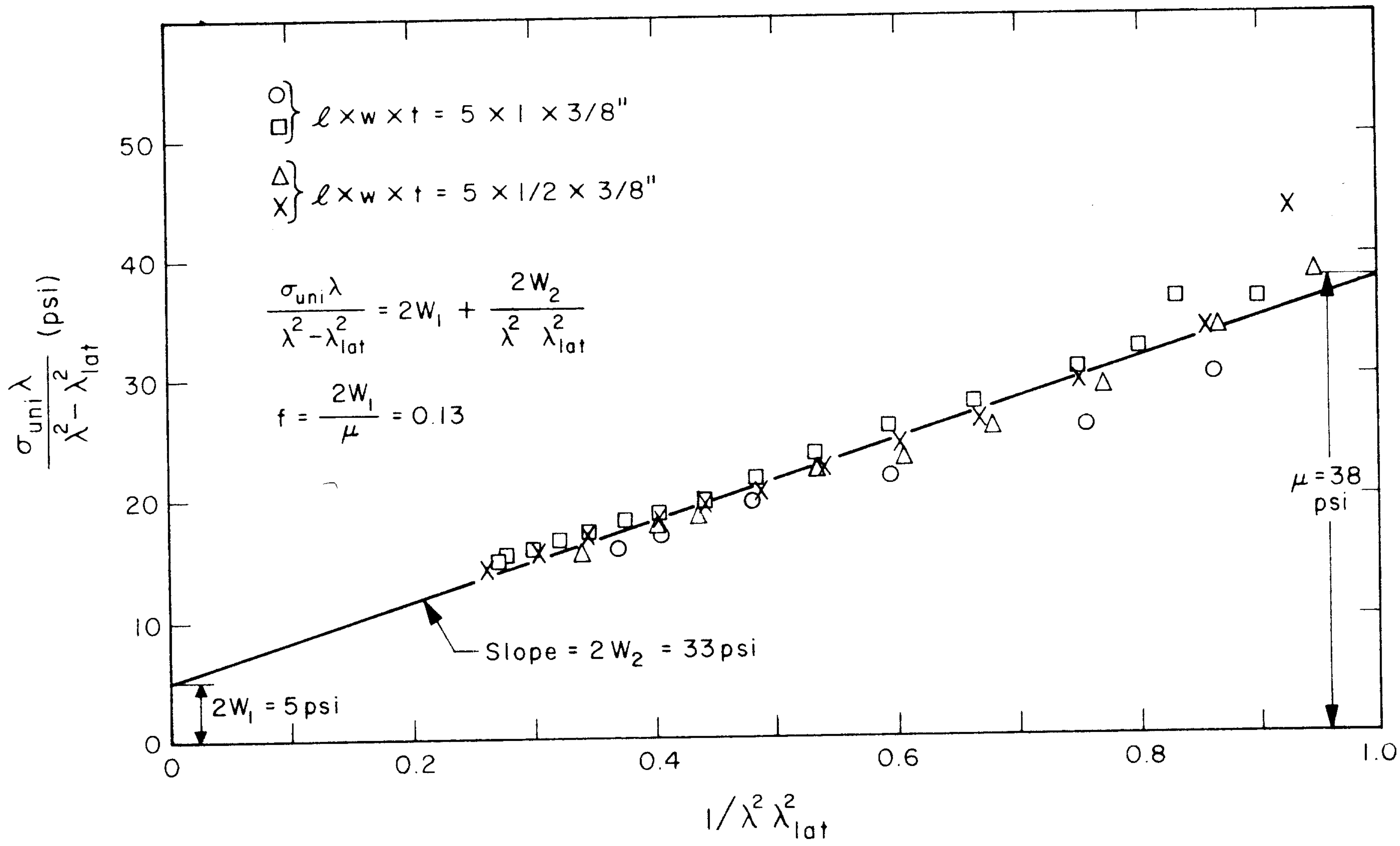

FIG. I. 13. Evaluation of W_1, W_2 From Rectified Uniaxial Data (Polyurethane Foam, 47 °/o Voids).

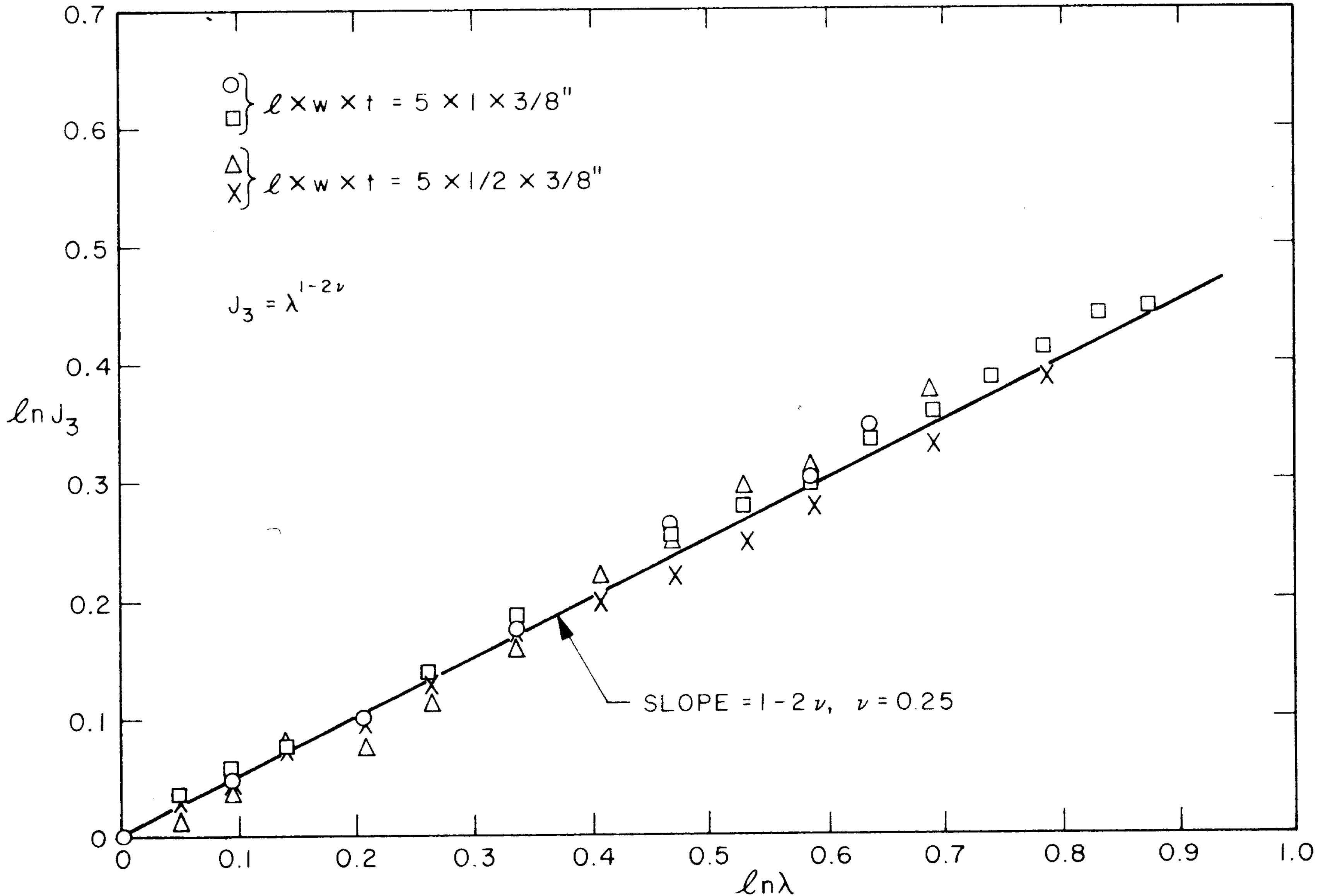

FIG. I. 14. Dependence of Uniaxial Dilatation on Longitudinal Extension Ratio (Polyurethane Foam, 47 °/o Voids).

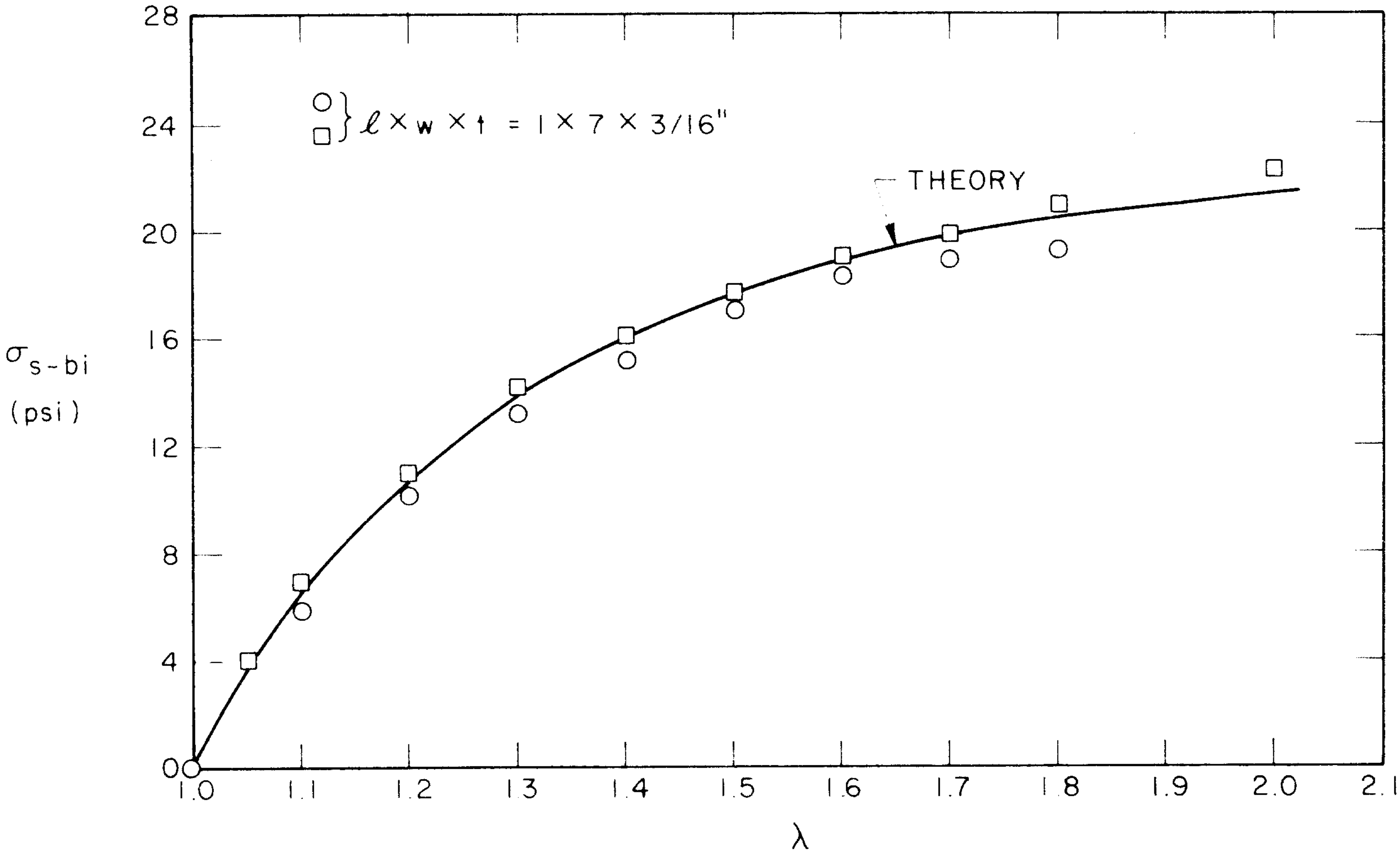

FIG. I. 15. **Strip-Biaxial Stress vs. Longitudinal Extension Ratio (Polyurethane Foam, 47 °/o Voids).**

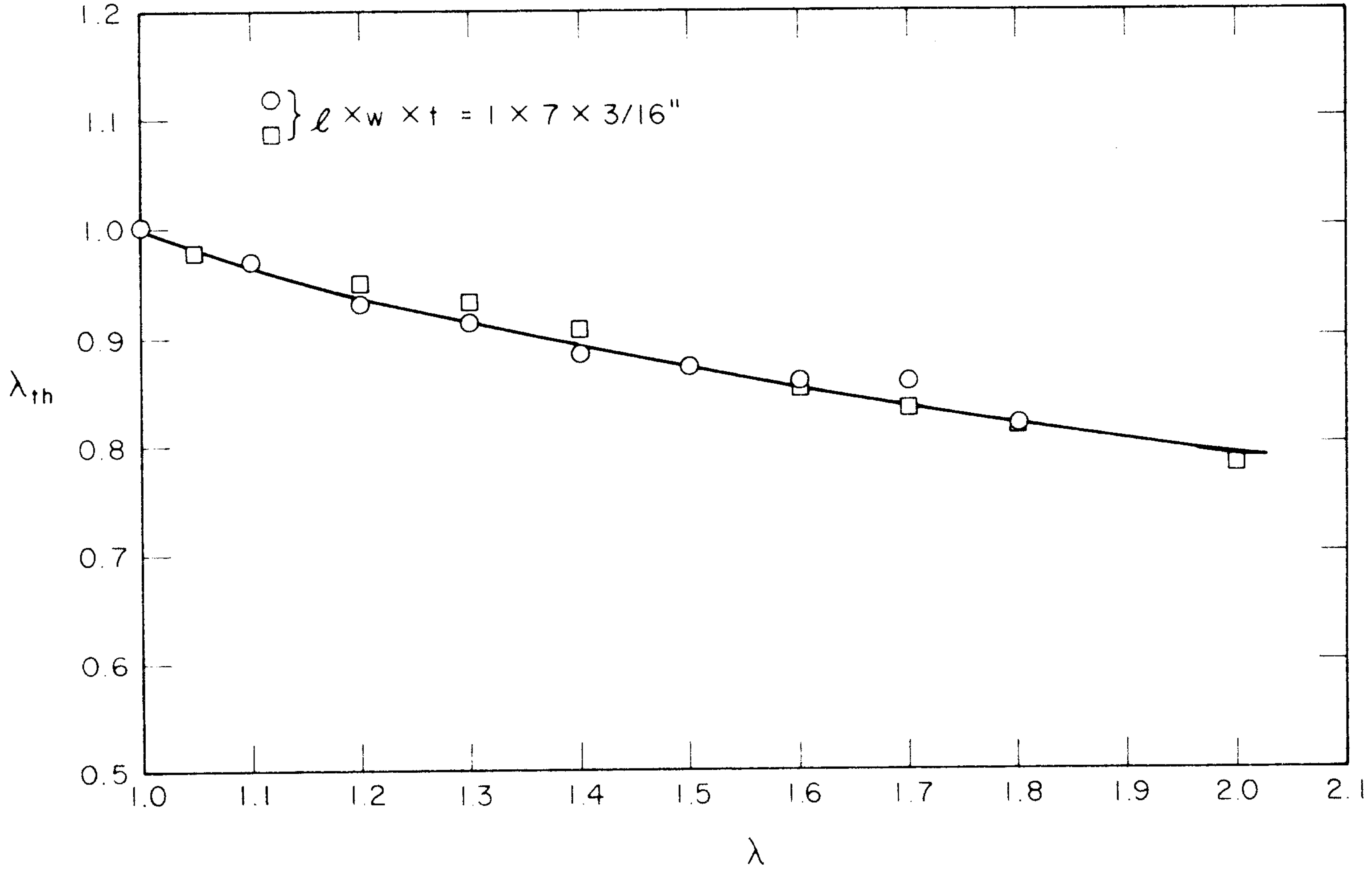

FIG.I.16. Strip-Biaxial Thickness Contraction Ratio vs. Longitudinal Extension Ratio (Polyurethane Foam, 47 °/o Voids).

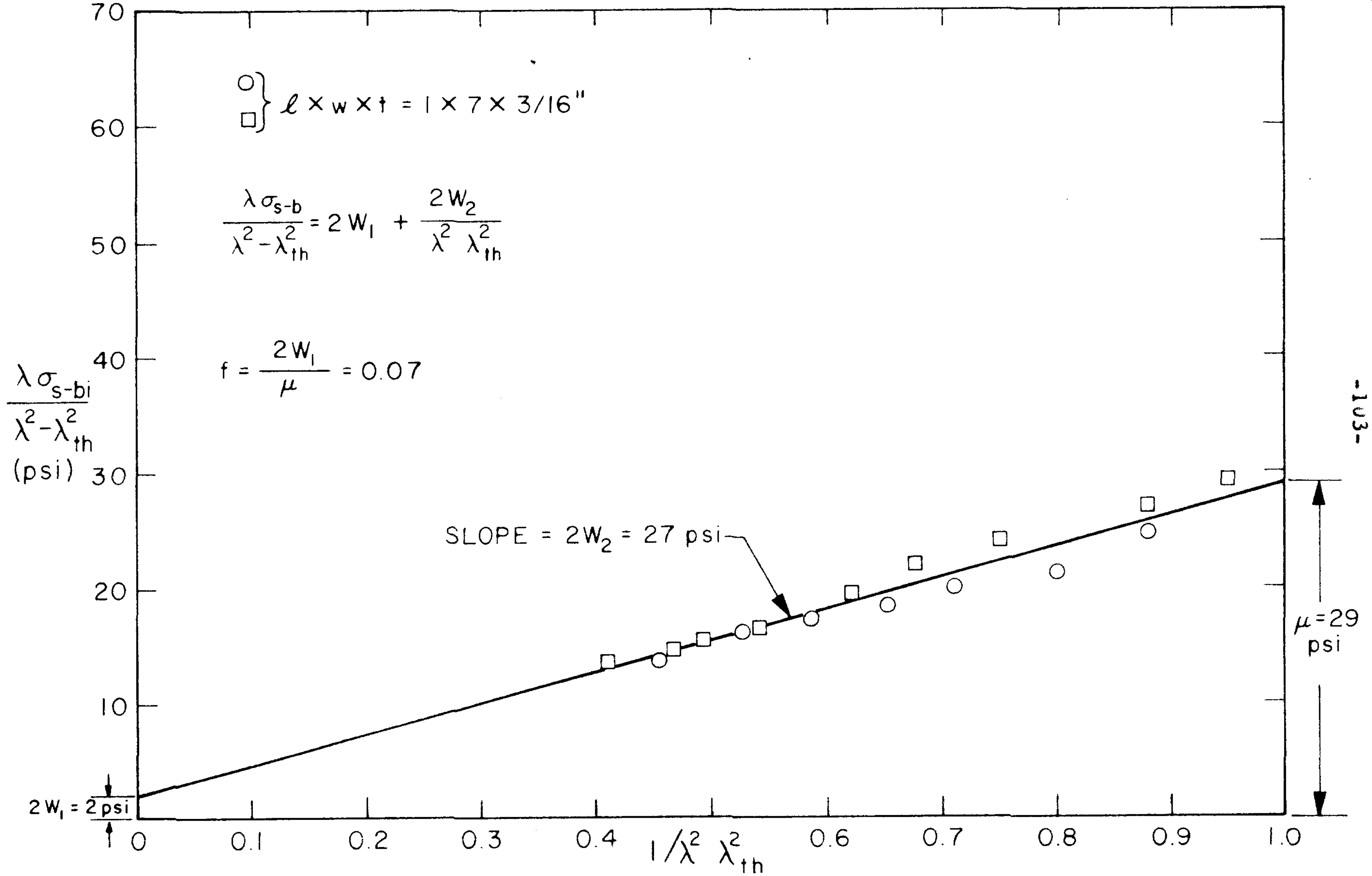

FIG. I. 17. Evaluation of W_1, W_2 From Rectified Strip-Biaxial Data (Polyurethane Foam, 47 °/o Voids).

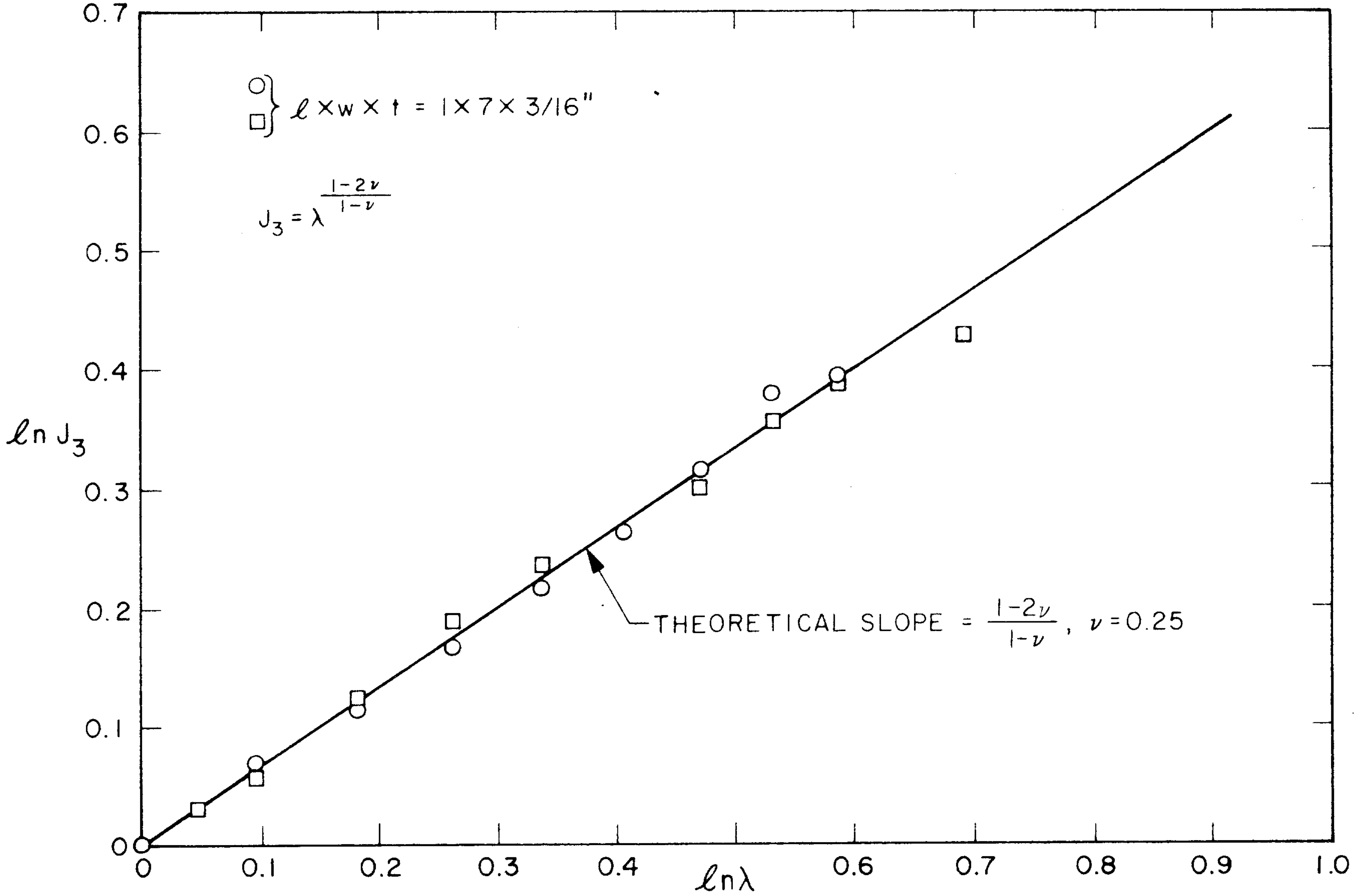

FIG. I. 18. Dependence of Strip-Biaxial Dilatation on Longitudinal Extension Ratio (Polyurethane Foam, 47 °/o Voids).

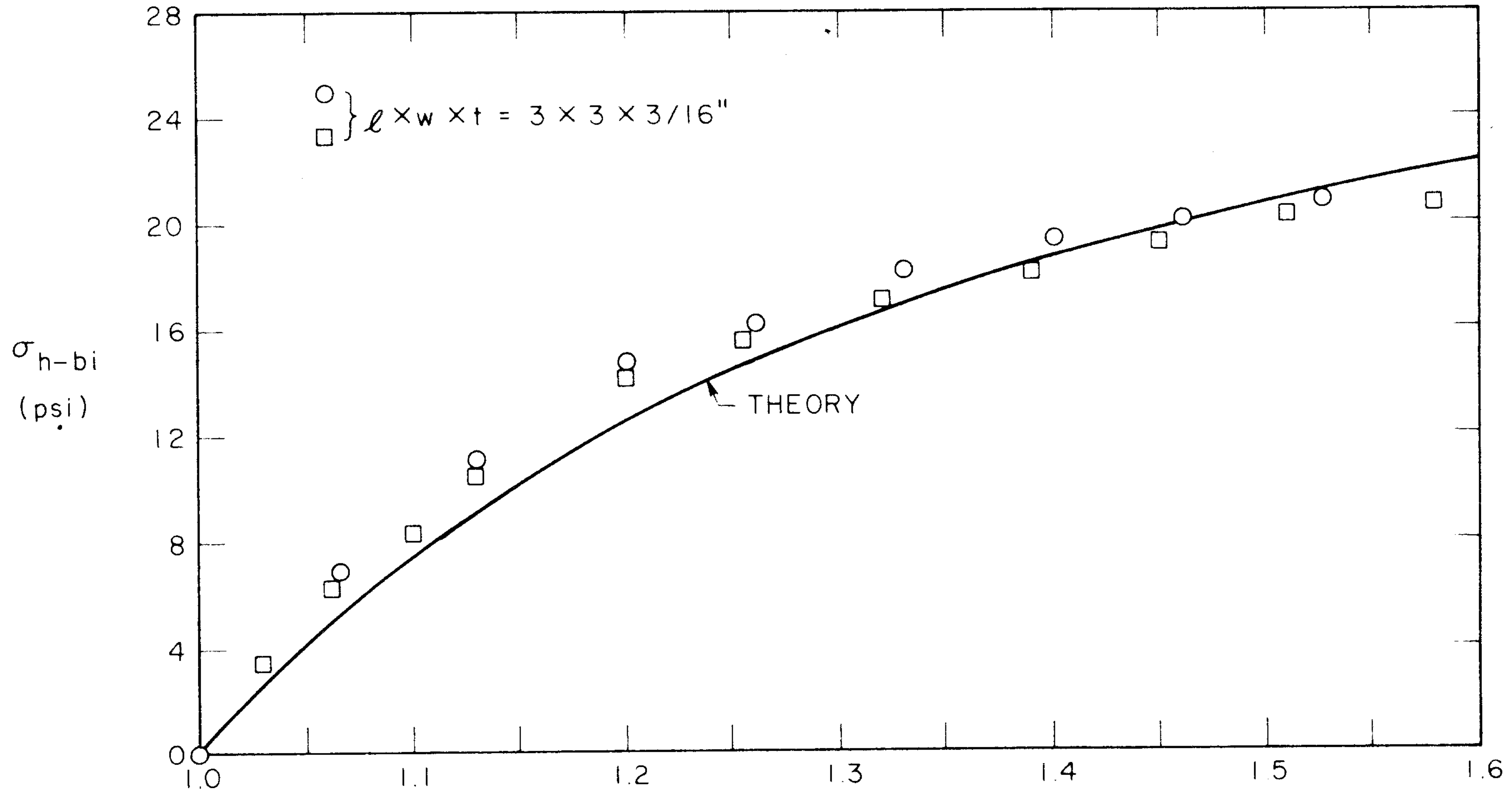

FIG. I. 19. Homogeneous-Biaxial Stress vs. Longitudinal Extension Ratio (Polyurethane Foam, 47 °/o Voids).

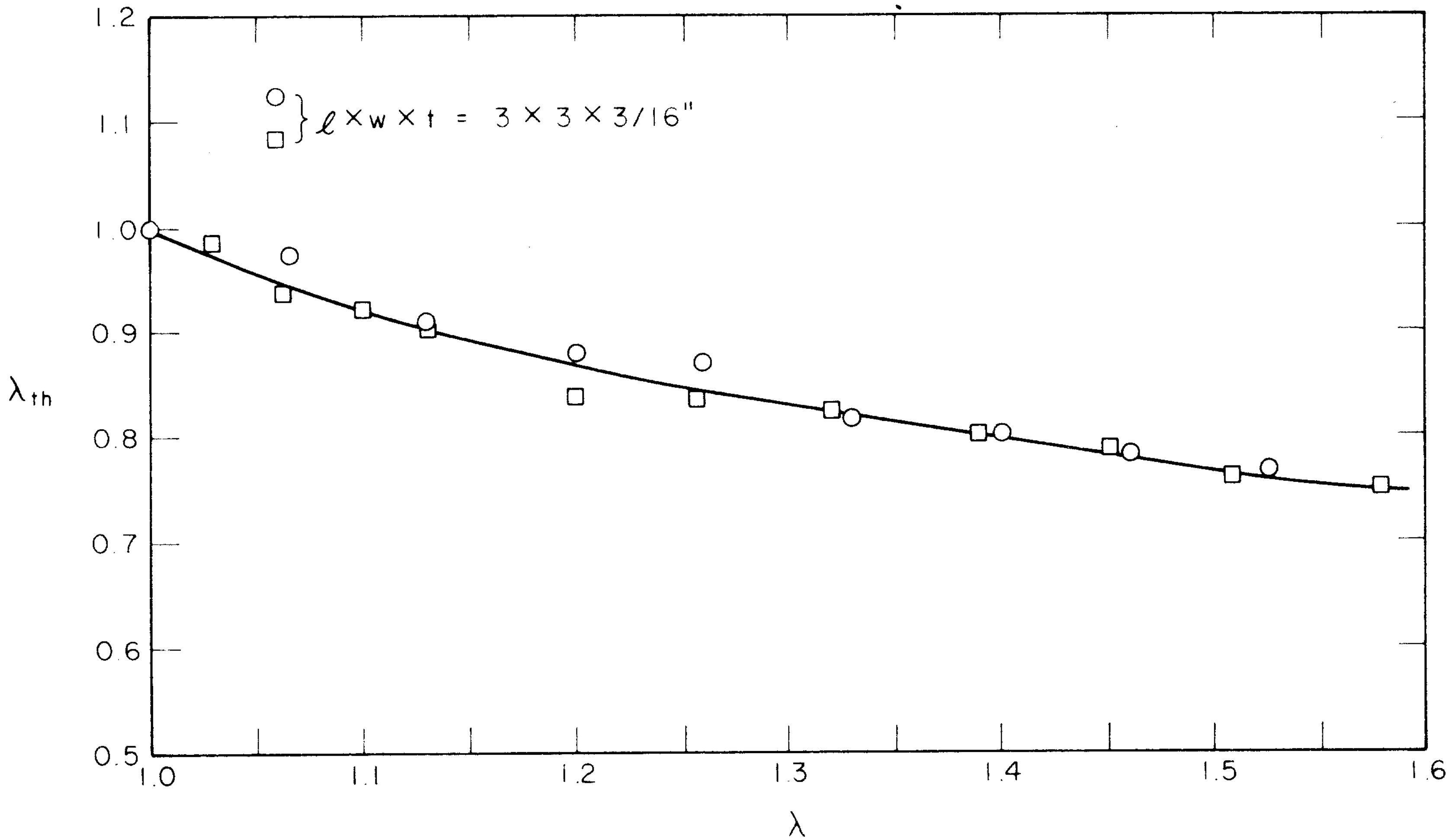

FIG. I. 20. Homogeneous-Biaxial Thickness Contraction Ratio vs. Longitudinal Extension Ratio (Polyurethane Foam, 47 ^{o}/o Voids).

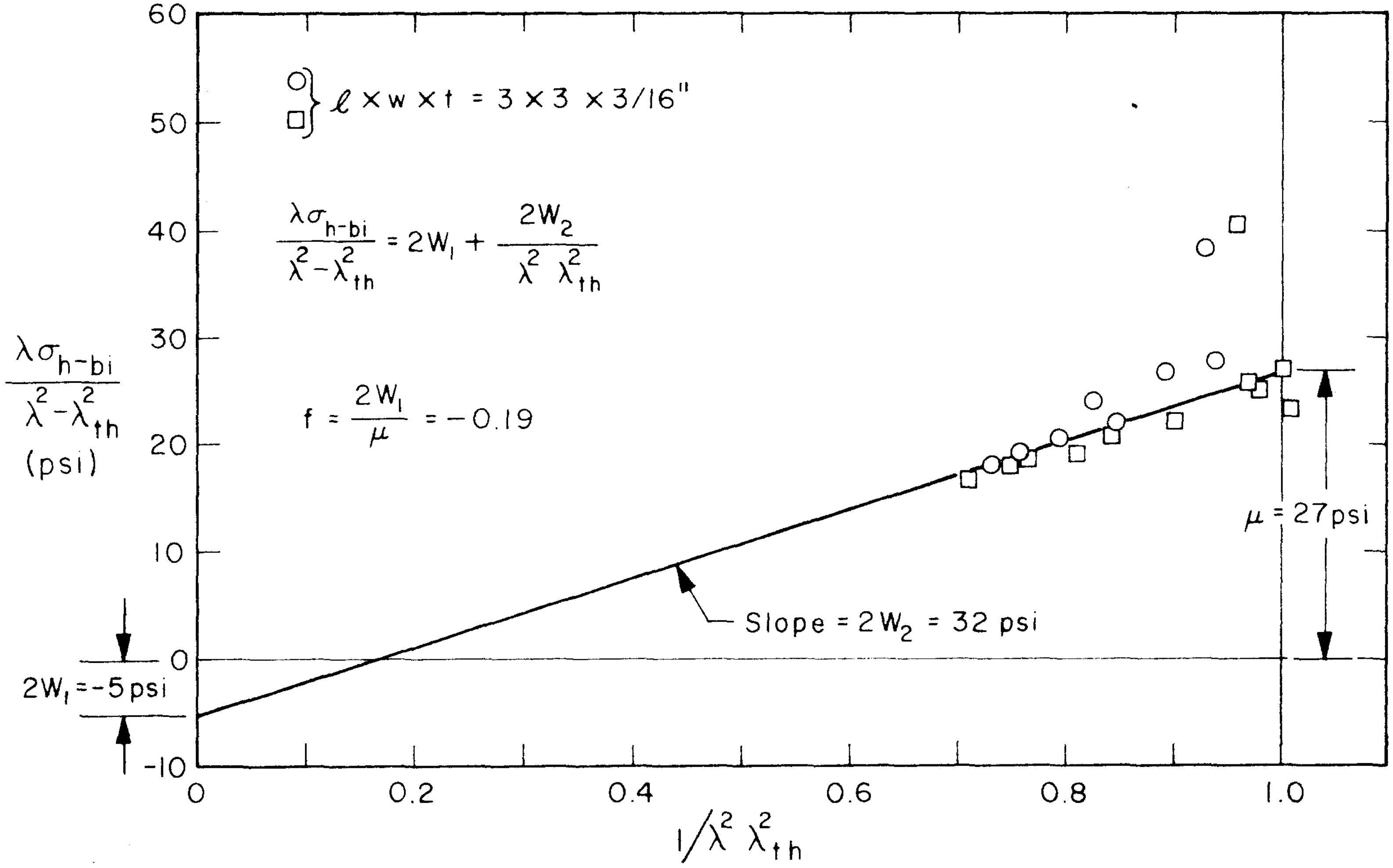

FIG.I.21. Evaluation of W_1, W_2 From Rectified Homogeneous-Biaxial Data (Polyurethane Foam, 47 °/o Voids).

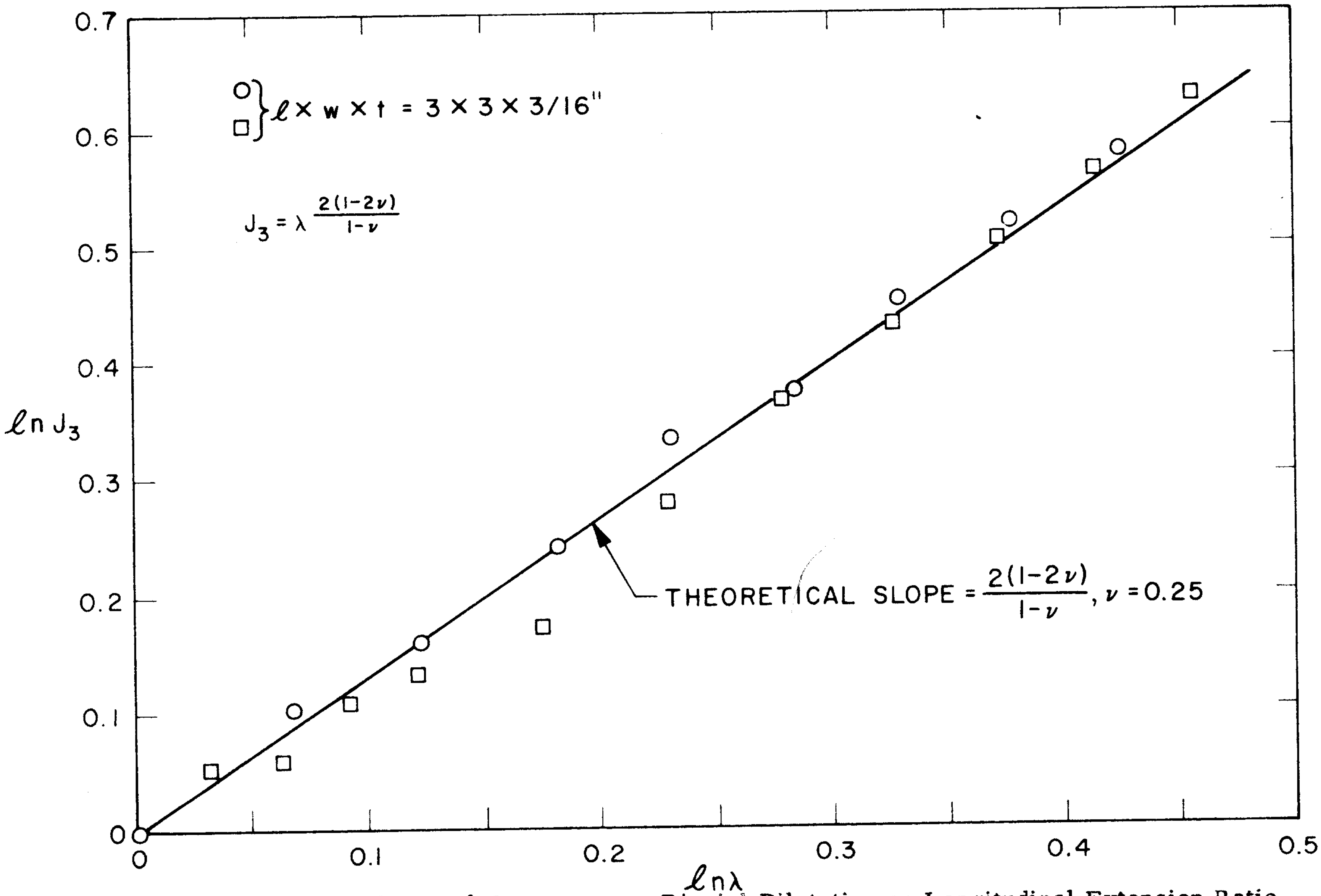

FIG. I. 22. Dependence of Homogeneous-Biaxial Dilatation on Longitudinal Extension Ratio (Polyurethane Foam, 47 °/o Voids).

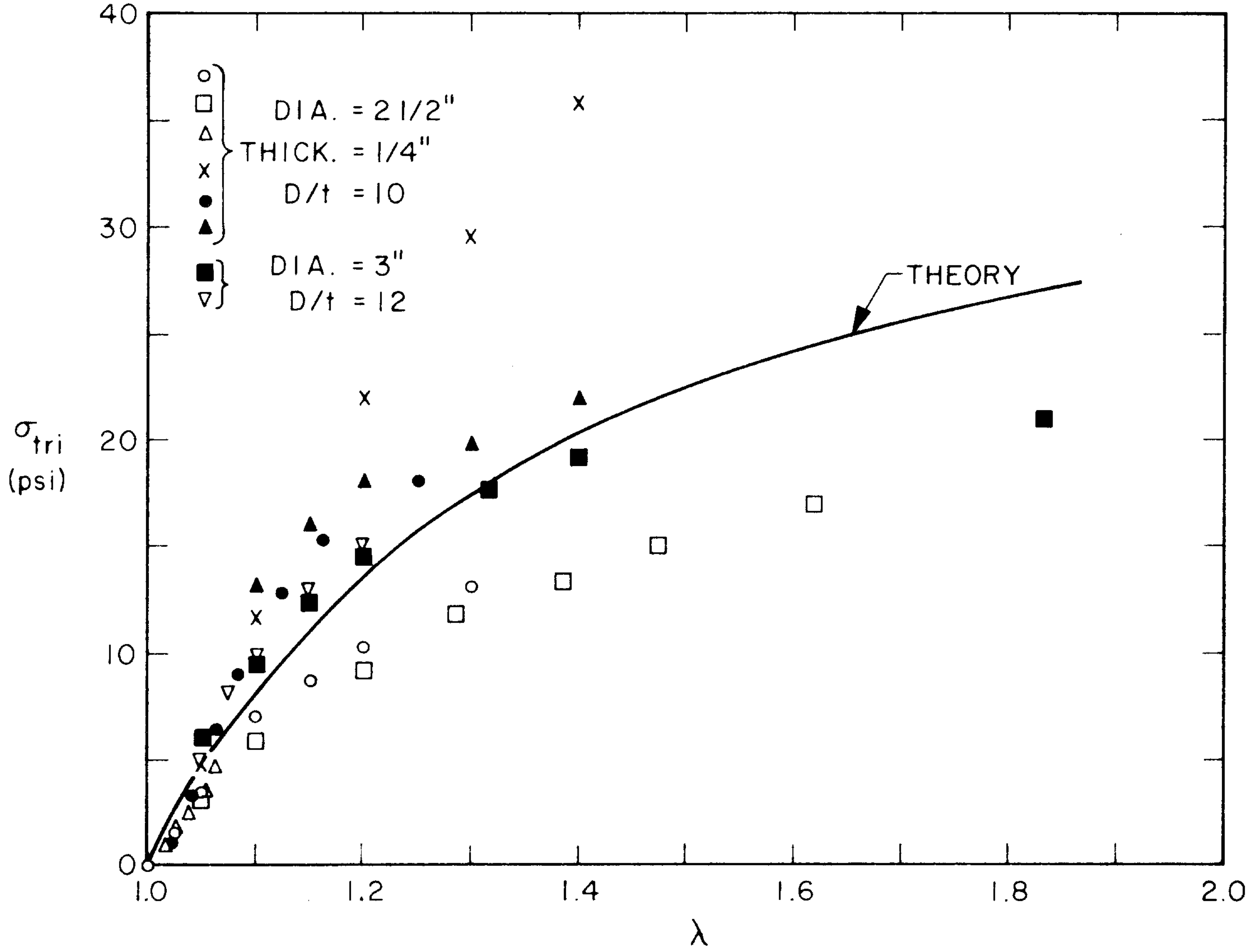

FIG. I. 23. Triaxial Stress vs. Thickness Extension Ratio (Polyurethane Foam, 47 °/o Voids).

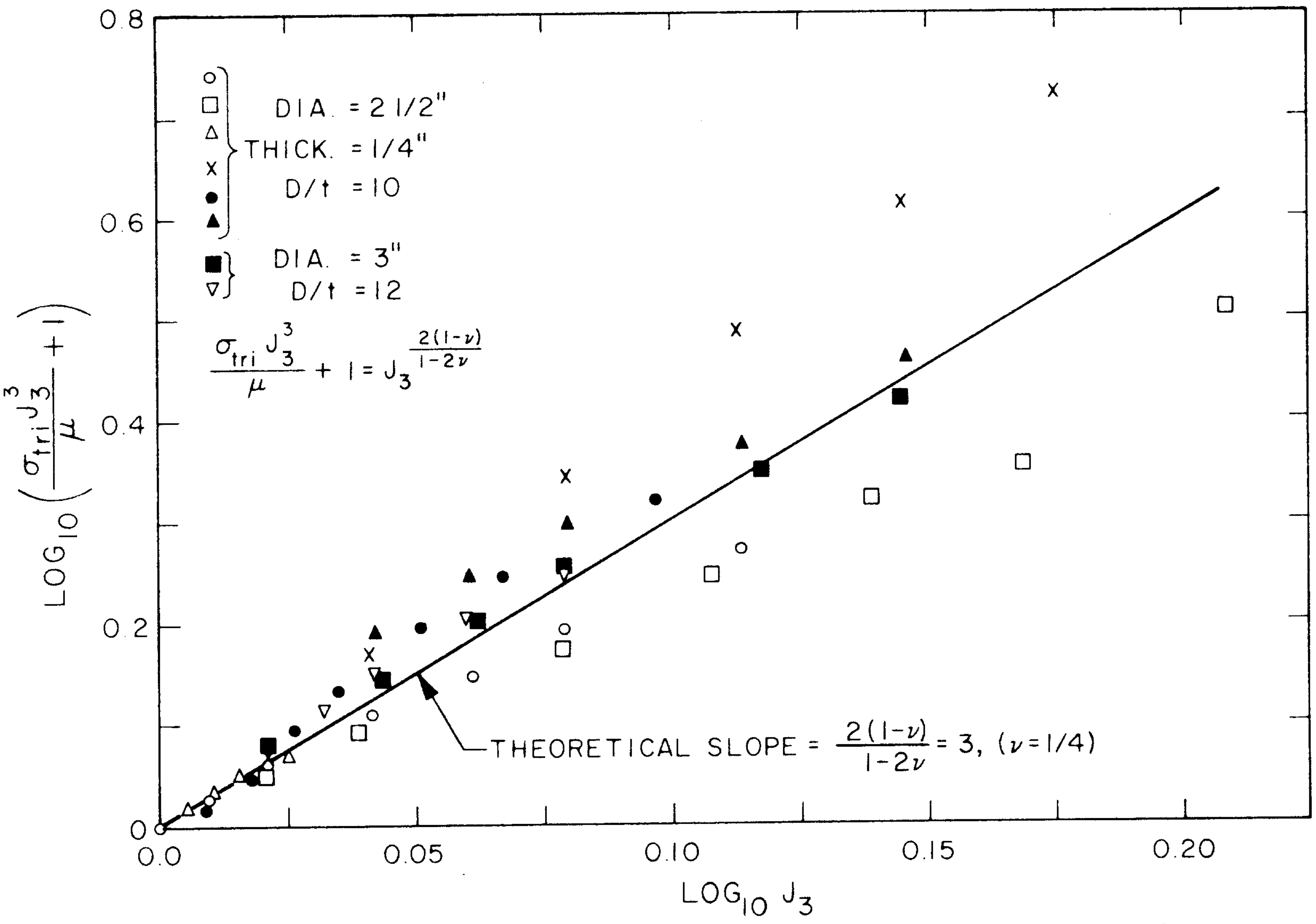

FIG. I. 24. Evaluation of ν From Triaxial Data (Polyurethane Foam, 47°/o Voids).

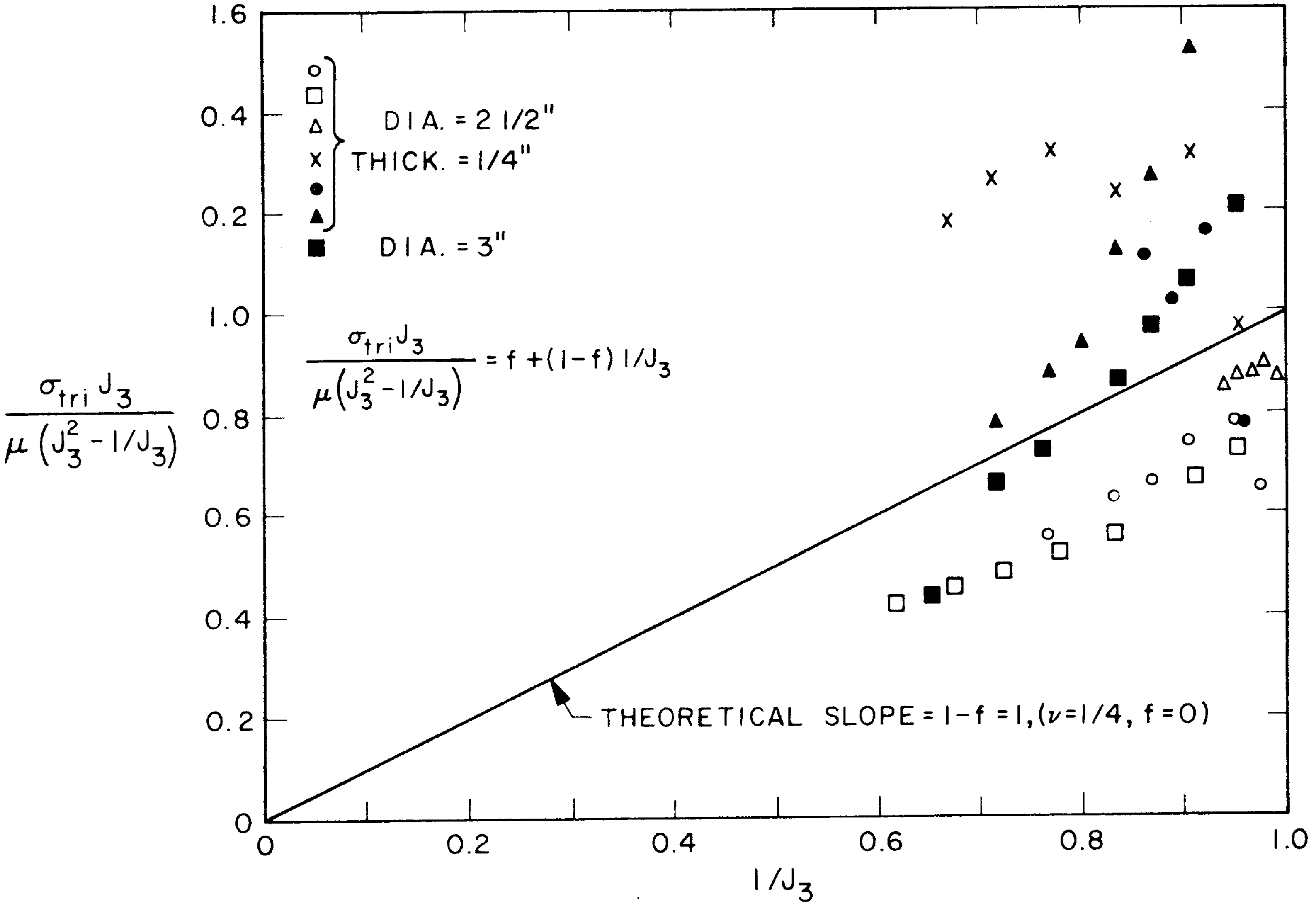

FIG. I. 25. Evaluation of f From Triaxial Data (Polyurethane Foam, 47 °/o Voids).

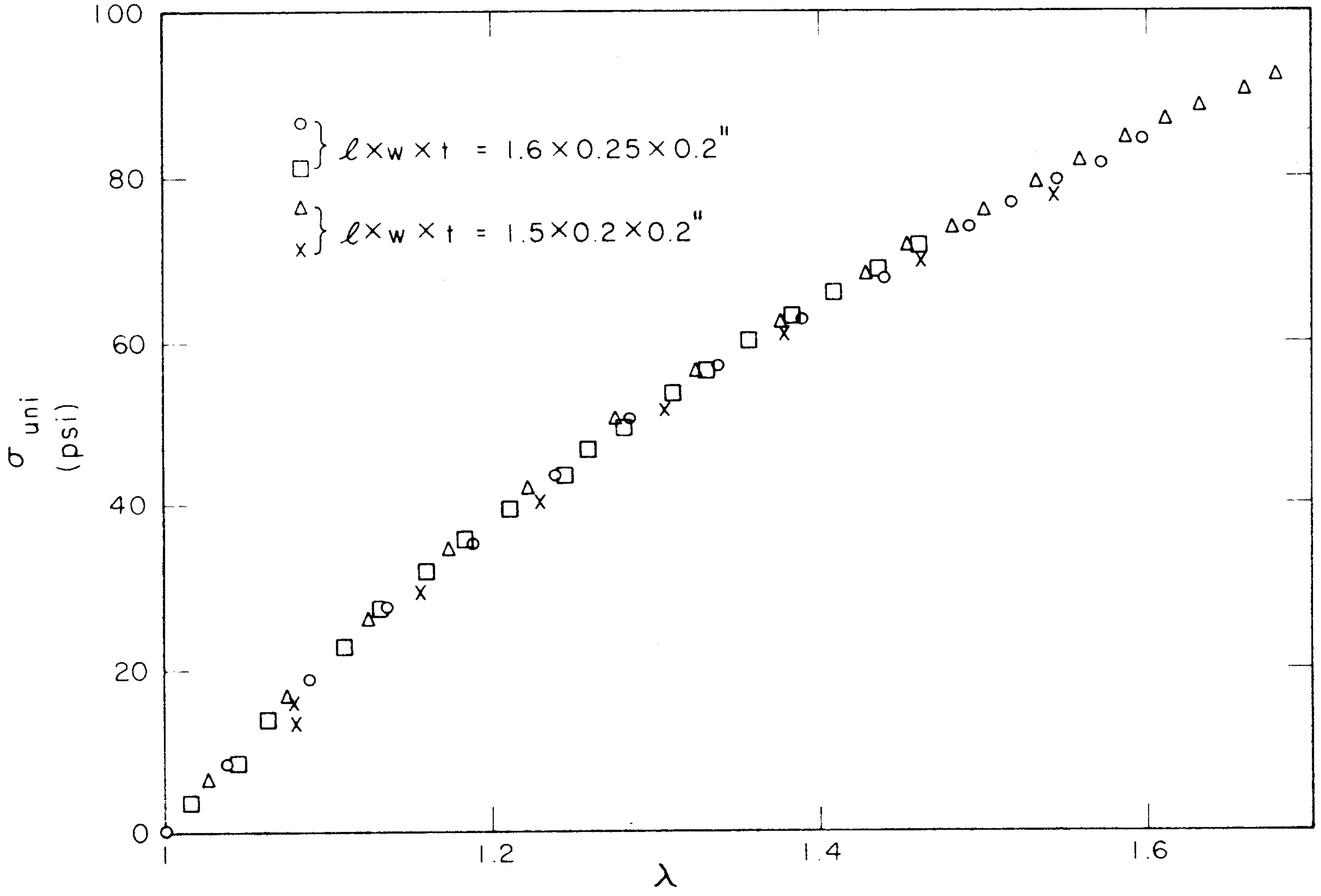

FIG.I.26. **Uniaxial Stress vs. Longitudinal Extension Ratio (Polyurethane Rubber).**

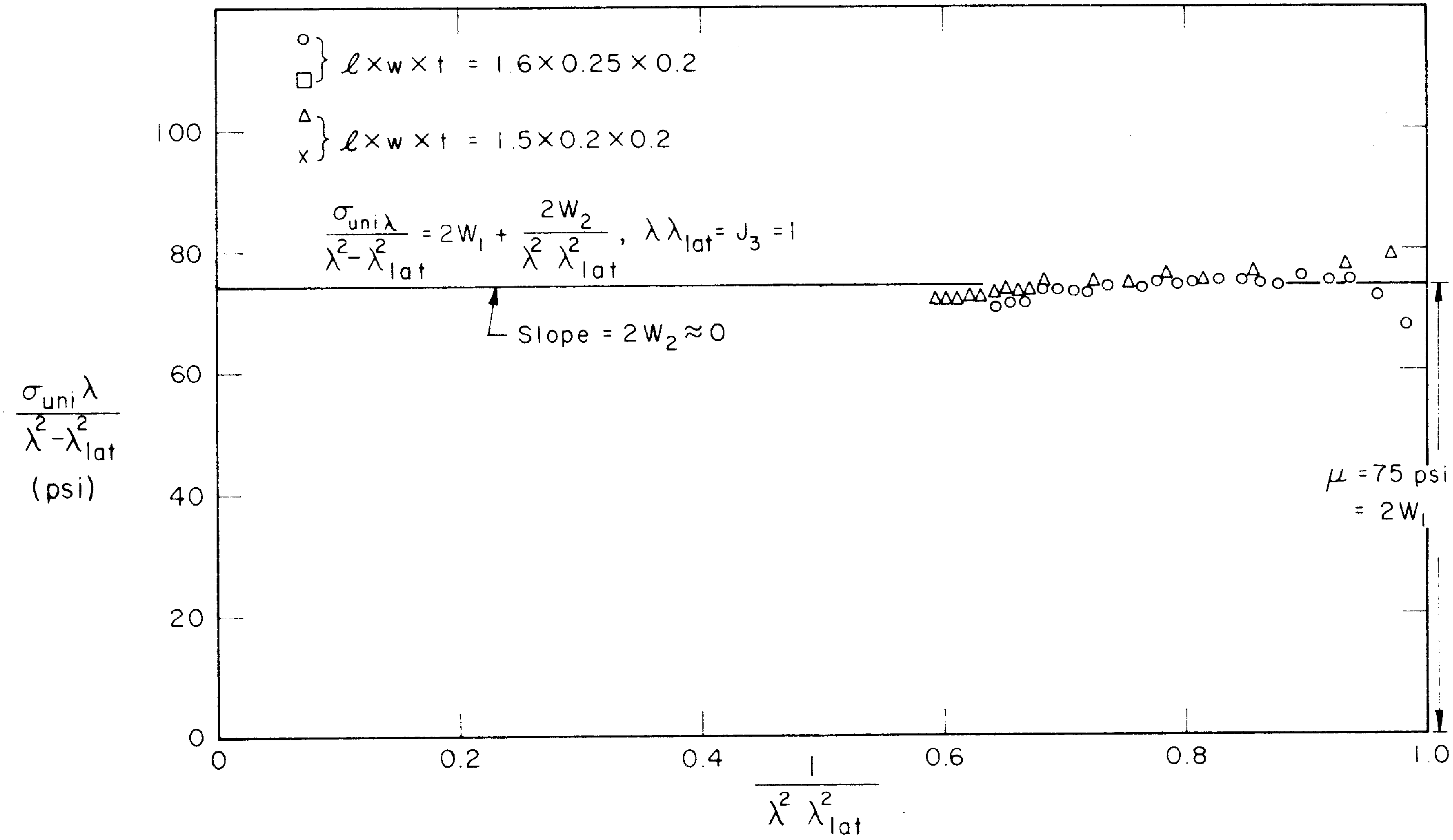

FIG. I. 27. Evaluation of W_1, W_2 From Rectified Uniaxial Data (Polyurethane Rubber)

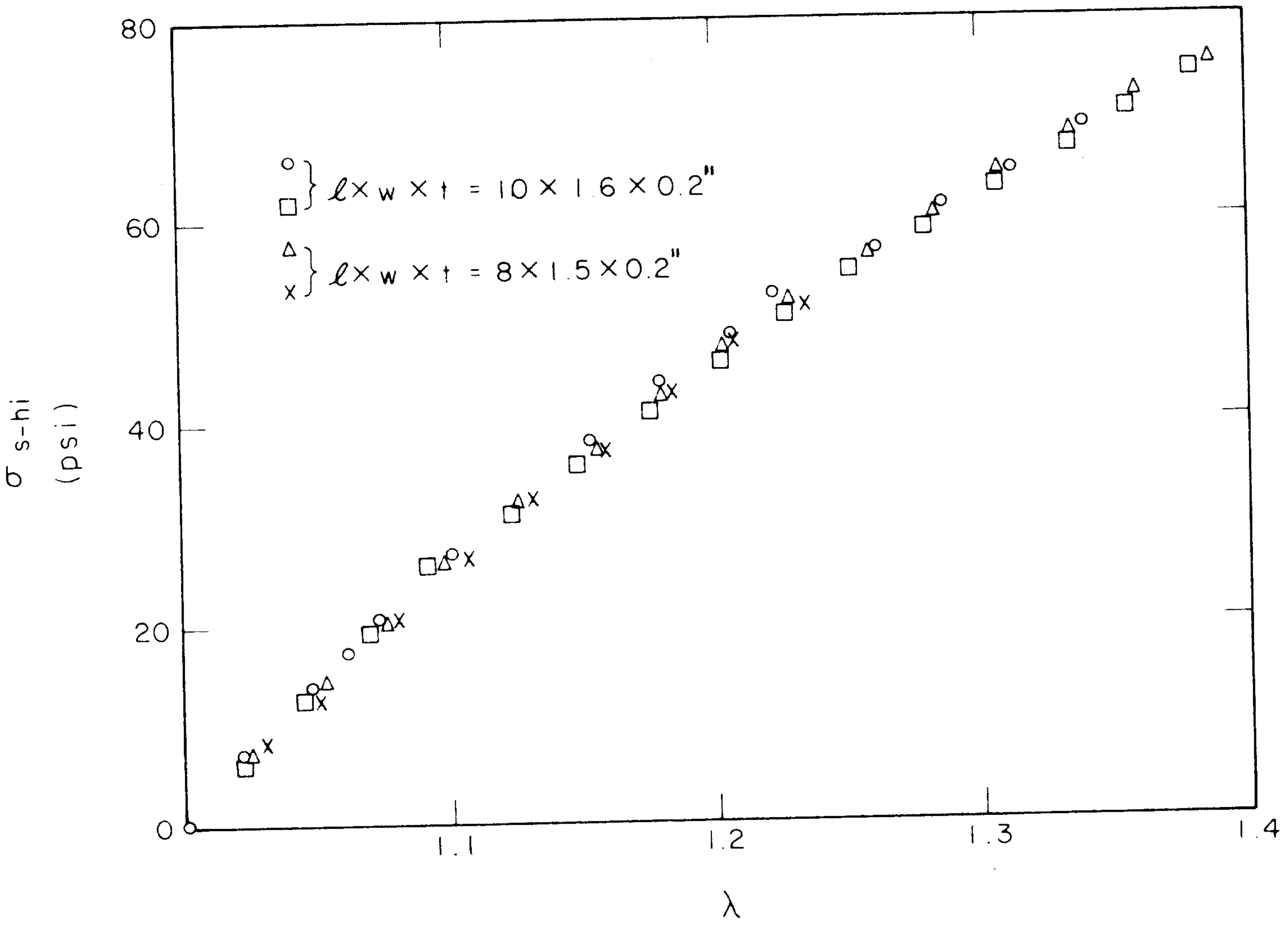

FIG. I. 28. **Strip-Biaxial Stress vs. Longitudinal Extension Ratio (Polyurethane Rubber).**

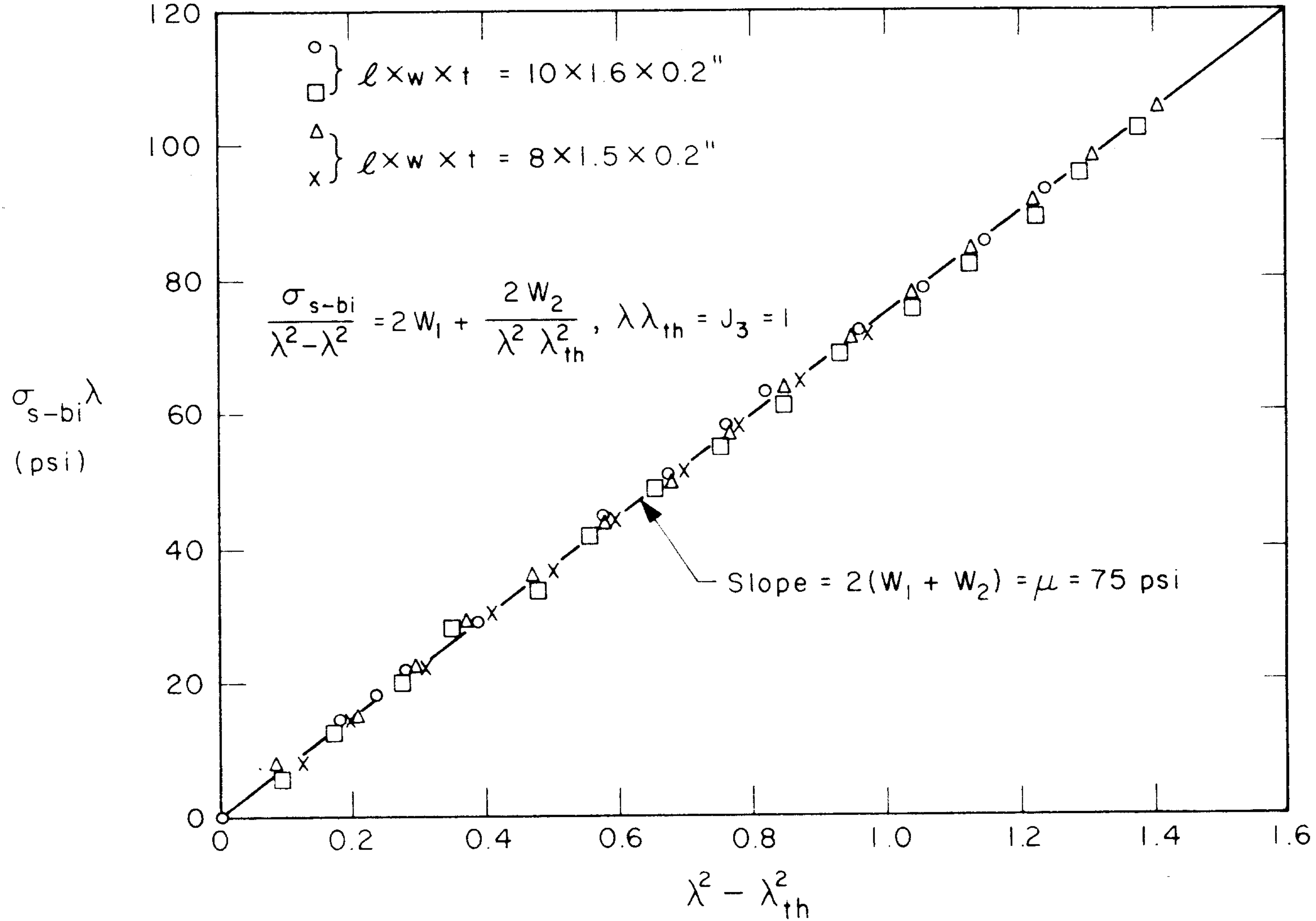

FIG. I. 29. Evaluation of $W_1 + W_2$ From Rectified Strip-Biaxial Data (Polyurethane Rubber)

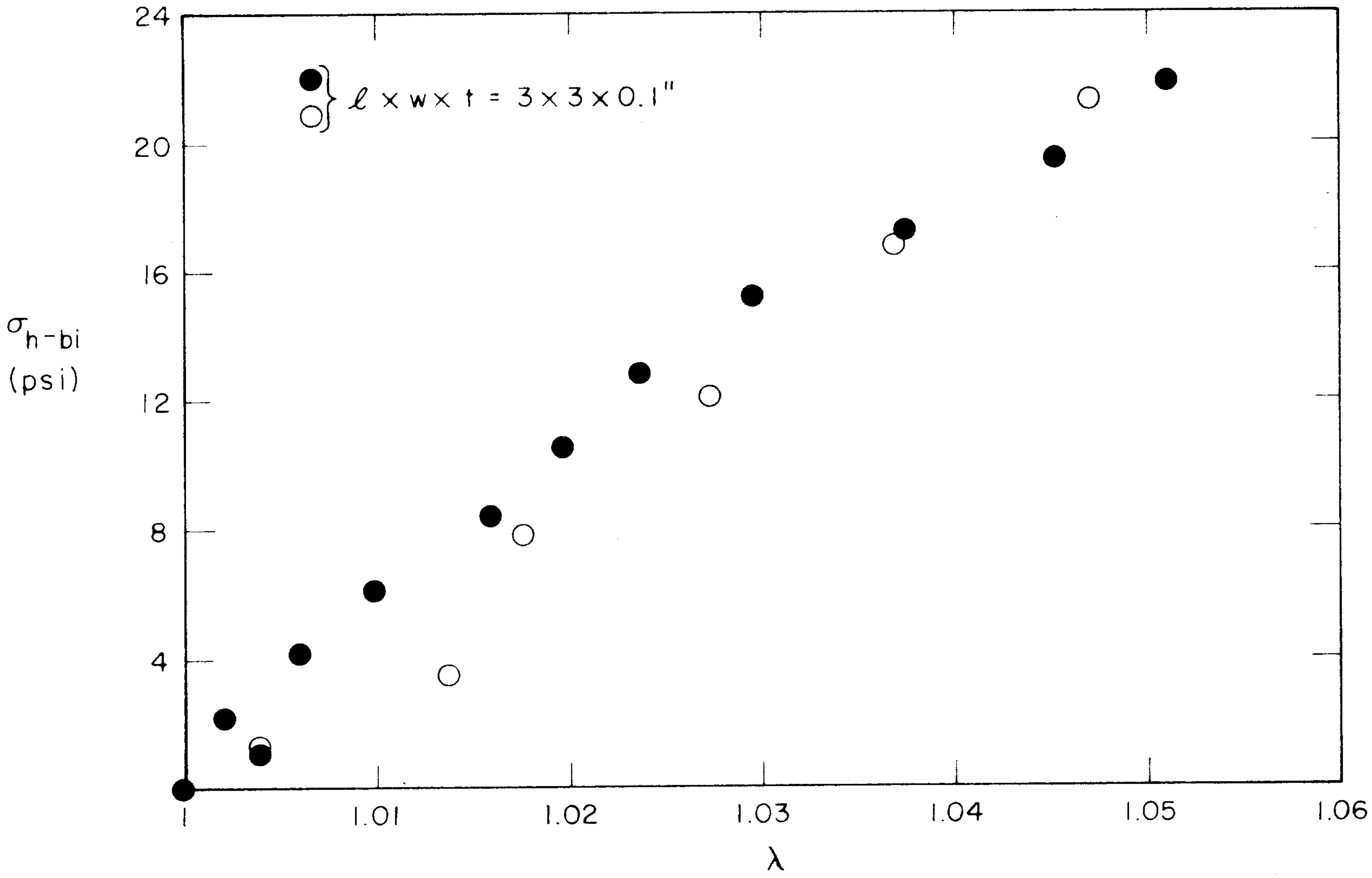

FIG.I.30. **Homogeneous-Biaxial Stress vs. Longitudinal Extension Ratio (Polyurethane Rubber).**

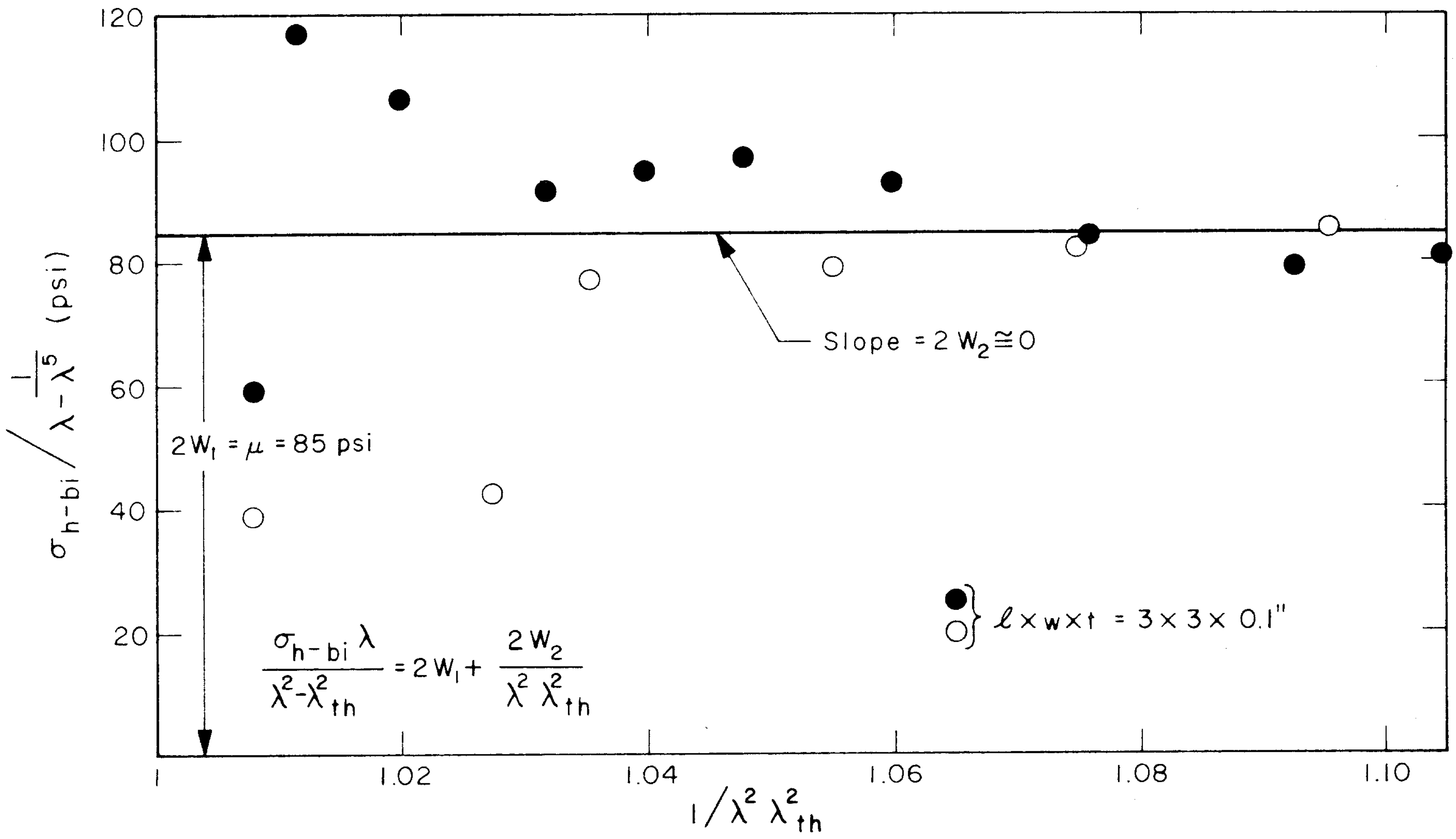

FIG. I. 31. Evaluation of W_1, W_2 From Rectified Homogeneous-Biaxial Data (Polyurethane Rubber).

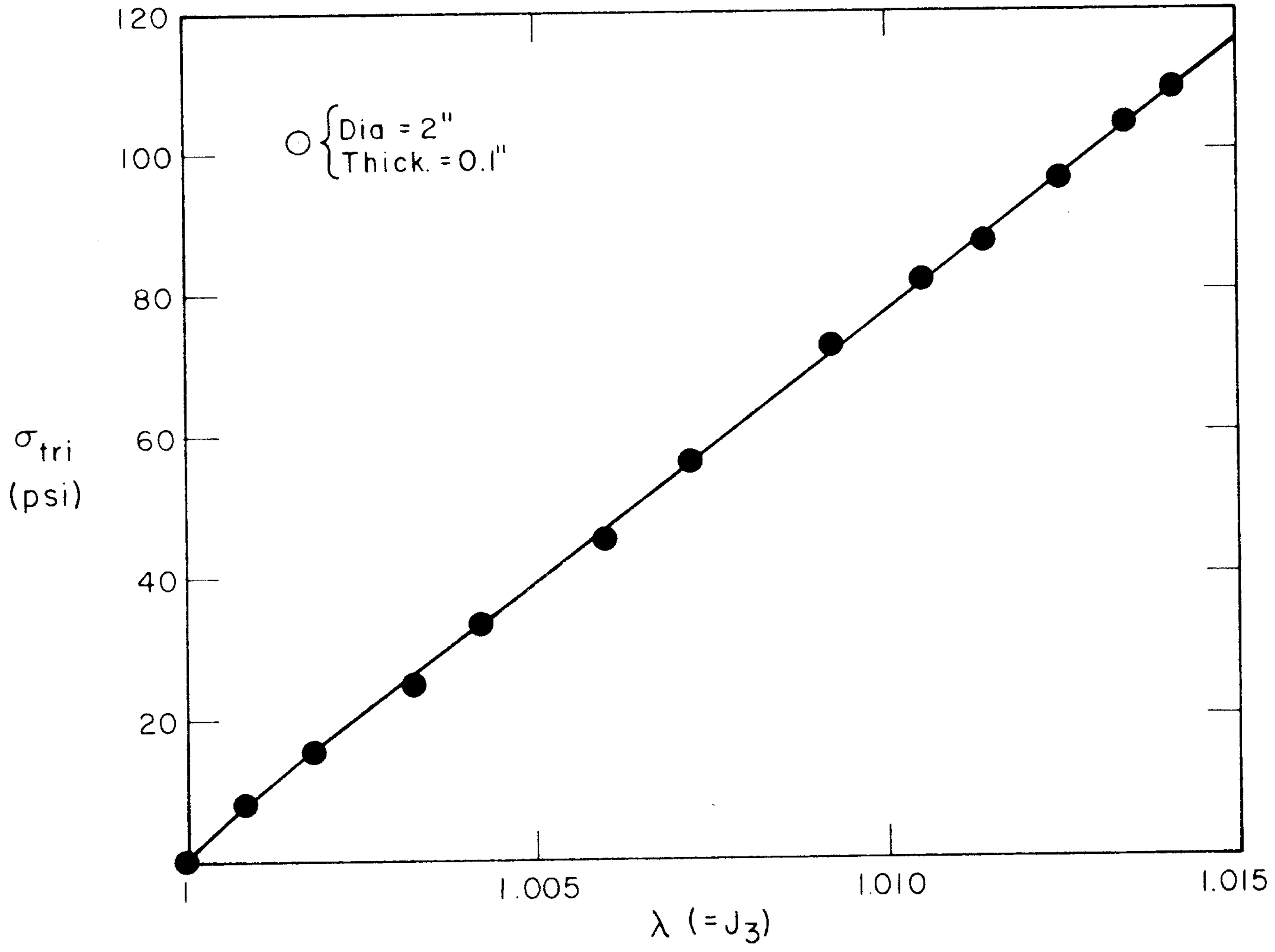

FIG. I. 32. **Triaxial Stress vs. Thickness Extension Ratio (Polyurethane Rubber).**

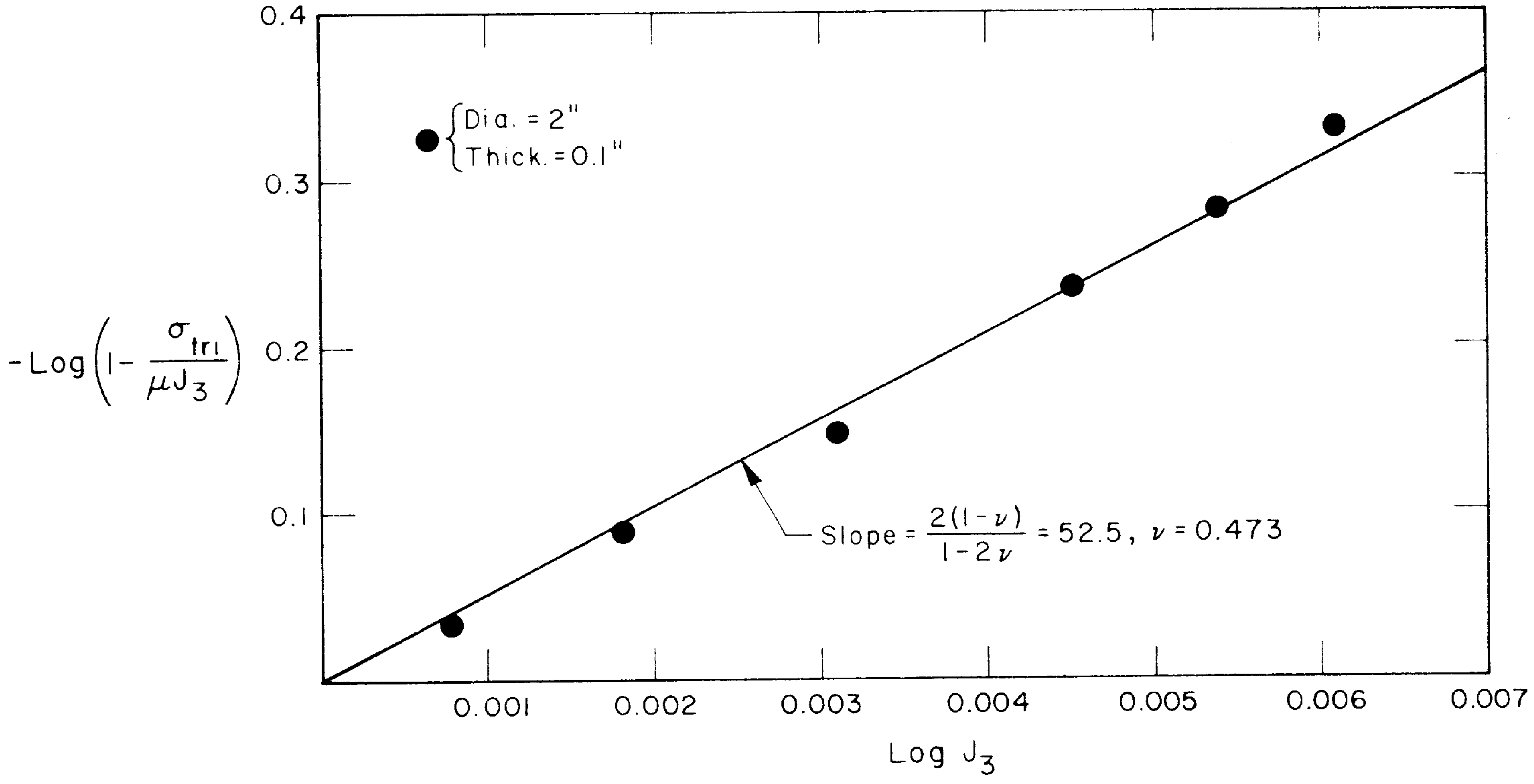

FIG. I. 33. **Rectification of Triaxial Tensile Data (Polyurethane Rubber).**

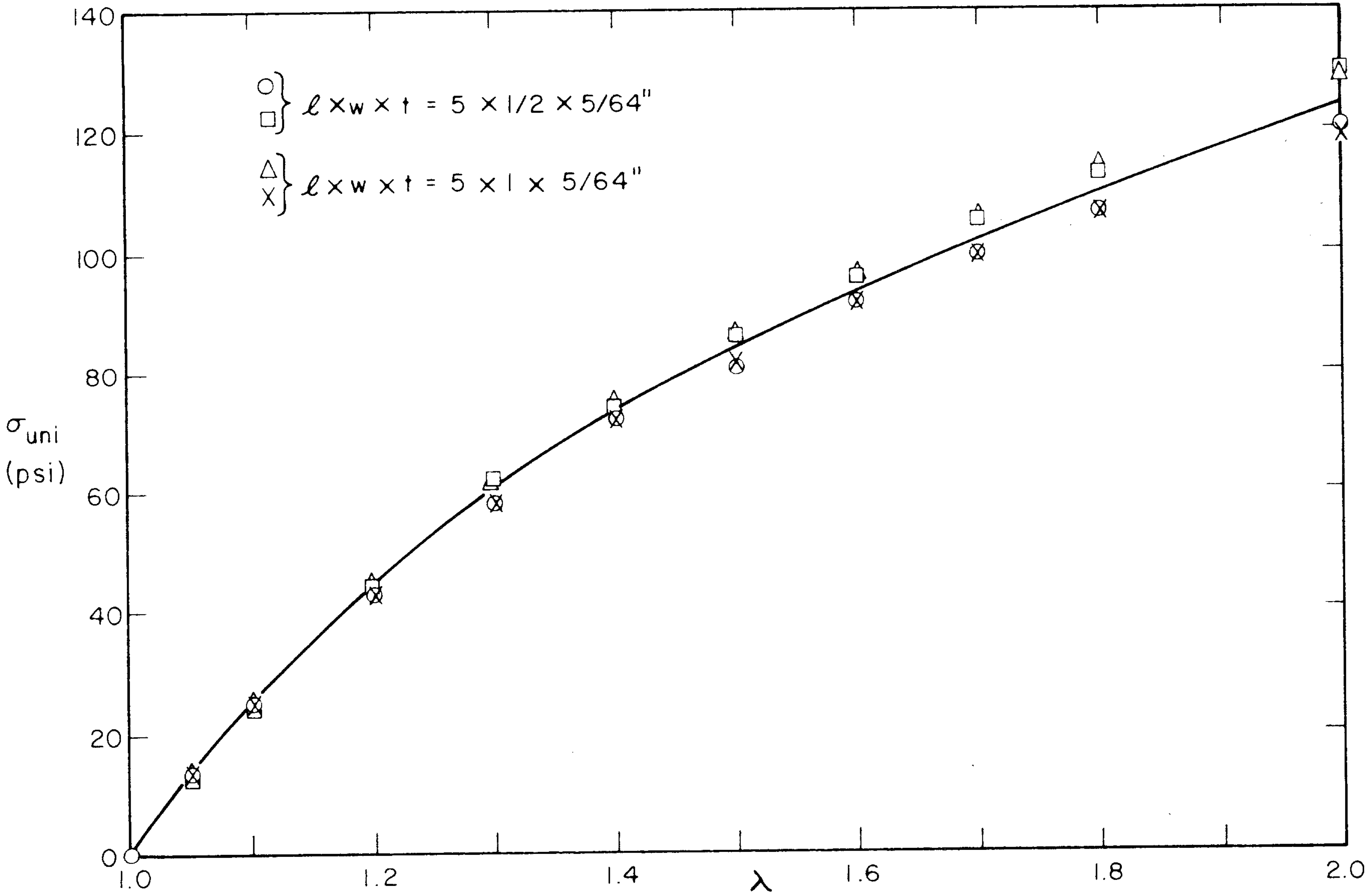

FIG.I.34. Uniaxial Stress vs. Longitudinal Extension Ratio (SBR-1500, 3 °/o Sulfur).

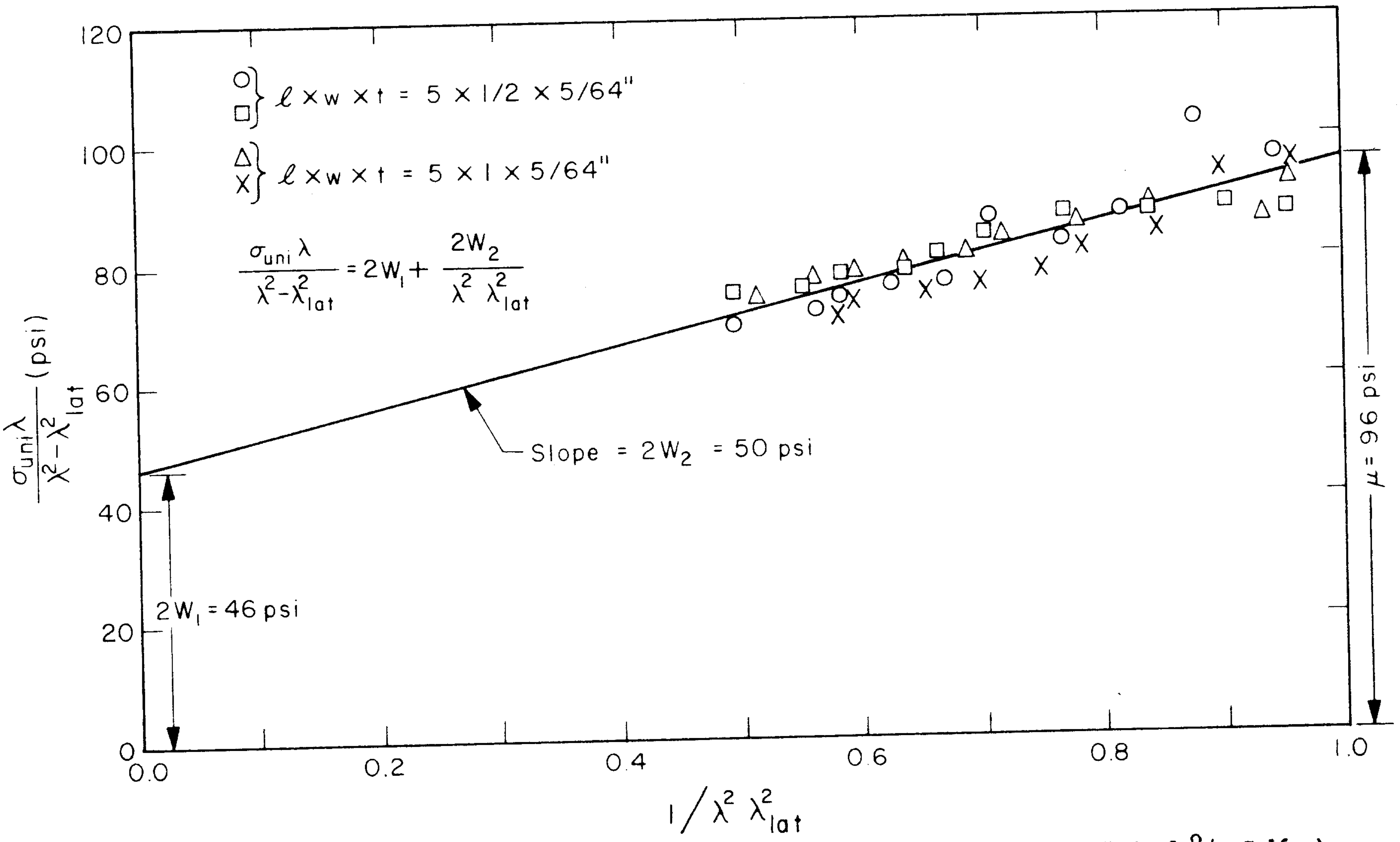

FIG. I. 35. Evaluation of W_1, W_2 From Rectified Uniaxial Data (SBR-1500, 3 °/o Sulfur).

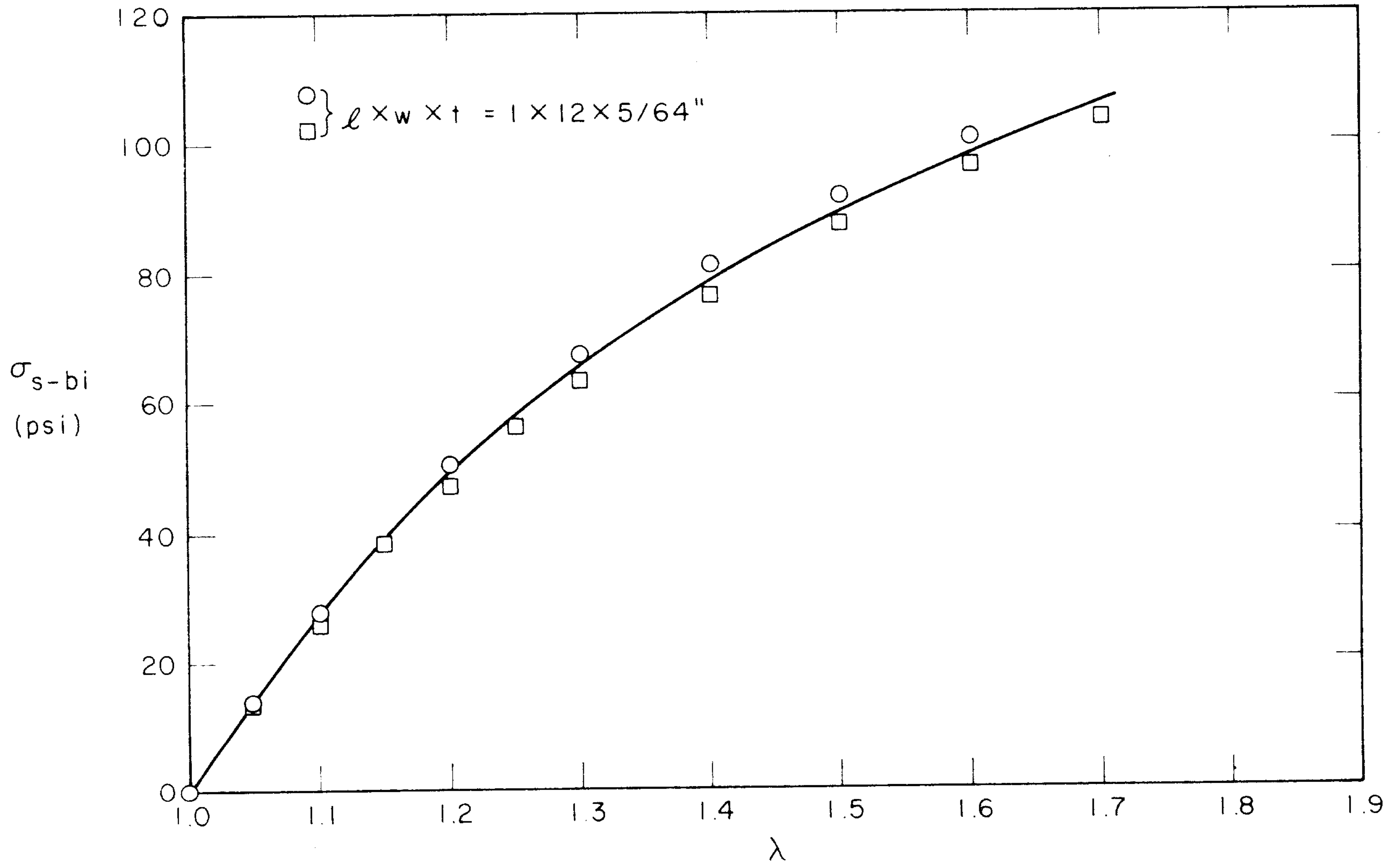

FIG. I. 36. Strip-Biaxial Stress vs. Longitudinal Extension Ratio (SBR-1500, 3 °/o Sulfur).

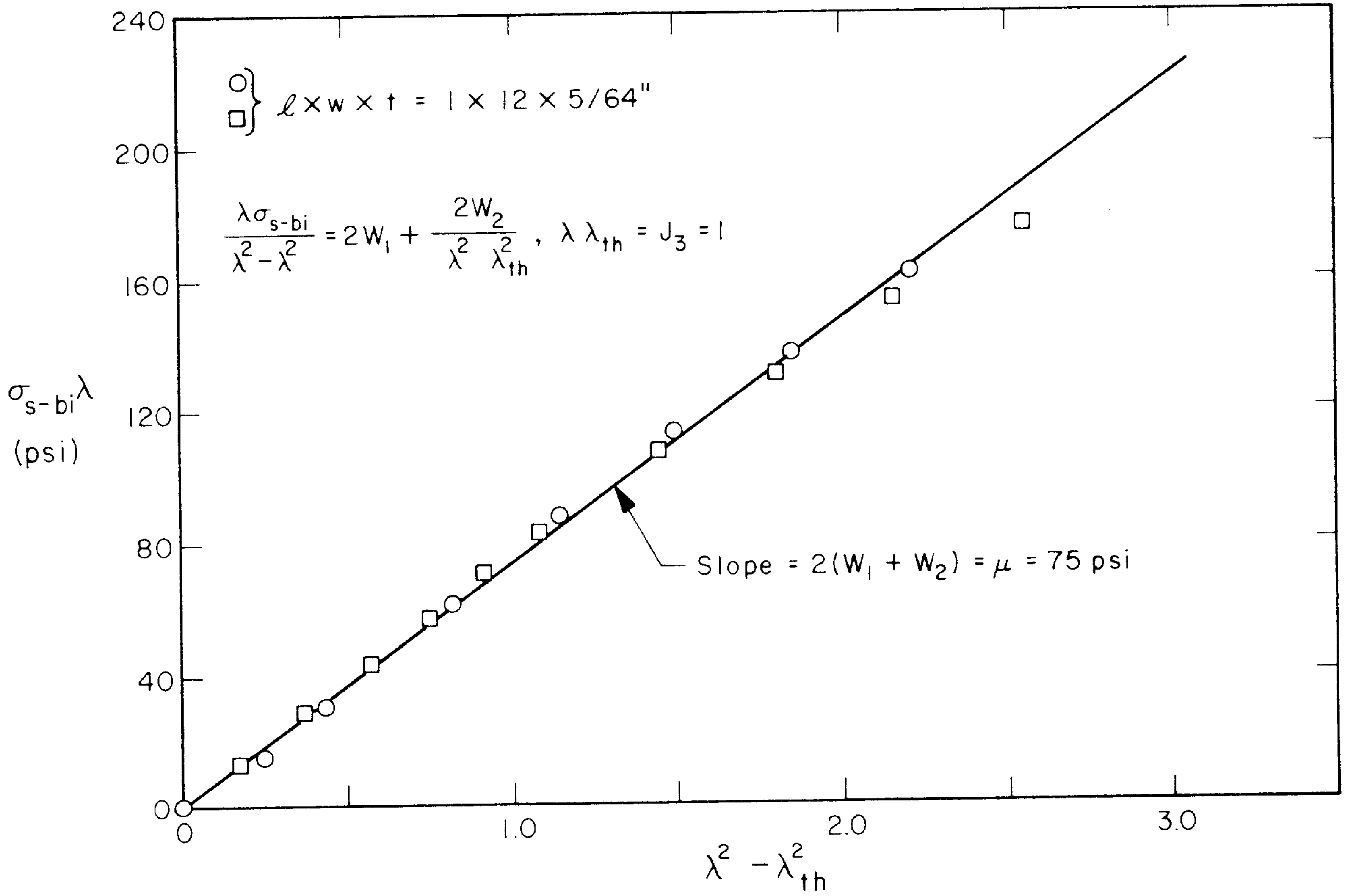

FIG. I. 37. Evaluation of $W_1 + W_2$ From Rectified Strip-Biaxial Data (SBR-1500, 3 °/o Sulfur).

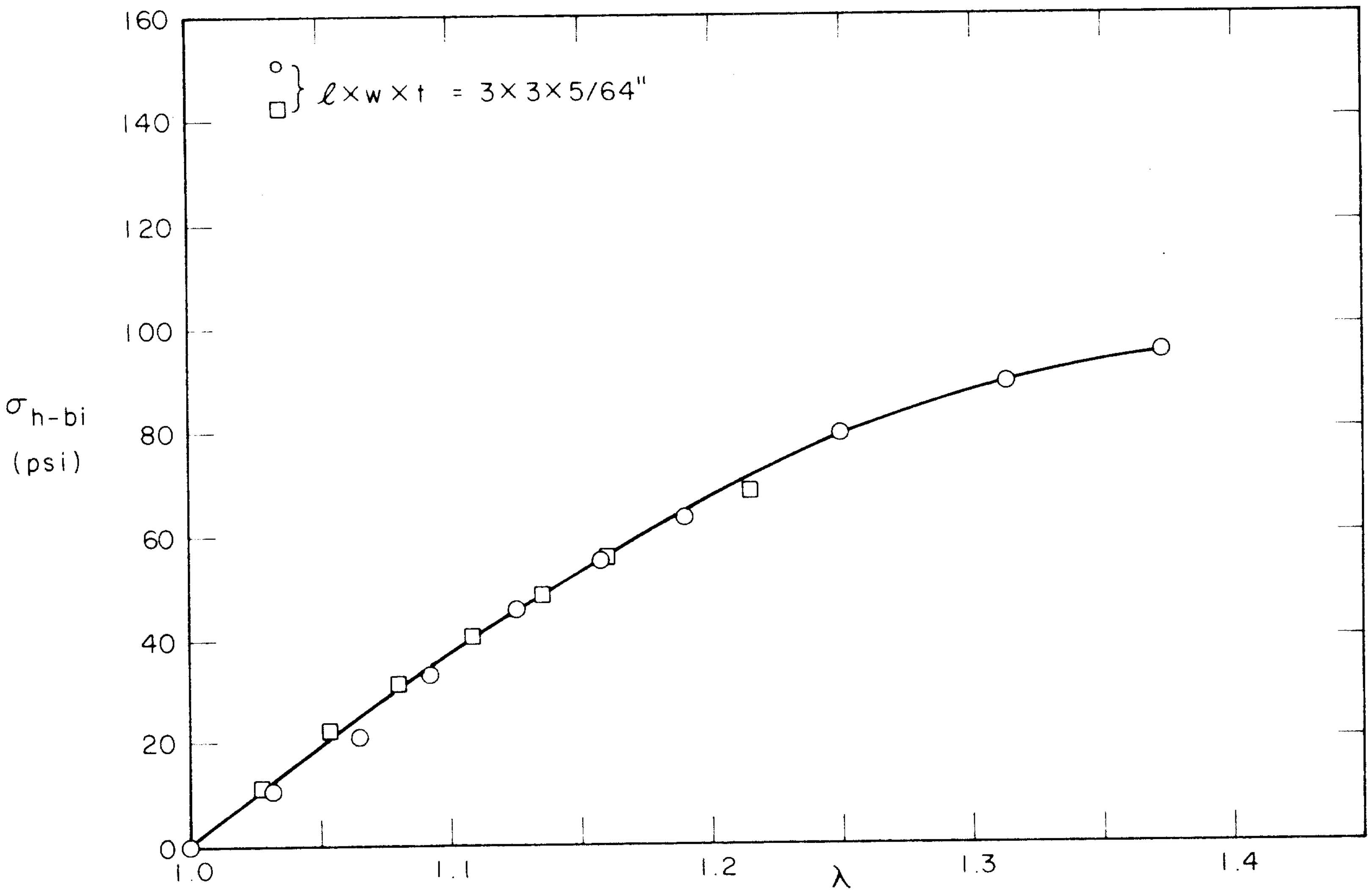

FIG. I. 38. Homogeneous-Biaxial Stress vs. Longitudinal Extension Ratio (SBR-1500, 3 °/o Sulfur).

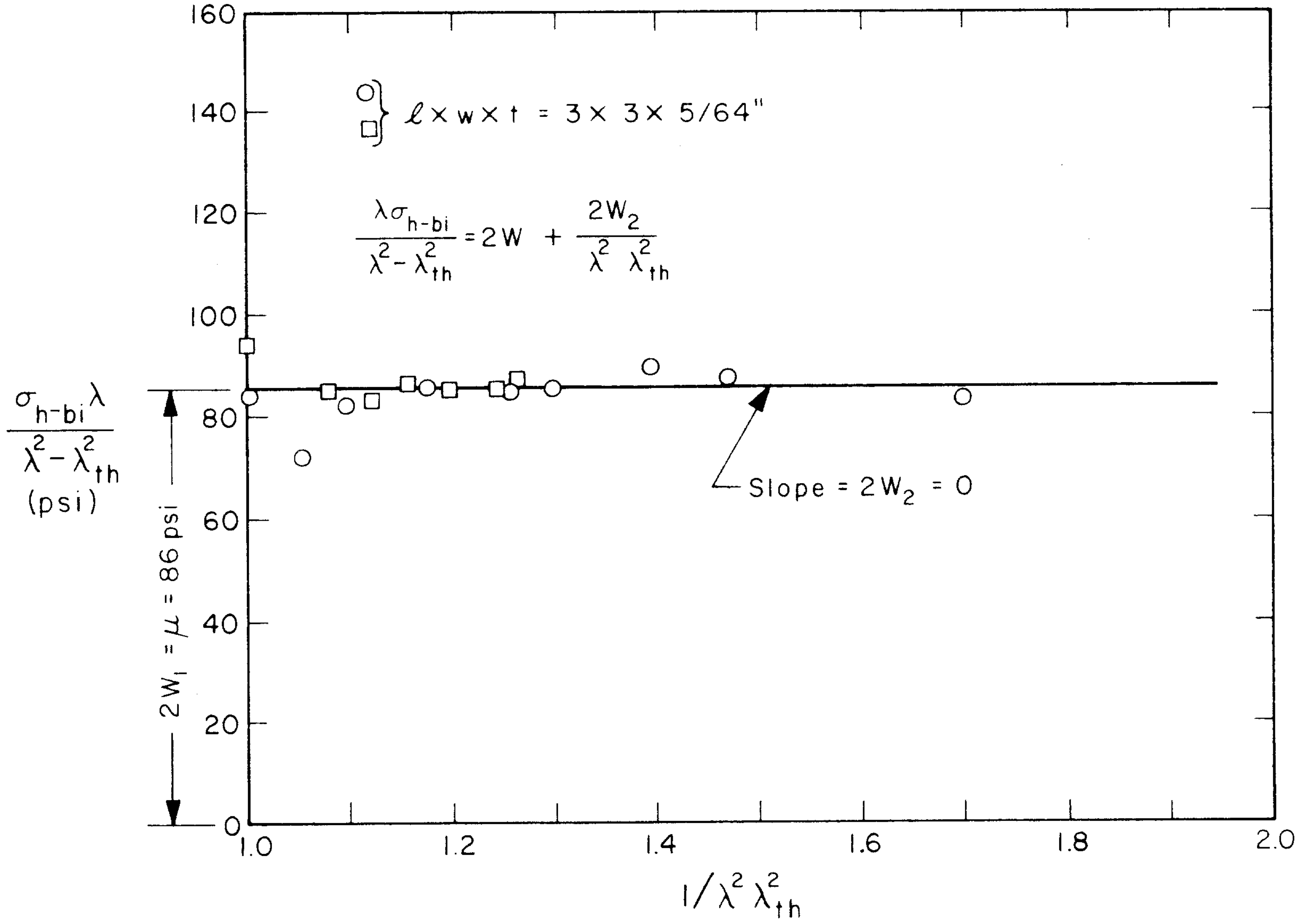

FIG. I. 39. Evaluation of W_1, W_2 From Rectified Homogeneous-Biaxial Data (SBR-1500, 3 °/o Sulfur).

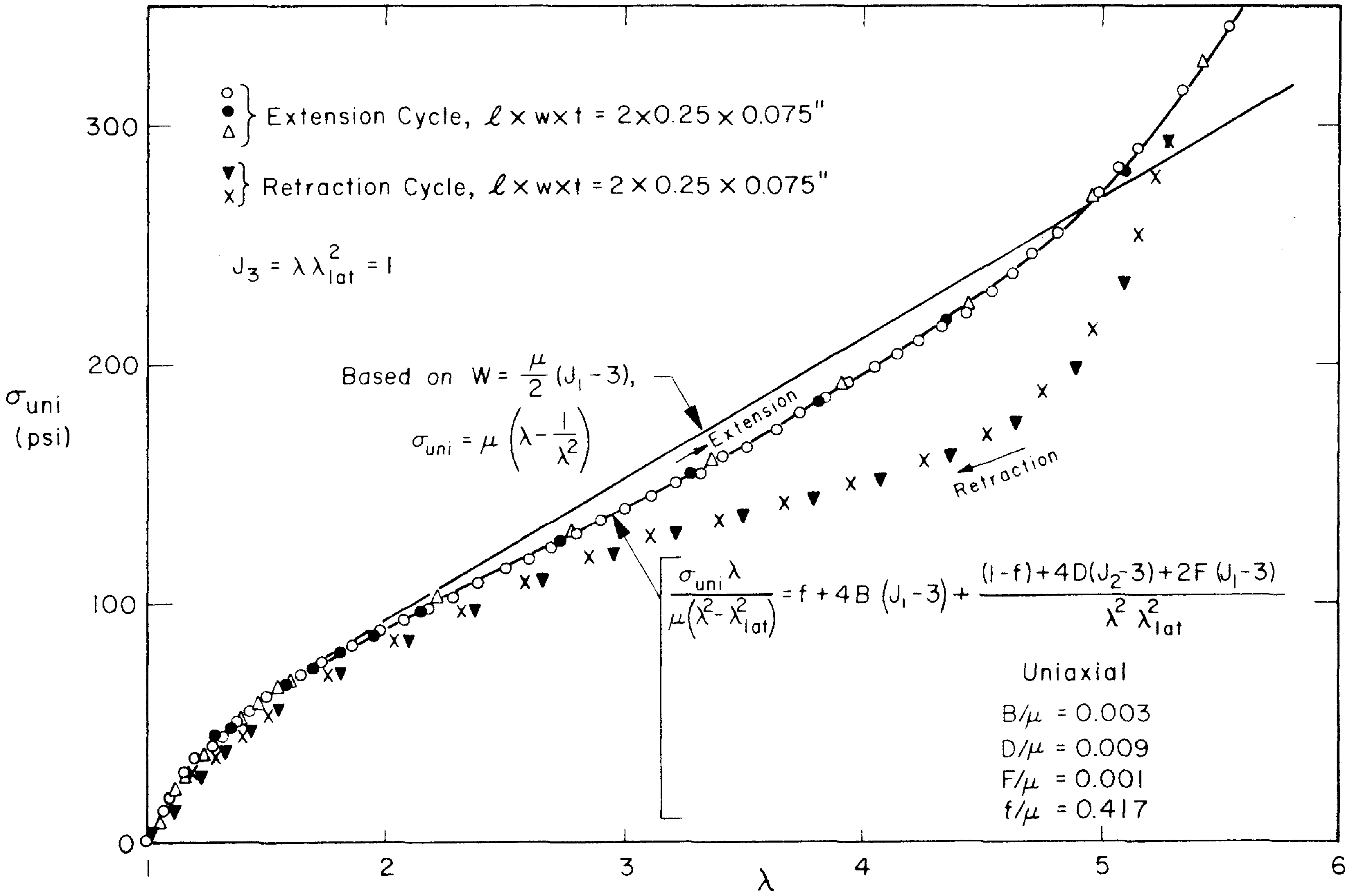

FIG. I. 40. Uniaxial Stress vs. Longitudinal Extension Ratio (Natural Rubber, 2 °/o Sulfur).

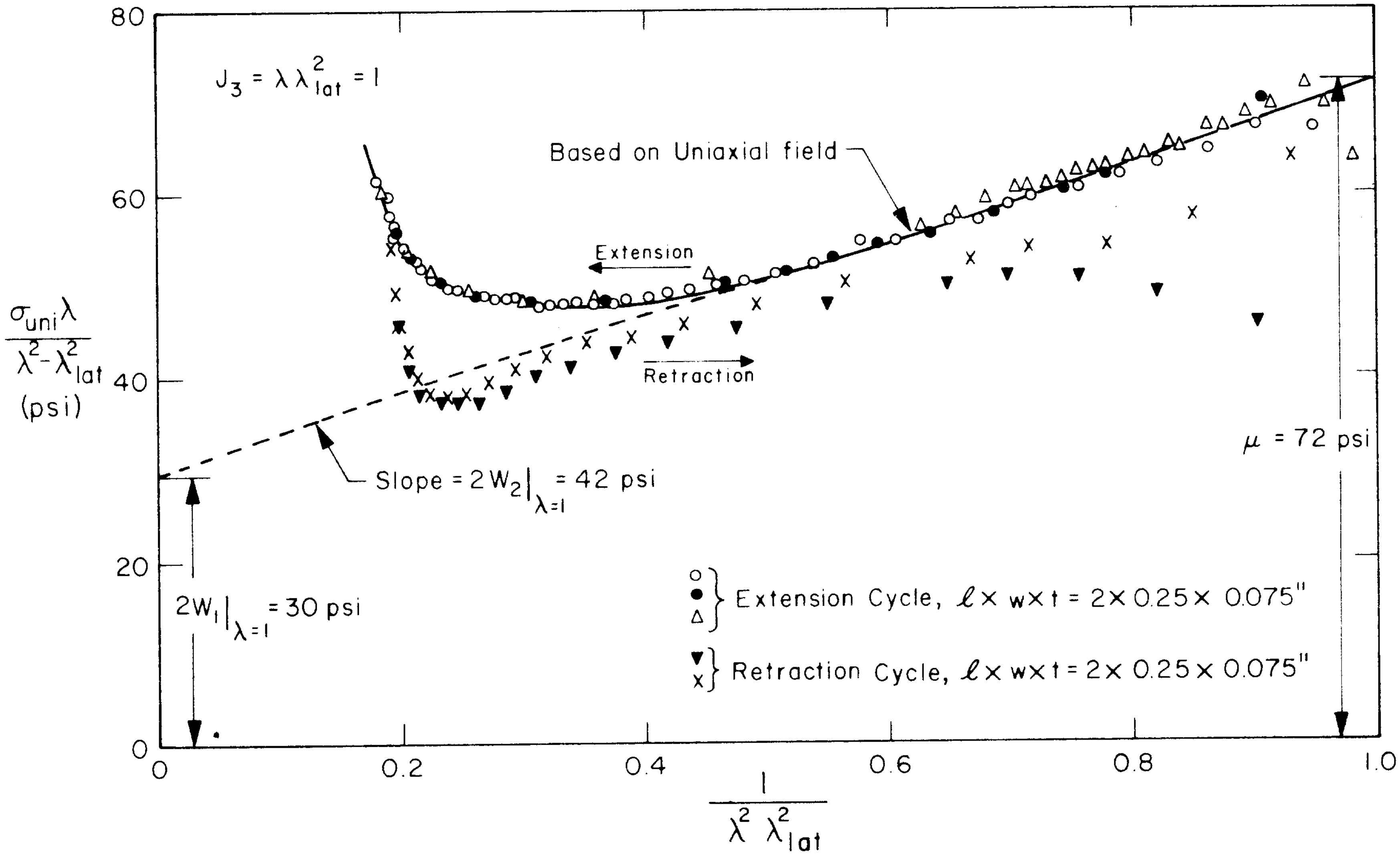

FIG. I. 41. Evaluation of W_1, W_2 From Rectified Uniaxial Data (Natural Rubber, 2 °/o Sulfur).

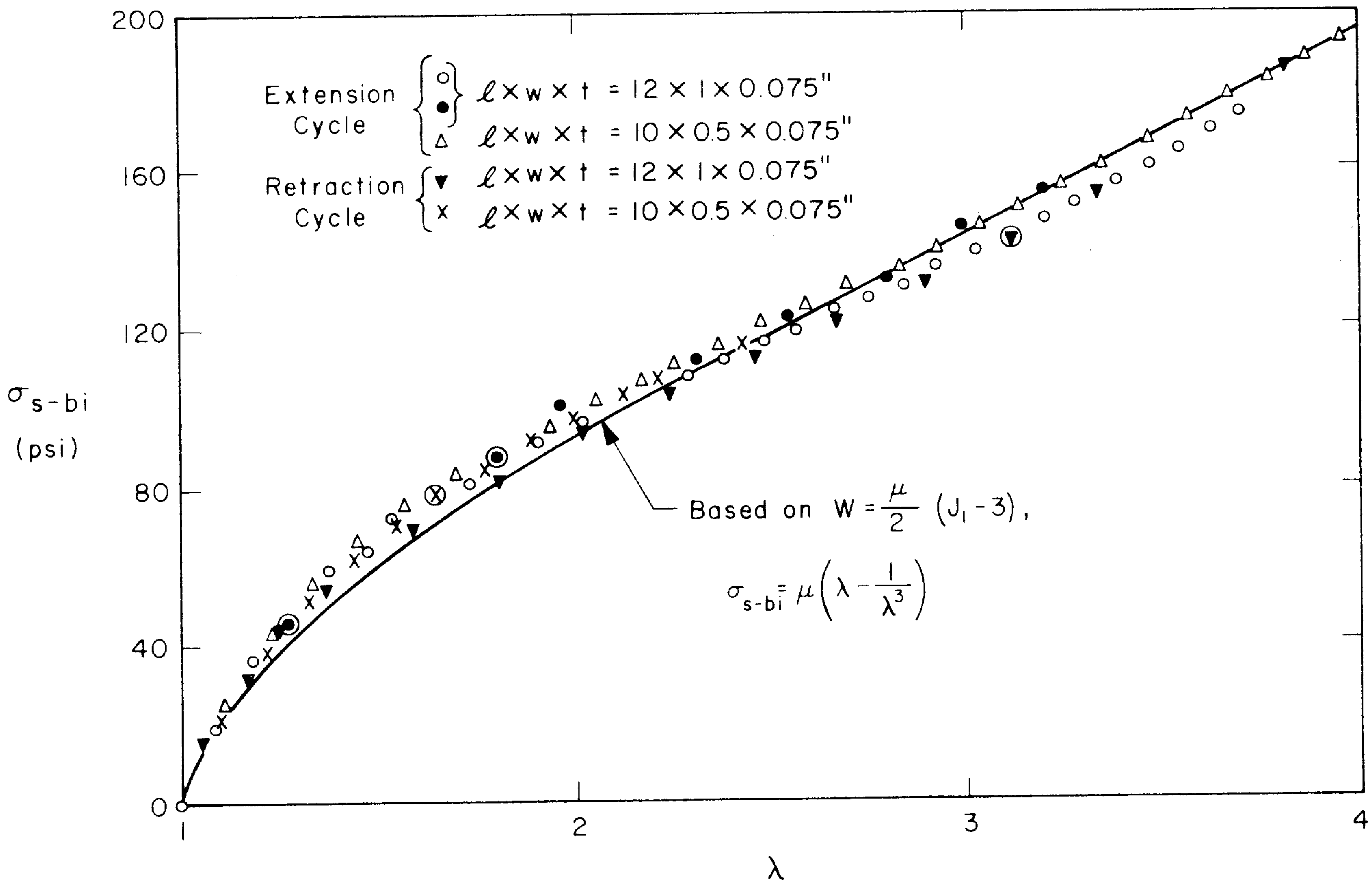

FIG. I. 42. Strip-Biaxial Stress vs. Longitudinal Extension Ratio (Natural Rubber, 2 °/o Sulfur).

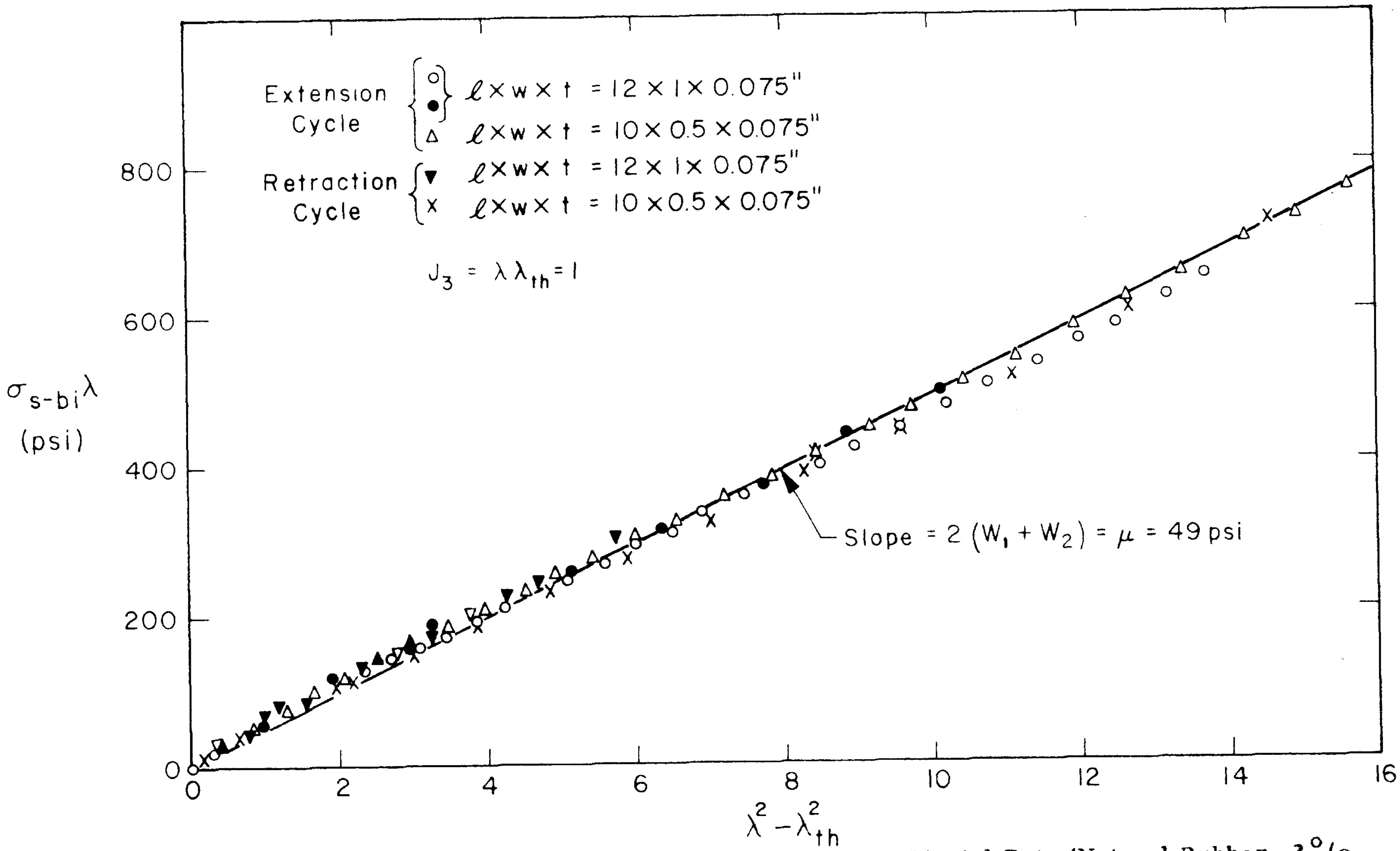

FIG.I.43. Evaluation of $W_1 + W_2$ From Rectified Strip-Biaxial Data (Natural Rubber, 2°/o Sulfur).

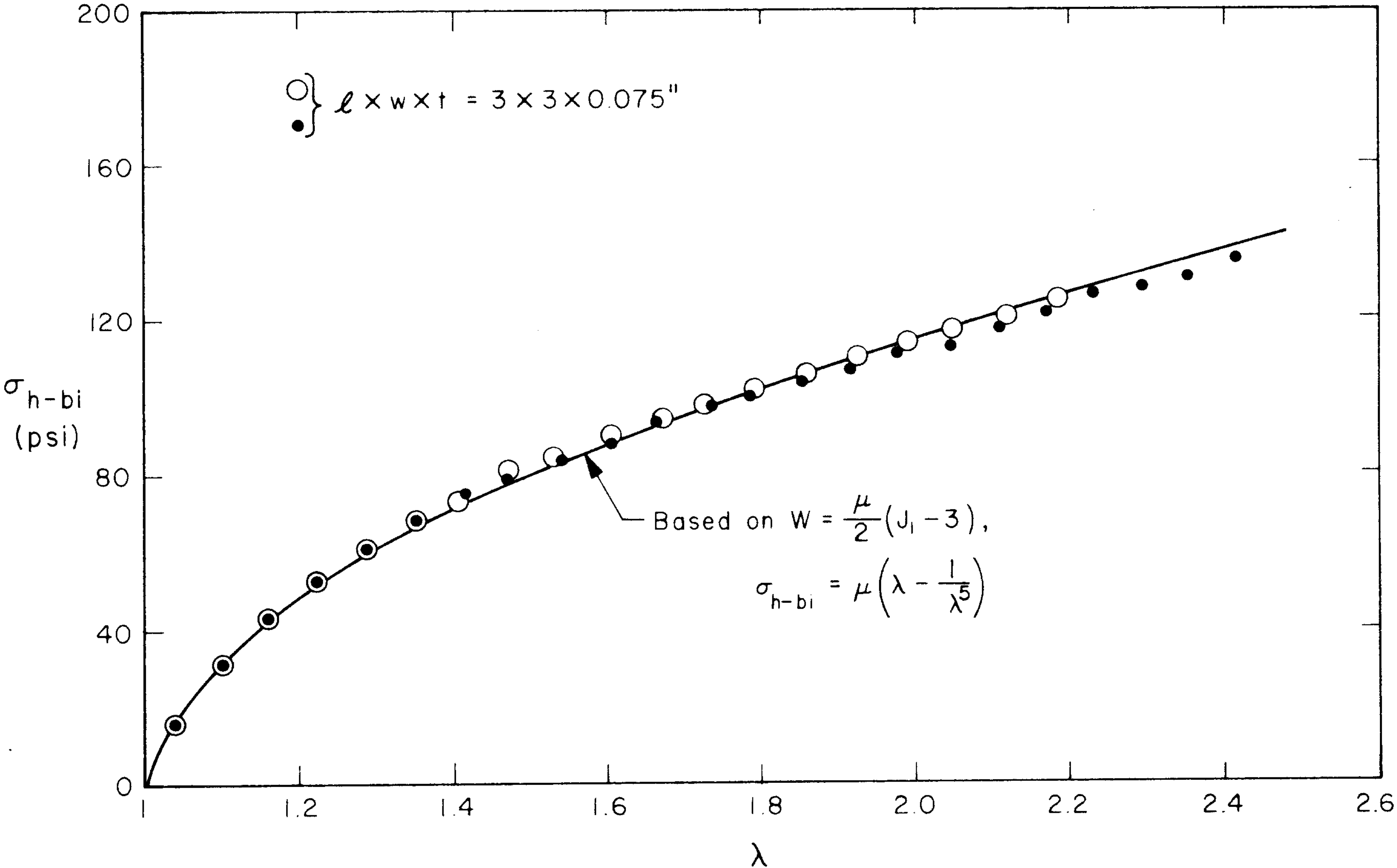

FIG. I. 44. Homogeneous-**Biaxial** Stress vs. Longitudinal Extension Ratio (Natural Rubber, 2 °/o Sulfur).

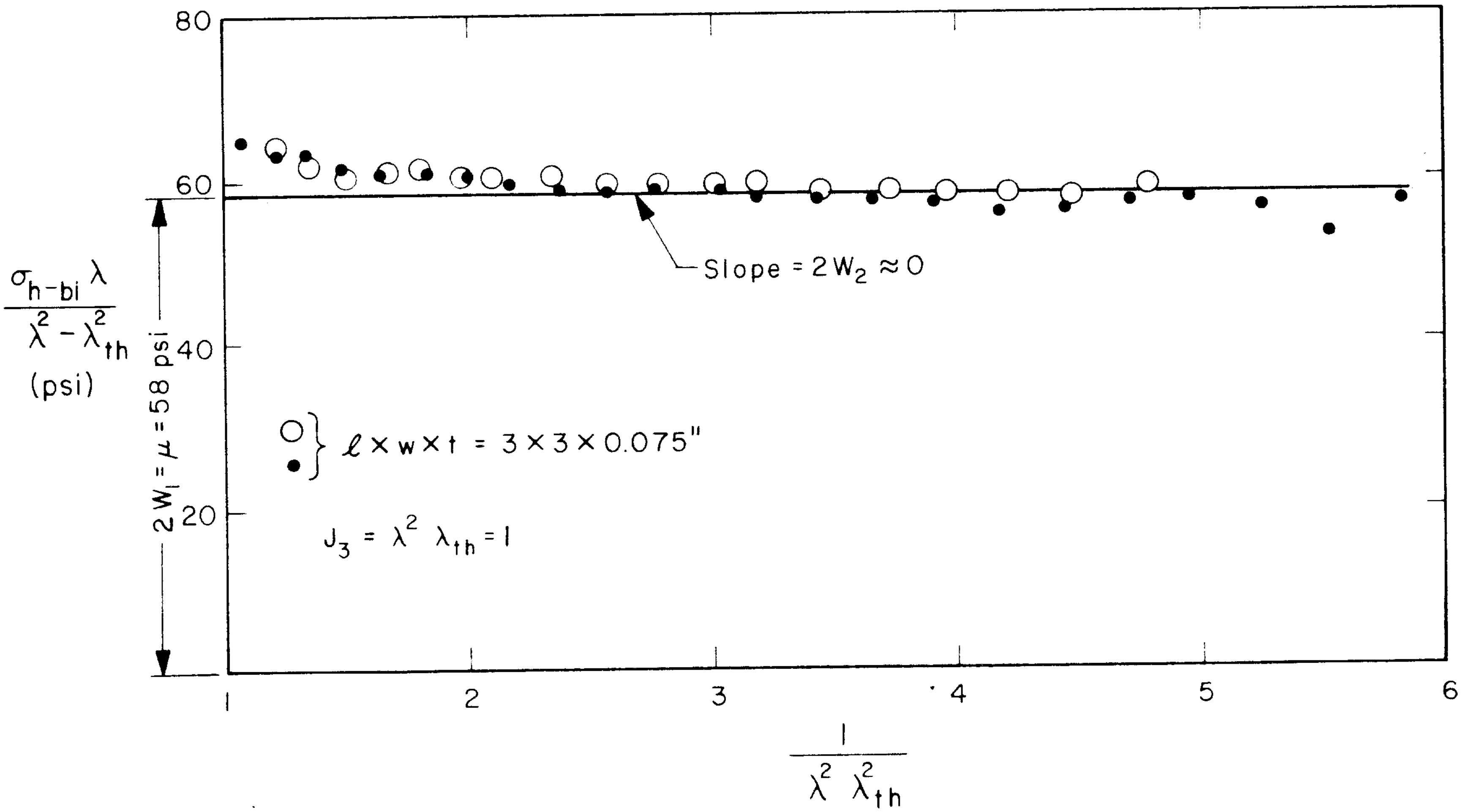

FIG. I. 45. Evaluation of W_1, W_2 From Rectified Homogeneous-Biaxial Data (Natural Rubber, 2 $^o/o$ Sulfur).

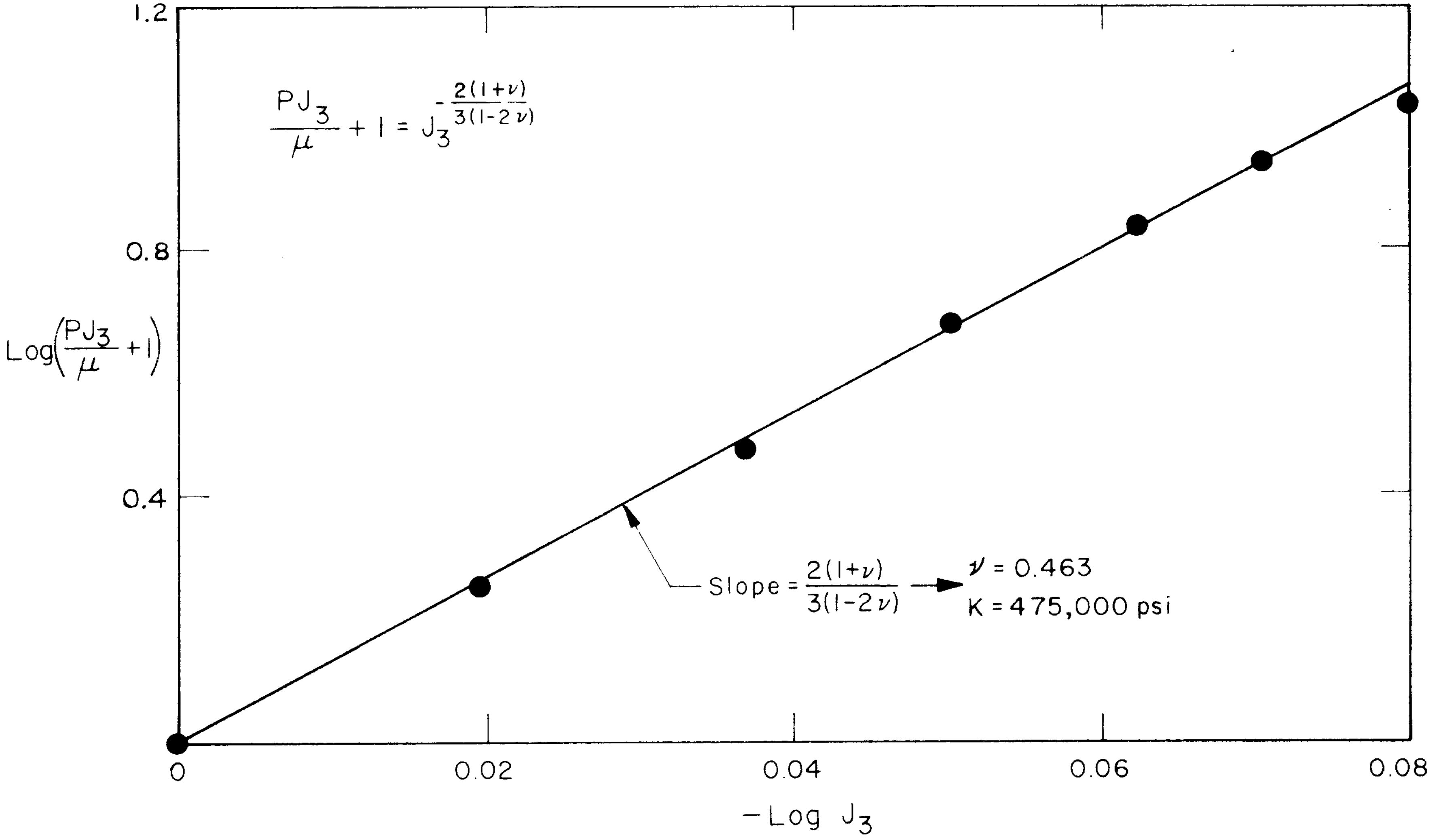

FIG. I. 46. Rectification of Hydrostatic Compression Data (Butyl Tread Rubber).

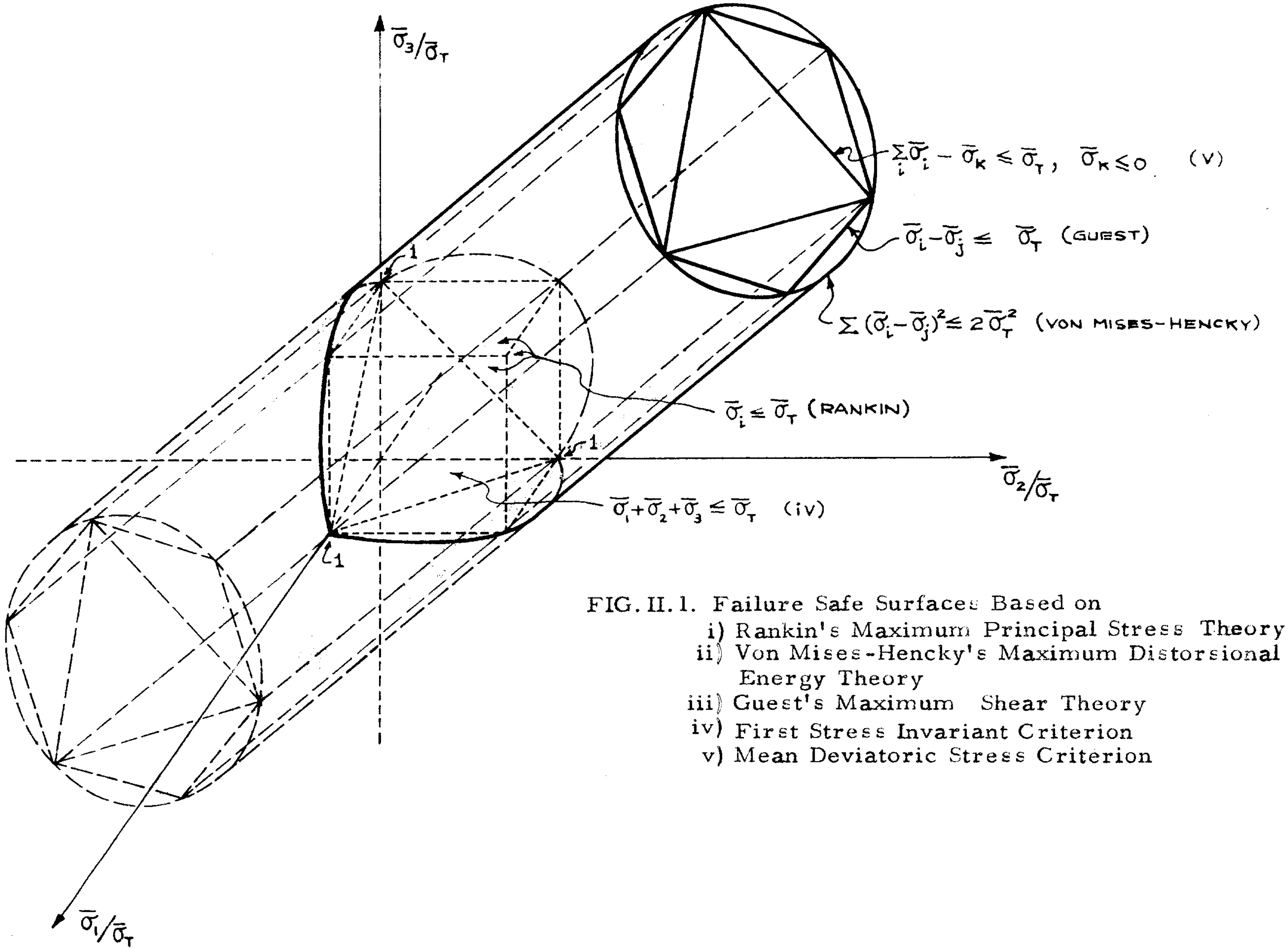

FIG. II.1. Failure Safe Surfaces Based on
i) Rankin's Maximum Principal Stress Theory
ii) Von Mises-Hencky's Maximum Distorsional Energy Theory
iii) Guest's Maximum Shear Theory
iv) First Stress Invariant Criterion
v) Mean Deviatoric Stress Criterion

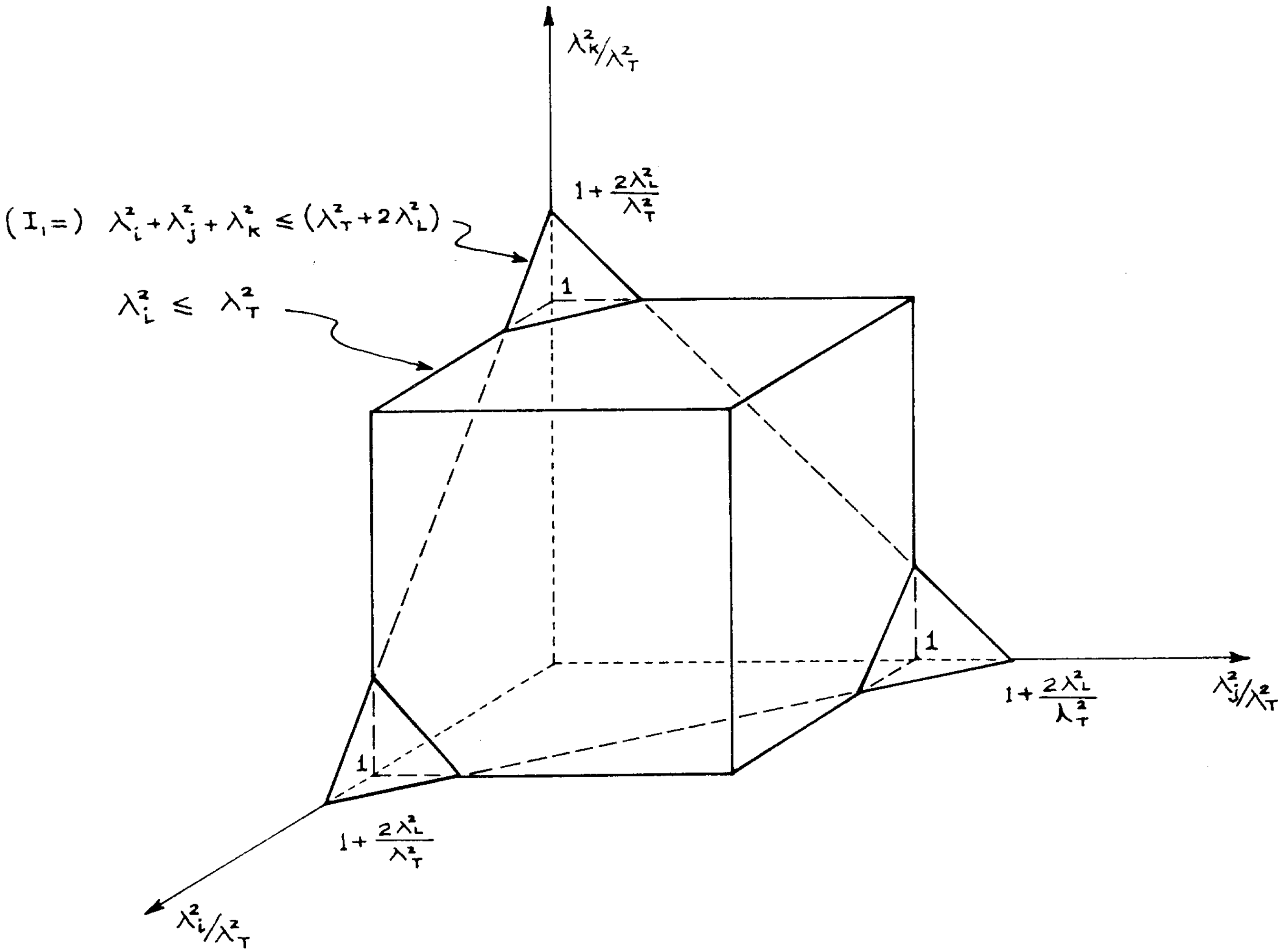

FIG. II. 2. Failure Surfaces Based on

1) Maximum Principal Stretch Criterion in Normal Stretch Space
2) Maximum First Stretch Invariant Criterion

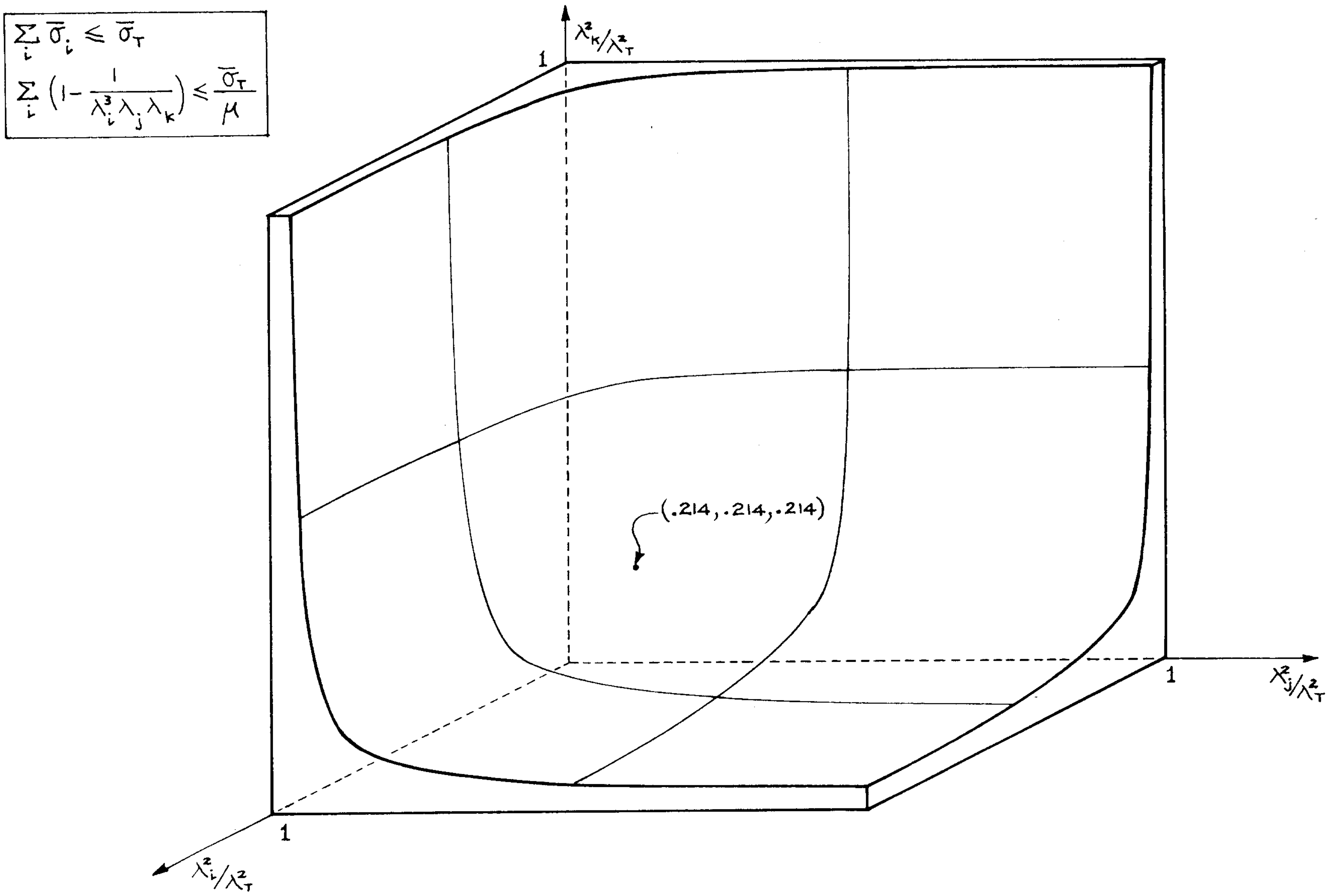

$$\sum_i \bar{\sigma}_i \leqslant \bar{\sigma}_T$$

$$\sum_i \left(1 - \frac{1}{\lambda_i^3 \lambda_j \lambda_k}\right) \leqslant \frac{\bar{\sigma}_T}{\mu}$$

FIG. II. 3. Failure Surface Based on Maximum First Stress Invariant Criterion in Normal Stretch Space

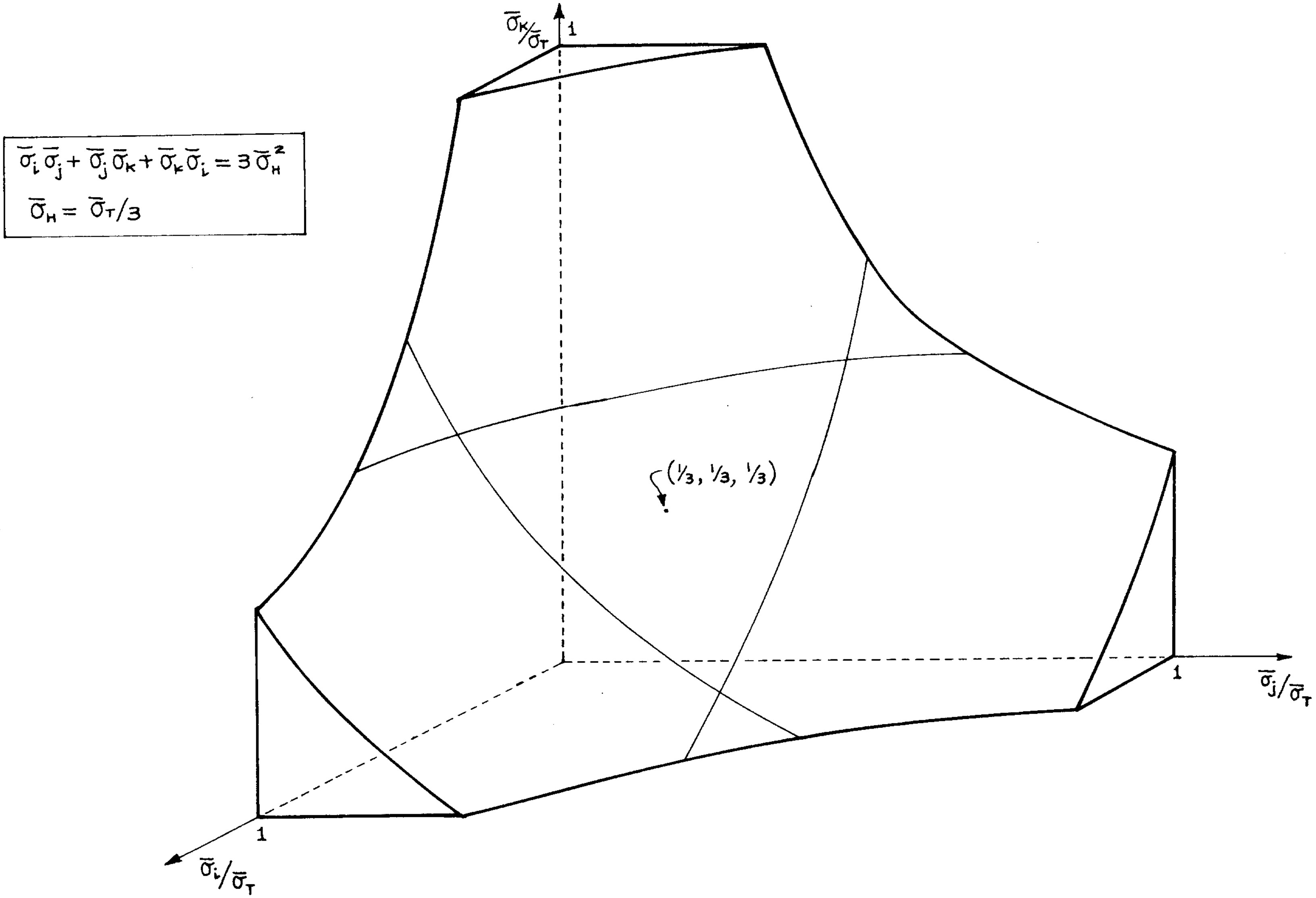

$$\bar{\sigma}_i\bar{\sigma}_j + \bar{\sigma}_j\bar{\sigma}_k + \bar{\sigma}_k\bar{\sigma}_i = 3\bar{\sigma}_H^2$$

$$\bar{\sigma}_H = \bar{\sigma}_T/3$$

FIG. II.4. Failure Surface Based on Maximum Second Stress Invariant Criterion in Normal Stress Space

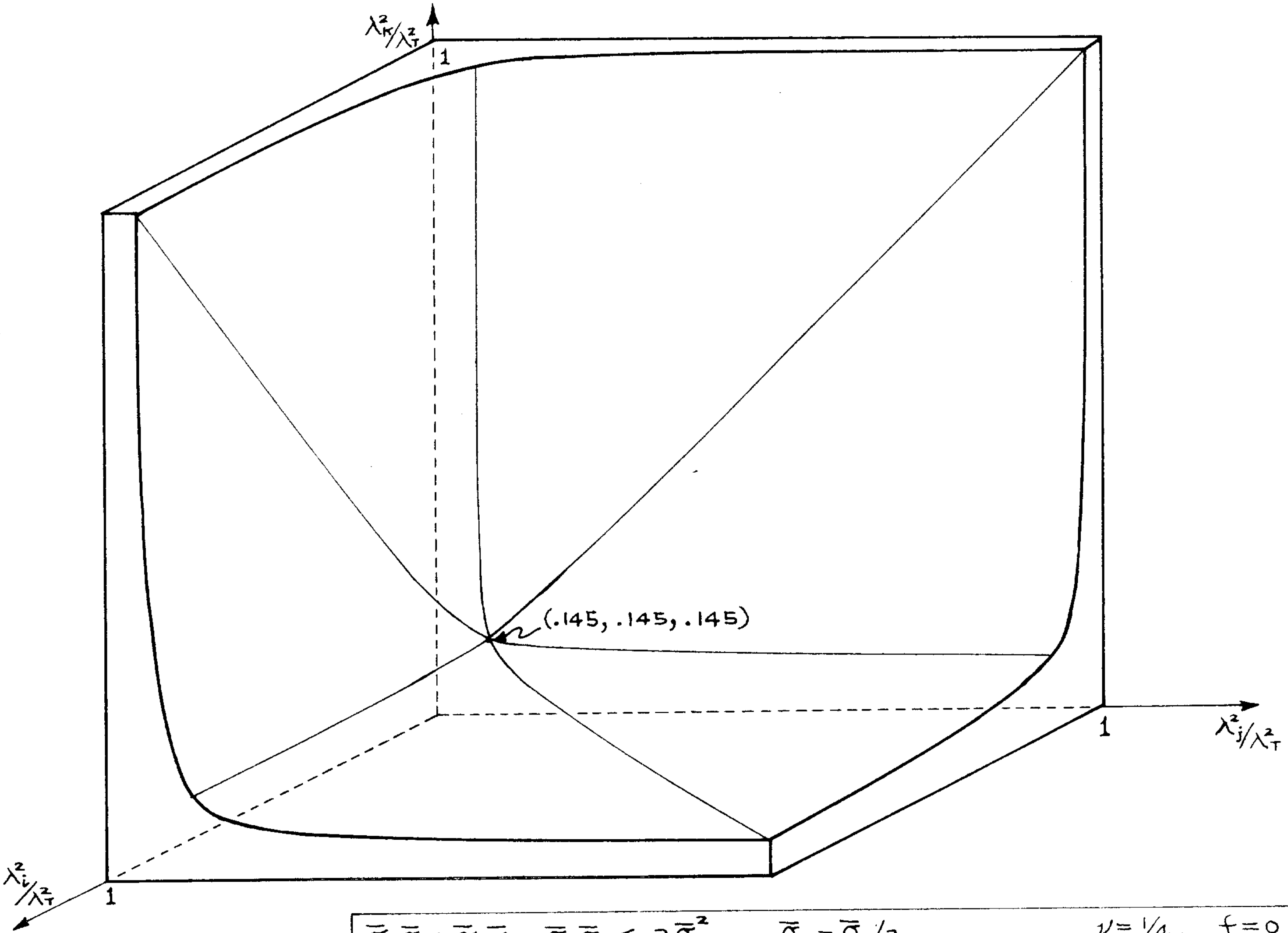

$$\bar{\sigma}_i\bar{\sigma}_j+\bar{\sigma}_j\bar{\sigma}_K+\bar{\sigma}_K\bar{\sigma}_i \leq 3\bar{\sigma}_H^2 \quad , \quad \bar{\sigma}_H=\bar{\sigma}_T/3 \quad , \qquad \nu=1/4 \, , \quad f=0$$

$$\left(1-\frac{1}{\lambda_i^3\lambda_j\lambda_K}\right)\left(1-\frac{1}{\lambda_i\lambda_j^3\lambda_K}\right)+\left(1-\frac{1}{\lambda_i\lambda_j^3\lambda_K}\right)\left(1-\frac{1}{\lambda_i\lambda_j\lambda_K^3}\right)+\left(1-\frac{1}{\lambda_i\lambda_j\lambda_K^3}\right)\left(1-\frac{1}{\lambda_i^3\lambda_j\lambda_K}\right) \leq \frac{3\bar{\sigma}_H^2}{\mu^2}$$

FIG. II. 5. Failure Surface Based on Maximum Second Stress Invariant Criterion in Principal Stretch Space.

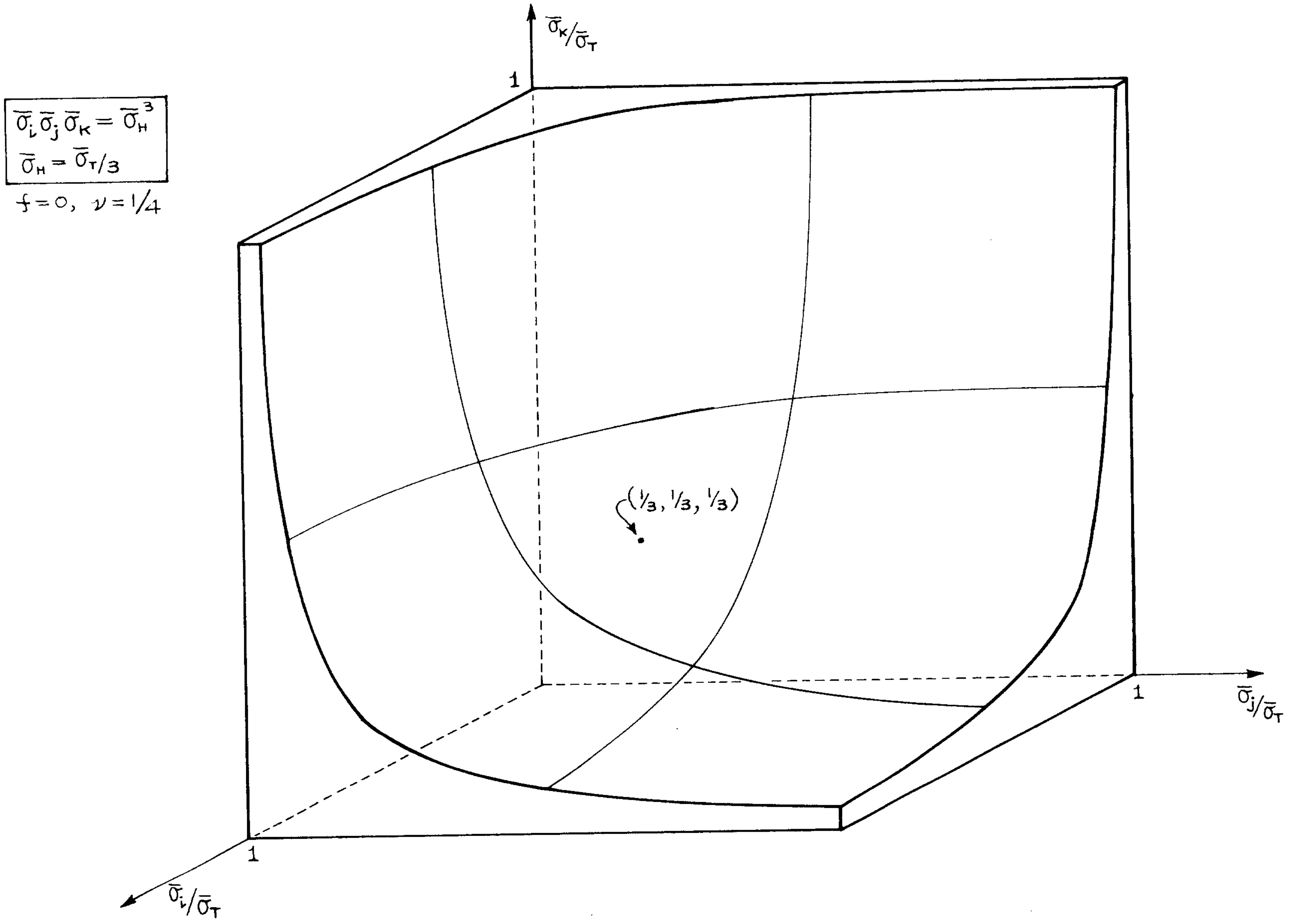

FIG. II.6. Failure Surface Based on Maximum Third Stress Invariant Criterion in Normal Stress Space

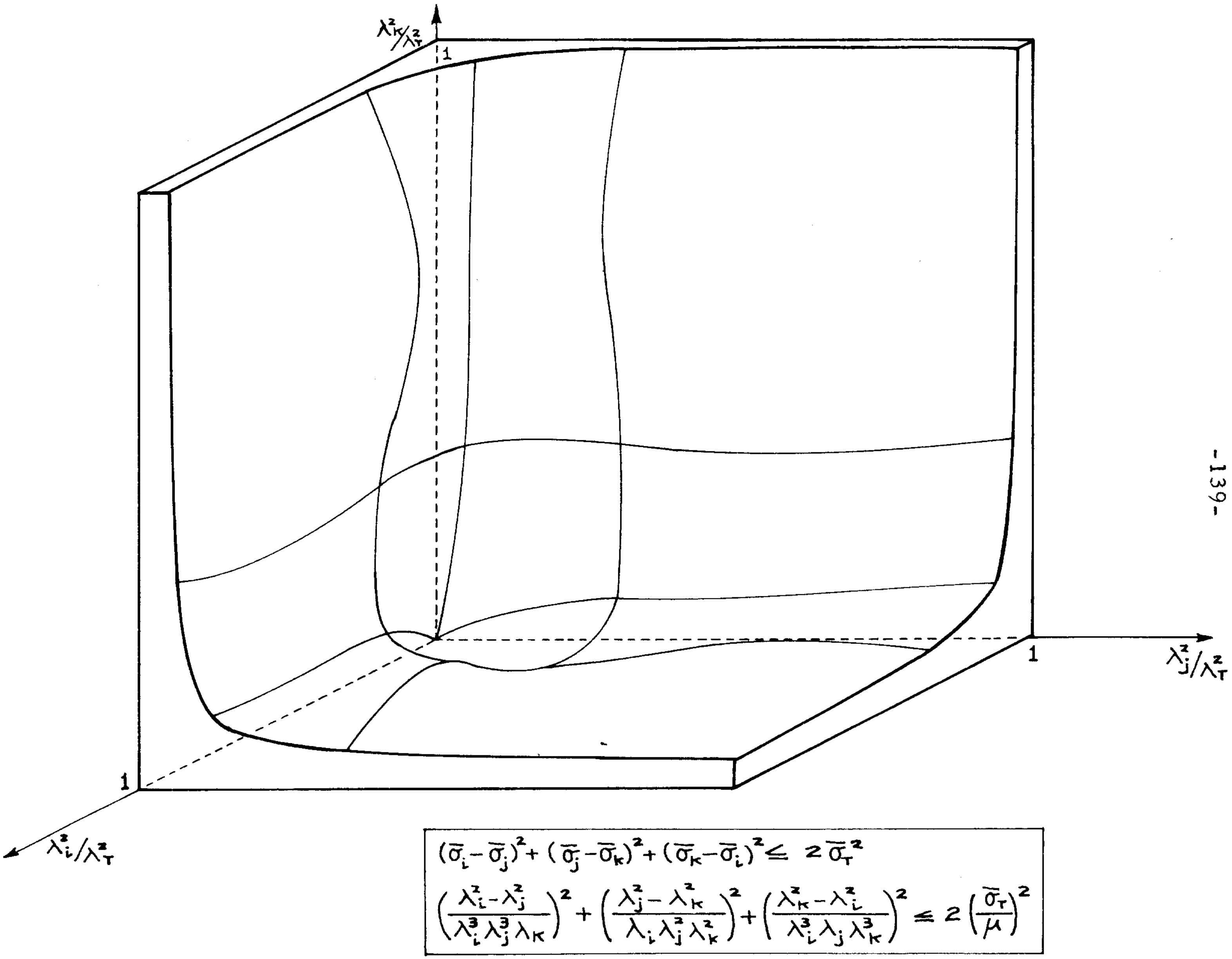

$$(\bar{\sigma}_i-\bar{\sigma}_j)^2+(\bar{\sigma}_j-\bar{\sigma}_k)^2+(\bar{\sigma}_k-\bar{\sigma}_i)^2 \leq 2\bar{\sigma}_T^2$$

$$\left(\frac{\lambda_i^2-\lambda_j^2}{\lambda_i^3\lambda_j^3\lambda_k}\right)^2+\left(\frac{\lambda_j^2-\lambda_k^2}{\lambda_i\lambda_j^2\lambda_k^2}\right)^2+\left(\frac{\lambda_k^2-\lambda_i^2}{\lambda_i^3\lambda_j\lambda_k^3}\right)^2 \leq 2\left(\frac{\bar{\sigma}_T}{\mu}\right)^2$$

FIG. II.7. Failure Surface Based on Maximum Octahedral Shear Stress Criterion in Normal Stretch Space

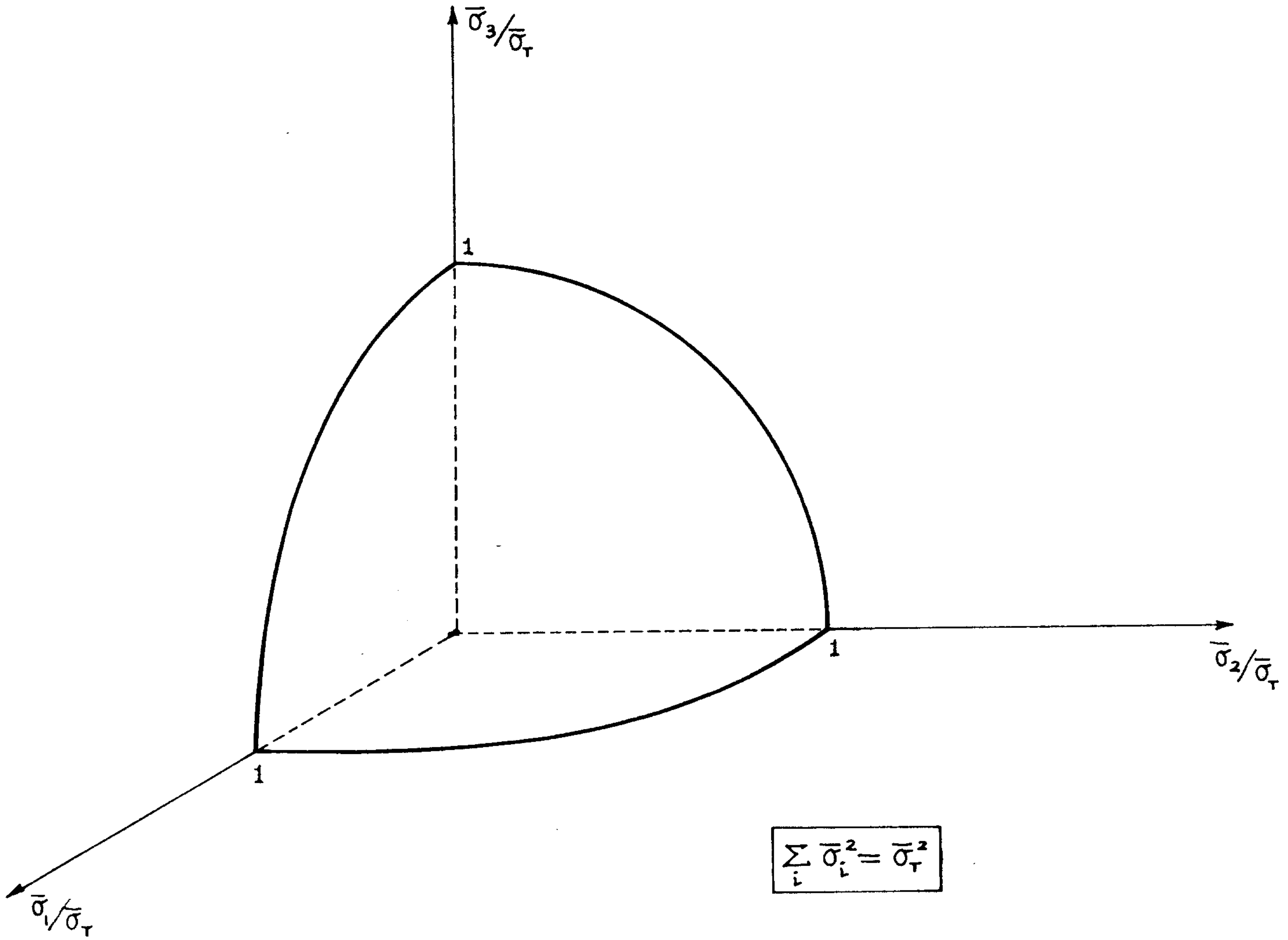

FIG. II. 2. Failure Surface Based on Maximum Stress Resultant in Normal Stress Space.

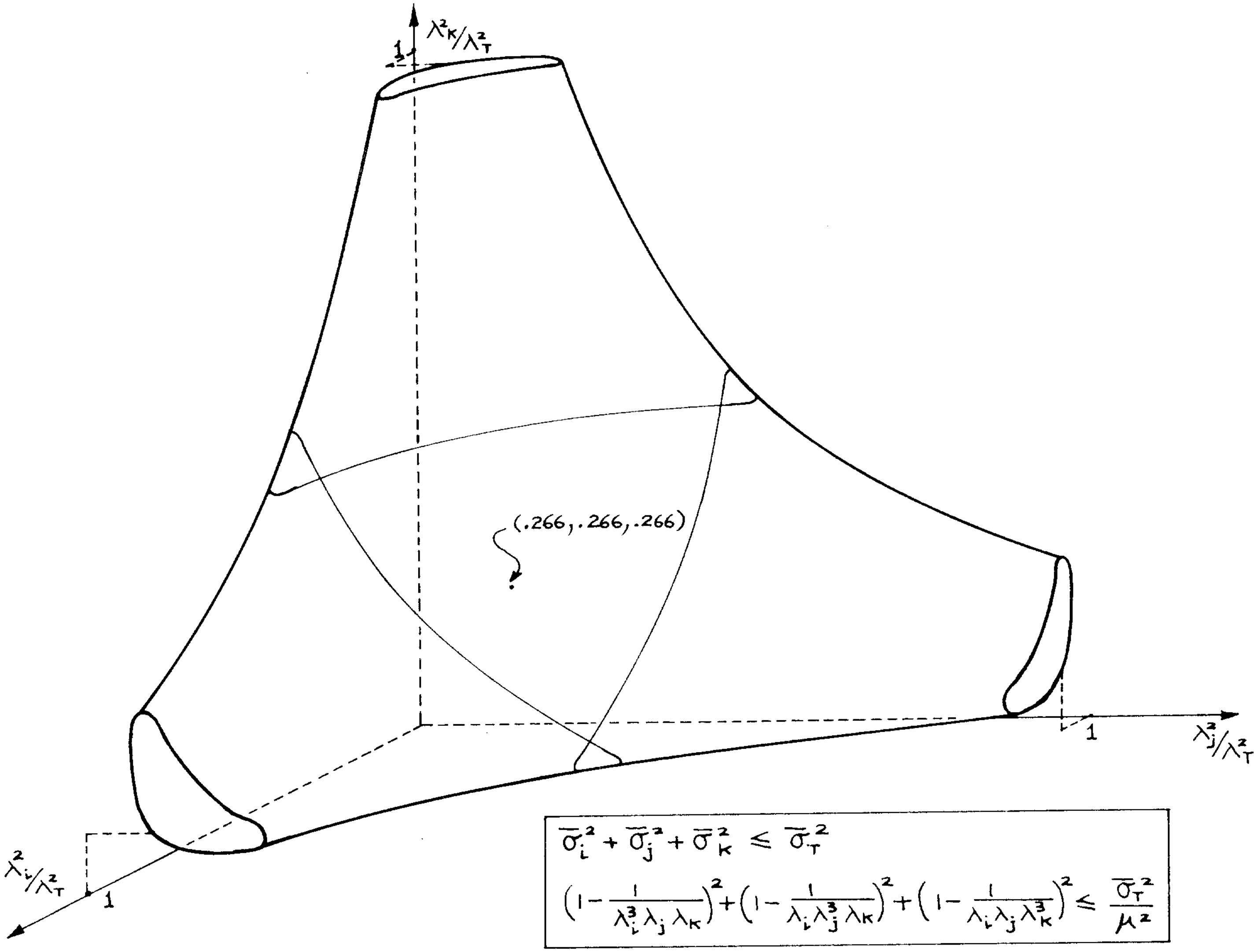

$$\overline{\sigma}_i^2 + \overline{\sigma}_j^2 + \overline{\sigma}_k^2 \leq \overline{\sigma}_T^2$$

$$\left(1 - \frac{1}{\lambda_i^3 \lambda_j \lambda_k}\right)^2 + \left(1 - \frac{1}{\lambda_i \lambda_j^3 \lambda_k}\right)^2 + \left(1 - \frac{1}{\lambda_i \lambda_j \lambda_k^3}\right)^2 \leq \frac{\overline{\sigma}_T^2}{\mu^2}$$

$f = 0, \quad \nu = 1/4$

FIG. II. 9. Failure Surface Based on Maximum Stress Resultant Criterion in Principal Stretch Space.

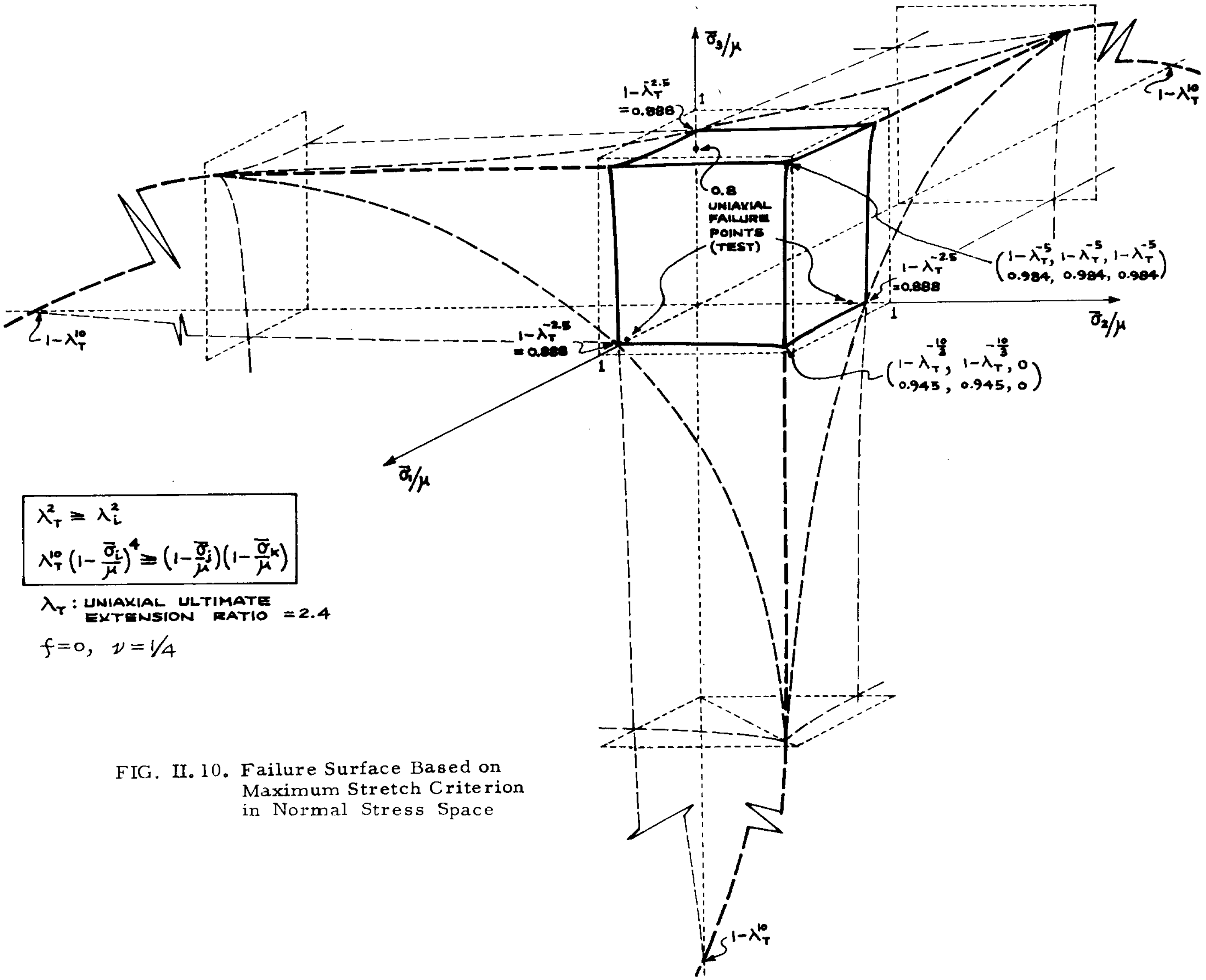

FIG. II. 10. Failure Surface Based on Maximum Stretch Criterion in Normal Stress Space

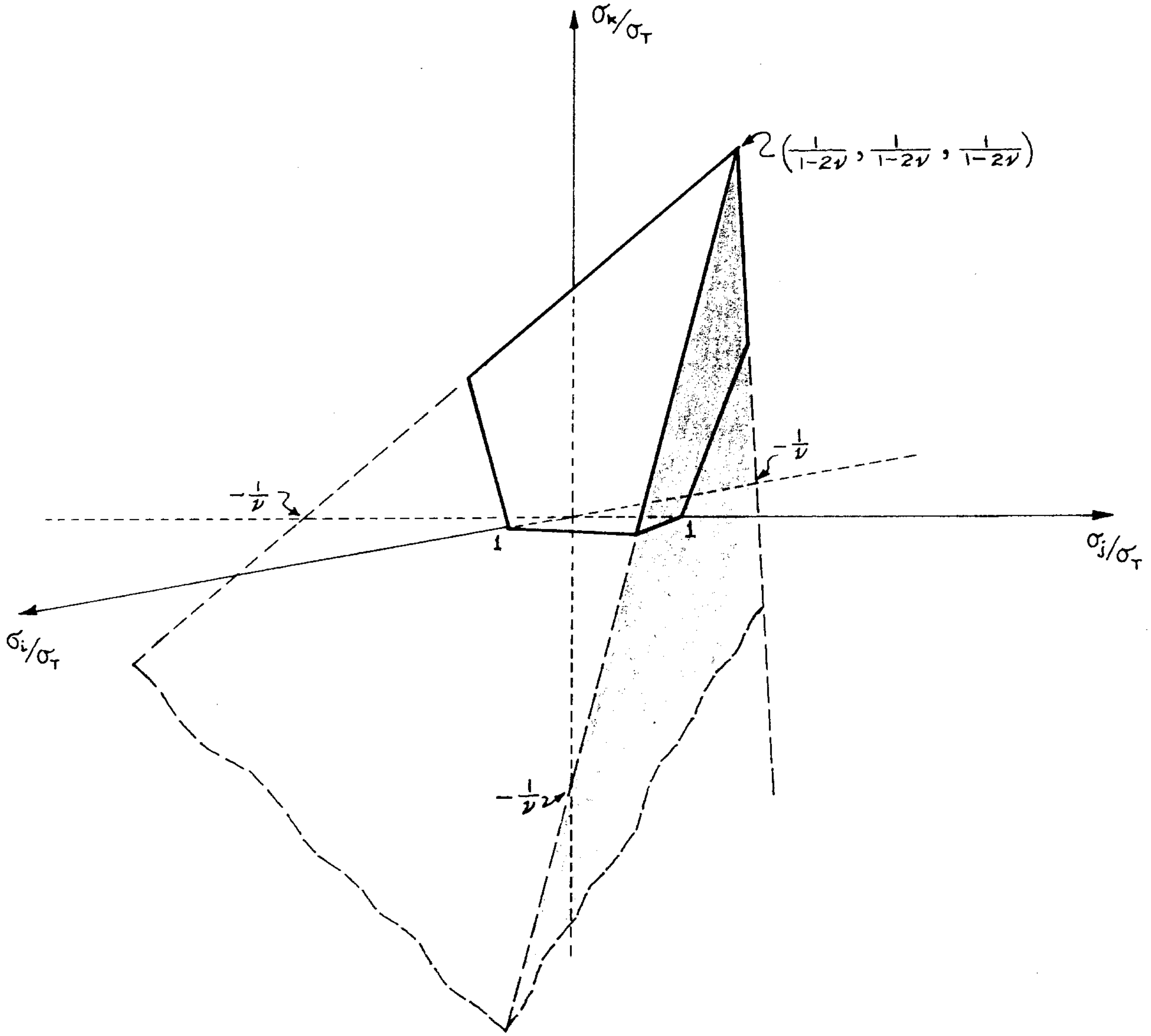

FIG. II.11. Yield Surface Based on Maximum Principal Strain (Saint Venant's Theory) in Normal Stress Space

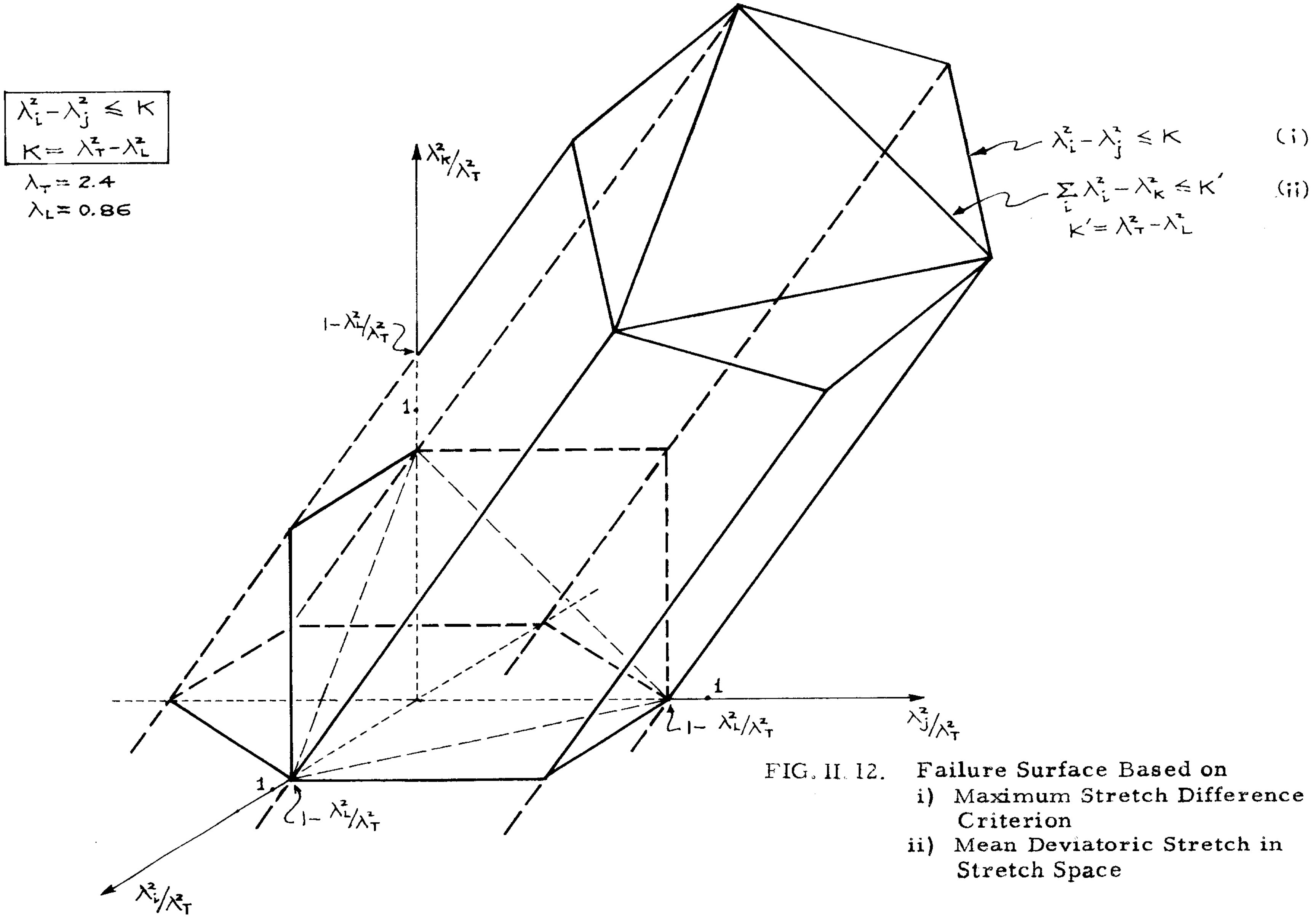

FIG. II. 12. Failure Surface Based on
i) Maximum Stretch Difference Criterion
ii) Mean Deviatoric Stretch in Stretch Space

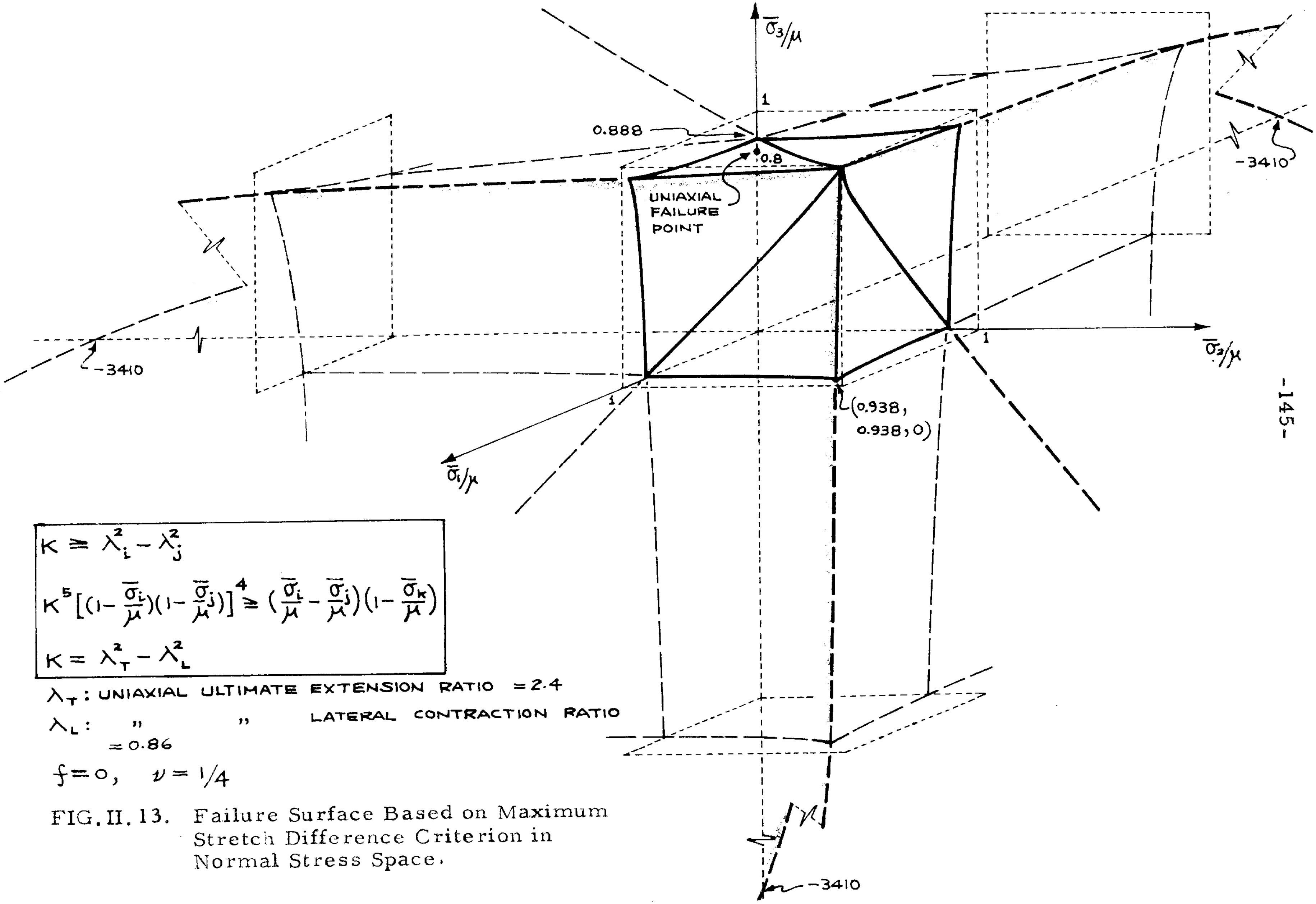

$$K \geq \lambda_i^2 - \lambda_j^2$$

$$K^5\left[\left(1-\frac{\overline{\sigma}_i}{\mu}\right)\left(1-\frac{\overline{\sigma}_j}{\mu}\right)\right]^4 \geq \left(\frac{\overline{\sigma}_i}{\mu}-\frac{\overline{\sigma}_j}{\mu}\right)\left(1-\frac{\overline{\sigma}_k}{\mu}\right)$$

$$K = \lambda_T^2 - \lambda_L^2$$

λ_T : UNIAXIAL ULTIMATE EXTENSION RATIO $= 2.4$

λ_L : " " LATERAL CONTRACTION RATIO $= 0.86$

$f = 0, \quad \nu = 1/4$

FIG. II. 13. Failure Surface Based on Maximum Stretch Difference Criterion in Normal Stress Space.

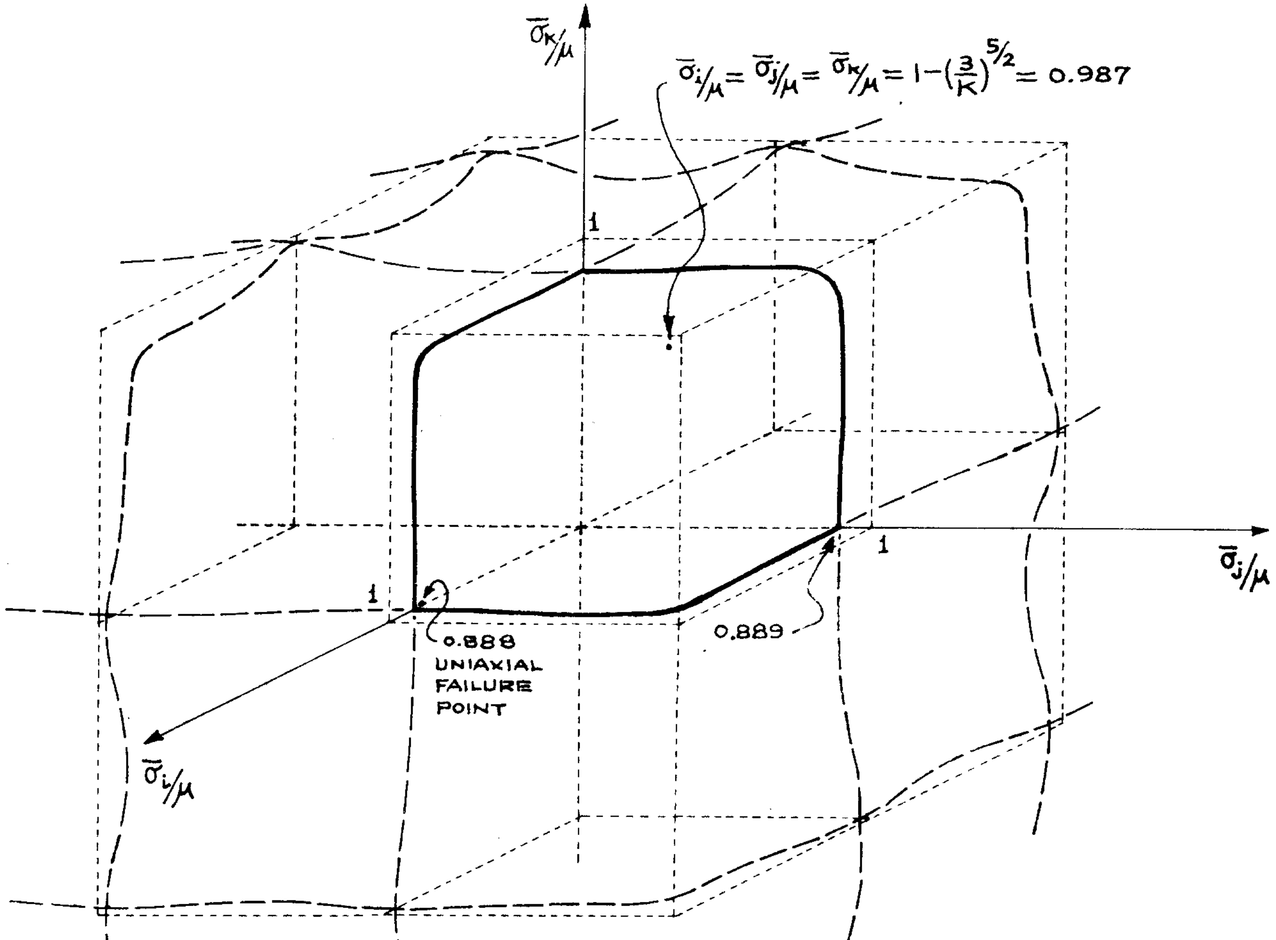

$$K \geq \sum \lambda_i^2 = I_1$$

$$K^5\left[\left(1-\frac{\bar{\sigma}_i}{\mu}\right)\left(1-\frac{\bar{\sigma}_j}{\mu}\right)\left(1-\frac{\bar{\sigma}_k}{\mu}\right)\right]^4 = \left[\left(1-\frac{\bar{\sigma}_i}{\mu}\right)\left(1-\frac{\bar{\sigma}_j}{\mu}\right) + \left(1-\frac{\bar{\sigma}_j}{\mu}\right)\left(1-\frac{\bar{\sigma}_k}{\mu}\right) + \left(1-\frac{\bar{\sigma}_k}{\mu}\right)\left(1-\frac{\bar{\sigma}_i}{\mu}\right)\right]^5$$

$$K = \lambda_T^2 + 2\lambda_L^2$$

$f = 0, \quad \nu = 1/4$

λ_T : UNIAXIAL ULTIMATE EXTENSION RATIO = 2.4
λ_L : UNIAXIAL ULTIMATE LATERAL CONTRACTION RATIO = 0.86

FIG. III. 14. Failure Surface Based on Maximum First Stretch Invariant Criterion in Normal Stress Space.

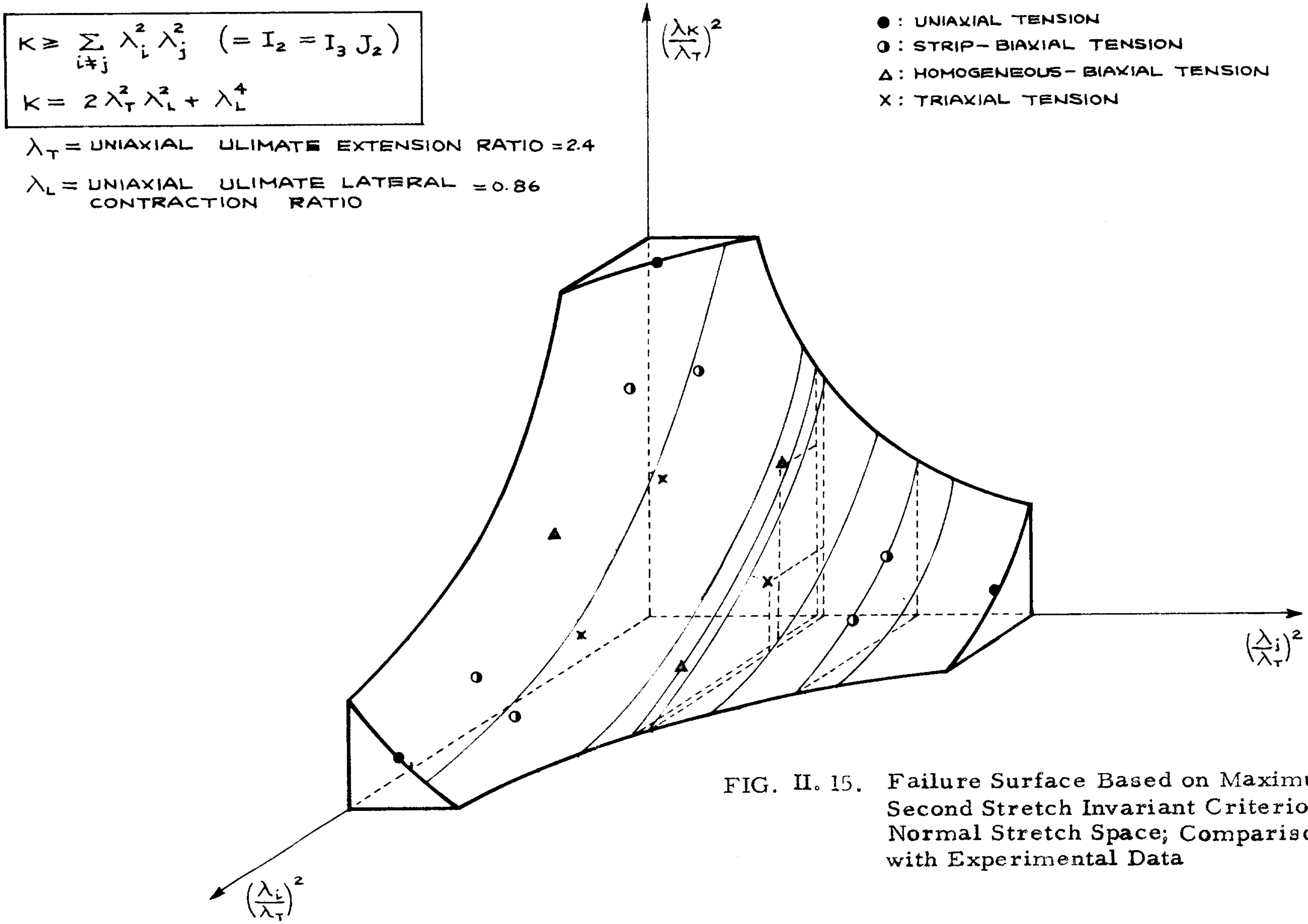

FIG. II. 15. Failure Surface Based on Maximum Second Stretch Invariant Criterion in Normal Stretch Space; Comparison with Experimental Data

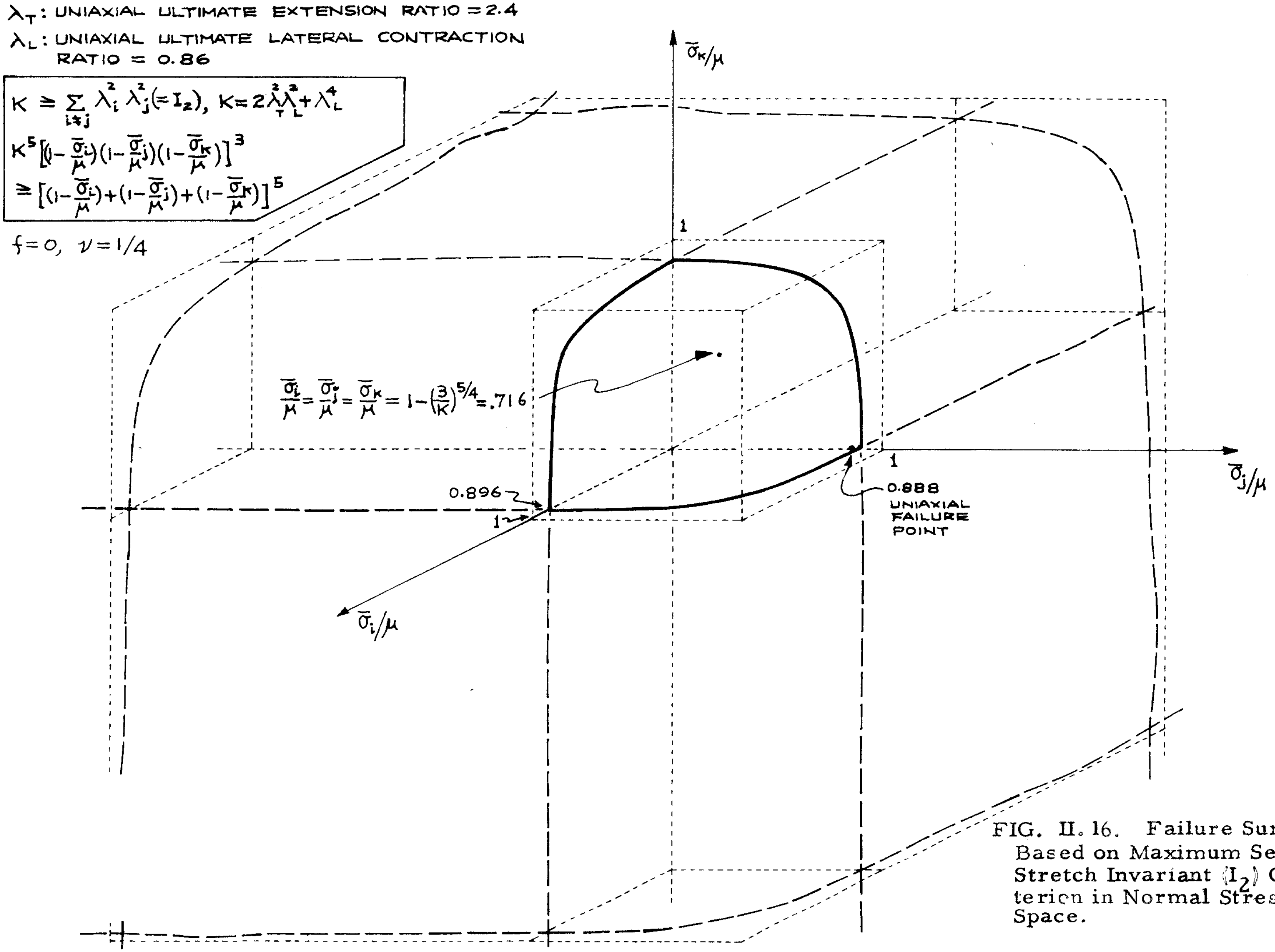

FIG. II. 16. Failure Surface Based on Maximum Second Stretch Invariant (I_2) Criterion in Normal Stress Space.

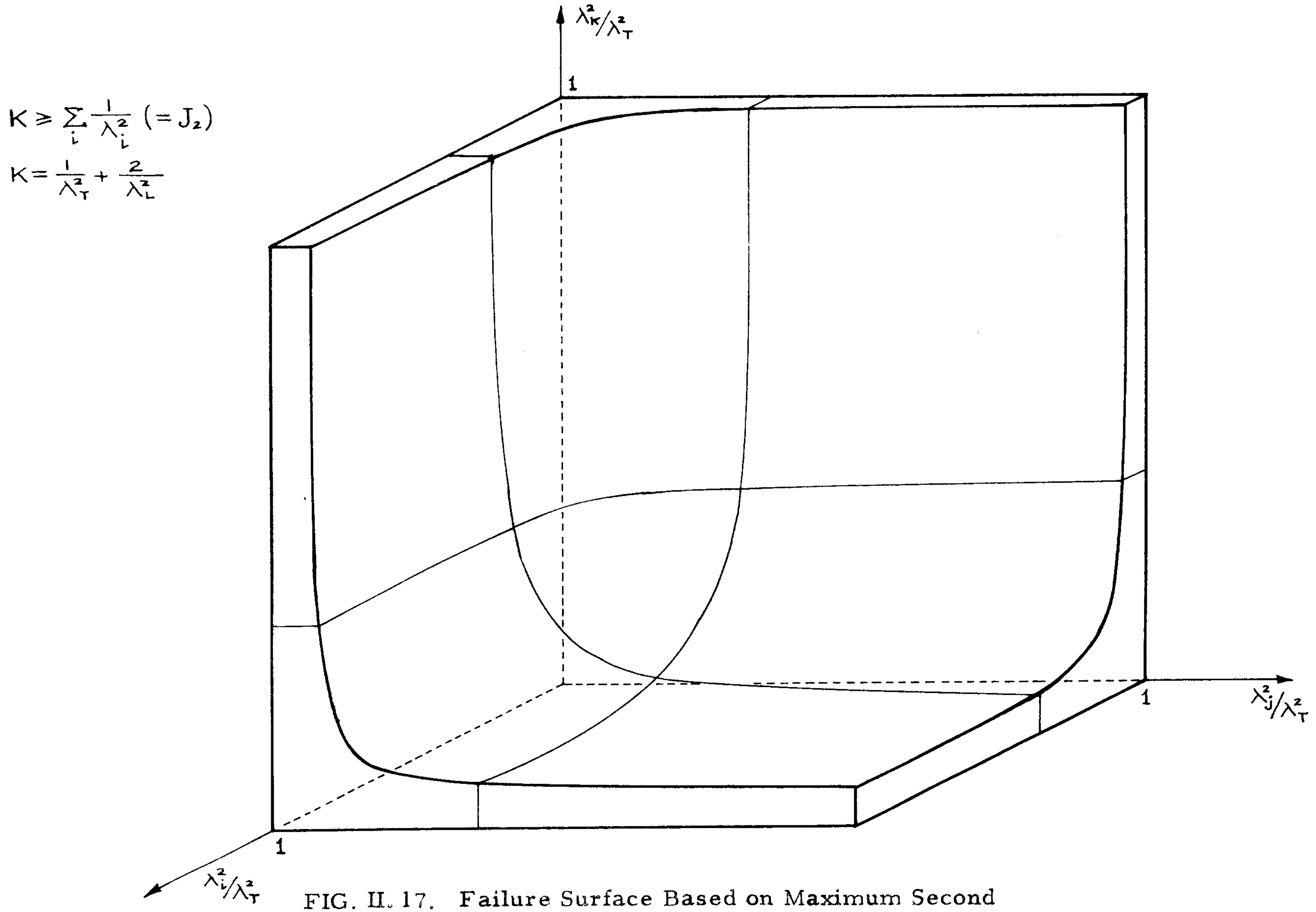

FIG. II. 17. Failure Surface Based on Maximum Second Stretch Invariant (J_2) Criterion in Normal Stretch Space

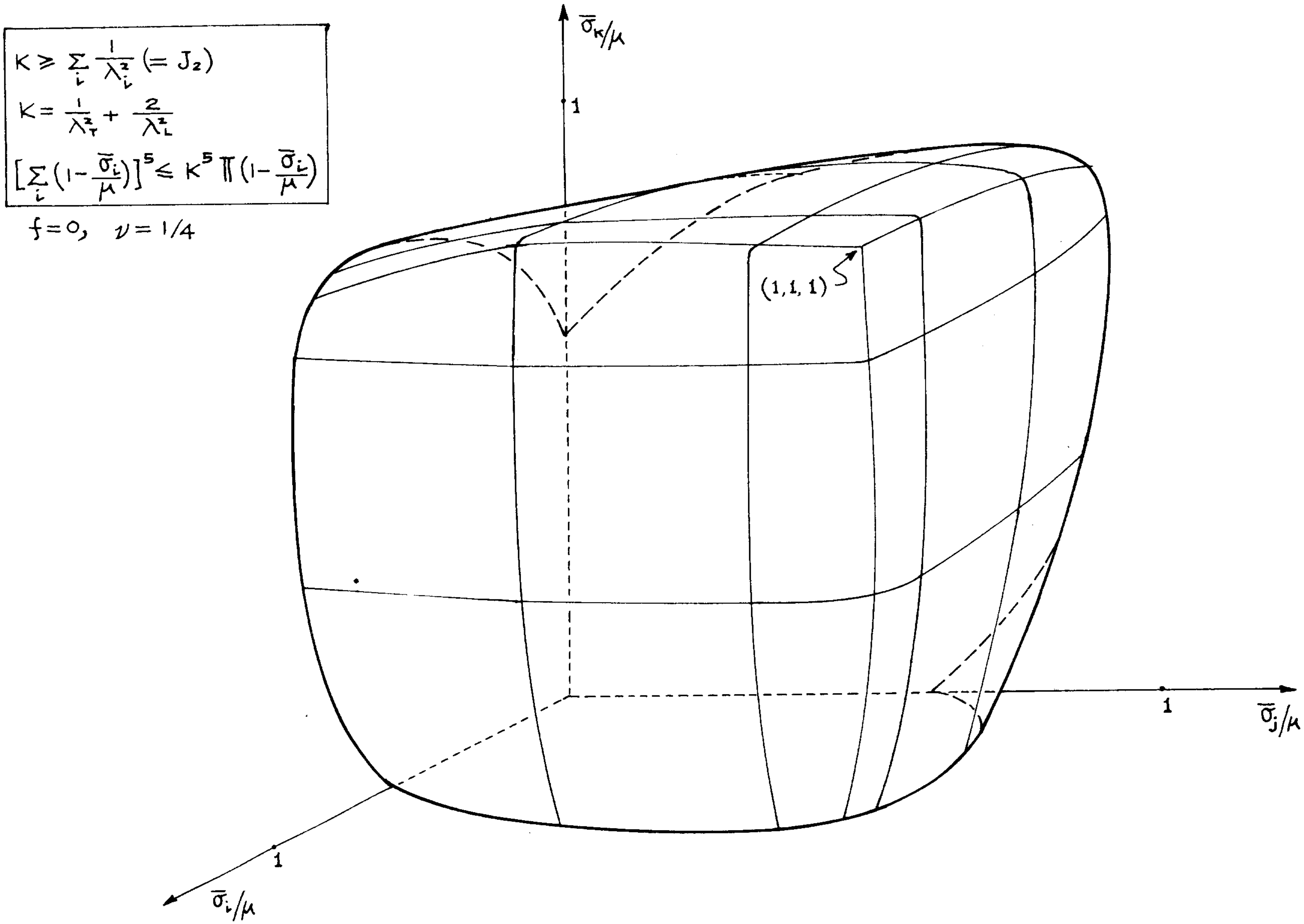

$$K \geqslant \sum_i \frac{1}{\lambda_i^2} \; (= J_2)$$

$$K = \frac{1}{\lambda_T^2} + \frac{2}{\lambda_L^2}$$

$$\left[\sum_i \left(1 - \frac{\bar{\sigma}_i}{\mu}\right)\right]^5 \leqslant K^5 \prod \left(1 - \frac{\bar{\sigma}_i}{\mu}\right)$$

$f = 0, \quad \nu = 1/4$

FIG. II. 18. Failure Surface Based on Maximum Second Stretch Invariant (J_2) Criterion in Normal Stress Space

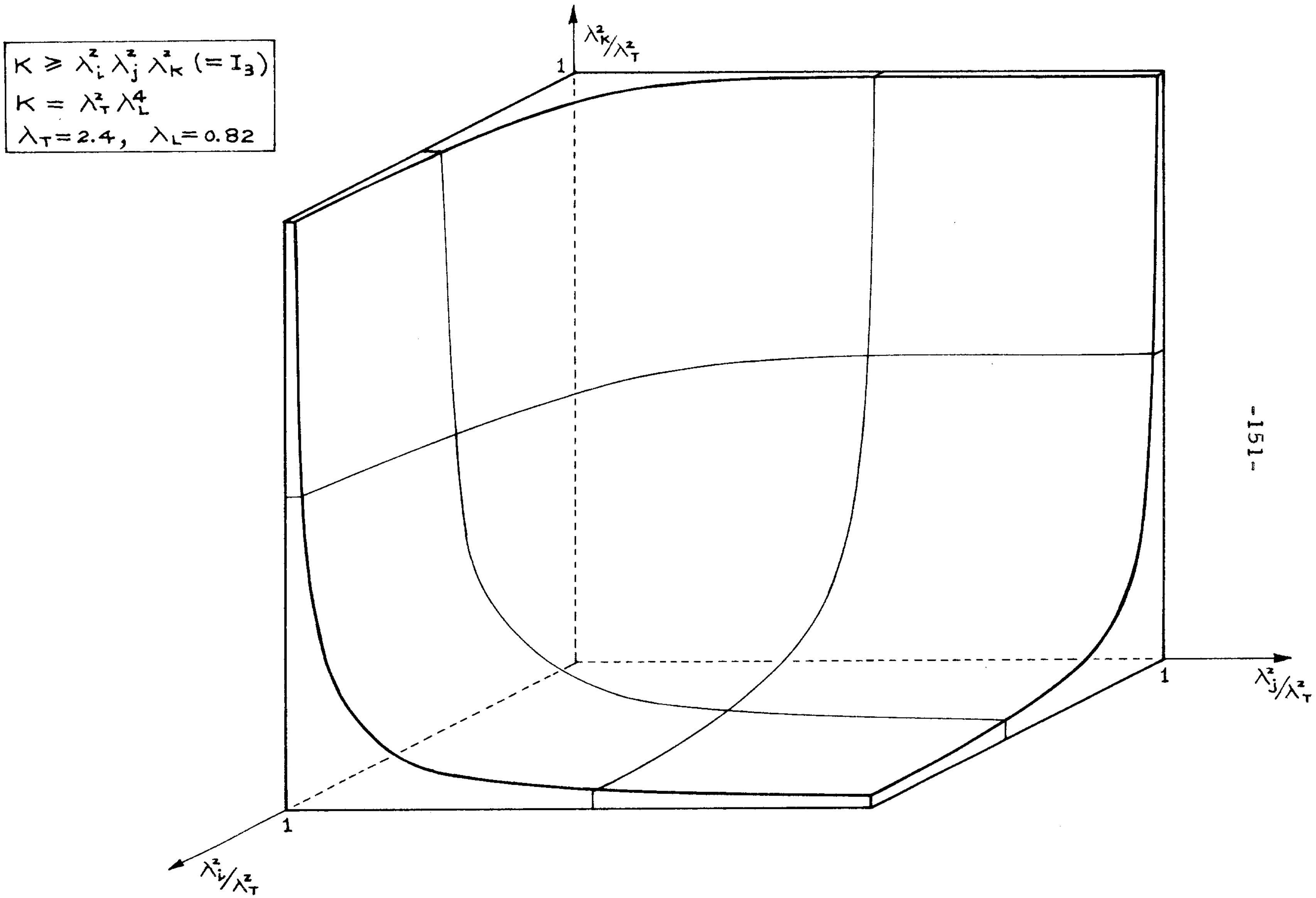

FIG. II.19. Failure Surface Based on Maximum Third Stretch Invariant Criterion in Normal Stretch Space

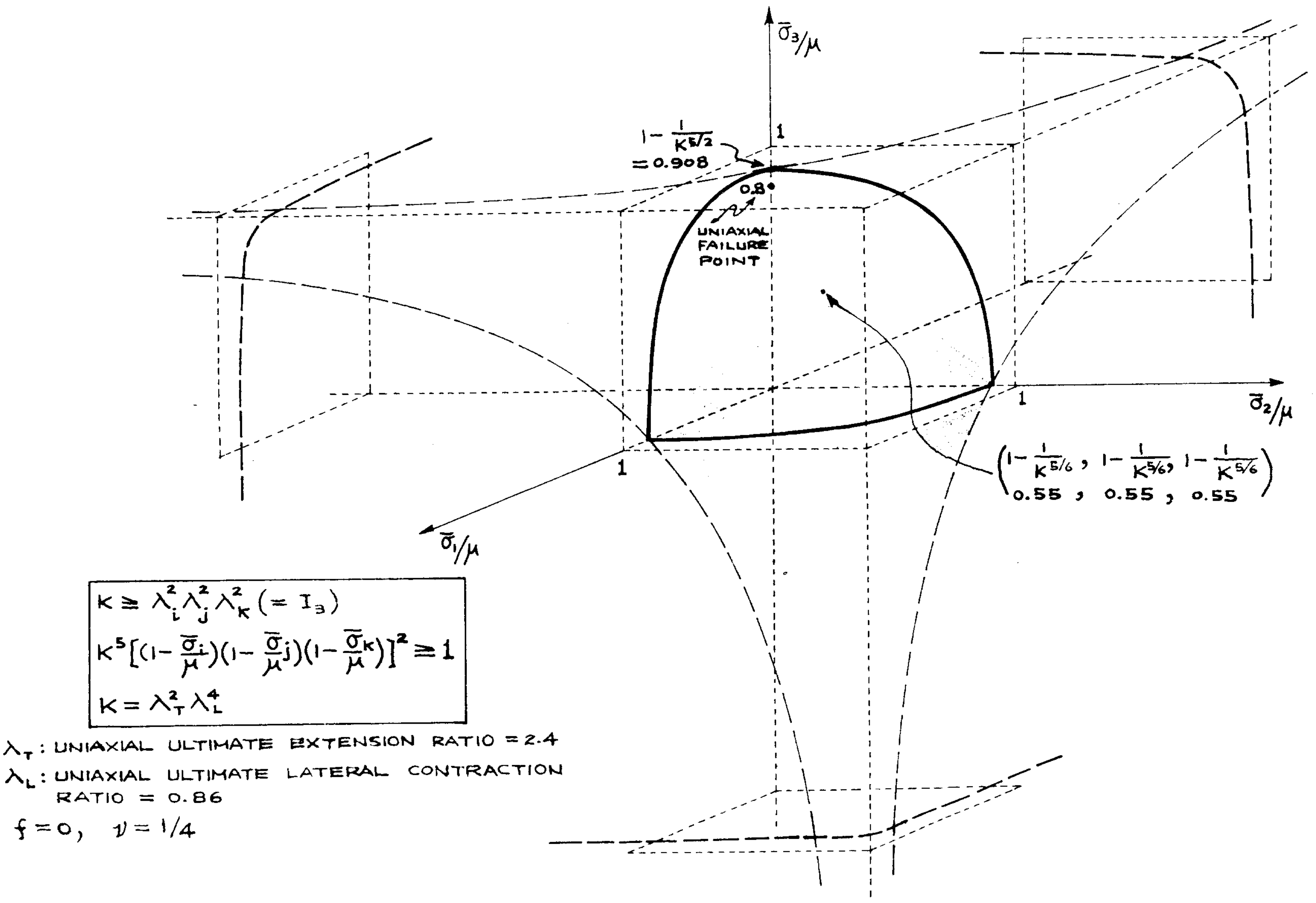

$$K \geqq \lambda_i^2 \lambda_j^2 \lambda_k^2 \ (= I_3)$$

$$K^5\left[\left(1-\frac{\bar{\sigma}_i}{\mu}\right)\left(1-\frac{\bar{\sigma}_j}{\mu}\right)\left(1-\frac{\bar{\sigma}_k}{\mu}\right)\right]^2 \geqq 1$$

$$K = \lambda_T^2 \lambda_L^4$$

λ_T : UNIAXIAL ULTIMATE EXTENSION RATIO = 2.4

λ_L : UNIAXIAL ULTIMATE LATERAL CONTRACTION RATIO = 0.86

$f = 0, \quad \nu = 1/4$

FIG. II. 20. Failure Surface Based on Maximum Third Stretch Invariant Criterion in Normal Stress Space

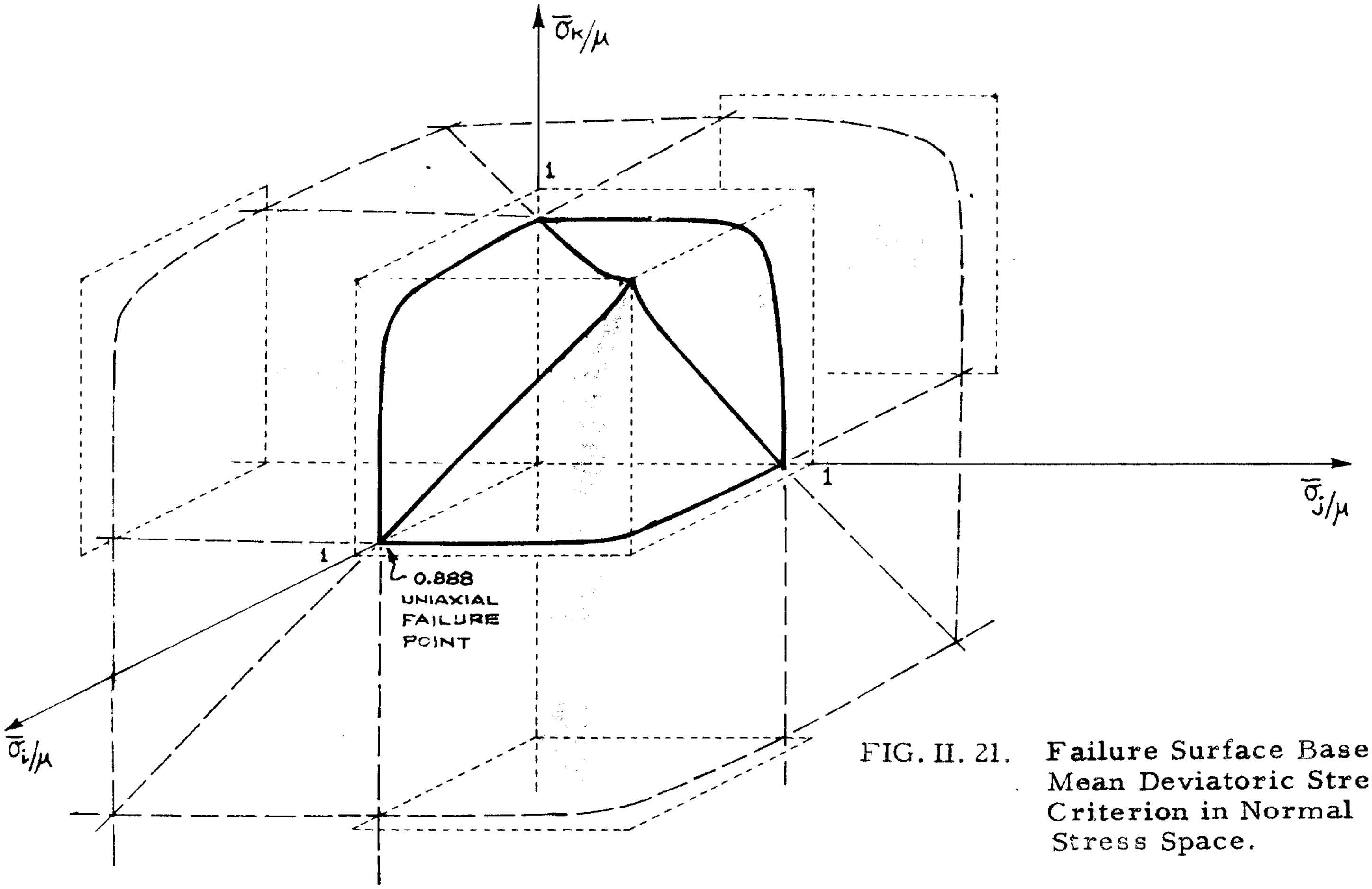

FIG. II. 21. Failure Surface Based on Mean Deviatoric Stretch Criterion in Normal Stress Space.

$$K \geq \lambda_i^2 + \lambda_j^2 - 2\lambda_K^2$$

$$K^5\left[\left(1-\frac{\bar{\sigma}_i}{\mu}\right)\left(1-\frac{\bar{\sigma}_j}{\mu}\right)\left(1-\frac{\bar{\sigma}_K}{\mu}\right)\right]^4 = \left[\left(1-\frac{\bar{\sigma}_j}{\mu}\right)\left(1-\frac{\bar{\sigma}_K}{\mu}\right)+\left(1-\frac{\bar{\sigma}_K}{\mu}\right)\left(1-\frac{\bar{\sigma}_i}{\mu}\right)-2\left(1-\frac{\bar{\sigma}_i}{\mu}\right)\left(1-\frac{\bar{\sigma}_j}{\mu}\right)\right]^5$$

$$K = \lambda_T^2 - \lambda_L^2$$

λ_T: UNIAXIAL ULTIMATE EXTENSION RATIO = 2.4

λ_L: UNIAXIAL ULTIMATE LATERAL CONTRACTION RATIO = 0.86 , $f = 0$, $\nu = 1/4$

$$W = \frac{\mu}{2}\left(J_2 + 2J_3 - 5\right)$$

$$\frac{2W}{\mu} + 5 = \frac{1}{\lambda_i^2} + \frac{1}{\lambda_j^2} + \frac{1}{\lambda_k^2} + 2\lambda_i\lambda_j\lambda_k$$

$f = 0$, $\nu = 1/4$

$W = 31$ psi., $\mu = 38$ psi.

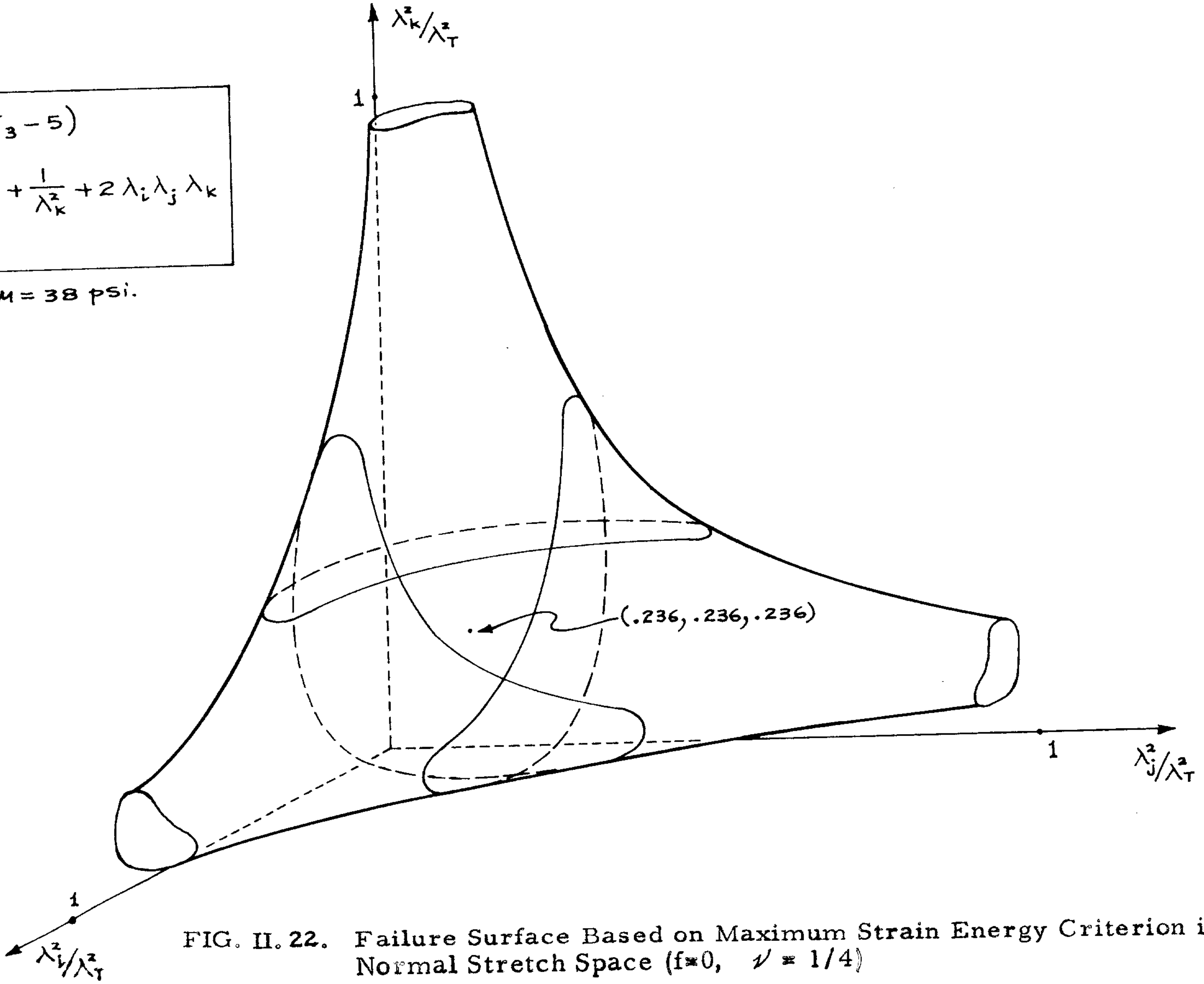

FIG. II. 22. Failure Surface Based on Maximum Strain Energy Criterion in Normal Stretch Space ($f=0$, $\nu = 1/4$)

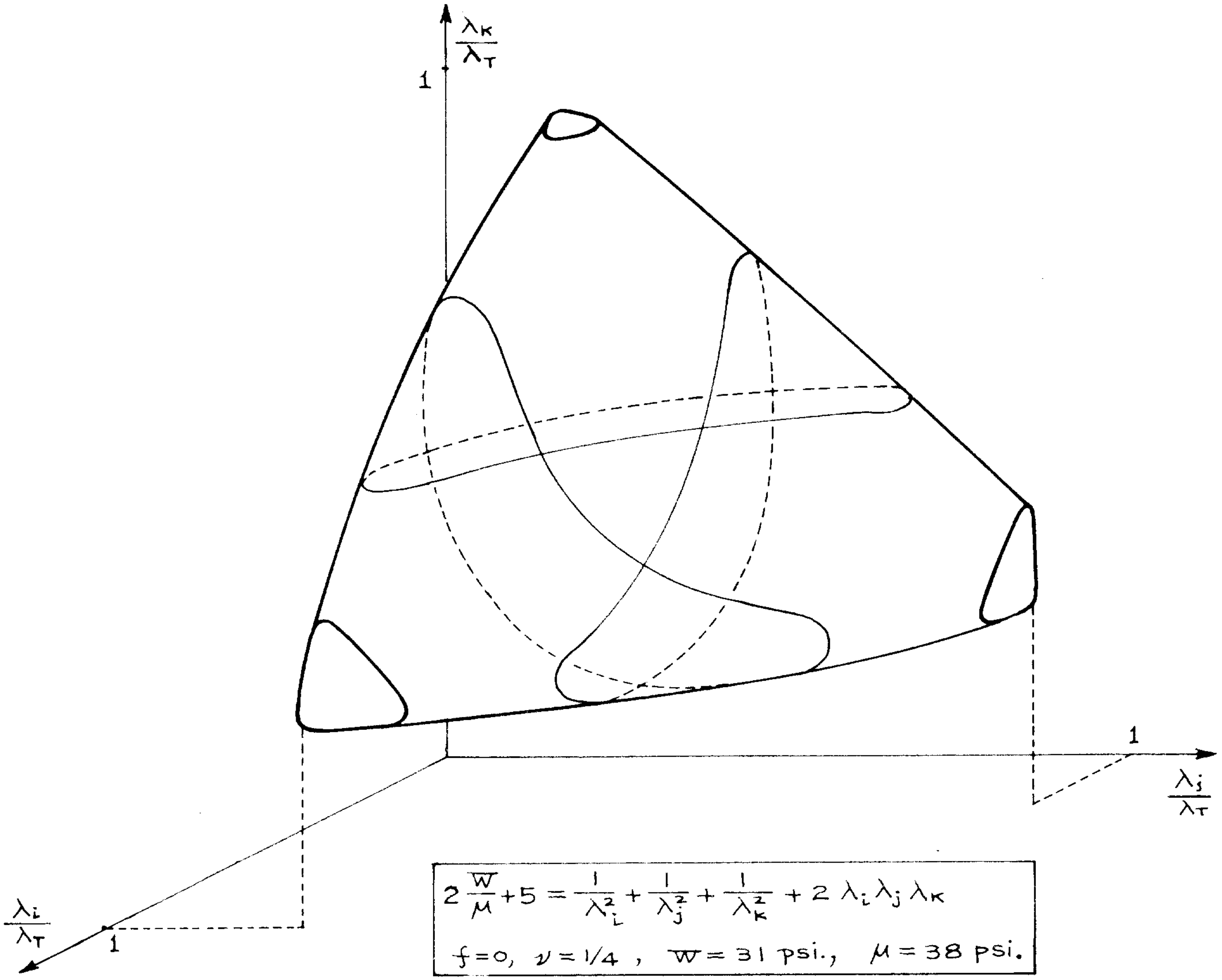

$$2\frac{\overline{W}}{\mu}+5=\frac{1}{\lambda_i^2}+\frac{1}{\lambda_j^2}+\frac{1}{\lambda_K^2}+2\lambda_i\lambda_j\lambda_K$$

$f=0$, $\nu=1/4$, $\overline{W}=31$ psi., $\mu=38$ psi.

FIG. II. 23. Failure Surface Based on Maximum Strain Energy Criterion in Principal Stretch Space (f=0, ν = 1/4).

$$\overline{W} = \frac{\mu}{2}\left(J_2 + 2J_3 - 5\right)$$

$$K^5 \prod \left(1 - \frac{\overline{\sigma}_i}{\mu}\right) \geq \left[\sum_i \left(1 - \frac{\overline{\sigma}_i}{\mu}\right) + 2\right]^5$$

$$K = \frac{2\overline{W}}{\mu} + 5$$

$\overline{W}_{uni} = 31$ psi.

$\mu = 38$ psi.

$f = 0$

$\nu = 1/4$

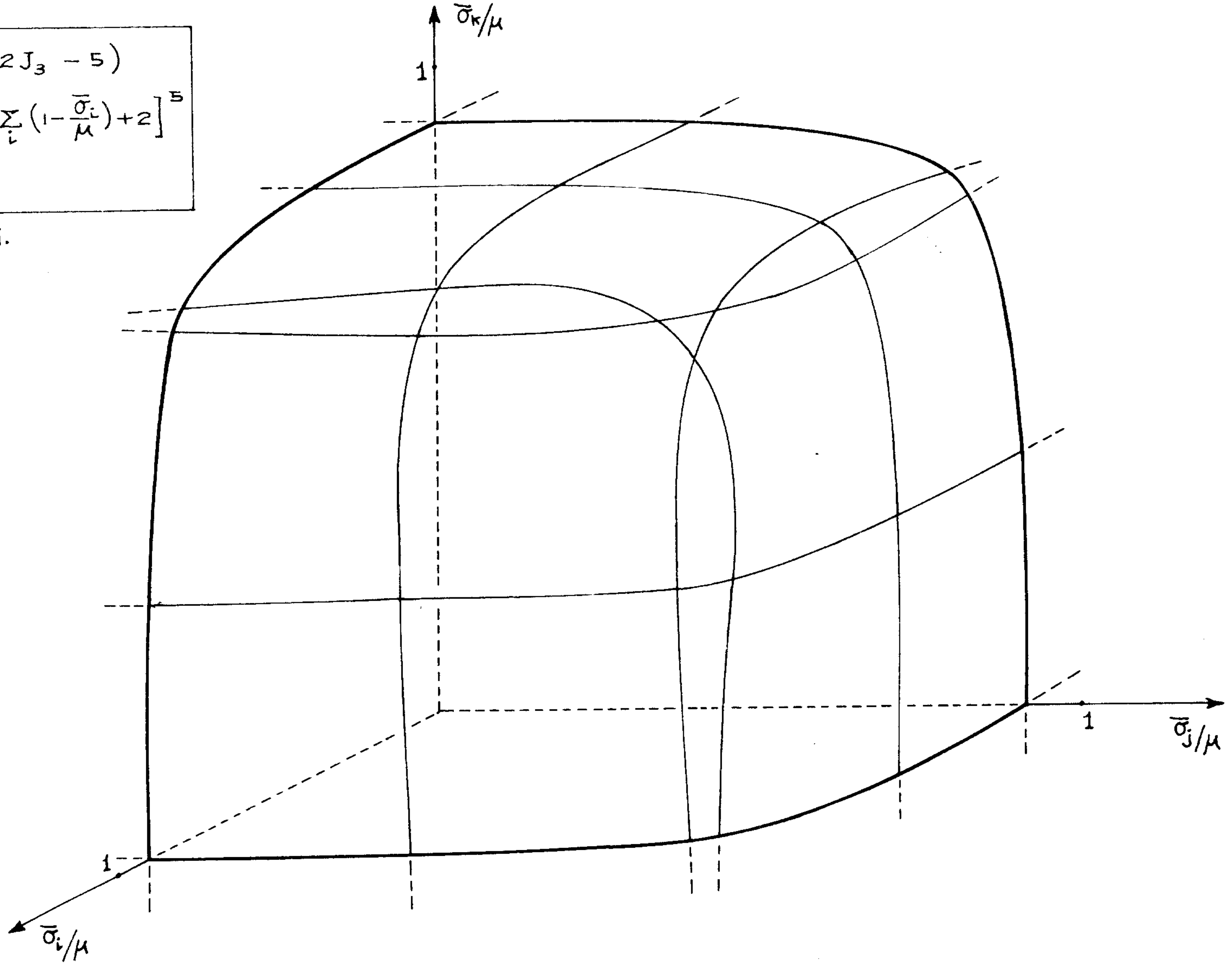

FIG. II. 24. Failure Surface Based on Maximum Strain Energy in Normal Stress Space ($f = 0$, $\nu = 1/4$)

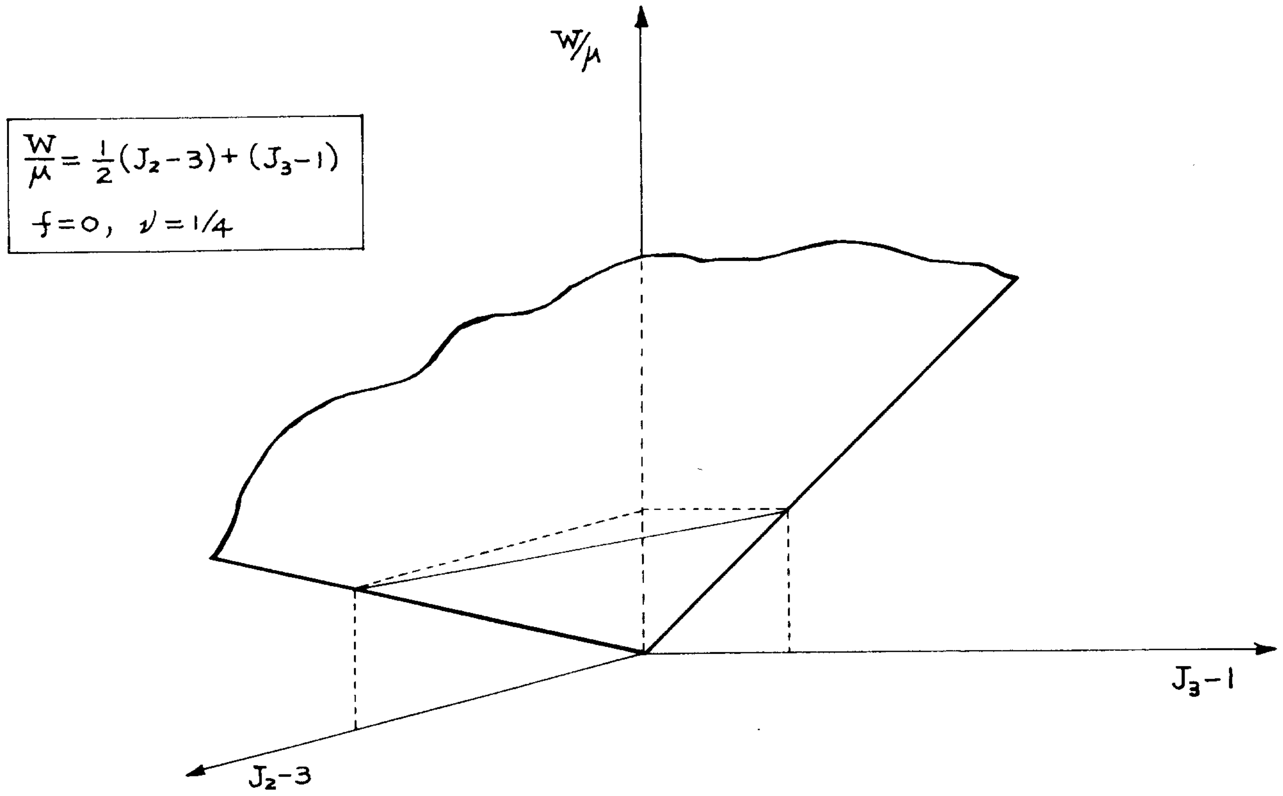

FIG. II. 25. Failure Surface Based on Maximum Strain Energy Criterion in Invariant Space.

$$\overline{W} = \frac{\mu}{2}(I_1 - 3) \; , \quad f = 1, \; \nu = 1/2$$

$$\frac{2\overline{W}}{\mu} + 3 = \lambda_i^2 + \lambda_j^2 + \lambda_k^2$$

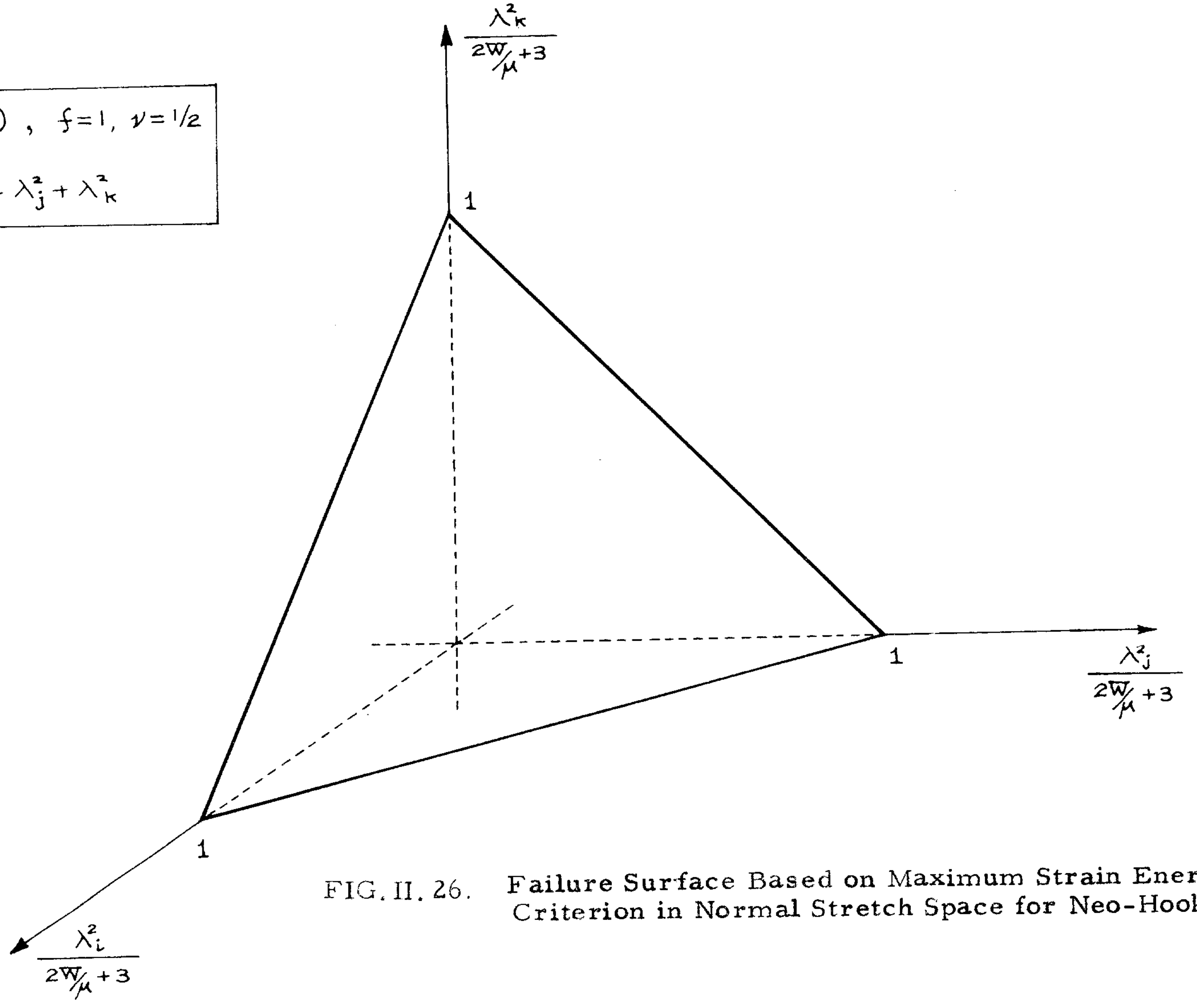

FIG. II. 26. Failure Surface Based on Maximum Strain Energy Criterion in Normal Stretch Space for Neo-Hookean Solid.

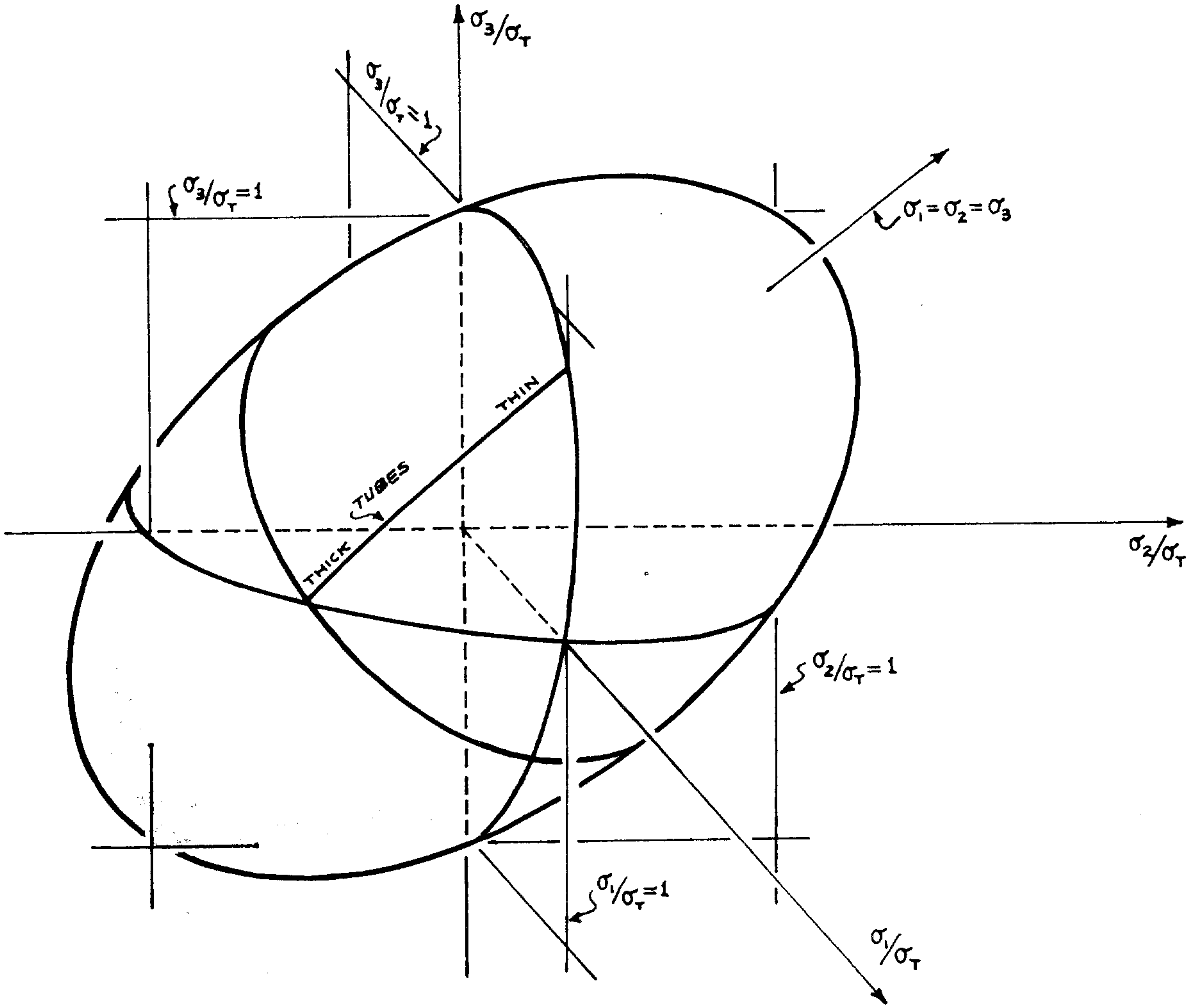

$$2EW = (\sigma_1^2 + \sigma_2^2 + \sigma_3^2) - 2\nu(\sigma_1\sigma_2 + \sigma_2\sigma_3 + \sigma_3\sigma_1) = \sum_i \sigma_i^2 - 2\nu \sum_{j\neq k} \sigma_j \sigma_k$$

$\sigma_T =$ Uniaxial Yield Stress

FIG. II. 27. The Ellipsoidal Yield Surface in Normal Stress Space Based on Haigh's Maximum Strain-Energy Theory.

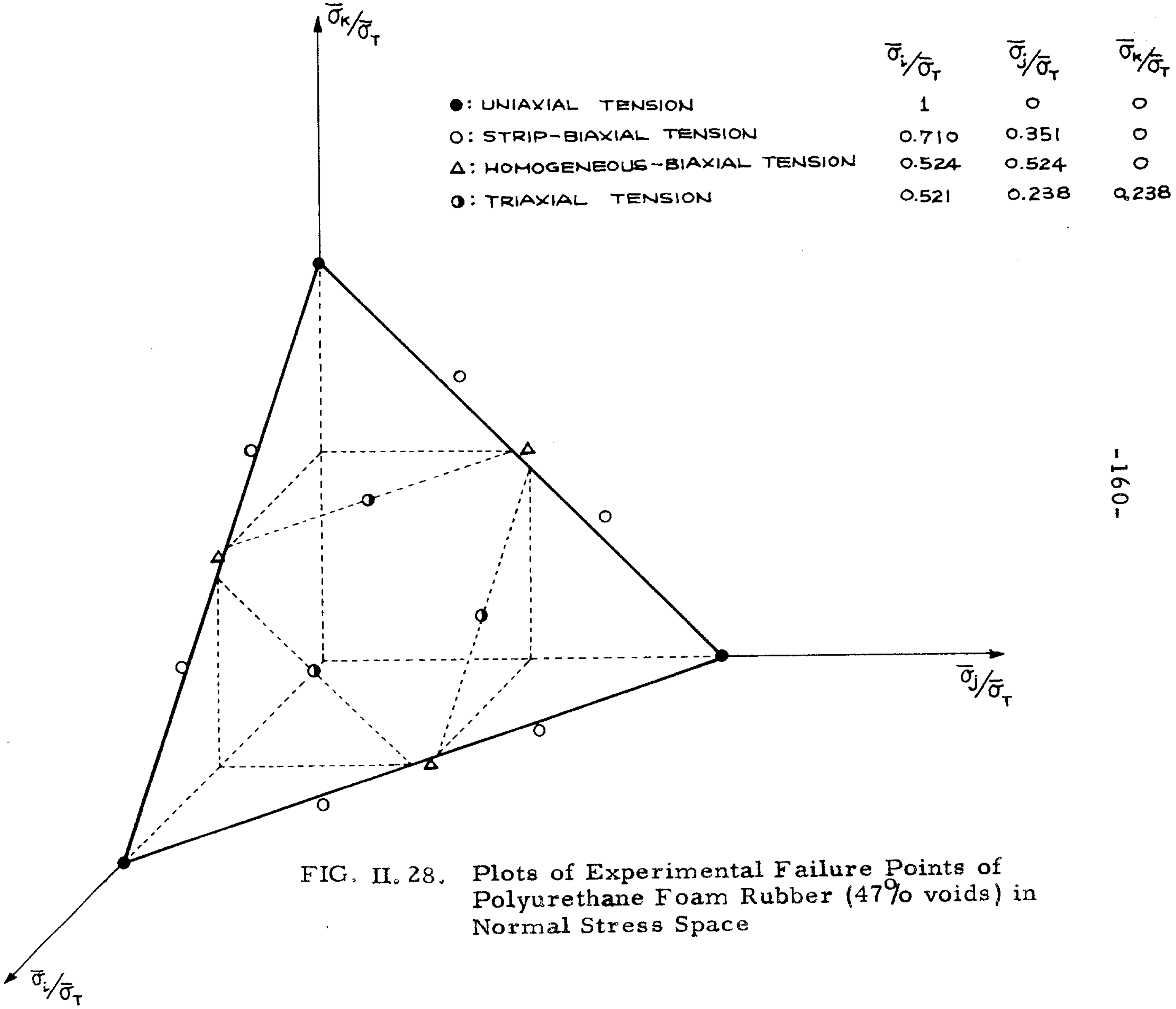

	$\bar{\sigma}_i/\bar{\sigma}_T$	$\bar{\sigma}_j/\bar{\sigma}_T$	$\bar{\sigma}_K/\bar{\sigma}_T$
●: UNIAXIAL TENSION	1	0	0
○: STRIP-BIAXIAL TENSION	0.710	0.351	0
△: HOMOGENEOUS-BIAXIAL TENSION	0.524	0.524	0
◐: TRIAXIAL TENSION	0.521	0.238	0.238

FIG. II. 28. Plots of Experimental Failure Points of Polyurethane Foam Rubber (47% voids) in Normal Stress Space

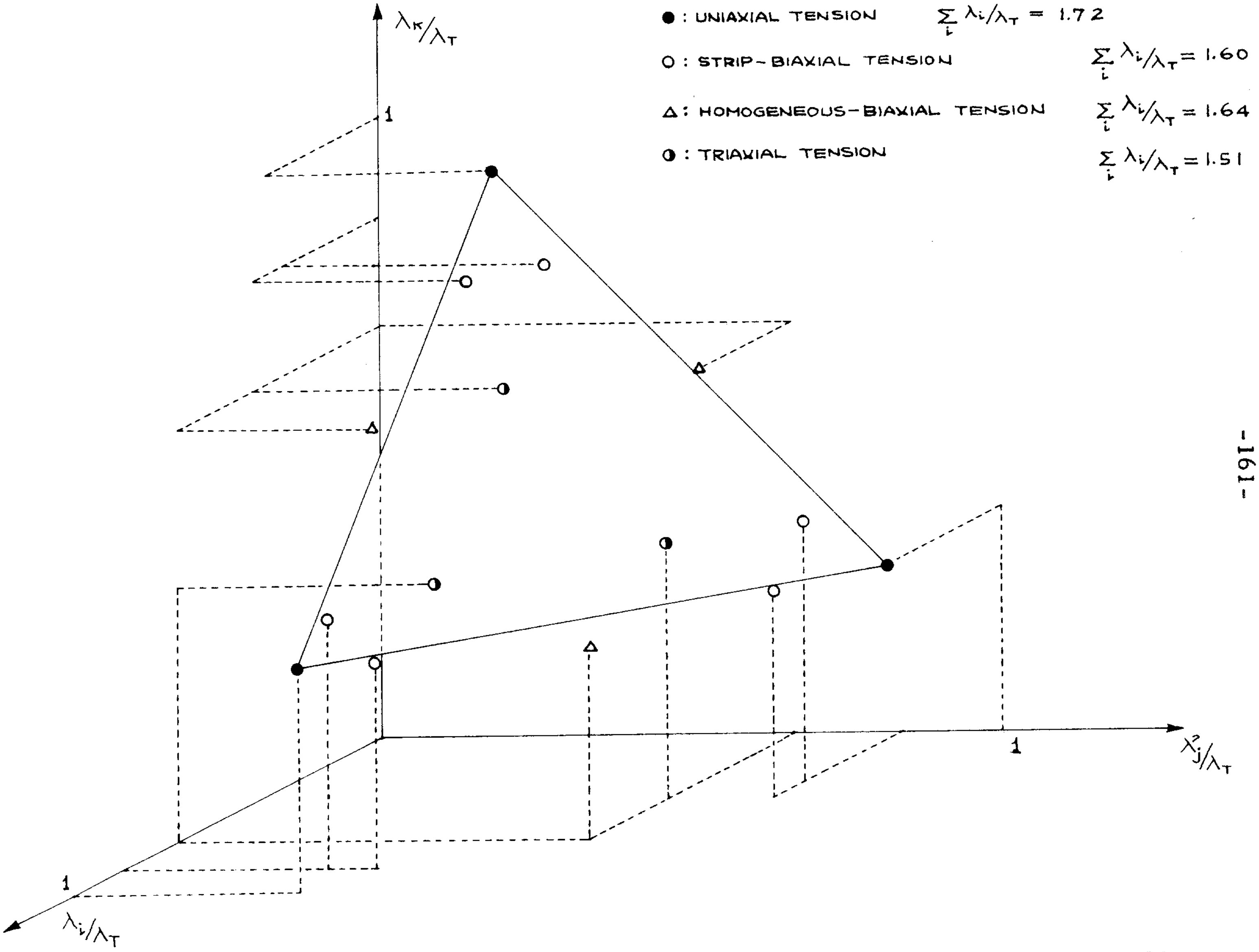

FIG. II. 29. **Plots of Experimental Failure Points of Polyurethane Foam Rubber (47% voids) in Normal Stretch Space**

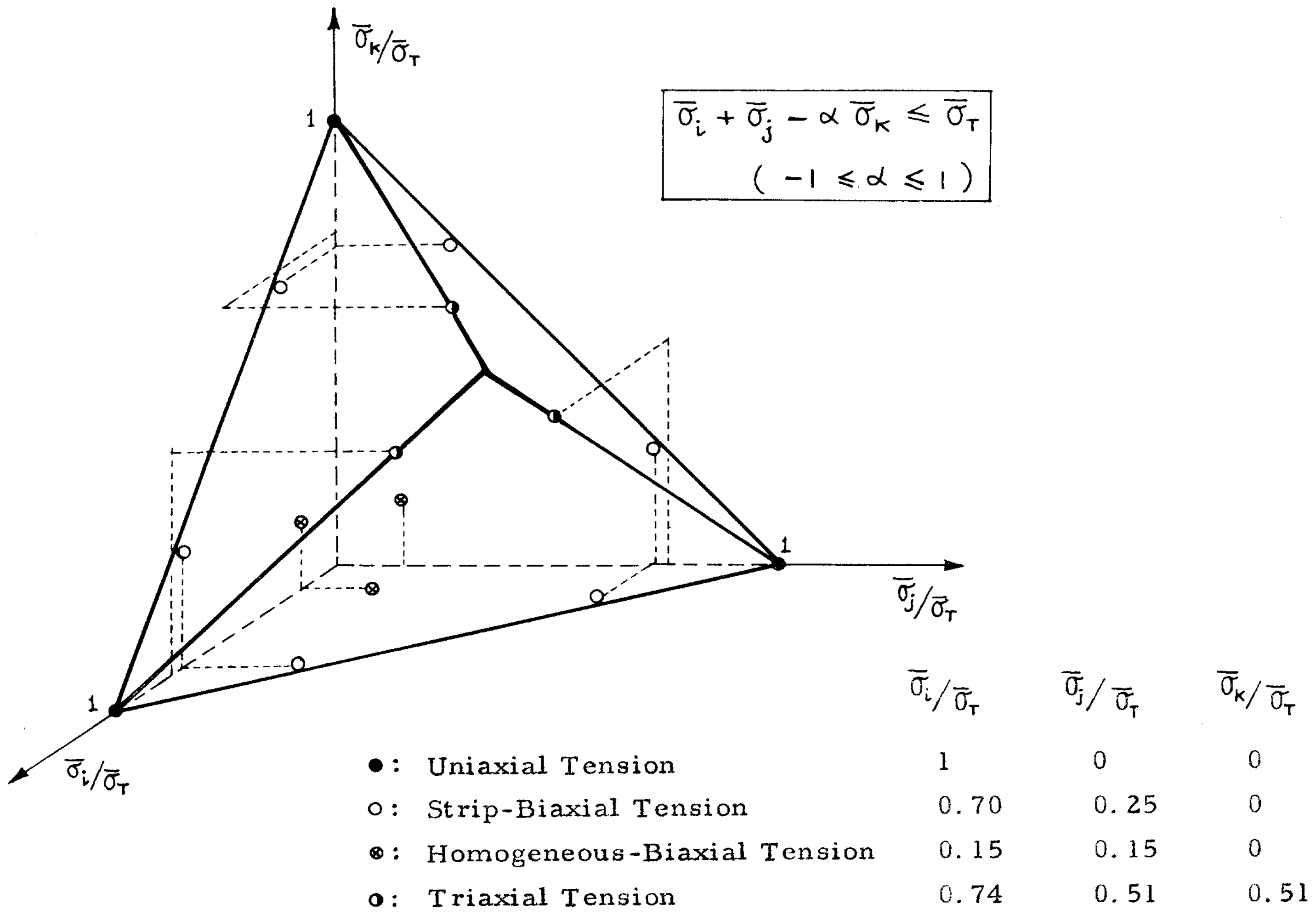

	$\bar{\sigma}_i/\bar{\sigma}_T$	$\bar{\sigma}_j/\bar{\sigma}_T$	$\bar{\sigma}_K/\bar{\sigma}_T$
●: Uniaxial Tension	1	0	0
○: Strip-Biaxial Tension	0.70	0.25	0
⊗: Homogeneous-Biaxial Tension	0.15	0.15	0
◐: Triaxial Tension	0.74	0.51	0.51

FIG. II. 30. Plots of Experimental Failure Points in Principal True Stress Space (Polyurethane Rubber).

		λ_i/λ_T	λ_j/λ_T	λ_K/λ_T
●:	Uniaxial Tension	1	0.427	0.427
○:	Strip-Biaxial Tension	0.822	0.593	0.428
⊗:	Homogeneous-Biaxial Tension	0.643	0.643	0.242
◑:	Triaxial Tension	0.600	0.593	0.593

$$\boxed{\sum_i \lambda_i = \text{CONST.}}$$

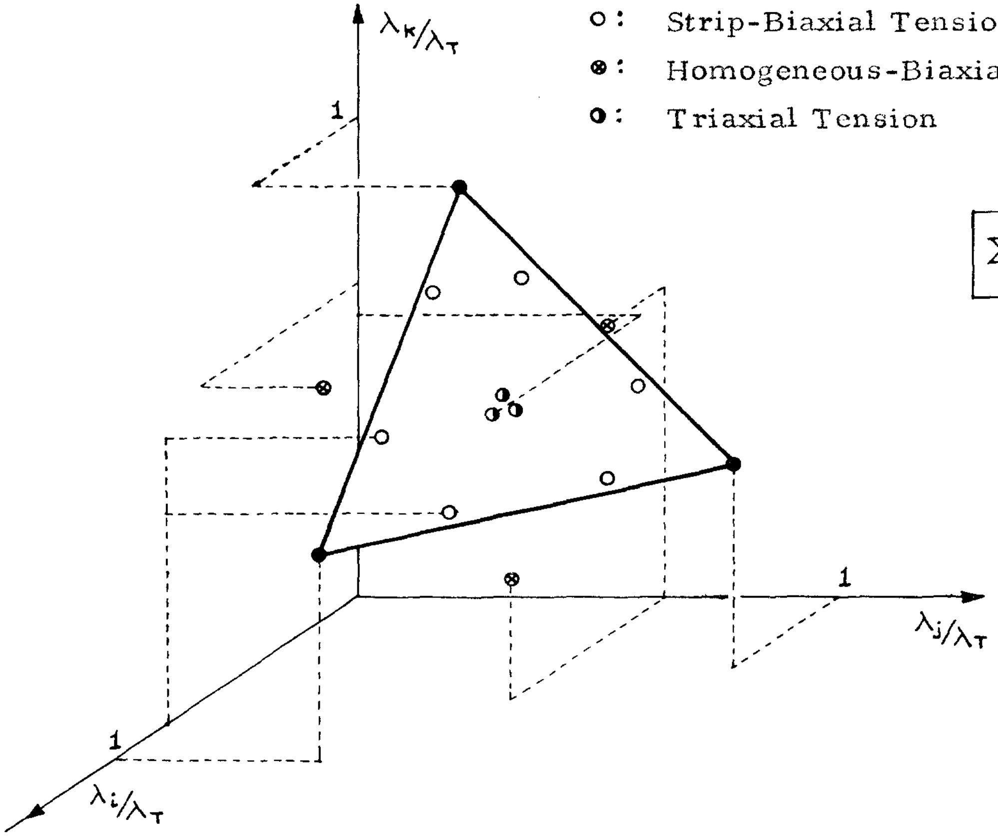

FIG. II. 31. Plots of Experimental Failure Points in Principal Stretch Space (Polyurethane Rubber).

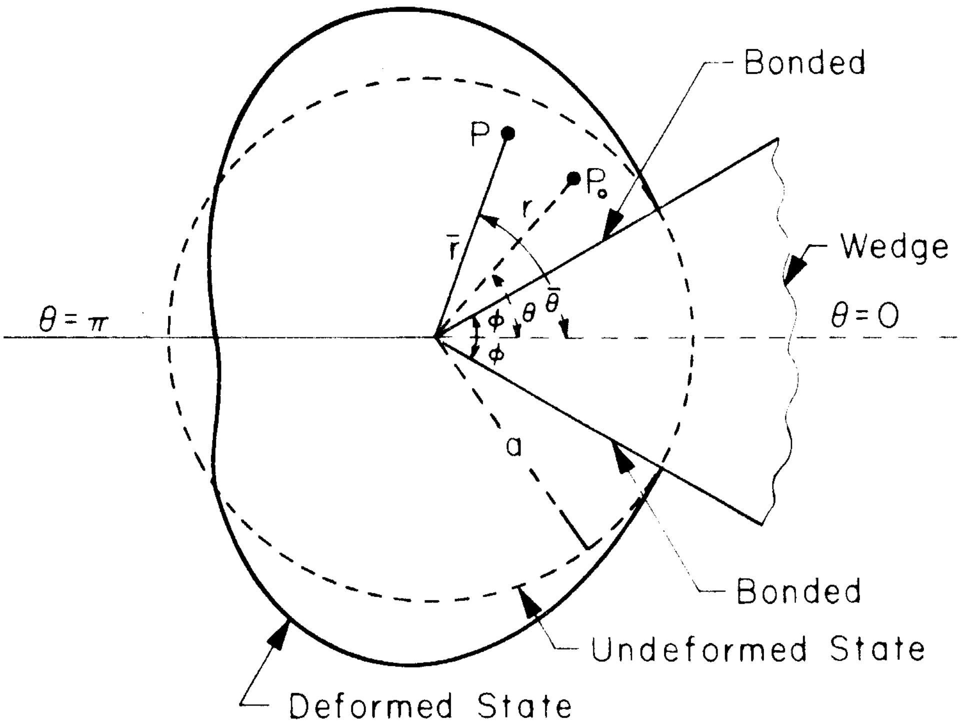

FIG. III. 1. Schematic Drawing of an Infinitely Long Rubber Log Spread Lengthwise by a Bonded Wedge.

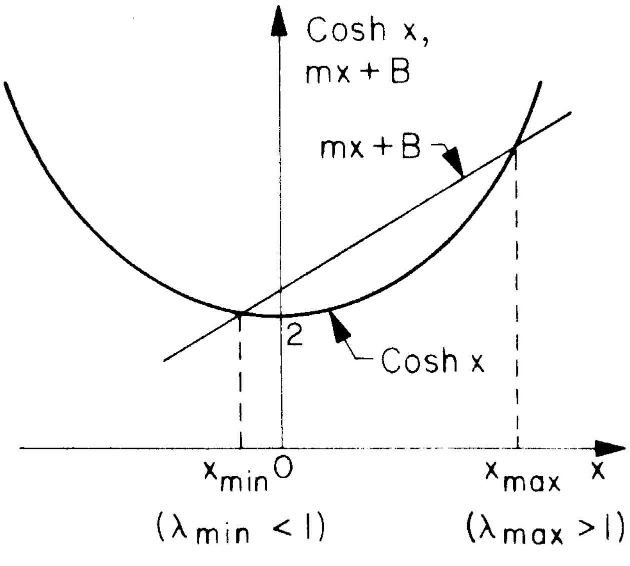

FIG. III. 2. Plots of Extreme Condition, $mX_{\alpha,\pi} + B - \cos hX_{\alpha,\pi} = 0$.

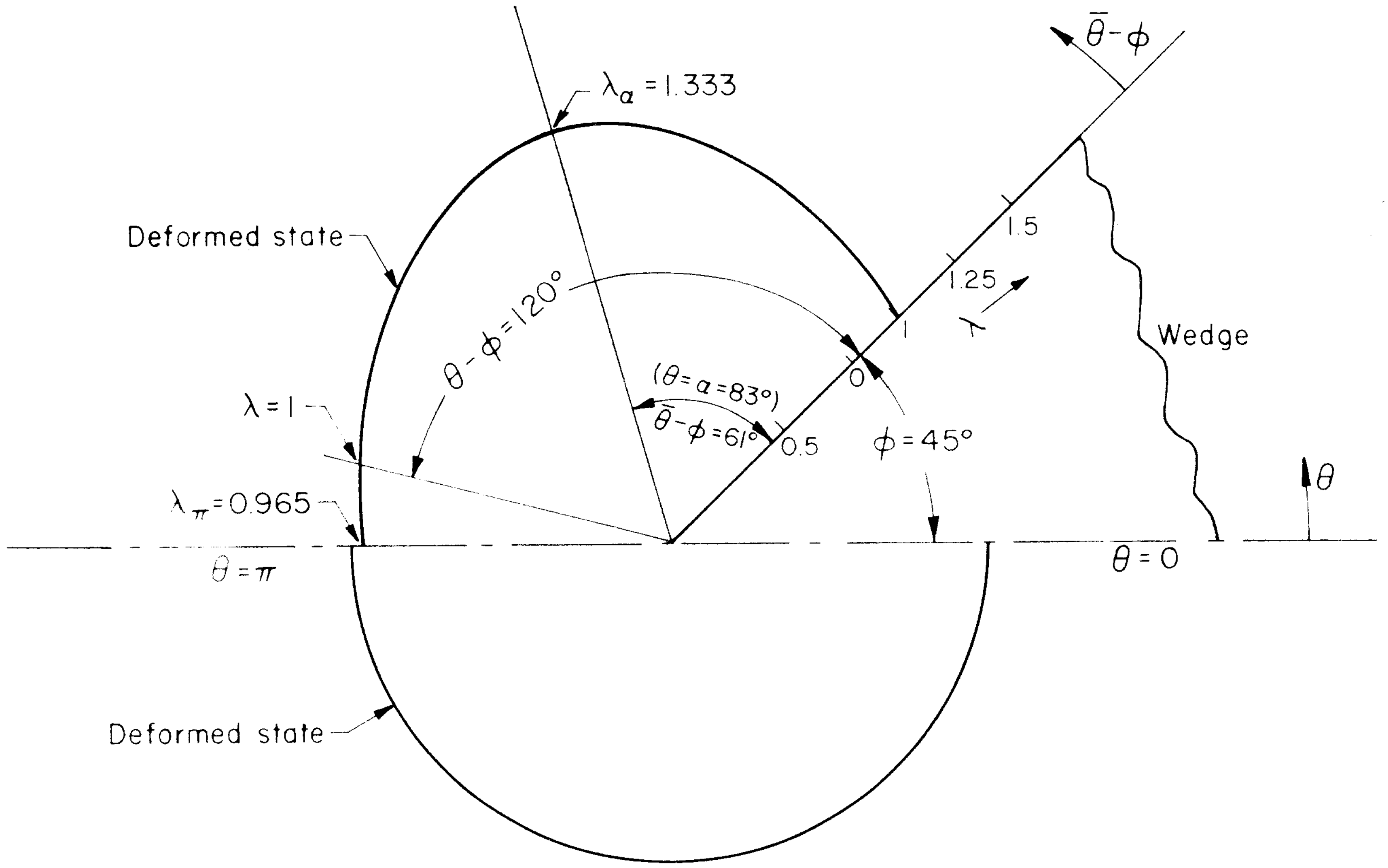

FIG. III. 3. Deformation of an Infinitely Long Rubber Log Spread Lengthwise by a Bonded Wedge (Flank Angle, $2\phi = 90°$).

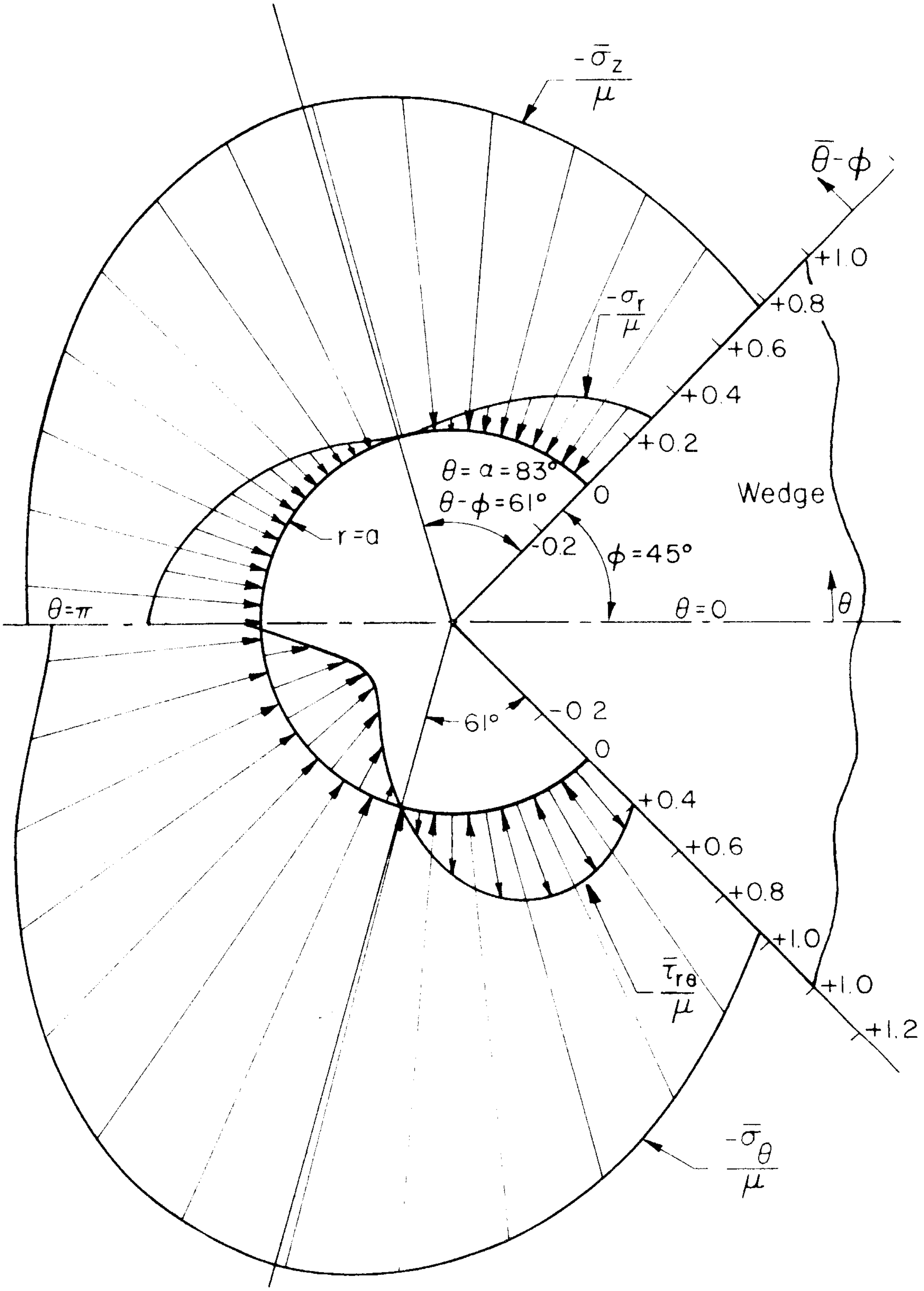

FIG. III. 4. Surface Tractions Required for the Specified Deformation Field (Flank Angle, $2\phi = 90^{\circ}$).

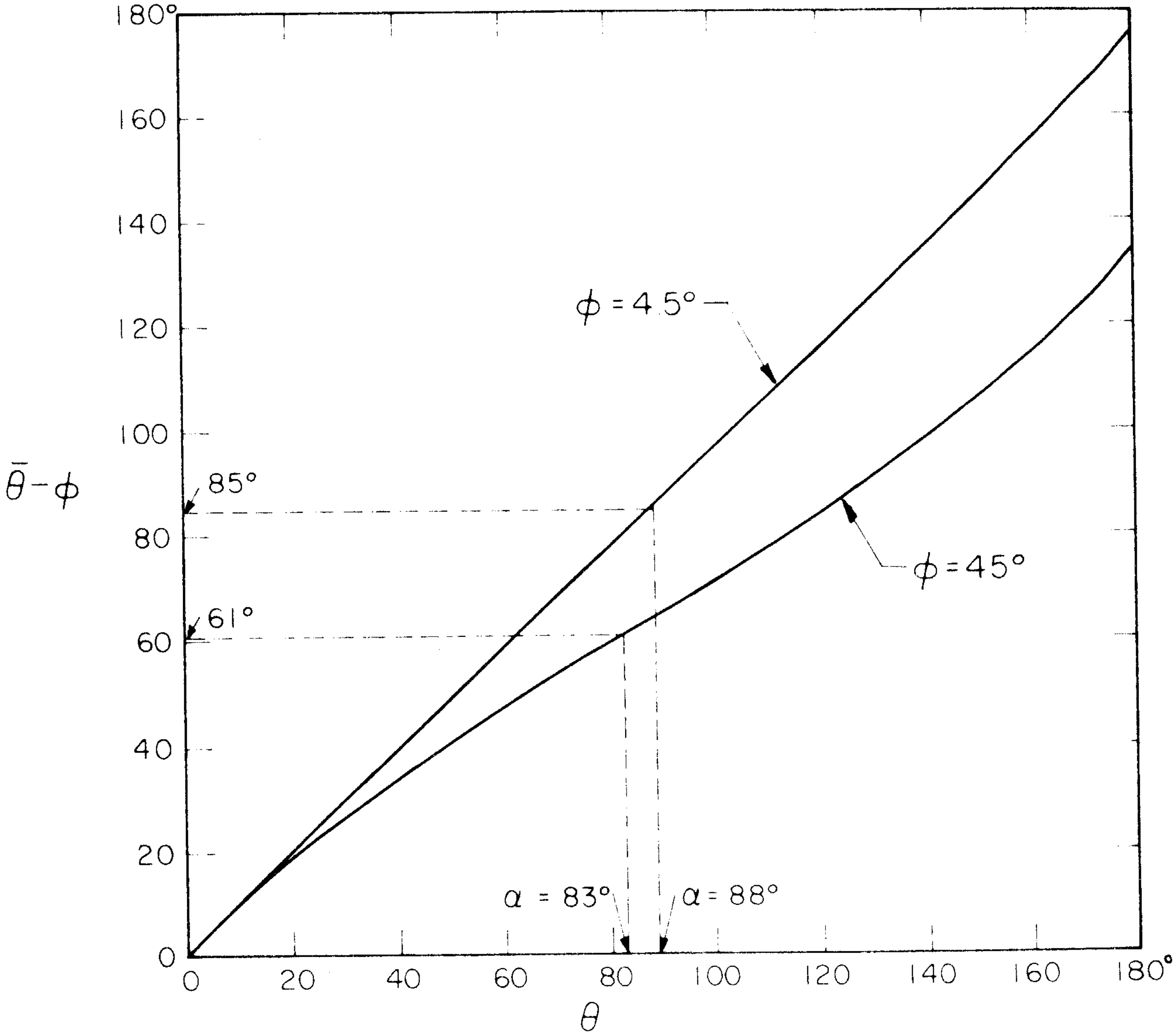

FIG. III. 5. Relations Between Undeformed and Deformed Tangential Coordinates.

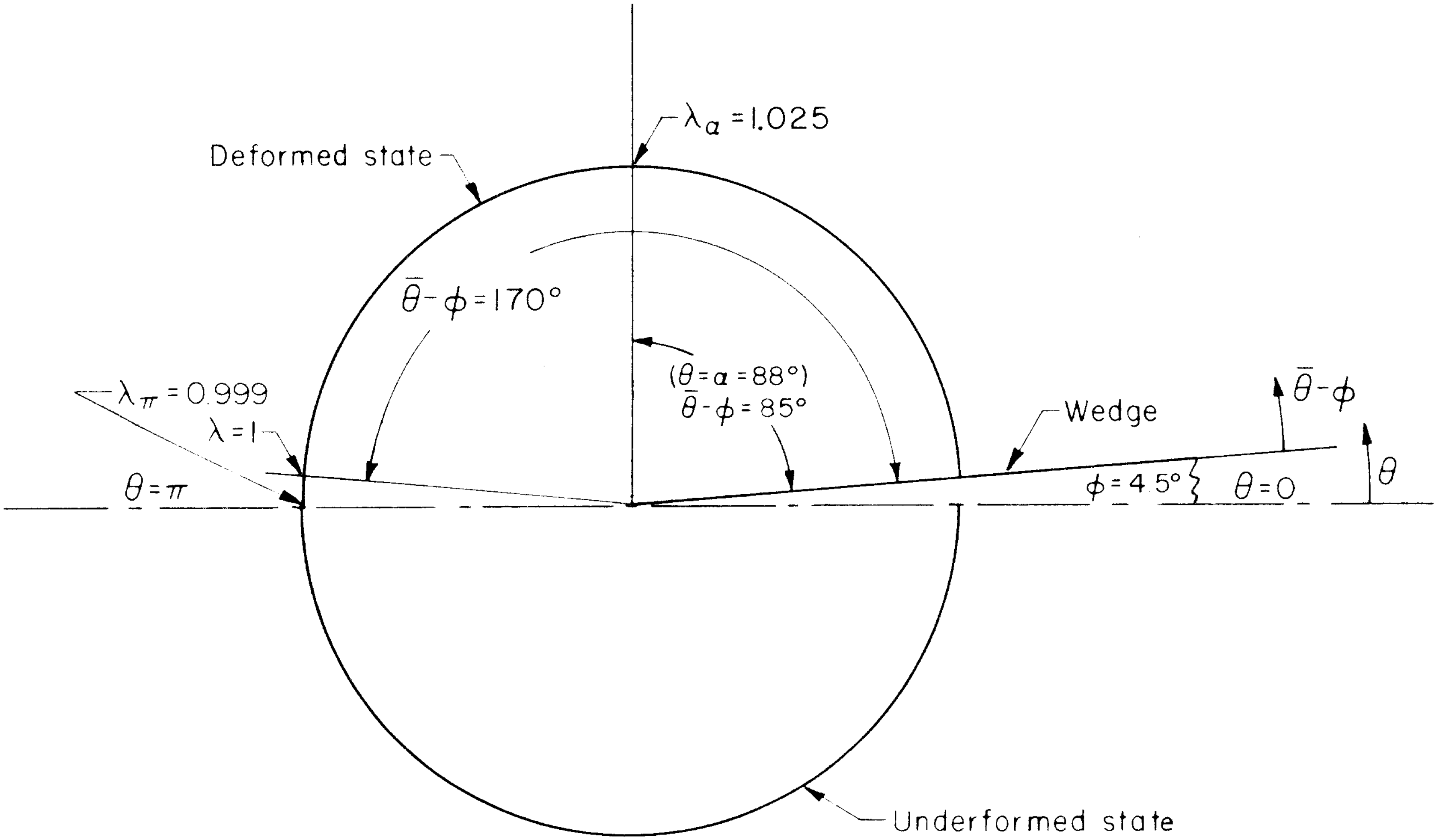

FIG. III. 6. Deformation of an Infinitely Long Rubber Log Spread Lengthwise by a Bonded Wedge (Flank Angle, $2\phi = 9^{o}$).

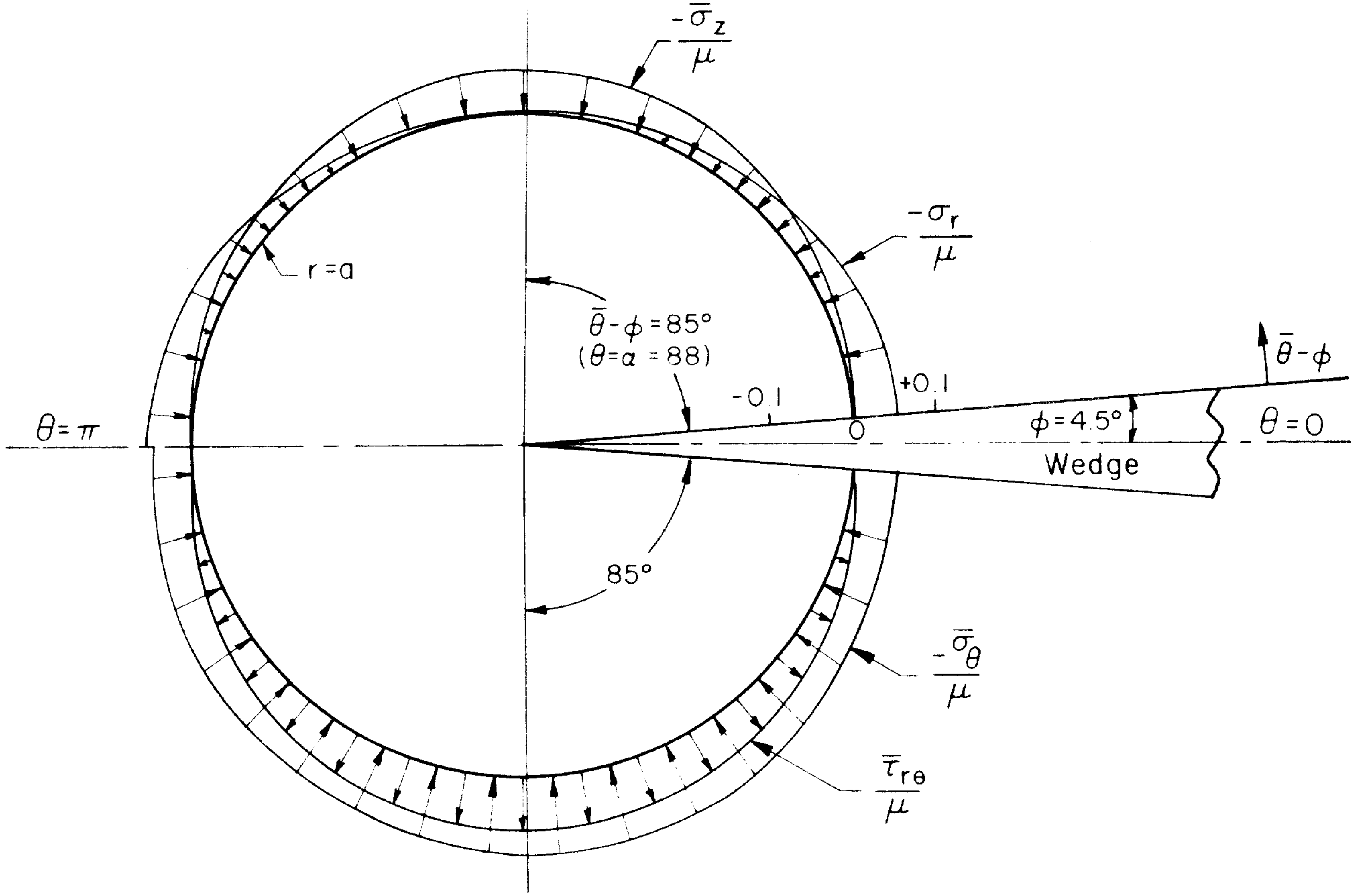

FIG. III. 7. Surface Tractions Required for the Specified Deformation Field (Flank Angle, $2\phi = 9^{\circ}$).

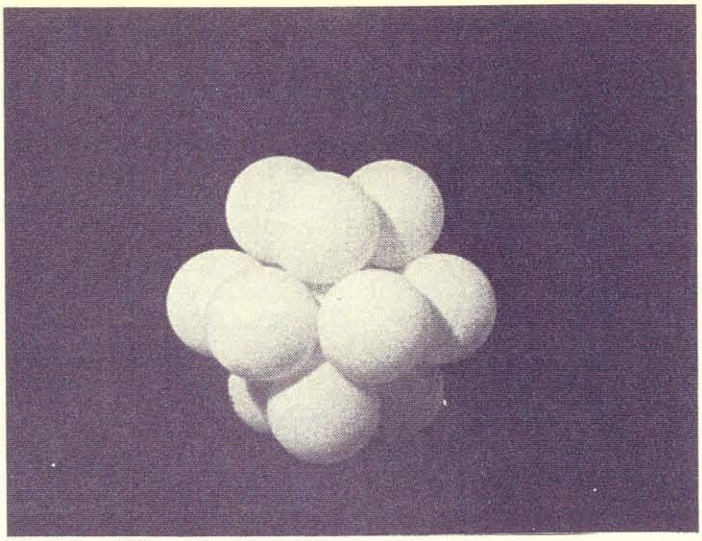

FIG. IV. 1. Hexagonal Closest Packing

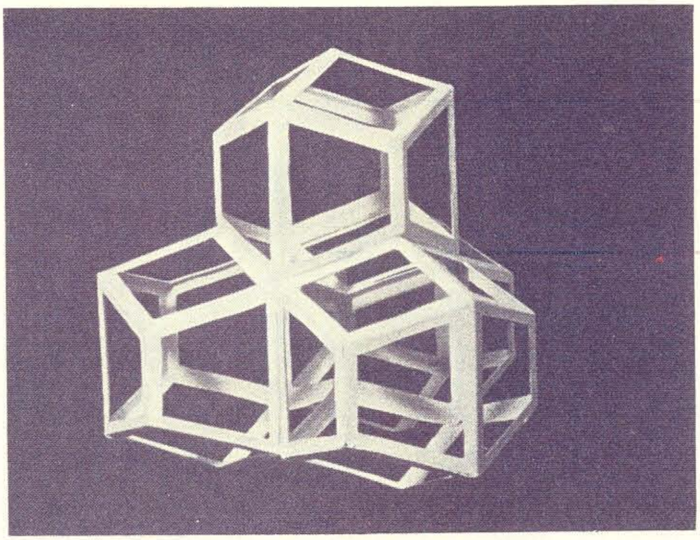

FIG. IV. 2. Interstices of Hexagonal Closest Packing

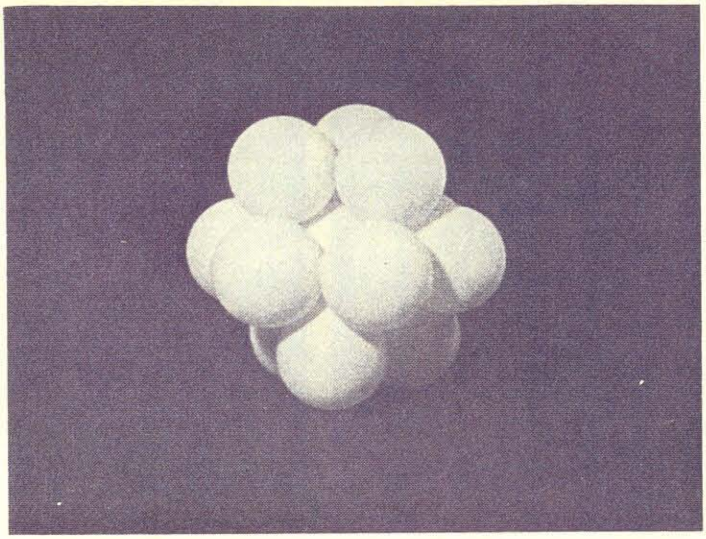

FIG. IV. 3. Face Centered Cubic Closest Packing.

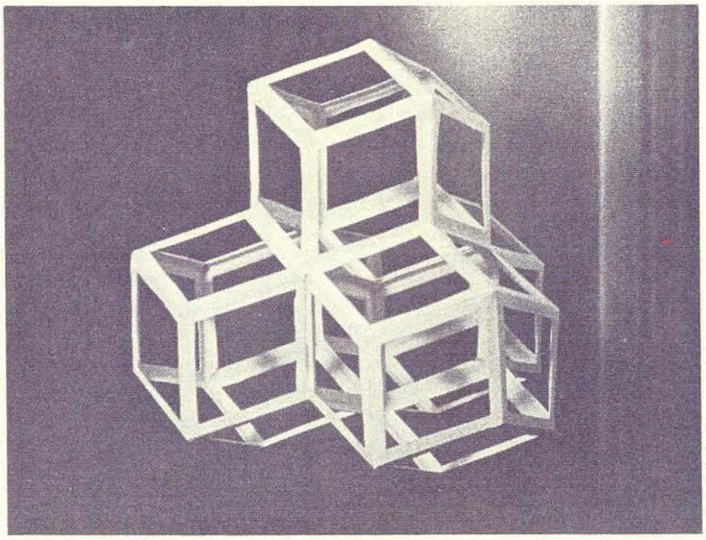

FIG. IV. 4. Interstices of Face Centered Cubic Closest Packing.

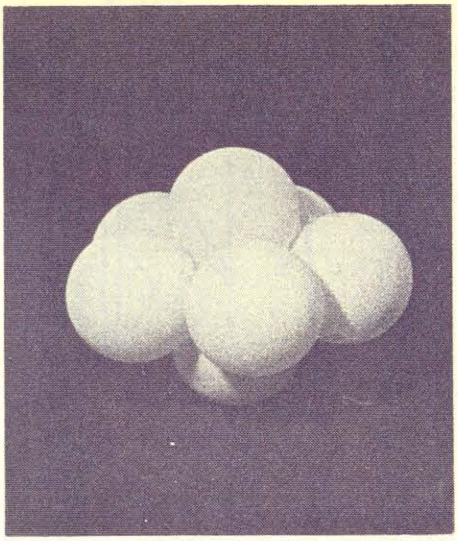

FIG. IV.5. Pentagonal Packing.

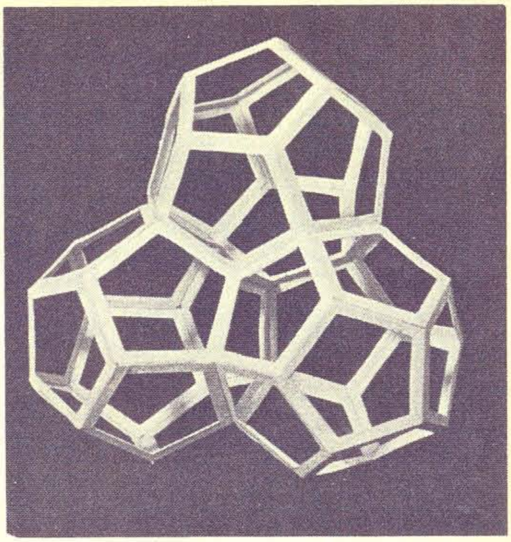

FIG. IV.6. Interstices of Pentagonal Packing

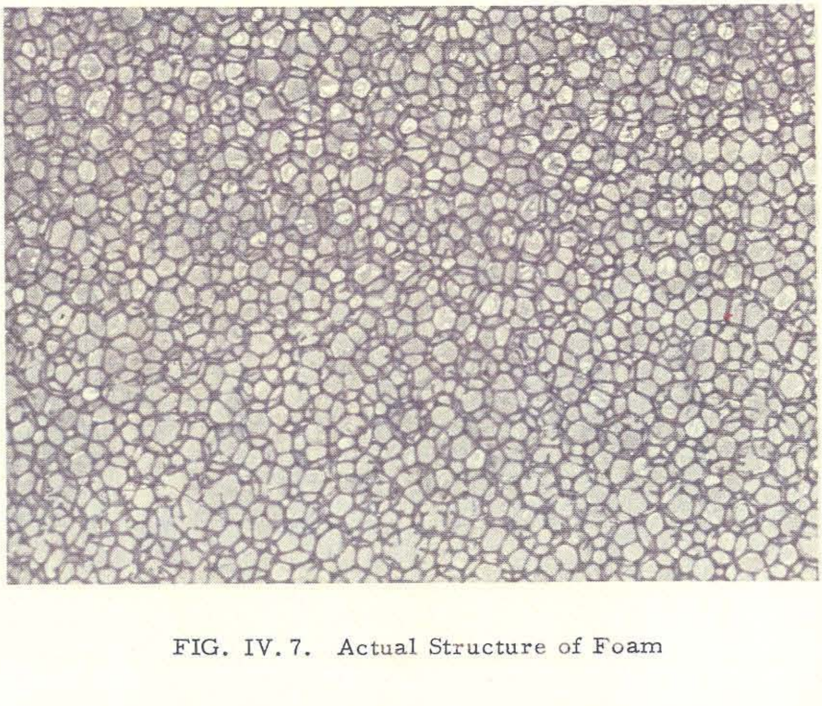

FIG. IV.7. Actual Structure of Foam

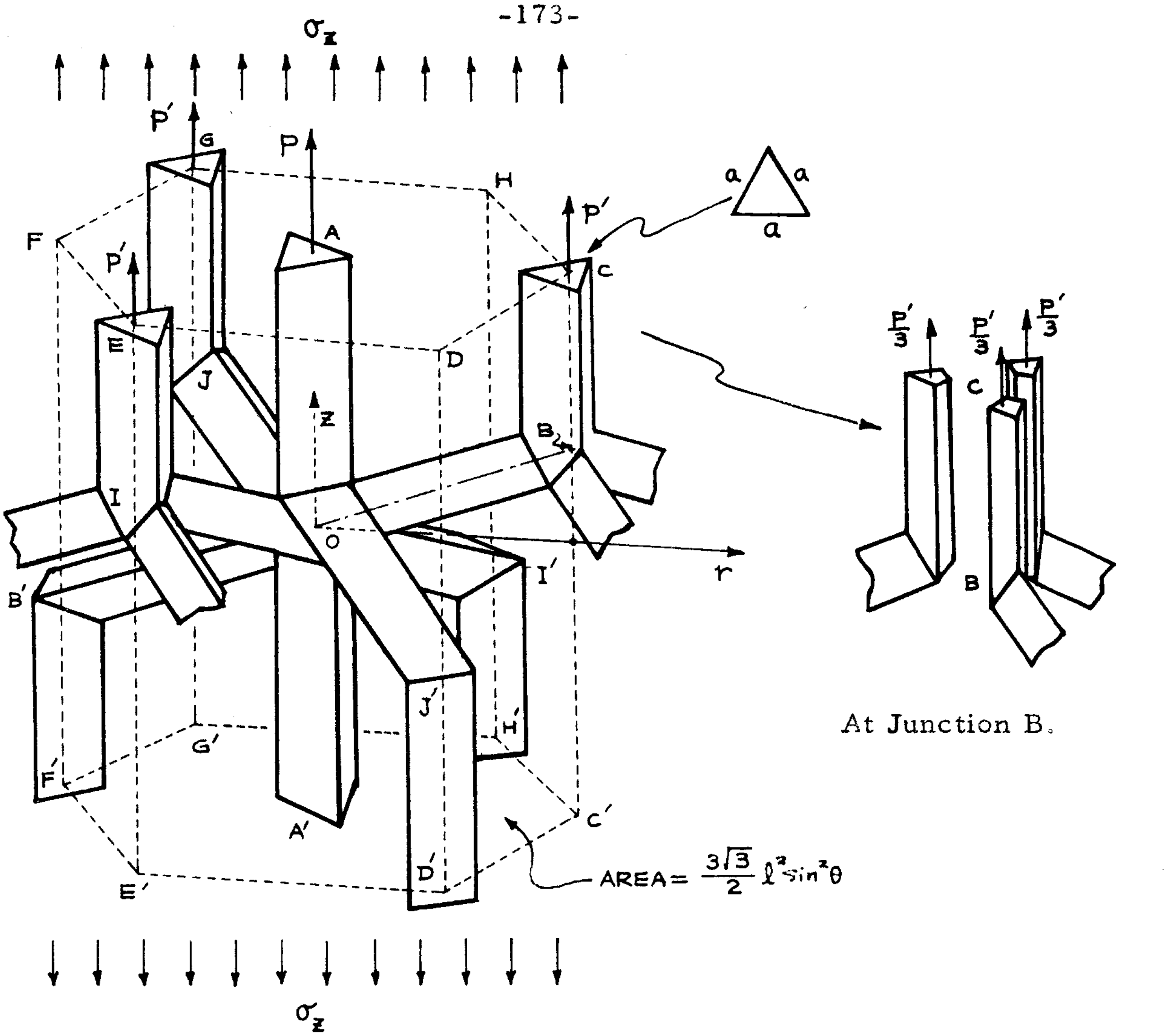

(a) Unit Structure

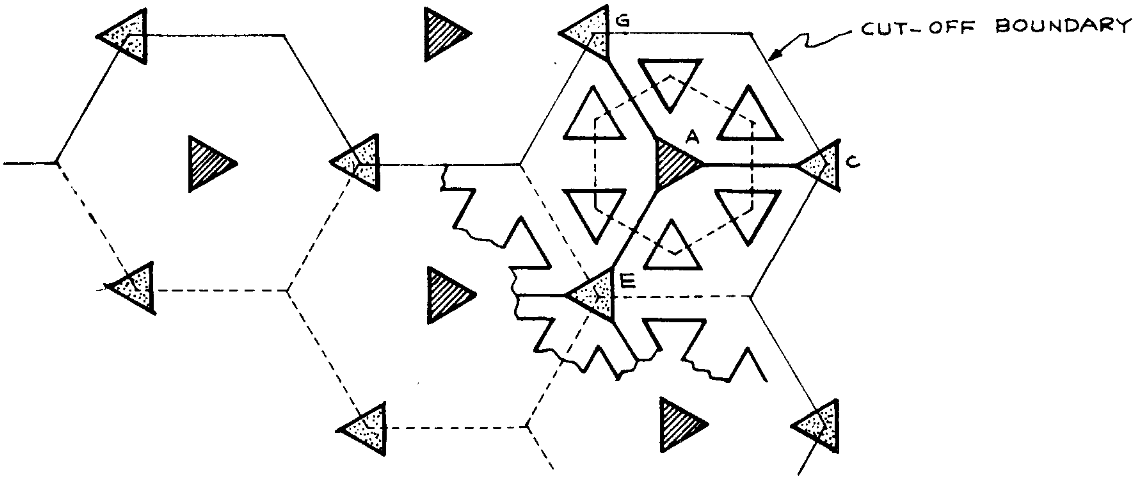

(b) Top View

FIG. IV.8. Idealized Interstices for Hexagonal Closest Packing.

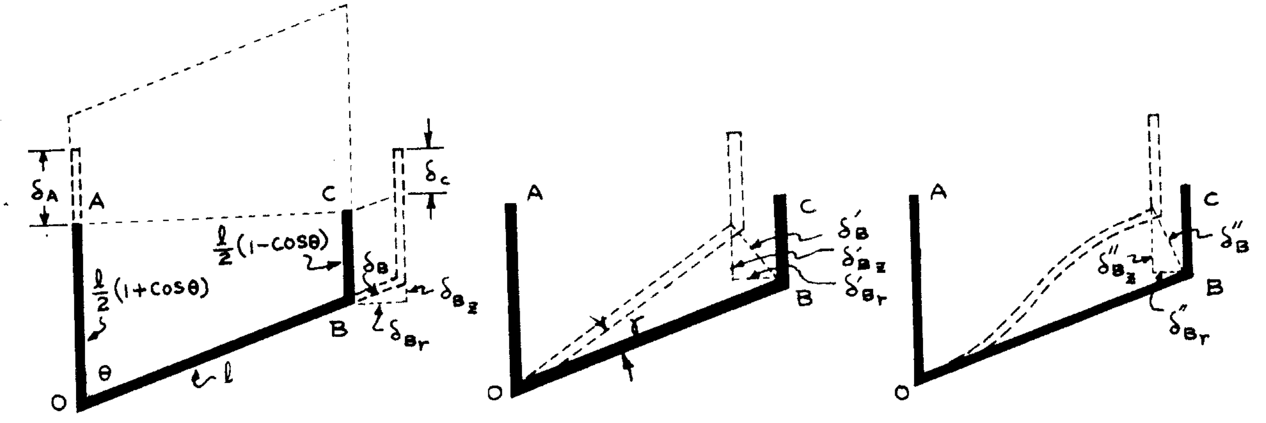

(a) Due to Tension (b) Due to Shear (c) Due to Bending

FIG. IV.9. Deformation of Member OB.

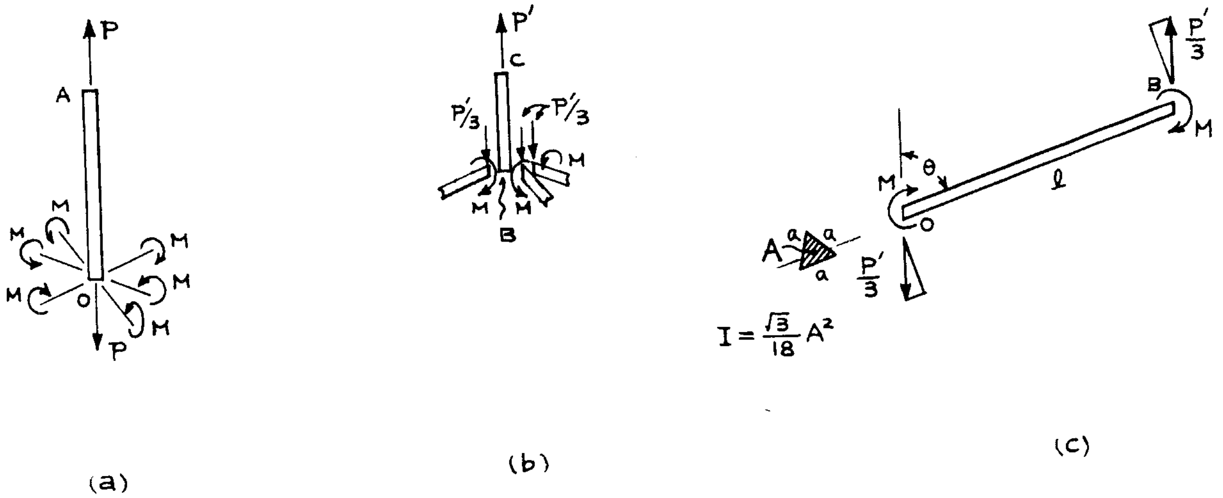

FIG. IV.10. Free Body Diagram of Members OA, BC, OB.

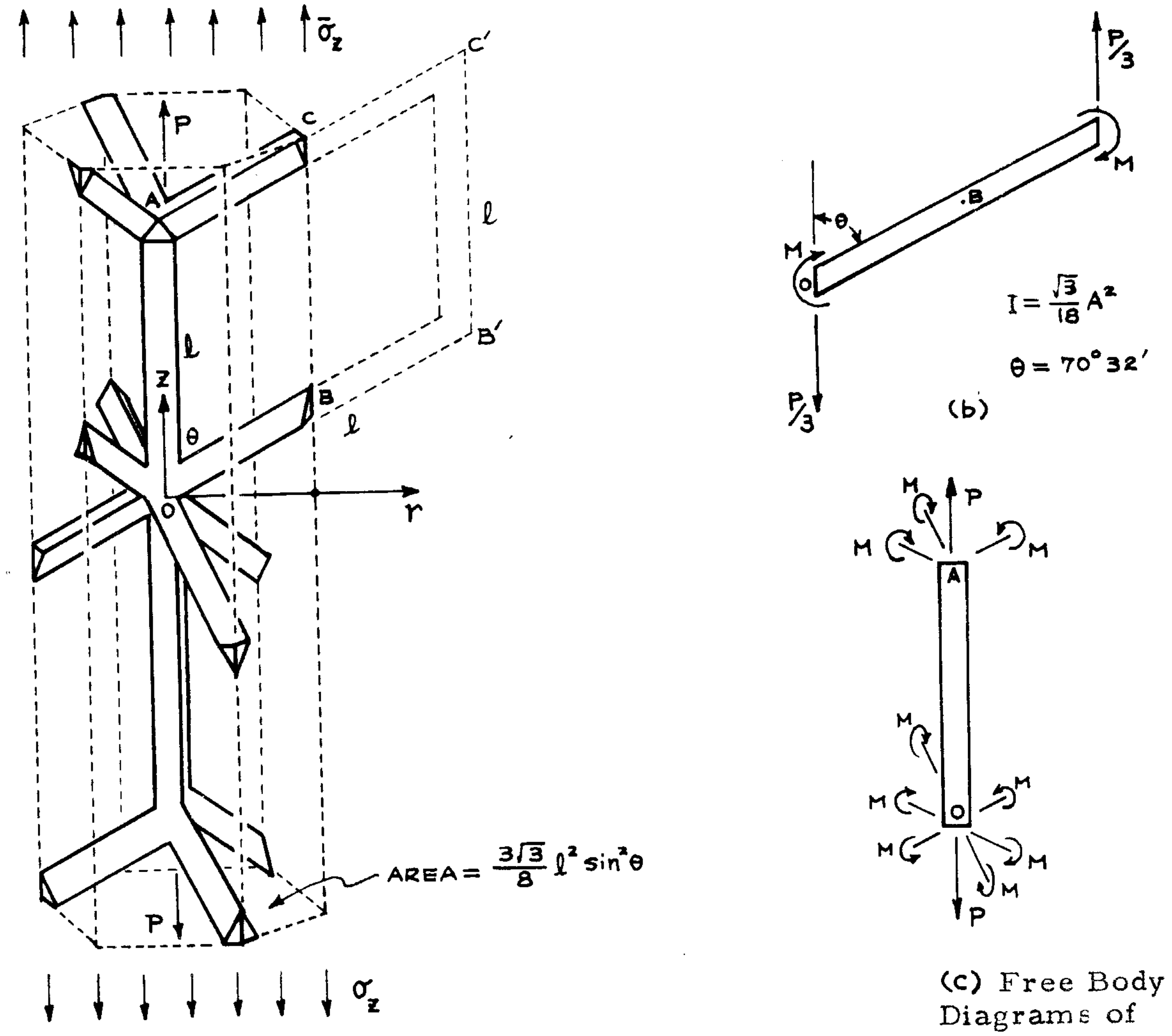

(c) Free Body Diagrams of OM and OA.

(a) Unit Structure

FIG. IV. 11. Idealized Interstices for Face Centered Cubic Packing.